Dynamics and thermal behaviour of films of oriented DNA fibres investigated using neutron scattering and calorimetry techniques

Jessica Valle Orero

École Normale Supérieure de Lyon

École doctorale de Physique et Astrophysique PHAST Lyon

Thèse

Pour l'obtention du grade de

Docteur de lÉcole Normale Supérieure de Lyon - Université de Lyon

Dynamics and Thermal Behaviour of Films of Oriented DNA Fibres Investigated using Neutron Scattering and Calorimetry Techniques

by

Jessica Valle Orero

Directeur et co-directeur de thèse:

Andrew Wildes et Michel Peyrard.

Membres du jury:

Tommy Nylander and Maria Barbi (rapporteurs)

Lambert van Eijck and Thierry Dauxois

Date de Soutenance: 26 Juin 2012

A papá, el mejor profesor que he tenido nunca, quién tomó mi mano y me enseñó el arte de aprender.

Abstract

The majority of structural studies on DNA have been carried out using fibre diffraction, while studies of its dynamics and thermal behaviour have been mainly performed in solution. When the DNA double helix is heated, it exhibits local separation of the two strands that grow in size with temperature and lead to their complete separation. This work has investigated various aspects of this phenomenon.

The experiments reported in this thesis were carried out on films of oriented fibres of DNA prepared with the Wet Spinning Apparatus. Thus, sample preparation and characterisation are essential parts of the research. The structures of two forms of DNA, A and B, have been explored as a function of relative humidity at fixed ionic conditions. A method to eliminate traces of ever-present B-form contamination in A-form samples was established.

The high orientation of the DNA molecules within the samples allowed us to investigate dynamical fluctuations and the melting transition of DNA using neutron scattering, which can provide the spatial information crucial to understand a phase transition, probing the static correlation length along the molecule as a function of temperature. The transition has been investigated for A and B-forms in order to understand its dependence on molecular configuration. Furthermore, after the first melting, denatured DNA films show typical glass behaviour. Their thermal relaxation has been explored using calorimetry.

Neutron and X-ray inelastic scattering (INS and IXS) were used in the past to measure longitudinal phonons in fibre DNA, and the results shown disagreement. Recent INS measurements supported with phonon simulations have been crucial to understand the different dispersion curves reported to date. Experiments using INS and IXS have been carried out to continue with this investigation. Attempts to observe the transverse fluc-

tuations associated to the thermal denaturing of DNA, never experimentally investigated before, have been made.

Résumé

La majorité des études structurales sur l'ADN avaient été réalisées par diffraction sur des fibres tandis que ses propriétés dynamiques thermiques avaient été essentiellement étudiées en solution. Lorsque la double hélice d'ADN est chauffée elle présente des séparations locales des deux brins, dont la taille augmente avec la température jusqu'à la séparation complète des brins. Ce travail étudie différents aspects de ce phénomène.

Les expériences présentées dans cette thèse ont été réalisées sur des films formés de fibres orientées d'ADN préparés par la méthode du "filage humide". La préparation et la caractérisation des échantillons en deux formes A et B de l'ADN ont constitué une partie importante de la recherche. Une méthode pour éliminer la contamination résiduelle de la forme B dans les échantillons de forme A a été mise au point.

La bonne orientation des molécules d'ADN dans les échantillons nous a permis d'étudier les fluctuations dynamiques et la transition de dénaturation thermique de l'ADN par diffraction de neutrons, sensibles à la longueur de corrélation statique le long de la molécule en fonction de la température. La transition a été étudiée pour les formes A et B pour déterminer comment elle dépend de la conformation. De plus, après la première dénaturation thermique, les films d'ADN présentent un comportement typique d'un verre. Leur relaxation thermique a été étudiée par calorimétrie.

La diffusion inélastique de neutrons et de rayons X (INS et IXS) avaient été utilisées antérieurement pour mesurer les phonons longitudinaux dans des fibres d'ADN, avec des désaccords entre les résultats. Des mesures INS récentes, complétées par des simulations, avaient été cruciales pour comprendre les différentes courbes de dispersion observées. Nous avons mené des expériences INS et IXS pour poursuivre cette analyse. Des tentatives pour observer les mouvements transversaux associés à la dénaturation thermique de l'ADN,

jamais observés expérimentalement, ont également été faites.

Acknowledgements

This research project would have never been possible without the experience, courage and enthusiasm of my two supervisors: Michel and Andrew. They have meant to me an altruist source of knowledge. But moreover, they promoted in me the development of three skills: independency, motivation and synergy, which I believe are very valuable if one wants to continue a scientific carrier. More specifically, to Andrew for being always so cheerful and making, with the help of youtube, those tedious nights in the instrument cabin more enjoyable... Et à Michel, pour avoir propulsé ce projet avec une passion, toujours aussi contagieuse.

A Jean-Luc et Jacques, tout a commencé par hasard... comme beaucoup des collaborations scientifiques j'imagine. Mais, avec vous je me suis senti accueillie, une voix à être écoutée et prise en compte. Hommes d'action, souvenir que je garderai de vous! Merci pour tous ce que vous m'avez enseigné, mais surtout pour la relation humaine que vous avez favorisé.

Among those years I had the chance to meet very experienced people in different fields with different ways of working, resulting in a perfect match to bring this work forward. For your ideas, time, effort, and most of all enthusiasm, which encouraged the project, I shall thank: Santiago Cuesta, Nikos Theodorakopoulos, Francis Merzel, Lambert van Eijck and Mark Johnson.

I would like to thank Trevor Forsyth for valuable discussions and predisposition to resolve doubts.

For their experimental and technical support I would like to thank: Michael Krisch, Elena Borissenko (ESRF); Andrew McCarthy, Jordi Xiol (EMBL); Martin Boehm, Monica, Sandrine (ILL); Manu and Abdel (CNRS).

A Karine Sultan, pour son efficacité, amabilité et de nous avoir faciliter le travail administratif rendant nos vies beaucoup plus faciles!
I would like to thank the ILL, for making me part of this family. To ENS, ILL and Michel for their funding. And to the respective research institutes for providing experimental time: ILL, ISIS (U.K), ANSTO (Australia), ESRF and CNRS.

From a more personal approach, I would like to thank:
To the friends I made during these three years. Science made possible the acquaintance, but it also separated us... to the day it will join us again... In order of appearance: Kent, Gergely, Mouna, Matxalen, Jordi, Miriam and Maite; and to those who were not crazy enough to go into science: Candice and Elise. Among all Martincin... for all our "moments", personal and professional. For the personal support at 3 am over life and choices, for the professional support at 3 am over a cryostat and choices... always available when I most needed you.
To my british office mates, Stu and Charlotte, for becoming my personal *wordreference*.
Para todos esos españoles, que van y vienen, pero que con los que compartí momentos memorables... y las fotos son la prueba de ello: Sergio, Javi, Willy, Elena, Victor, Leire, Pedro, Pilar....
A mis hermanas no-oficiales, porque os adoro y a pesar de tantos años de distancia siempre os he sentido cerca: Natalia, Adriana, Anna, Paula y Marieta.
Gordito, for all our rides: work-home-work-home-work-spain-work-garage-home....
A mi verdadera familia, por vuestro amor, por creer en mi... y por estar siempre ahí para festejar mis pequeños logros, y acoger mis fracasos. A Cari, por haber compartido una vez mas mi vida conmigo. A mamá, por ser el cariño personificado. A mi brillante hermano Segio por su inmerecida adoración, siempre tan orgulloso de su hermana. A Tali por su generosidad, y por seguir protegiéndome. Y a ti papá, por inspirarme! Con tu modelo me enseñaste dos cosas: que la ambición no debería de ser más que el fuerte deseo de aprender, y que saber no es una cuentión de inteligencia sino de perseverancia, y lo mas importante de disfrutar con ello.
And finally to Mike for your unconditional support and patience. For always being ready to help, although not every time your advice made things easier, they certainly made them better. Because you have been with me during these three years, and even closer during my writing.

Contents

Chapter 1

Introduction

Watson and Crick revealed the static structure of DNA from an X-ray diffraction image obtained from a sample of fiber DNA [1]. The crystallographic analysis probed the double helix structure whose strands are joined together by nitrogen base pairs arranged periodically along the molecular axis.

Despite the interest in investigating DNA in solution, the environment for which it is found in physiological conditions, diffraction experiments made clear that structural information could only be obtained through the fiber form of DNA where its molecules are oriented. In the early 60's Allan Rupprecht designed the Wet Spinning apparatus, a technique to turn these individual micro fibers into films of few cm^2 in size [2]. The process consists in injecting a diluted solution of counterion-DNA into concentrated EtOH. The DNA aggregates and consequently precipitates, to finally been rolled up on a cylinder. The configurational flexibility of oriented fibers permits the penetration of water, and leaves space for the DNA to change structure. Depending on the initial conditions of the DNA solution, such as nature of the counter-ion and concentration, or changes in hydration (relative humidity) different DNA conformations can be induced. Through X-ray and neutron diffraction techniques, oriented fibers DNA have been characterised under different structures: including A-form, B-form and mixed A/B-forms.

DNA is far from having the static structure the diffraction images suggest. At biological temperatures the nitrogen base pairs can fluctuate, or even break temporarily. These emerging bubbles can be activated by heating, local openings of the double helix grow and extend over the full molecule leading to a complete separation of the two strands. It is called denaturing or melting of DNA. Watson and Crick already suspected that this

phenomena played a crucial role in genetic processes,

" Now our model for deoxiribonucleic acid is, in effect, a pair of templates, each of which is complementary to the other. We imagine that prior to duplication the hydrogen bonds are broken, and the two chains unwind and separate. Each chain then acts as a template for the formation on to itself of a new companion chain, so that eventually we shall have two pairs of chains, where we only had one before. Moreover, the sequence of the pairs of bases will have been duplicated exactly"

It is this phenomena which led to their famous phrase: *"We have discovered the secret of life!"*. Watson and Crick's contribution raised questions about the relation between form and function, statics and dynamics. This new dynamical system not only led biologist on the threshold because of its genetic implications, but the whole world was watching. DNA has become the most multidisciplinary sample of our time.

To date, the thermal stability upon heating of the DNA in solution has been investigated in detail using bulk techniques such as Raman spectroscopy, UV absorbance, and calorimetry [3][4]. Physicists have investigated thermal denaturing of DNA as a phase transition detected in the form of these emerging bubbles. The phase transition describes the structural change from double to single stranded DNA through the behaviour of the order parameter, in our case the number of helix base pairs, as a function of temperature. Structural information is essential to characterise the denaturation transition. Neither these bulk techniques nor having DNA in solution, can provide any information on the spatial distribution of the closed base pairs regions.

We have mainly used calorimetry and neutron scattering techniques to study the melting properties of several DNA conformations induced under different conditions. Calorimetry gives access to the thermodynamic macroscopy quantities such as enthalpy, heat capacity, melting temperature and entropy. Furthermore it is used as a preliminary study of the melting profile of the different structures. Once these have been established, structural information needs to be obtained for a full understanding of the transition. The dynamical fluctuations leading to the melting transition can be investigated using neutron scattering techniques which allow one to probe the static correlation length along the DNA molecule as a function of temperature. This became possible by the use of oriented fibers of DNA, as they are analogous to low dimensional systems oriented along the helical axis.

A theoretical analysis of the neutron scattering experiments with a mesoscopic model of

DNA fluctuations and denaturation has been carried out. The mesoscopic model corresponds to the Peyrard-Bishop-Dauxois statistical physics model [5][6], applied to a 1-D crystal composed of consecutive closed base pairs. The model reproduces the melting curves for different DNA sequences, and moreover it has been extended to account for spatial correlations along the molecule through the melting transition [7] [8].
A phase transition, at high temperature, is driven by a particular normal mode by destabilising the whole crystal structure of the system [9]. That is why the major interest in phonons evolved towards their influence on the melting of DNA. Transverse phonons associated with the thermal fluctuations of the base pairs perpendicular to the helical axis have a major role in denaturing [10], but still very little is known about them. In addition, longitudinal acoustic modes have been shown to provide direct information about the flexibility of DNA, and thus contribute to the formation of local denatured regions [11].
Furthermore, after the first melting, thermal denaturation in DNA films has shown to be irreversible, but instead typical glass like behaviour is observed. The properties of this biological glass have also been investigated [12].

Thesis Outline

1. Chapter 2 provides a description of the main experimental techniques used to carry out the experiments presented in this manuscript: Neutron and X-ray scattering techniques, as well as Differential Scanning Calorimetry.

2. Chapter 3: Presents a brief historical review of DNA fibre. First it gives an overview of the general properties of DNA, to finally describe the experimental studies in DNA fibre. References to the work carried out on fiber DNA to investigate the characterisation of different structures, as well as high and low amplitude dynamics, have been given.

3. Chapter 4: The first part of the chapter reviews the equipment and technique of the wet spinning apparatus with which oriented samples DNA were prepared. These samples have been used to carry out all the experiments presented in this thesis. The second part of the chapter gives an extensive characterisation of the different DNA structures using X-ray fiber diffraction, neutron diffraction, calorimetry and optic microscopy.

4. Chapter 5: The thermal denaturation of B- and A-DNA has been investigated using DSC and neutron scattering techniques. The chapter first presents a comparison of the melting curves and thermodynamical properties at the transition of the different investigated structures using DSC. Then, it provides the experimental analysis of the structural correlations as a function of temperature and melting properties of DNA films using neutron scattering techniques, complemented with a theoretical analysis using the PBD model.

5. Chapter 6: Corresponds to the study of the glassy properties of DNA films after heated above the thermal denaturation temperature. The non-equilibrium glass state has been characterised by the relaxation time of the DNA films by the means of the fictive temperature, and its enthalphic spectrum associated to the experimental method.

6. Chapter 7 includes a description of several experiments to investigate longitudinal and transverse phonons in oriented DNA films using inelastic X-ray and neutron scattering techniques.

Chapter 2

Experimental Methods

2.1 Foreword

The aim of this section is to take the reader into the basic principles of neutron scattering, X-ray scattering and calorimetry techniques, including the main formula that have been explicitly and implicitly used for the completion of the experimental part of this thesis.

2.2 Neutron scattering

A brief description of the different techniques used: triple axis and time-of-flight spectrometry, will be discussed. The theory presented only alludes to nuclear scattering; no mention will be given to magnetic scattering since this topic was never investigated. Neither will the neutron spin contribution be included in the mathematical analysis since polarised neutrons were never used.
This section has been prepared with the help of different sources but all the treatment can be found in the following books: Squires [13]; Furrer, Mesot and Strässle [14]; Celotta and Levine [15]; and Ashcroft and Mermin [16].

2.2.1 Principles

The discovery of the neutron by Chadwick in 1932 promoted the creation of neutron sources to investigate this particle and its applications. It was soon considered as a potential probe to study matter, and only 14 years later, Ernest O Wollan and Clifford G Shull established the basic principles of neutron diffraction technique using the Graphite

Reactor at the Oak Ridge National Laboratory, US. Between the 50′s-70′s decades a series of neutron research reactors were built aimed to become centres for the scientist to develop their research. In 1972 the Institute Laue-Langevin started to operate as one of the most intense sources in the world. The experiments within these facilities already covered a broad range of fields, from the study of magnetic materials to biophysics, since the instruments were suited to samples of different nature: soft, liquids, solid, etc. In the last decades, the expansion of this technique has been specially due to the consolidation of a variety of techniques: diffraction, inelastic scattering, small angle scattering, diffuse scattering, spin echo spectroscopy, the use of polarised neutrons... and their applications. Altogether, these techniques have become some of the most powerful tools to study the structure and dynamics of materials at the atomic and molecular level. They have also become the main source to contribute in the investigation of magnetic and hydrogenous materials.

The properties of the neutron

Neutrons for scattering experiments are produced in a nuclear reactor by fission or in a spallation source by spallation of heavy nuclei. The neutrons are slowed down by a moderator which consists of atoms of similar masses to neutrons, hydrogen or deuterium, through the exchange of energy by collisions. Their energies can be described with Maxwellian distributions after they have been moderated. There are three classifications of resulting neutrons depending on the temperature of their moderation medium. They are: hot, thermal and cold neutrons. Thermal neutrons hold energies $\sim k_B T_M$, of the order of 10-100 meV. They interact with the nucleus of the atoms via the strong interaction force, which makes them very penetrating source. Even if the neutron is not charged, it has a spin magnetic moment resulting from a 1/2 spin, which interact with the magnetic moments of the particles. One of the most important characteristics of the neutron lies in the properties of wave-particle duality, and is in this wave behaviour that the principles of neutron scattering lie. From the de Broglie theory, a particle having a mass and velocity can be expressed as a wave function whose momentum, $\mathbf{k}$, can be expressed with the following equation,

$$\mid \mathbf{p} \mid = \frac{h}{\lambda} = \hbar \mid \mathbf{k} \mid . \tag{2.1}$$

The momentum vector for non-relativistic particles is also defined by

$$\mathbf{p} = m\mathbf{v}, \tag{2.2}$$

where m is the mass and $\mathbf{v}$ is the velocity of the particle, λ is the wavelength and h is Planck's constant. The kinematics of the neutron are defined by energy E and $\mathbf{k}$.

In a scattering experiment the energy and momentum exchanged by the neutron with the sample are measured by the changes in the momentum and energy of the neutron. The momentum process is described mathematically by the following formulae,

$$\mathbf{Q} = \mathbf{k_i} - \mathbf{k_f}, \tag{2.3}$$

where $\mathbf{Q}$ is the momentum transfer or also called the scattering vector, $\mathbf{k_i}$ and $\mathbf{k_f}$ are the initial and final wavevectors of the neutron.

The energy conservation is given by the equation,

$$\hbar\omega = E_i - E_f, \tag{2.4}$$

where the energy change is expressed by an angular frequency, ω, and E_i and E_f are the initial and final energies of the neutron. By using the de Broglie relation, the energy of a neutron can be expressed as:

$$E = \frac{h^2}{2m_n\lambda^2} = \frac{\hbar^2k^2}{2m_n} = \frac{m_nv^2}{2} \simeq k_BT, \tag{2.5}$$

where m_n is the mass of the neutron.

It is very useful to know the conversion equations between energy, momentum,wavelength and temperature:

$$E[meV] = 81.81\frac{1}{\lambda^2}[\text{Å}^2] = 2.072k^2[\text{Å}^{-2}] = 5.227v^2\left[\left(\frac{km}{s}\right)^2\right] = 0.08617T[K]. \tag{2.6}$$

From these relations we can express the energy transfer in terms of the wavenumber,

$$\hbar\omega = \frac{\hbar^2(k_i^2 - k_f^2)}{2m_n}. \tag{2.7}$$

And from equations 2.3 and 2.4 the dynamical kinematic triangle is expressed as,

$$\frac{\hbar^2 Q^2}{2m_n} = 2E_i - \hbar\omega - 2\sqrt{E_i(E_i - \hbar\omega)}\cos 2\theta. \tag{2.8}$$

Scattering cross-sections

In order to analyse a scattering process in detail, we shall first define the cross-section equations. In a scattering process, what it is measured is the number of neutrons with an initial wavevector $\mathbf{k_i}$, and energy E_i, that are scattered by a target into a solid angle $d\Omega$ with a final wavector $\mathbf{k_f}$ and a final energy E_f. The following figure summaries the scattering process using polar coordinates. With the aid of Figure 2.1 we can describe the three cross-sections equations.

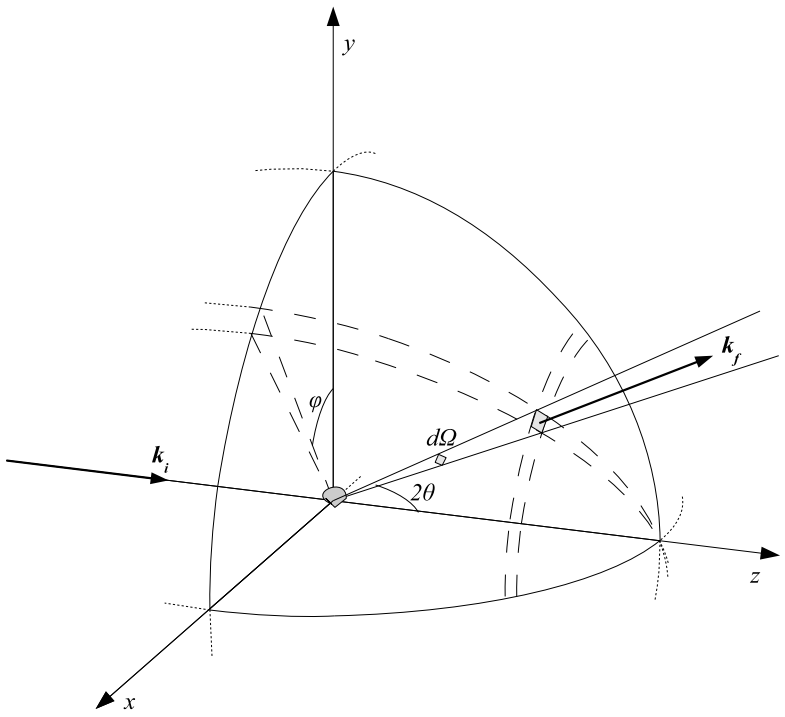

Figure 2.1: Geometry for scattering experiment. The picture is courtesy of Dr. Gergely Nagy

The scattering geometry in figure 2.1 assumes that the detector is very far from the target, the neutrons are scattered into a solid angle $d\Omega$ with a final energy in the range of E_i - $E_f + dE$. This leads to an expression of the partial differential cross-section:

$$\frac{d^2\sigma}{d\Omega dE_f} = \text{particle flux scattered into a solid angle } d\Omega \quad (2.9)$$
$$\text{in a direction given by } (\theta, \phi) \text{ with a final energy } E_f + dE,$$
$$\text{divided by the incoming intensity.}$$

The units of equation 2.9 are given as an area. If the differential cross-section is integrated with respect to the energy change dE, a second cross-section equation is defined: the differential cross-section

$$\frac{d\sigma}{d\Omega} = \int_0^\infty \left(\frac{d^2\sigma}{d\Omega dE}\right) dE, \quad (2.10)$$
$$\frac{d\sigma}{d\Omega} = \text{particle flux scattered into } d\Omega$$
$$\text{in a given direction, } (\theta, \phi) \text{ divided by the incoming intensity.}$$

When neither energy change nor direction of scattering is analysed, the differential cross section becomes the total scattering cross-section:

$$\sigma_{tot} = \int_{alldir} \left(\frac{d\sigma}{d\Omega}\right) d\Omega, \quad (2.11)$$
$$\sigma_{tot} = \text{scattered particles into all directions}$$
$$\text{divided by incident intensity.}$$

When a single elastic scattering event takes place, the probability per second that the neutron and scattering system in a initial state $\mid \mathbf{k_i}, \mathbf{n_o}\rangle$ undergoes a transition into a final state $\mid \mathbf{k_f}, \mathbf{n_1}\rangle$, is described by the transition rate, $W(\mathbf{k_i}, n_o \rightarrow \mathbf{k_f}, n_1)$. If k_i, n_0 and n_1 remained fixed, the sum over all possible values of k_f comprising in $d\Omega$ have to be considered, so hence the cross-section is given as,

$$\left(\frac{d\sigma}{d\Omega}\right)_{n_0 \rightarrow n_1} = \frac{1}{\Phi_i}\frac{1}{d\Omega} \sum_{\mathbf{k}_f \text{in d}\Omega} W(\mathbf{k_i}, n_o \rightarrow \mathbf{k_f}, n_1), \quad (2.12)$$

where Φ_i is the flux of incident neutrons. A nuclear interaction occurs at a very short range (fm). The wavelength of the neutron is of the order of 10^5 times bigger. This is a

very important fact since it allows some assumptions to be made regarding the scattering cross-sections. When scattering from a single, fixed nucleus, the neutron may be assumed to experience a point-like potential $V(\mathbf{r})$, and thus the scattered wave is a spherical symmetric wave, or s-wave, expressed as $\Psi = \frac{-b}{r}e^{ikr}$. The transition from an initial state k_i, n_0 to a final state k_f, n_1 (final sample state is fixed) will only occur for the values $|k_f|$ lying in the small solid angle, otherwise the probability is negligible. Within this scenario, Fermi's Golden Rule can be used to evaluate the transition rate expression,

$$\sum_{k_f \text{ in } \mathrm{d}\Omega} W_{\mathbf{k}_i, n_0 \to k_f, n_1} = \frac{2\pi}{\hbar}\rho_{\mathbf{k}_f} \mid \langle \mathbf{k}_f, n_1 \mid V(\mathbf{r}) \mid \mathbf{k}_i, n_0 \rangle \mid^2, \tag{2.13}$$

where $\rho_{\mathbf{k}_f}$ is the density of final states in $d\Omega$, and $V(\mathbf{r})$ is called Fermi pseudopotential. The expression on the right hand side of the equation can be solved using the Born Approximation, based on the first order perturbation theory. This approximation can be used in the basis of two assumptions: the incident and scattering wave are considered plane waves and the interaction between the neutron and nucleus is weak, given by the Fermi pseudo-potential.

If the scattering process is inelastic, the cross-section becomes the double differential equation where the conservation of energy and momentum between sample and neutron must be ensured. This results in,

$$\frac{d^2\sigma}{d\Omega dE_f} = \left(\frac{m}{2\pi\hbar^2}\right)^2 \frac{k_f}{k_i} \mid \langle \mathbf{k_f}, n_1 \mid V(\mathbf{r}) \mid \mathbf{k_i}, n_o \rangle \mid^2 \delta(\varepsilon_{n_1} - \varepsilon_{n_o} - \hbar\omega). \tag{2.14}$$

where $V(\mathbf{r})$ must be regarded as a short range attractive/repulsive potential between a fixed nucleus and a neutron.

$$V(\mathbf{r}) = \sum_j b_j \delta(\mathbf{r} - \mathbf{R_j}). \tag{2.15}$$

From the equation, $\mathbf{R_j}$ is the position vector of each nuclei, $\mathbf{r}$ is the neutron's position vector and b_j is the scattering length for each nuclei.

The variable b is properly called the scattering length. It is (θ, ϕ) independent, and for the majority of the elements b is also neutron energy independent. Its value is subjected to the nucleus and the spin state between nucleus-neutron, knowing that the neutron has $\frac{1}{2}$ spin, all nuclei with non-zero spin ($I \neq 0$)will have two values of b (for each of the total spin: $I + \frac{1}{2}$ and $I - \frac{1}{2}$). In such a case, each b will only depend on the spin orientation of

the nucleus of the atoms and the isotopes. The scattering length is written as a complex quantity with the imaginary part related to the absorption. High neutron absorbers are, ^{113}Cd, ^{103}Rh or Gd, but most materials have negligible absorption. The total cross section is calculated by taking the average of the scattering lengths.

Henceforth, the final double differential cross-section for nuclear scattering can be obtained by applying the following steps: inserting equation (2.15) into equation (2.14), expressing the δ- function as a time integral by introducing the Heisenberg time-dependent operators, sum over all final states n_1 for a fixed initial state n_0 and finally average over all n_0,

$$\frac{d^2\sigma}{d\Omega dE_f} = \sum_{n_0,n_1} p_{n_0} \left(\frac{d^2\sigma}{d\Omega dE_f}_{n_0 \to n_0} \right) \tag{2.16}$$

$$= \frac{k_f}{k_i} \frac{1}{2\pi\hbar} \sum_{j,j\prime} b_j b_{j\prime} \int_{-\infty}^{\infty} \langle e^{-i\mathbf{Q}\hat{\mathbf{R}}_{\mathbf{j}\prime}(0)} e^{i\mathbf{Q}\hat{\mathbf{R}}_{\mathbf{j}}(t)} \rangle e^{-i\omega t} dt. \tag{2.17}$$

This finally leads to the most important form of the differential cross-section in neutron scattering theory since it is directly related to the dynamical structure factor or scattering function, $S(\mathbf{Q}, \omega)$. This relation was first expressed by Van Hove in 1954 [17].

$$\frac{d^2\sigma}{d\Omega dE_f} = N \frac{k_f}{k_i} \frac{\sigma_{tot}}{4\pi} S(\mathbf{Q}, \omega), \tag{2.18}$$

where σ_{tot} is the mean total scattering cross-section for a non-monoatomic sample, and it may be written as,

$$\sigma_{tot} = \frac{4\pi}{N} \sum_j \bar{b_j^2} \tag{2.19}$$

The aim of a scattering experiment is to measure the scattering function, $S(\mathbf{Q}, \omega)$. It provides information about the momentum and energy transferred by the neutron to the sample, and thus the positions and motions of the atoms comprising the sample can be determined.

Correlation functions

L. van Hove showed the relation between the dynamical structure factor, $S(\mathbf{Q}, \omega)$ and the space-time pair correlation function, $G(\mathbf{r}, t)$ through Fourier transformations. These are,

$$S(\mathbf{Q},\omega) = \mathcal{F}_t[\mathcal{F}_r^{-1}[G(\mathbf{r},t)]], \tag{2.20}$$

$$\propto \int\int e^{i(\mathbf{Q}\mathbf{r}-\omega t)} G(\mathbf{r},t) dr dt. \tag{2.21}$$

This relation demonstrates that the pair correlation function can be experimentally attainable by measuring the double differential equation, equation 2.17. $\mathbf{G}(\mathbf{r},t)$ is the most general expression to characterise the statics and dynamics of an atomic system, describing the probability of having two atoms correlated in space and time, i.e. given an atom, j' at time $t=0$ and position $r'+r$, it gives the probability of finding another atom, j at a later time t and position r'. This is mathematically expressed by,

$$G(\mathbf{r},t) = \frac{1}{N}\left\langle \sum_{j',j=1}^{N} \int \delta(\mathbf{r}+\mathbf{r}'_j(0)-\mathbf{r}')\delta(\mathbf{r}'-\mathbf{r_j(t)})\right\rangle. \tag{2.22}$$

Coherent *vs.* Incoherent Scattering

Recall that the scattering length b_j depends on the intrinsic characteristics of each nucleus, i.e. the spin quantum number and the isotope, so that $b_{j,j'}$ of two nuclei are independent. We may divide the sum in equation 2.17 in two parts: where $j = j'$, and where $j \neq j'$. This results into two contributions to the differential scattering cross section: incoherent and coherent scattering.

The coherent signal appears as the result of pair correlation between the atoms. It is a collective phenomenon which permits the determination of the probability that an atom is at a position with respect to the rest of the sample. Bragg diffraction and phonon scattering are examples of elastic and inelastic coherent scattering respectively. On the other hand, incoherent scattering is due to the interference of the different phases (non-preferred direction) of random scattering centres, it is isotropic. It evaluates the self-correlated motions in space and time of individual particles, such as diffusion. When carrying out a scattering experiment, the data will be composed of those two main features, coherent and incoherent signal and the amplitudes of the signals are given by cross-sections, σ_{coh} and σ_{inc}.

$$(\frac{d^2\sigma}{d\Omega dE_f})_{coh} = N\frac{k_f}{k_i}\langle b\rangle^2 S_{coh}(\mathbf{Q},\omega), \tag{2.23}$$

$$(\frac{d^2\sigma}{d\Omega d\omega})_{incoh} = N\frac{k_f}{k_i}[\langle b^2\rangle - \langle b\rangle^2]S_{incoh}(\mathbf{Q},\omega), \tag{2.24}$$

where σ_{coh} is calculated with the average scattering length over the whole sample, while σ_{incoh} describes self-correlation expressed as the variance in the scattering lengths:

$$\begin{aligned} \sigma_{coh} &= \langle b\rangle^2, \\ \sigma_{incoh} &= [\langle b^2\rangle - \langle b\rangle^2]. \end{aligned} \tag{2.25}$$

Examples of σ_{coh} and σ_{incoh} for two different elements, hydrogen and deuterium, are showing in the table below. The units of the cross-sections are $10^{-28}m^2$.

Element	σ_{coh}	σ_{incoh}
^1H	1.8	80.2
^2H	5.6	2.0

Table 2.1: Coherent and incoherent total cross-section for hydrogen (^1H) and deuterium (^2H).

Experimentally, the incoherent scattering normally appears as a background in the total scattering signal. However, a material with high incoherent scattering cross-section can be useful for standard calibration of the neutron flux of the spectrometer at the positions where the sample was measured. This is the case of vanadium metal with $\sigma_{inc} = 276\sigma_{coh}$.

2.2.2 Scattering by crystals

Bragg scattering

Bragg scattering is an elastic coherent scattering process. Elastic processes tells us about the time-averaged structure of the systems, where the atoms are distributed within the lattice. The scattering cross sections expressed in the previous section described the interaction of a neutron with a system of atoms. The correlation function is given by a periodic lattice. The scattering is given by the Fourier Transform of this lattice and may be expressed in momentum, or reciprocal space. Thus, the real ($\mathbf{r}$) and reciprocal ($\mathbf{G}$) coordinate system are related by the Fourier transforms. Considering the simplest case

of a Bravais lattice (one atom per unit cell), this is expressed as

$$n_{\mathbf{G}} = \frac{1}{V_{cell}} \int n(\mathbf{r}) e^{\mathbf{Gr}} dV, \tag{2.26}$$

where $n(\mathbf{r})$ is the spatial density distribution of the scatterer, $n_{\mathbf{G}}$ is the Fourier transform of $n(\mathbf{r})$ and V_{cell} is the volume of a unit cell. If we define $\mathbf{R}$ as a vector of each point in the Bravais lattice, then $\mathbf{r} \rightarrow \mathbf{r} + \mathbf{R}$. Putting this back into equation 2.26,

$$e^{\mathbf{rG}} = e^{(\mathbf{r}+\mathbf{R})} = e^{\mathbf{RG}} = 1. \tag{2.27}$$

And thus, $\mathbf{GR}$=2πn. The inverse relation between the coefficients of the real vector of a Bravais lattice $\mathbf{R} = u_1\mathbf{a_1} + u_2\mathbf{a_2} + u_3\mathbf{a_3}$, and the correspondent reciprocal lattice vector, $\mathbf{G} = v_1\mathbf{b_1} + v_2\mathbf{b_2} + v_3\mathbf{b_3}$ can be defined as, $\mathbf{b_i a_j} = 2\pi\delta_{ij}$.

To define the cross-section for Bragg reflection, one has to go back to equation (2.17), taking the time integral results in a δ-function, $\delta(\hbar\omega)$ with non-zero value when $\hbar\omega$=0, and thus $|\mathbf{k}_i|$ =$|\mathbf{k}_f|$,

$$\begin{aligned} (\frac{d\sigma}{d\Omega}) &= \frac{\sigma_{coh}}{4\pi} N \frac{(2\pi)^3}{V_{cell}} e^{-2W(\mathbf{Q})} \sum_G \delta(\mathbf{Q} - \mathbf{G}) && (2.28) \\ \text{and } W &= \frac{1}{2}\langle(\mathbf{Q}\cdot\mathbf{u})^2\rangle. && (2.29) \end{aligned}$$

N is defined as the number of atoms per unit cell, and W is the Debye Waller factor which accounts for the time dependent displacements of the atoms from a perfect lattice. In general it considers harmonic interatomic forces and thus linear displacements, with the vector $\mathbf{u}$ describing the instantaneous displacement of the atom from its equilibrium position $\mathbf{r}$.

This equation states Bragg's Law where coherent scattering will only take place if $\mathbf{Q} = \mathbf{k}_i - \mathbf{k}_f = \mathbf{G}$.

And therefore we can express the magnitude of the scattering vector as,

$$\begin{aligned} &|\mathbf{Q}| = |\mathbf{G}| = 2|\mathbf{k}| \sin\theta_s, \\ &n\lambda = 2d \sin\theta_s, \\ &|\mathbf{Q}| = \tfrac{4\pi sin\theta}{\lambda}, \end{aligned} \tag{2.30}$$

where 2θ is the scattering angle, between $\mathbf{k_i}$ and $\mathbf{k_f}$.

The following diagrams shows the scattering from a Bragg geometry, i.e. the relation between real and reciprocal space. Here d_{hkl} is the distance between diffracted planes, and G is the reciprocal lattice vector which is normal to the diffraction plane.

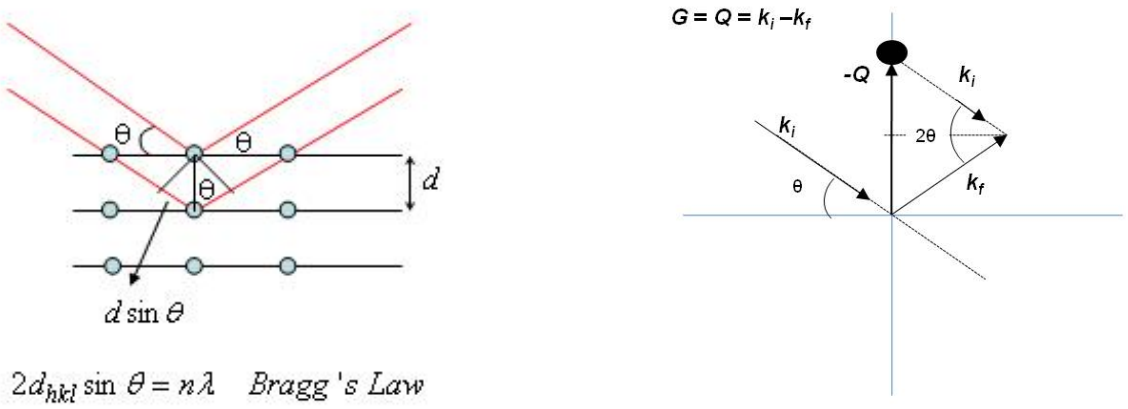

(a) Real Space

(b) Reciprocal Space

Figure 2.2: Relation between **G** and **Q** in Bragg scattering: in real space (a) and reciprocal space (b).

For the case of a non Bravais lattice equation (2.31) becomes,

$$\left(\frac{d\sigma}{d\Omega}\right)_{cohel} = N\frac{(2\pi)^3}{v_0}e^{-2W(\mathbf{Q})}\sum_G |S_G|^2\delta(\mathbf{Q}-\mathbf{G}) \tag{2.31}$$

$$\text{and } S_G = S_{hkl} = \sum_r b_r e^{i\mathbf{G}_{hkl}\cdot\mathbf{r}}. \tag{2.32}$$

S_G is called the nuclear unit-cell structure factor. It provides information about the location of the atoms in the unit cell through the evaluation of the intensities of the Bragg reflections. In crystallography it is more common to use S_{hkl}, as the scattering is simply expressed via the reflection planes indexed by the Miller indices *(h,k,l)*. The magnitude of the reciprocal lattice vector is, $|\mathbf{G}_{hkl}| = \frac{2\pi}{d_{hkl}}$.

Inelastic scattering

Inelastic neutron scattering is a powerful tool to study dynamics such as phonon dispersion curves, molecular motions, hydrogen modes or critical scattering. The condition for an

inelastic phenomenon is that $\hbar\omega \neq 0$. Neutron inelastic scattering provides information about the dynamical picture of the system. It is a time-dependent event with an energy scale of 0 to 100 meV for thermal neutrons.

In the case of lattice dynamics there is a very important phenomenon which will be discussed in detailed in this section. This is the phonon dispersion curve and phonon density of states using a coherent and incoherent analysis respectively.

Coherent scattering: the phonon dispersion relation

Lattice dynamics is an essential topic in the understanding of the thermal properties of solids. Phonon excitations ar quantised modes of vibrations of a lattice crystal. The simplest model is to consider a monoatomic chain where each atom vibrates within a collective movement described by a sinusoidal wave. This wave will propagate along the chain and act as a distortion of the lattice. The propagation of the wave can occur in the same direction as the movements of the atoms or perpendicular to them, these results in two possible wave polarisations, longitudinal or transversal. By stating the equation of motion of the system and assuming a wave-like solution, one can derive a relation between the frequency and the wavevector. This is called the phonon dispersion curve, which will be described in detailed in the next section.

A lattice with N atoms per unit cell gives rise to $3N$ normal modes, or phonon branches, 1N longitudinal and 2N transversal. Phonons are described by a three variables: wavenumber, $\mathbf{q_s}$, angular frequency, ω_s and a polarisation, e_s, where the index s denotes each mode.

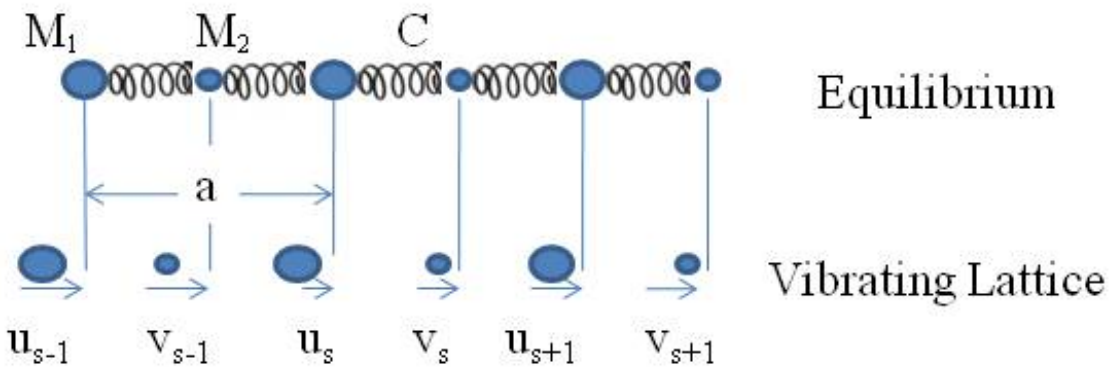

Figure 2.3: Lattice vibration of two atoms per unit cell, s.

In a scattering experiment, the inelastic interaction of neutrons with the lattice creates or annihilates phonons, which results in peaks of intensity when the energy and momentum conservation laws are obeyed. That is,

$$\mathbf{Q} = \mathbf{k_i} - \mathbf{k_f} = \mathbf{G} \pm \mathbf{q}_s \text{ Momentum conservation,} \tag{2.33}$$

$$E_i - E_f = \pm\hbar\omega = \pm\hbar\omega_s \text{ Energy conservation,} \tag{2.34}$$

$$\frac{\hbar^2}{2m}(\mathbf{k}_i^2 - \mathbf{k_f}^2) = \pm\hbar\omega_s \text{ Energy and momentum relation.} \tag{2.35}$$

The last equation defines the energy of the phonon in terms of the change of the kinetic energy of the neutron.

Furthermore, for a non-Bravais lattice the position of the atoms in the crystal are defined by $\mathbf{R} + \mathbf{r}$. Where again $\mathbf{R}$ is the position of the unit cell in the crystal, and r is the

position of the rth atom within the unit cell. the final phonon cross section is then given by,

$$
\begin{aligned}
(\frac{d^2\sigma}{d\Omega dE'})_{coh\pm1} &= \frac{1}{2}\frac{(2\pi)^3}{v_0}\frac{k_f}{k_i}\sum_{s,\mathbf{q}}\frac{1}{\omega_s(\mathbf{q})}|S(\mathbf{Q})|^2 \qquad (2.36)\\
&\times [(n_s(\mathbf{q})+1)\delta(\omega-\omega_s(\mathbf{q}))\sum_{\mathbf{G}}\delta(\mathbf{Q}-\mathbf{q}-\mathbf{G})\\
&+ n_s(\mathbf{q})\delta(\omega+\omega_s(\mathbf{q}))\sum_{\mathbf{G}}\delta(\mathbf{Q}+\mathbf{q}-\mathbf{G})],\\
\text{where } S(\mathbf{Q}) &= \sum_r \frac{\overline{b}_r}{\sqrt{m_r}}(\mathbf{Q}\cdot\mathbf{e}_{\mathbf{r},\mathbf{s}})e^{\mathbf{Qr}}e^{-W_r}. \qquad (2.37)
\end{aligned}
$$

This equation contains a lot of information:

1. The δ-functions in the second and third lines state the condition in momentum and energy for scattering to occur. The second line describes the process of *phonon creation or emission*, where the loss of energy of the neutron equals the energy needed to create the normal mode, $E_i - E_f = \hbar\omega_s$. The third line describes the opposite process, in which the neutron gains energy by the annihilation of a normal mode, $E_i - E_f = -\hbar\omega_s$; this process is called *phonon absorption or annihilation*.

2. The phonon intensity is a function of $|Q|^2$, appearing from two different terms. The first term corresponds to $\mid S(\mathbf{Q}) \mid^2 \rightarrow (\mathbf{Q}\cdot\hat{\mathbf{e}}_{js})^2$. The second one rises from the Debye Waller factor, $e^{-W} = e^{-(\mathbf{Q}\cdot\mathbf{u})^2}$ (equation 2.23). The first term dominates over the exponential at low Q, while the latter dominates at high Q.

3. In order to create a longitudinal or transversal excitation the neutron momentum transfer vector must have a component parallel to the phonon vector. This is expressed in $(\mathbf{Q}\cdot\mathbf{e_{js}})$. The following diagrams describe the scattering configuration to measure longitudinal and transversal phonons.

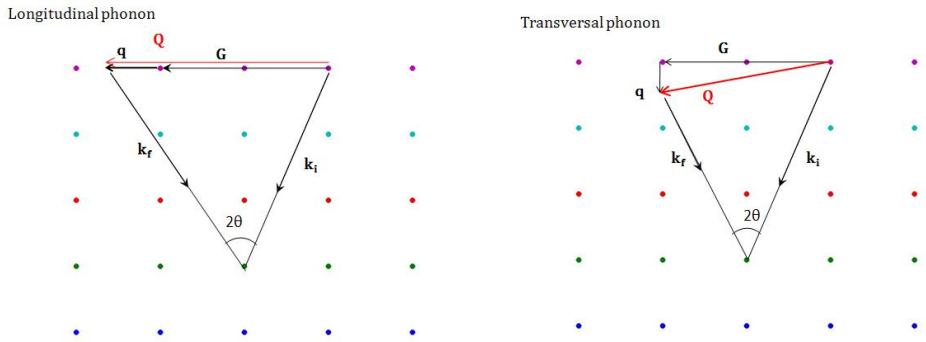

Figure 2.4: Phonon measurement in reciprocal space

4. The terms $(n_s(\mathbf{q}) + 1)$ and $n_s(\mathbf{q})$, describe the probability of phonon creation and annihilation, given by the phonon population, $n_s(\mathbf{q})$. In the first place it states that the probability of phonon creation is higher than the probability of phonon annihilation. Because phonons are bosons, the higher the temperature the higher the population at that phonon energy state.

In conclusion, the alternate probability of phonon creation/annihilation is described by the dynamical structure factor. It depends on the temperature of the sample and therefore the population of states. At high temperatures the probability of creating or annihilating an excitation increases, since the number of available states increases. At low temperatures the spectrum will look asymmetric, with a peak of higher intensity in the neutron energy-lost side(Stokes) than on the neutron energy-gained side (anti-Stokes). This is known as the principle of detailed balance and it is mathematically expressed as,

$$S(-\mathbf{Q}, -\omega) = e^{-\frac{\hbar\omega}{k_B T}} S(\mathbf{Q}, \omega). \tag{2.38}$$

Phonon dispersion curves calculation

Having a system of several atoms in a lattice, the interaction between atom-pairs is described by the harmonic approximation, analogous to a chain of atoms joined by springs. At zero temperature the system is in its ground state. If the atoms are excited thermally, it appears a restoring force given by the inter-atomic bonds between neighbours, responsible for the linear displacement of the atoms about an equilibrium position. Figure 2.3 illustrates the vibrations in a crystal of two-atom basis with masses M_1 and M_2 connected by springs with a force constant C. From this image the equations of motions

can be written using solutions in the form of harmonic waves. These can be expressed as $\mathbf{u}_s = ue^{i\mathbf{q}_s(as)}e^{-i\omega t}$, where $\mathbf{u}_s$ is the vector displacement, a is the distance between nearest identical atoms and s is an integer; similarly, $\mathbf{v}_s = ve^{i\mathbf{q}_s(as)}e^{-i\omega t}$. By writing the equations in terms of a matrix and diagonalising it, the dispersion curves which are momentum-frequency q-ω dependence can be calculated.

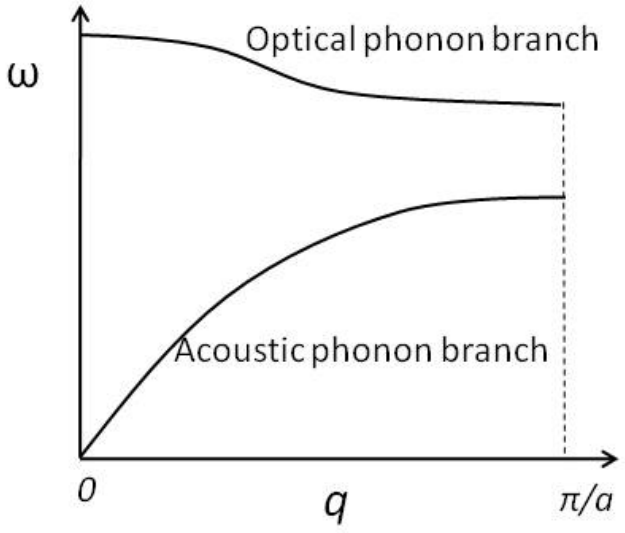

Figure 2.5: Optical and acoustic branches of the phonon dispersion relation for a diatomic linear lattice. Only half on the first Brillouin zone has been represented.

For a unit cell with more than one atom $p-atom$ basis, the dispersion curve is composed of the two types of branch: optical and acoustic. A $n-dimensional$ system with a $p-atom$ basis will have: $n(p-1)$ optical modes and n acoustic modes. For a general case of a three-dimensional system, there will be three acoustic branches corresponded to two types of polarisation: one longitudinal and two transverse. The optical branch is a mixed polarisation.

At the Brillouin zone (BZ) centre $q = 0$, the acoustic mode is the lower energy branch with $\omega = 0$. The physical meaning of this picture can be understood as a mode of infinite

wavelength, all atoms vibrating in the same direction in an uniform movement, as so no energy is involved. On the contrary, the optical mode is higher in energy at $q = 0$ because the atoms are oscillating in opposite directions, out of phase with respect to each other. The dispersion comprises all possible motions of atoms relative to each other, from the longest to the shortest wavelength of vibration. The physics are the same in all Brillouin zones, since $e^{iqsa} = e^{iqsa}e^{i2\pi s} = e^{i(k+\frac{2\pi}{a})sa}$ and thus the boundaries are fixed by $-\pi/a < q < \pi/a$.

Phonon density of states

The density of states describes the number of available states per unit energy interval, i.e. the number of phonons in a energy range, no q-dependence. The phonon density of states is defined by Z(ω).

The phonon density of states can be calculated using the incoherent approximation. Only the energy condition, $\delta(\omega \mp \omega_s)$, must be satisfied, i.e. single-phonon incoherent scattering occurs for a continuous range of k_f values at a given initial configuration. The cross-section does not depend on the direction of the neutron, so that the scattering is computed for any value of $\mid \mathbf{Q} \mid$, as long as they have the correct ω_s.

The complete expression for both, coherent and incoherent single-phonon scattering cross-section for a non-Bravais crystal is shown below,

$$(\frac{d^2\sigma}{d\Omega dE'})_{coh\pm1} = \frac{k_f}{k_i}\frac{(2\pi)^3}{2\upsilon_0}\sum_s\sum_{\mathbf{G}}\frac{1}{\omega_s}|\sum_r\frac{\bar{b}_r}{\sqrt{M_r}}e^{-W_r}e^{i\mathbf{Q}\cdot\mathbf{r}}(\mathbf{Q}\cdot\mathbf{e}_{r,s})|^2 \tag{2.39}$$

$$\times \begin{cases} \langle n_s+1\rangle\delta(\omega-\omega_s)\delta(\mathbf{Q}-\mathbf{q}-\mathbf{G}) \text{ phonon emission} \\ \langle n_s\rangle\delta(\omega+\omega_s)\delta(\mathbf{Q}+\mathbf{q}-\mathbf{G}) \text{ phonon absorption,} \end{cases} \tag{2.40}$$

$$(\frac{d^2\sigma}{d\Omega dE'})_{inc\pm1} = \frac{k_f}{k_i}\sum_r\frac{1}{2M_r}\{\overline{b^2}-(\bar{b})^2\}e^{-2W_r}\times 3NZ(\omega)\frac{\langle(\mathbf{Q}\cdot\mathbf{e_s})^2\rangle}{\omega}\begin{cases}\langle n+1\rangle \text{ phonon emission} \\ \langle n\rangle \text{ phonon absorption.}\end{cases} \tag{2.41}$$

Figure 2.6 shows the experimental measurements of the phonon dispersion curves and the density of states for GaAs.

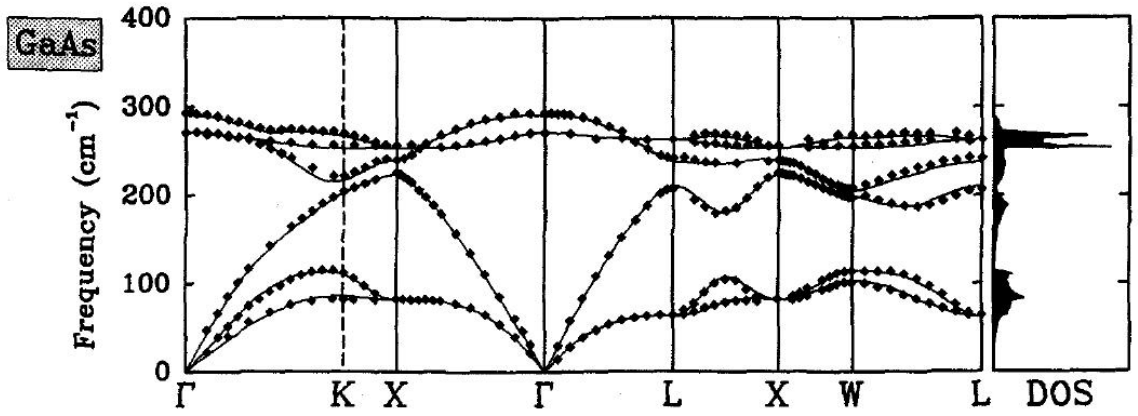

Figure 2.6: Phonon dispersion curves, acoustic and optic branches, of GaAs. The spectrum on the right, DOS, corresponds to the phonon density of states. This image was reproduced from [18]-FIG. 2.

2.2.3 Static Approximation

Before studying the structure of a system subjected to changes as a function of time, like in a liquid or a phase transition due to fluctuations, it is crucial to understand the differences between two approaches: diffraction and the static approximation. The principles of their measurements are the same, but the interpretation of the structure factors gives very different results.

Essentially, in order to understand the analysis one has to go back to the time dependent pair correlation function, $G(\mathbf{r}, t)$, which is simply the Fourier transforms in space and time of the dynamical structure factor, $S(\mathbf{Q}, \omega)$. Both expressions relate real and reciprocal space. The pair correlation function describes the correlation between an atom j' with coordinates $(\mathbf{r}\prime, t = 0)$ with another atom j at a position $(\mathbf{r}\prime + \mathbf{r})$ at a later time t. It calculates the probability that those two atoms will be space and time correlated.

What happens when $G(\mathbf{r}, t)$ is considered within two limits, when $t = \infty$ and $t = 0$? The resulting microscopic picture is different. When $G(\mathbf{r}, t)$ is evaluated at $t = \infty$, the Fourier transform with respect to t results in a delta-function which only equals to 1 when $\omega = 0$, this is the scenario in a diffraction or elastic mode. At that limit the temporal correlation of the atoms is lost. This does not affect the results of the structure analysis of a crystal, but it does not hold for a liquid, in which the probability of having two atoms correlated in space at $t = \infty$ is simply zero.

On the contrary, the static approximation, also called snapshot, describes the structural configuration of the sample at an instantaneous moment and so $G(\mathbf{r}, t)$ is evaluated at $t = 0$. The integral of $S(\mathbf{Q}, \omega)$ is considered over all energies so that the signal measured accounts for all the excitations of the sample within the measured direction. The static correlation function can be studied through the effects of external parameters in the sample, such as temperature, magnetic field, etc.

The following equations give a mathematical description of the correlations functions in real and reciprocal space, for both scattering methods.

Static Approx (2.42)

$$\begin{aligned} S(\mathbf{Q}) &\propto \int_{-\infty}^{\infty} S(\mathbf{Q}, \omega) d\omega \\ &\propto \int_{-\infty}^{\infty} G(\mathbf{r}, t) e^{i(\mathbf{Q}\mathbf{r} - \omega t)} d\mathbf{r} dt d\omega \\ &\propto \int_{-\infty}^{\infty} G(\mathbf{r}, 0) e^{i(\mathbf{Q}\mathbf{r})} d\mathbf{r} \ , \end{aligned}$$

Time averaged (2.43)

$$S(\mathbf{Q}, 0) \propto \int_{-\infty}^{\infty} S(\mathbf{Q}, \omega) \delta(\omega) d\omega \tag{2.44}$$

$$\propto \int_{-\infty}^{\infty} G(\mathbf{r}, \infty) e^{i(\mathbf{Q}\mathbf{r})} d\mathbf{r}.$$

Experimentally measuring in the static approximation has been achieved by removing the analyser in a triple axis spectrometer. The goal is to set up the instrument so that the neutron's incident energy is very high, to be as close as possible to the condition of the integral where the upper limit is ∞. In principle, the neutron can give to the sample all the energy it has available, the higher the incident energy the higher the energy available to create excitations. In the case of a coherent inelastic event, like neutron-phonon, the maximum available energy to the neutron will be given by the mode with the highest frequency. When integrating over energy all these modes, from lowest to highest will be summed up, and the intensity and width of the peak will be affected.

2.2.4 Neutron Spectroscopy

Three-axis spectrometer

This technique was designed by Brockhouse in the mid 50′s, and became an important tool for inelastic scattering experiments since it provides access to the scattering function $S(\boldsymbol{Q},\omega)$ at any point in reciprocal space $(\boldsymbol{Q},\omega)$. This allows experimental configuration to scan with fixed energy ω, or momentum transfer $\mathbf{Q}$.

The spectrometer is composed of a monochromator made of single crystals, which selects an incident wavelength from the white neutron beam via the Bragg's law. The same principle is use for the analyser. In general, the curvature, vertical and horizontal, of both monochromators can be adjusted to modify resolution and flux. The instrument allows to work in diffraction mode by selecting $\triangle E = 0$, so that $|\mathbf{k_i}|=|\mathbf{k_f}|$.

The sample table possesses a motor allowing rotations around the sample axis, ϑ. The sample alignment can be refined with the use of goniometers for tilts relative to the scattering plane. To control the beam size and divergence, and to shield against background, collimators and diaphragms can be manually placed in the path of beam. Filters such as pyrolitic graphite (PG) or Beryllium can be also used to eliminate $(n\lambda)$ diffracted by the monochromator or analyser, responsible for spurious signals.

The flexibility of a three axis comes from having an axis of rotation at each of the monochromator, sample and analyser positions. The incident and final wavelengths are provided by the crystal monochomator and analyser respectively. The direction of the initial and final wavevectors with respect to the sample is defined by the angles of each axis. Any combination of $\mathbf{k_i}$ and $\mathbf{k_f}$ can be selected as long as the vector triangle $\mathbf{k_i} - \mathbf{k_f} = \mathbf{Q}$ can close.

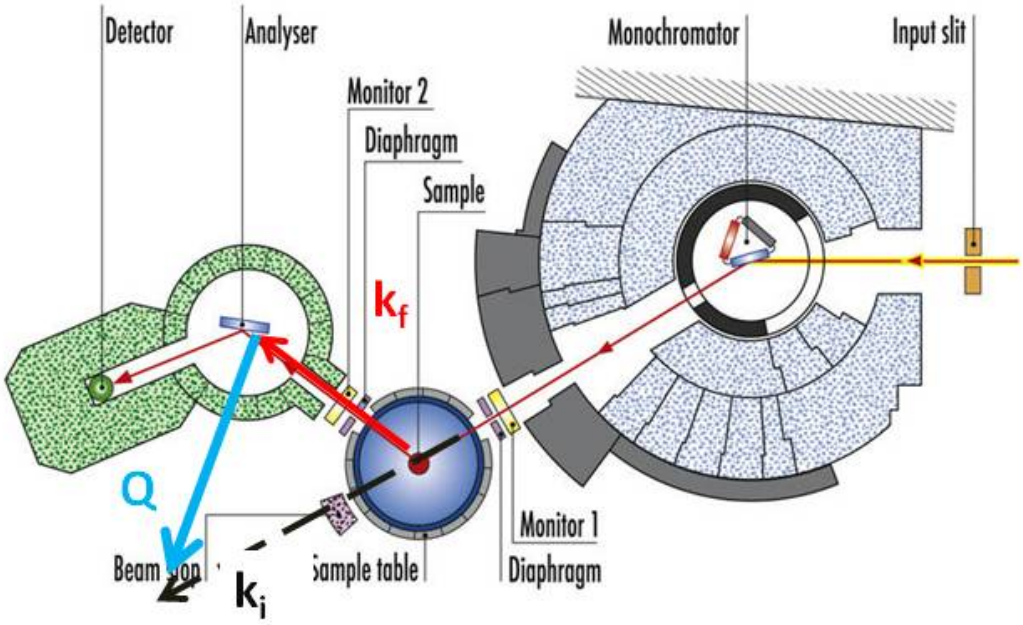

Figure 2.7: Scheme of a three axis spectrometer, highlighting the main components of the instrument and the scattering triangle. Figure adapted from [19].

Table 2.2 presents three-axis spectrometers used during this thesis: IN8 and IN3 at the ILL (Grenoble)[20] and TAIPAN at ANSTO (Sydney) [21]. Their main characteristics are also given.

Characteristics	IN8	IN3	TAIPAN
Source	thermal	thermal	thermal
		Monochromator (k_i in Å^{-1})	
Crystal	PG(002) for 2.662 and 4.1 Cu(200) for 4.1 and 7.0 Si(111) for 2.662 and 4.1	PG(002) for 2.662 Cu(111) for 2.662 Heusler(111) for 2.662	PG(002) Cu(200)
Flux (10^8 $\frac{n}{cm^{-2}s^{-1}}$)	PG(002): 2 and 6.5 Cu(200): 4.6 and 3 Si(111): 0.8 and 3.4	PG(002): 0.093 Cu(111): 0.036 Heusler(111):0.02	2 for k_i=4.9
Analyser	doub-focus PG(002), Si(111), flat Cu(111)	H focus PG(002)	PG(002) 24' mosaic
Detector	^{3}He detector	^{3}He detector	^{3}He detector

Table 2.2: Table of characteristics for three TAS instruments: IN8 and IN3 (ILL, France), and TAIPAN (ANSTO, Australia).

Resolution function

In a three axis measurement the intensity measured in the detector $I(\boldsymbol{Q},\omega)$ is the convolution between the dynamical structure factor, $S(\boldsymbol{Q},\omega)$ and the instrumental resolution function, $R(\boldsymbol{Q},\omega)$.

The resolution function for a neutron triple axis spectrometer is given by the following expression,

$$R = R_0 exp(\frac{1}{2}\chi^T M \chi), \tag{2.45}$$

where R is the resolution function, M is the matrix of the resolution function; χ is a four-vector defined by (Q_X,Q_Y,Q_Z,E), and χ^T its transpose vector.

The resolution volume for a specific ($\mathbf{Q}$,ω) configuration corresponds to 4-D ellipsoids. These ellipsoids depend on parameters like beam divergence and wavelength spreads. To calculate these 4-D ellipsoids there have been several theoretical approaches, such as Cooper and Nathans [22]. These are used in the ILL three-axis matlab data evaluation package "*Rescal*". In order to obtain the resolution matrix, $[M]$, a matlab function routine called CN_rescal can be used. It is based on Cooper-Nathan's method. $[M]$ is created based on the input spectrometer parameters, defined before starting an experiment, and

stored in the file information of each scan. These comprise: d-spacing of the monochromator and analyser and their mosaic spread; horizontal and vertical collimation before and after the monochromator, sample, and analyser; and the length of reciprocal lattice vectors and angles between them.

In the experiments described in this thesis, the reciprocal space was defined in $(\text{Å})^{-1}$ and not by Miller indices. The lattice parameters are orthogonal with angles (α, β, γ)=90° and magnitude of the reciprocal lattice vectors (a*,b*,c*)= 2π.

To a good approximation the TAS resolution function is described by a Gaussian, which shape depends mainly on four variables: incident and final wavevectors, the collimation angles, mosaic widths and scattering senses[23]. Experimentally, the Q-resolution can be measured by mapping the reciprocal space of the Bragg peak of a single crystal, eg. Si(1 1 1) Bragg reflection for silicon. This will be further explained in Chapter 5.

Direct geometry Time of Flight (ToF)

This technique measures the change in the velocity of a pulse of monochromatic neutrons due to interaction with a sample from the time they take to arrive to the detectors. Since the path length, initial time and energies are known, conversion from time to energy change can be easily performed. Additionally ToF spectrometers have an array of detectors covering a large solid scattering angle, hence detection position in 2θ can be converted to momentum transfer, thus large portions of $S(Q, \omega)$ can be probed simultaneously.

The IN5 (ILL) spectrometer monochromates the incident neutron beam before it reach the sample by one or many choppers. The choppers define the time of the initial pulse, t_0 with the selected energy E_i. On IN5, a monochromatic neutron burst is the result of six phased choppers turning at 2,000-17,000 rpm, providing a resolution of 10 μeV at an incident λ=10 Å.

Figure 2.8 shows the layout of a time-of-flight instrument, IN5.

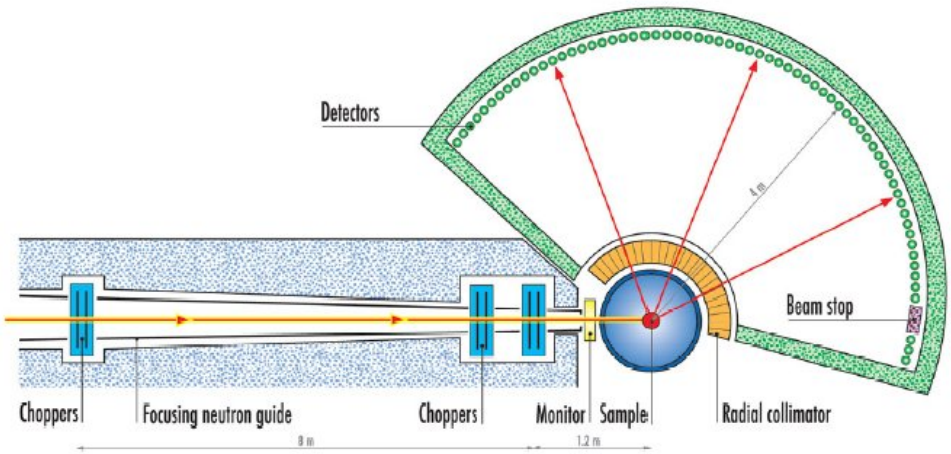

Figure 2.8: Scheme of a time-of-flight instrument, IN5 at the ILL (Grenoble) [20].

Characteristics	IN5b
Source	cold
Chopper velocity (rpm)	2000-17000
Incident wavelength (Å)	1.8 to 20
Flight path (m)	4
Energy resolution	$\delta E/E = 1\%$
Optimal use	10μeV-100meV
Flux at sample $(n/cm^2/s)$	at 5Å, 6.83×10^5

Table 2.3: Time-of-flight, IN5 instrument table

The instrument described above follow a direct geometry, where the E_i is defined by the chopper and the final energy, $E_f = E_i - \hbar\omega$, corresponded to the times of flight of the neutrons is measured in the detectors. Within this configuration there is a parabolic trajectory in (Q, ω) space which is experimentally accessible for each detector so that one can simultaneously cover, in a reasonable time, a large area in (Q, ω) space. A big limitation of this instrument has been that the detectors could not resolve in Q-vector but 2θ, i.e. $|\mathbf{Q}|$, comprising the measurements of single crystals. This has recently been overcome on IN5 by introducing position sensitive detectors, which provide information in (Q_x, Q_y, Q_z). Despite this development the instrument is not optimal to measure in a particular high symmetry Q-direction, this type of measurement is often better done

on a triple-axis spectrometer. This could still be done by installing a rotating table, to measure rocking curves (ϑ), if the configuration of the ToF instrument allows it.
The trajectories in $S(Q, \omega)$ space are shown in Figure 2.9.

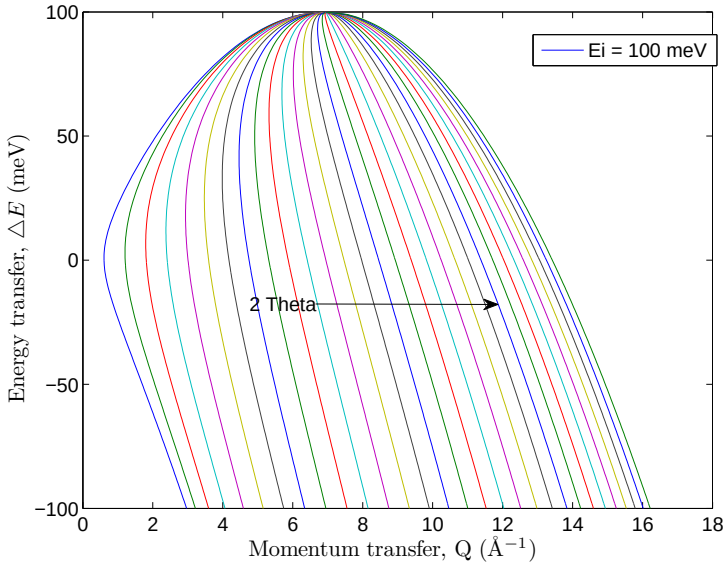

Figure 2.9: An example of trajectories in (Q,ω) space for a direct geometry spectrometer, at different 2θ angles, from 5° to 150°.

2.3 X-ray Introduction

These theory have been elaborated mainly with the assistance of the following references: the book of J. Als-Nielsen and Des McMorrow [24] and the book comprising the lectures notes covered at the HERCULES course in Grenoble [25].

2.3.1 X-ray characteristics

The X-ray wavelength is similar to the interatomic distances, and therefore it has been one of the primary techniques to study the structure of matter. X-rays can be produced by laboratory sources where photons are generated by de-excitations of electrons; or from synchrotron facilities in which a beam of charged particles is accelerated producing X-rays. The ESRF is a so-called third generation of synchrotron sources, and their brightness is up to 10^{12} higher than the beams produced in a lab source.
In a synchrotron source, X-rays are produced as a white polarised beam. The polarisation is in the direction of the electric field. The resulting monochromatized beam, as for

neutrons, is a plane wave of the form: $\psi = e^{i(\mathbf{k}z-\omega t)}$, where $\mathbf{k}$ is the wavevector and ω the angular frequency. As for neutrons, X-rays must be understood from a wave-particle duality approach, in which an X-ray beam is quantised into photons of energy $\hbar\omega$ and momentum $\hbar\mathbf{k}$. While neutrons must be treated in the non-relativistic limit, where the energy is given by $E = \frac{(\hbar k)^2}{2m_n}$; X-rays have no rest mass and have energies which must be expressed in the relativistic limit, $E = \hbar kc$, where c is the speed of light. From these equations we can show the following wavevector relations:

1. $k_{neutron}[\text{Å}^{-1}] = \frac{E_{neutron}[meV]}{2.0716}$.
2. $k_{X-rayphoton}[\text{Å}^{-1}] = \frac{E_{X-rayphoton}[keV]}{1.973}$. This implies that a wavelength of 1 (Å) corresponds to an X-ray energy 10^6 times bigger than that of the neutron.

2.3.2 The interaction of X-ray with matter

When a photon interacts with matter, there are different processes that can occur: absorption, scattering and refraction. For the purposes of our thesis, scattering is the only process that will be discussed.

Interaction with one electron Due to its electromagnetic nature, the interaction of an X-ray with an atom occurs with its electron cloud. In the elastic approach, when an X-ray interacts with an electron, its electric field makes the electron vibrate in the direction of the polarisation of the incident wave, to finally radiate a spherical scattered wave. The probability to scatter an X-ray is given by the scattering length. For the simplest case of a photon free electron interaction, it is given by the Thomson scattering length, r_0, which in turn is the classical electron radius. This is analogous to the scattering length, b, for neutrons.

When a plane wave, ψ_0 is scattered by a point, the scattered wave, ψ_s in the far-field results in a spherical wave with a phase shift of π with respect to the incident wave, given by $\psi = \psi_0 + \psi_s$. Due to the point-like scattering approximation between a neutron and a nucleus, the phase shift resulted from the scattering event will have an effect in the sign of the scattering length, negative or positive. For X-rays the scattering length is always positive and increases with the number of electrons, Z. Thus, the X-ray cross section is dominated by heavy elements.

The measured intensity recorded in the detector is given by the number of photons per second, I_{sc}. The relation between the incident and scattered intensity can be expressed as,

$$\frac{I_{sc}}{I_0} = \frac{|E_{rad}|^2 R^2 \triangle\Omega}{|E_0|^2 A_0}. \tag{2.46}$$

The scattered and incident wavelength have a cross-sectional area of $R^2\triangle\Omega$ and A_0 respectively; E_{rad} and E_0 are the radiated and incident electric field.

Interaction with an atom Scattering from different contributions of the atom must be considered. If we consider the scattered from different volume elements, the sum of all contributions will result in the total scattered radiation field. But one cannot forget the phase shift that an incident wave undergoes when interacting with a volume element. The phase difference between the incident $\mathbf{k_i}$, and scattered $\mathbf{k_f}$ waves occurring in two different volume elements is obtained by considering the relative displacements between the two volume elements given by $\mathbf{r}$. This gives,

$$\triangle\phi(\mathbf{r}) = (\mathbf{k_i} - \mathbf{k_f}) \cdot \mathbf{r} = \mathbf{Q} \cdot \mathbf{r}. \tag{2.47}$$

This phase difference is implicit in the form factor *f(**Q**)*, given by the following expression:

$$f(\mathbf{Q}) = \int d\mathbf{r}\rho(\mathbf{r})e^{i\mathbf{Q}\cdot\mathbf{r}}, \tag{2.48}$$

where $\rho(\mathbf{r})$ is the electron charge distribution for each atom, and it is related to the atomic number in the form of, $Z = \int \rho(\mathbf{r})d\mathbf{r}$. We can see that equation 2.48 is the Fourier transform of the electron density, $\rho(\mathbf{r})$. There are two limits to consider for the form factor, when Q tends to 0 and when Q tends to ∞. The former case implies that all different elements scatter in phase, so that the form factor, $f(\mathbf{Q} \to 0) = Z$; in the other limit $f(\mathbf{Q} \to \infty) = 0$.

An important property of electrons in the atom is their occupation of the different energy levels. This has direct implications in the form factor. If the photon energy is lower than that of the most bound electron shell, they will not feel the electric field as much as if they were free, and thus the scattering length will be reduced.

To account for resonance effects an extra term in the form factor is needed, $f'(\hbar\omega)$, which is energy dependent. Furthermore, absorption effects affecting the imaginary part of the

scattering length can be also included by the element $f''(\hbar\omega)$.
In resume, the form factor for an atom is described as,

$$f(\mathbf{Q}, \hbar\omega) = f(\mathbf{Q}) + f'(\hbar\omega) + if''(\hbar\omega), \tag{2.49}$$

the last two terms are called dispersion corrections.
Only when the X-ray photon energies are higher than the bound electrons they can be treated as free electrons, and the total scattering cross-section from an atom can be well described by Thomson scattering cross section, $\sigma_T = 4\pi(Zr_0)$.
The principles of scattering by a crystal described for neutrons earlier on in this chapter are applicable to X-rays.

2.3.3 Inelastic scattering

Cross-section

As discussed before with neutron scattering, the scattering cross section can be split into two terms, coherent and incoherent. Any scattering process must obey the energy and momentum conservation law, $\triangle E = \hbar\omega = E_i$ - E_f and $\hbar\mathbf{Q} = \hbar(\mathbf{k}_i - \mathbf{k}_f)$. When considering scattering of X-ray, in most cases the energy transfer, $\triangle E$, is much smaller than the incident Energy, E_i, so that when applying the cosine rule to solve the $\mathbf{k}_i - \mathbf{k}_f - \mathbf{Q}$ triangle (equation 2.8), for $|k_i| = |k_f|$ the momentum transfer can be simply expressed as,

$$\hbar\mathbf{Q} = 2\hbar\mathbf{k}_i \sin\theta, \tag{2.50}$$

where θ is half the scattering angle.
The double differential equation can be simplified as [17]:

$$\frac{d^2\sigma}{d\omega_f d\Omega} = (\frac{d\sigma}{d\Omega})S(\mathbf{Q}, \omega), \tag{2.51}$$

which calculation becomes much easier by being able to solve each of the two contributions separately. The first element is defined as the intrinsic differential cross section associated to the effects of beam-scattering system; while the second is the scattering function alluding to the properties of the sample. The double differential cross section can be solved by applying the first Born approximation. This is possible by considering a weak coupling

between the photon electromagnetic field and the scattering electron, which implies: the energy transfer is negligible compared to the energy of the scattered photon or particle; **Q** is simply defined by the scattering angle; and $\frac{d\sigma}{d\Omega}(\theta)$ can be expressed in terms of the pair distribution function, $G(\mathbf{r}, t)$ [17]. Within this scenario the intrinsic cross section becomes the Thomson scattering cross section, $\left(\frac{\sigma}{\Omega}\right) = \left(\frac{d\sigma}{d\Omega}\right)_{Th} \propto r_0^2$.

X-rays are not a highly penetrating probe like neutrons. Their interaction with matter is not weak, and thus the first order perturbation theory becomes insufficient to describe the inelastic scattering process, therefore only under the conditions mentioned above the Born approximation can be used. On the other hand for neutrons, this approximation is almost always adequate.

Until now, we have only taken into account the electric force interaction of the incident photon with the electron, described by Thomson scattering cross section. The magnetic field vector is also responsible for interactions with the magnetic moment of the electron. As for magnetic neutron scattering, magnetic contributions in the X-ray scattering function is beyond of the scope of this section.

Single particle properties Far from the classical approach, the X-ray interaction with a free and at rest electron results in the inelastic process of Compton scattering, which is better described by a photon-electron interaction. From the collision, the scattered photon lowers its energy, resulting in a scattered wave which difference in wavelength is proportional to the Compton scattering length. It provides information about single-particle properties. Compton scattering dominates at large scattering angles and with increasing incident X-ray energy. Experimentally this is measured as a diffuse background. Thermal excitations such as lattice vibrations (phonons) are examples of collective motions as a consequence of interferences from many particles of the system. Their energies are of the order of meV; so the interaction of the neutrons with these type of excitations is directly reflected in the magnitude and direction of the scattering wavevector. In the case of X-rays (E[keV]), in order to detect the excitation in the meV limit, an energy resolution of 10^{-6} is essential. Today, sophisticated experimental techniques such as ID28 (ESRF) can provide these high energy resolutions, so that it has become suitable tool to study excitations that first belonged to the neutron domain. This type of excitation will be discussed in detail in Chapter 7.

The coherent inelastic neutron scattering description is applicable to the inelastic scatter-

ing for x-rays for phonons under the special case where the Born approximation can be applied, as explained before. And moreover, assuming the adiabatic approximation where nuclei-electrons move together. When the nucleus experiences a phonon, the movement will be instantaneously followed by the electrons. By inelastic X-ray measurements the electron charge density variations produced by phonons can be observed. The scattering for neutrons (section 2.2) also applies to X-rays by substituting the scattering length b, by the atomic form factor, $f(\boldsymbol{Q})$.

2.3.4 Instruments (ESRF, Grenoble)

ID14 eh2

ID14 is a macromolecular crystallography beamline to carry out fibre diffraction measurements [26]. It provides a collimated X-rays beam of a wavelength of 0.933 Å. If slits are used, the beamsize can achieve 50-200 microns, and a maximum resolution of 0.97 Å. The main components of the beamline are: mini-diffractometer with a miniKappa goniometer, ADSC Q4 CCD detector and an Oxford Cryostream for 100 K data collection. Figure 2.10 shows a cartoon of the ID14-eh2 apparatus with the main elements in the experimental hutch.

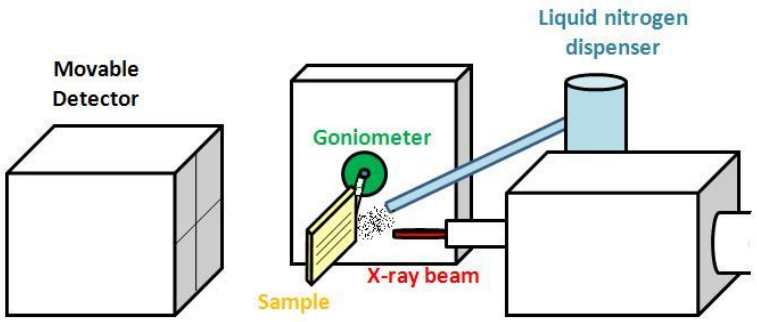

Figure 2.10: ID14 eh2 layout, the main elements have been labelled. A DNA fibre film has been drawn to represent the sample.

ID28

The ID28 is one of the ESRF beamline dedicated to the study of inelastic scattering processes (IXS) in both, momentum and energy transfers, $S(\mathbf{Q},\omega)$ [27]. It is most suitable to study phonon dispersion, and therefore based on the same principles as inelastic neutron scattering technique (INS). The advantages of this IXS compared to INS is that it provides information in the Q-E range inaccessible to INS, and can measure very small samples where neutron scattering would be intensity limited. The incident photon can have energies of 13840, 15817, 17794 and 21747 eV, for energy resolutions of: 7.0, 5.5, 3.0 and 1.5 meV. The inelastic excitations can be measured from 0 to 200 meV, and momentum transfers from 1-100 nm^{-1}. By placing slits in the line path of the beam, the momentum resolution can be improved to 0.03 nm^{-1}.
Figure 2.11 shows a standard layout of the ID28 instrument. It is analogous of a triple-axis spectrometer, which axis are defined by: the pre-monochromator (first axis), the sample goniometer (second axis) and the crystal analyser (third axis). The main elements of the instruments have been drawn in the figure. Slits can be placed along the beam path, before and after the sample. The post monochromator is an optional element, as well as collimating and focussing Be lens which have not been shown in this figure. The whole beamline covers a distance of 75 m.

Description of the elements:

1. Storage Ring: Defines the mode at which the electrons are accelerated. It is cycle dependent. Our experiments were done using the highest intensity mode.

2. Undulators: Electrons from the storage ring are accelerated when passing through the undulators resulting in the generation of electromagnetic radiation.

3. Pre-monochromator: Silicon crystal monochromator which defines the wavelength.

4. Main monochromator: Defines the incident energy, E_i. In order to get sufficient wavelength resolution ($\left(\frac{\delta\lambda}{\lambda}\right) = cot\theta\delta\theta$), the monochromator must work in backscattering ($\theta = 90°$). It will change depending on the energy transfer, $\triangle E$ of interest. Since phonon excitations are of the order of meV in energy, $E_i \gg \triangle E$, to change the initial energy by meV the monochromator is heated up or cooled down ($KT \simeq$ meV) to achieve the desired energy transfers.

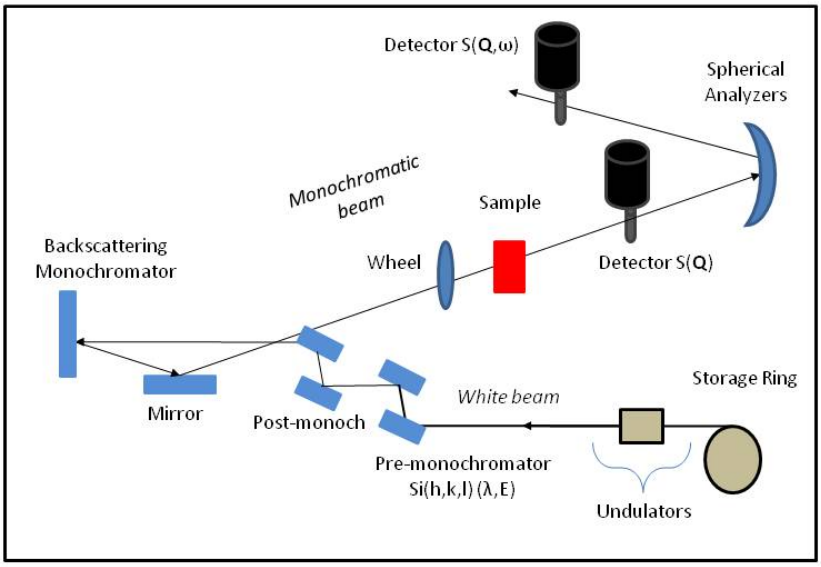

Figure 2.11: Layout of the main elements of the X-ray Inelastic scattering instrument, ID28.

5. Wheel: This is used to attenuate direct beam, to avoid saturating the detectors.

6. Analysers: These are configured in inelastic mode for an $S(\boldsymbol{Q},\omega)$ experiment. These are five different analysers allowing maximum of five momentum transfer $\mathbf{Q}$, to be recorded simultaneously at each energy transfer.

7. $S(\boldsymbol{Q})$ detector: This is used for elastic configurations. The detector comes down into the path of the beam in front on the analysers, so there is no energy analysis.

8. $S(\boldsymbol{Q},\omega)$ detector: There are five silicon detectors. For an inelastic measurement, the $S(\boldsymbol{Q})$ detector lifts out of the beam and the scattered beam continues directly to the analysers, to finally reach the detectors.

2.4 Differential Scanning Calorimetry

Differential Scanning Calorimetry (DSC) has become one of the most useful tools to study the thermodynamical properties of complex systems like polymers, proteins or DNA. It covers a broad array of thermodynamical processes and applications: folding, interactions, first and second order phase transitions, glass transition, melting temperature...

This section has been mainly constructed with the aid of the books of *Höhne* [28] and the one edited by Brown [29]. In addition, specific articles have been used to provide complementary technical material and they will be referred in the pertinent sections.

2.4.1 Principles of thermodynamics

Any dynamical process can be described by the thermodynamical potentials: internal energy ($\triangle U$), enthalpy ($\triangle H$), Gibbs free energy ($\triangle G$) and the Helmholtz Free Energy ($\triangle F$). These properties can be expressed as a function of temperature, pressure, volume or entropy of the system. Using the convenient relations, any of the thermodynamic quantities can be calculated, such as: the enthalpy as a function of entropy and pressure. The following formulae are given as a review of some of the principles of thermodynamics; some of these relations were used in the data analysis, and thus should be mentioned in this section.

At constant pressure, the stability of a system is commonly studied using the Gibbs free energy. The system is in equilibrium when $\triangle G$=0.

The change in Gibbs free energy involved in a process at constant temperature and pressure is defined as:

$$\triangle G = \triangle H - T\triangle S, \tag{2.52}$$

where $\triangle S$ is the entropy. The enthalpy $\triangle$H, at constant pressure is given by,

$$\triangle H = \triangle U + p\triangle V. \tag{2.53}$$

Both enthalpy and entropy can be calculated from the analysis of specific heat at constant pressure Cp, as a function of temperature. As expressed in the following equations,

$$(\triangle H)_p = \int_{T_1}^{T_2} Cp dT, \tag{2.54}$$

$$(\triangle S)_p = \int_{T_1}^{T_2} \frac{Cp}{T} dT. \tag{2.55}$$

Cp is the fundamental thermodynamic quantity measured by calorimetry and hence, it

seems more relevant to define it as:

$$Cp = (\frac{dH}{dT})_p. \tag{2.56}$$

2.4.2 DSC technique

DSC is a calorimetric technique in which the heat capacity of a sample is measured as a function of temperature, T. There are two types of DSC systems: Power-compensated DSC and Heat Flux DSC. All measurements in this thesis were taken using the Heat Flux DSC technique in a microcalorimeter, MicroDSC III from Setaram company. Figure 2.12 shows a photograph of the instrument. MicroDSC III covers a temperature range from -20°C to 120° with a sensitivity of 0.2 mW, at scanning rates between 0.001-1.2 K/min. It possesses high sample flexibility, from liquid, gel, powder to solid; for which a specific experimental cell is designed, to a total of seven different ones.

The experiments carried out in this thesis have used a batch closed cell made of hastelloy, adapted for solid or liquid samples. It weights 6.6685 g and a volume of 1 ml. It was chosen as it is suitable to measure phase transitions with high sensitivity at rather low scanning rates.

This technique has been described previously in detail in reference [30], [31], [32] and [33].

Figure 2.12: Picture of the MicroDSCIII of SETARAM company, reproduced from [34].

The technique consists in recording the temperature change of a sample relative to a reference giving the changes in the heat capacity of the specimen under study as a function of temperature. Figure 2.13 gives the schematic of the DSC set up. This type of DSC is composed of two thermally isolated cells, joined to a common furnace by a thermopile, via the heat exchange coefficient K. The temperature difference between the cells is measured in time by means of two thermopile mounted in opposition. This temperature difference can be computed in electrical potential via de Seebeck effect, $\triangle V = \mathcal{S}\triangle T$, where $\mathcal{S}$ is the Seebeck coefficient. Also this potential can be transformed in differential power, where the coefficient K is measured at each temperature. The relation is given by the following expression,

$$\triangle P = K\triangle T = \frac{K}{S}\triangle V \tag{2.57}$$

The output signal in a DSC is given in the form of the difference in the heat flow between the sample and the reference, $\triangle P$.

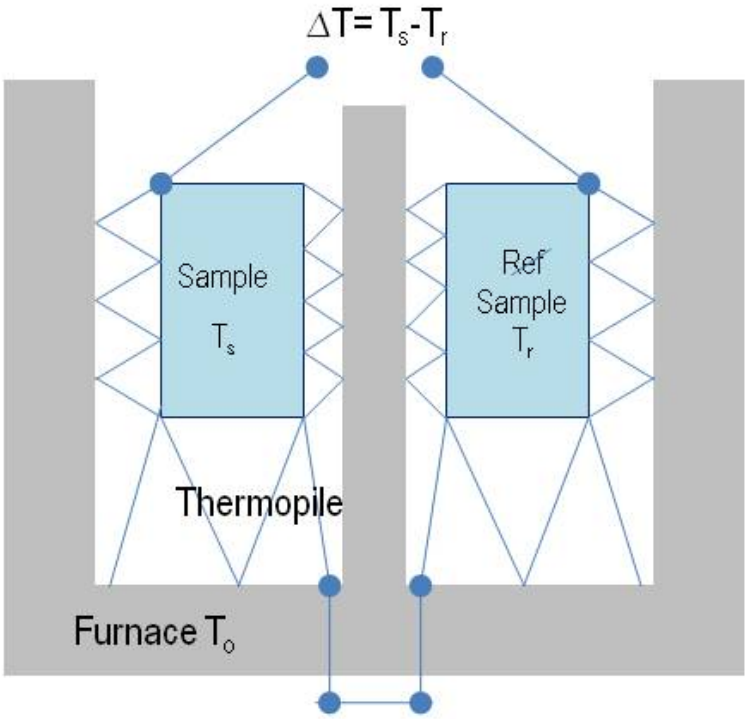

Figure 2.13: Layout of the DSC apparatus

The temperature of the furnace, T_0, is ramped by means of a PID control loop. The

temperature of the cells follows the ramp with a certain delay, intrinsic to the apparatus, and once the stationary regime is reached a constant temperature difference between sample and reference is established due to the difference in heat capacity. The scanning rate is a parameter that may be varied.

By investigating the thermodynamic process for each cell individually, we can derive the mathematic expression that relates the difference in the heat capacity between the sample and the reference with the temperature difference:

$$\text{Sample cell: } P_s = C_s \frac{dT_s}{dt} + K(T_s - T_0), \tag{2.58}$$

$$\text{Reference cell: } P_r = C_r \frac{dT_r}{dt} + K(T_r - T_0), \tag{2.59}$$

where P_s and P_r are the heat flow supplied or released at the level of each cell, sample and reference, respectively; C_s and C_r are the sample and reference heat capacity; and K is the heat exchange coefficient, assumed to be identical for each cell. Since there is no compensation power applied by the DSC, $P_s = P_r = 0$, equations 2.58 and 2.59 can be rearranged as,

$$\triangle T = -\frac{\triangle C}{K}\frac{dT_r}{dt} - \frac{C_s}{K}\frac{d(\triangle T)}{dt}, \tag{2.60}$$

where the scanning rate, β is defined as $\beta = \frac{dT_r}{dt}$, and $\tau_{ins} = \frac{C_s}{K}$ corresponds to the thermal time constant of the calorimeter [35]. The difference in heat capacity is given by $\triangle C = C_s - C_r$, to a first approximation $\triangle C \ll C_s, C_r$ so that $\tau_{ins,s} \simeq \tau_{ins,r}$ and thus, $\tau_{ins,s} = \frac{C_s}{K} = \frac{C_r + \triangle C}{K} \sim \frac{C_r}{K}$. The heat exchange coefficient K, can be determined by a previous calibration procedure. Using these assumptions, equation 2.60 can be expressed as,

$$\triangle T = -\frac{\triangle C}{K}\beta - \tau_{ins}\frac{d\triangle T}{dt}. \tag{2.61}$$

The principles of differential scanning calorimetry lie in equation 2.61. If both cells were kept empty or filled with the same specimen, then C_s=C_r and so T_s=T_r since both cells are equally heated by the furnace, and thus equation 2.61 will equal to zero. Only when there is a difference in heat capacity between both cells there will be a signal to measure. In a stationary regime the second term will equal to zero, as $\triangle$T is constant. The regime

will be non-stationary when the sample undergoes a physic-chemical transition.

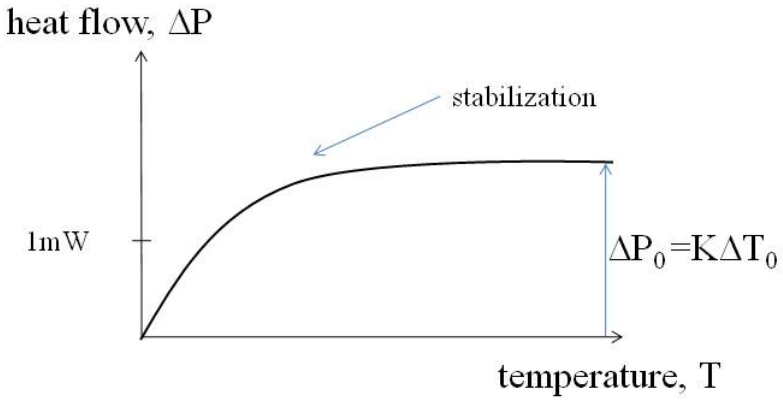

Figure 2.14: Reaching the quasi-static regime

As stated in equation 2.57, the temperature difference and the differential heat flux are related by the heat exchange coefficient K, which is measured in the quasi-static condition $\triangle P_0 = K \triangle T_0$.

$$\triangle P = K \triangle T = -\beta \triangle C - \tau_{ins} \frac{d(\triangle P)}{dt}. \tag{2.62}$$

The differential heat capacity is then obtained as a function of the measured differential heat flux.

$$\begin{aligned} \triangle P &= -\beta \triangle C - \beta \tau_{ins} \frac{d(\triangle P)}{dT} \text{ (J/s)}, \\ \triangle C &= -\frac{\triangle P}{\beta} - \tau_{ins} \frac{d(\triangle P)}{dT} \text{ (J/K)}. \end{aligned} \tag{2.63}$$

The differential heat capacity consists of the "convolution" of the measured signal with the time constant of the calorimetry [36]. Equation 2.63 allows the correction of the data by adding the contribution of the thermal time constant τ_{ins}, multiplied by the derivative of the measured signal to the measured heat flow $\triangle P$, as it is expressed in the second term of the equation. Because the DSC is not an ideal apparatus, there is a heat conduction path between the cells and the furnace where any temperature change is initiated. This

deconvolution procedure generally increases the noise because of the presence of the first order derivative of the measured heat flow.

As previously stated, in a DSC the corrected data $\triangle Cp$, corresponds to the difference in heat capacity between the sample and reference cells. In order to isolate the sample contribution, the reference component has to be added to the total signal. In mathematical terms this is expressed as,

$$\begin{aligned} \triangle Cp &= m_s Cp_s - m_r Cp_r \text{ (J/K)}, \\ Cp_s &= (\triangle Cp + m_r Cp_r)/m_s \text{ (J/gK)}. \end{aligned} \tag{2.64}$$

When a thermal process takes place within a sample, the temperature difference changes. The direction of the heat flow ($=\triangle T$) will depend on whether the reaction is exothermic or endothermic. In the latter process, heat is absorbed by the sample and thus a higher heat flux will be flowing to the sample. As examples, melting and glass transitions are endothermic processes while crystallisation is exothermic.

Before performing a DSC experiment the following steps must be considered:

1. One has to determine the substance of the reference cell suitable for the sample under study. It should be chosen a neutral reference which, by comparison with the sample, does not undergo any physico-chemical process in the scanning temperature range. If the reference cell is left empty, and assuming that the two empty cells have the same heat capacity, the sample heat capacity is given directly by the differential heat capacity measured. This has been the scenario in most of the experiments carried out throughout the thesis.

2. The experiment procedure must be performed based on the thermodynamical properties of the sample and transition under investigation, as well as choosing the scanning rate β convenient for the purposes. The latter is critical to be able to monitor any transition.

The choice of the scanning rate can affect the appreciation of the transition and even make it undetectable. Indeed, the signal that is measured in DSC is proportional to the scanning rate; therefore, it should be selected based on the energy scales of the event of interest.

The resolution in heat capacity depends on the relation between the β and τ_{ins}. The faster the scanning rate, the faster the system has to exchange heat. If the instrument has also a high value of τ_{ins}, the energy transferred or absorbed by the sample occurs too quickly compared to τ_{ins}, so no heat is lost via the thermal link, and thus all the energy is stored by the sample in the form of thermal capacity, $E = C\triangle T$ (adiabatic condition). Mathematically, this was expressed in equation 2.63 by the product, $\tau_{ins} \cdot \beta$. In this case the deconvolution procedure is critical. The drawback of having a high β or a high τ_{ins} is that, for the former the sample does not have time to reach equilibrium, while having a high τ_{ins} increases the noise within the deconvoluted signal.

On the other hand, the product of those two terms is inversely related to the temporal resolution in temperature. The smaller these variables are, the higher the temperature resolution, and thus it is possible to separate two thermal events close to each other.

Knowing the temperature and energy scales of the phase transitions of interest is crucial to define the most convenient experimental method before starting a DSC experiment.

Once the scanning rate has been established the experiment is ready to be launched. Subsequent measurements on the same sample at different scanning rates can be determinant to stress any instrumental dependency or kinetic induced events. Thermal constants can be determined via two methods: by calibration scans using a material of well known thermal transitions; or by monitoring the time it takes to the instrument to respond to an instantaneous power change, for example when turning off the DSC calibration heater.

Figure 2.15 shows an example of relevant information that can be extracted from a DSC curve. In this figure the data is expressed in heat flow as a function of temperature. DSC data is normally plotted in terms of $\triangle Cp$ as a function of temperature when the experiment is conducted with $\triangle T$ at a constant rate, which has been the case of the experimental curves in this thesis. The curves are then normalised using the baseline, as a reference, which accounts for instrument resolution. The baseline is defined as the heat capacity of the sample where no transition processes occur during that temperature/time. As an example, a glass transition process can be described as a shift of the baseline underlying the heat capacity at each state, liquid to glass. A sloping baseline requires extrapolation to the transition temperature and makes it easy to calculate $\triangle Cp$ at that temperature. Once this is determined, the enthalpy involved in the transition can be obtained by calculating the integral of the peak above the baseline, see equation 2.54.

From a DSC curve the transition temperatures are easily obtained. In Figure 2.15 three transitions have been represented characterised by the following temperatures: T_g (glass transition), T_c (crystallisation transition) and T_m (melting transition). The width of a DSC curve can comprise relevant information about the transition.

A DSC profile provides enough information to understand not only the final physical phase of the system, but the molecular events involved within the bulk sample during a thermodynamic transformation.

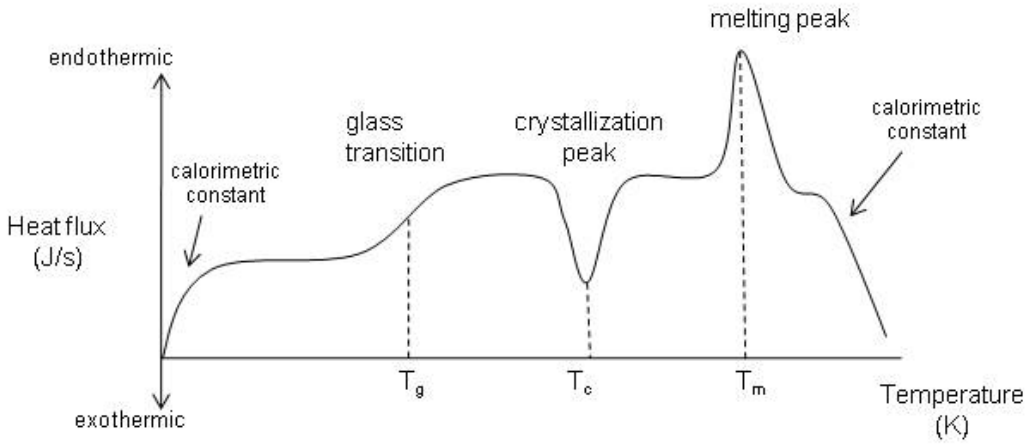

Figure 2.15: Example of a differential scanning calorimetry scan. Three transitions are present: glass, crystallisation and melting.

Although DSC is a straightforward tool in determining the enthalpy, one must take into account that the integration includes all thermodynamic events occurring in the sample as heat is supplied, i.e. it gathers information about any other thermodynamical process that may obstruct the transition of interest: hydration effects, parasitic effects due to mechanical movements of the sample in the holder tube, etc. Systematic series of measurements will help to distinguish the reproducibility of the transition.

Half of the material presented in this thesis have been produced using the differential scanning calorimetry technique. It became crucial to characterise the denaturing tran-

sition for different DNA conformations, and it gave the first insight of a conformational transition later investigated with neutron scattering. The glass transition of denatured DNA covering Chapter 6, was discovered when trying to test reversibility of the melting transition. The possibility of measuring on heat capacity gave direct proof of this transition.

Chapter 3

Literature Review of Fibre DNA

3.1 Foreword

The purpose of this chapter is to give a brief introduction of the properties of DNA, such as structure and dynamics which make the molecule a very interesting subject of study for physicists. The discussion will give a historical review of the work carried out on DNA, centred on the experimental studies of DNA fibre which motivated the research presented in this thesis.

3.2 Properties of DNA-the double helix

3.2.1 Structure

DNA (Deoxyribonucleic Acid) is found in human beings inside the 23 pairs of chromosomes in the form of thin wound strings. The genes occupy specific positions on a chromosome, and are formed by the sequences of DNA. The structure of DNA is composed of chemical building blocks called nucleotides, which in turn are divided into three parts: the phosphate group, the sugar group and the nitrogen bases. The phosphate and sugar group are joined by ester bonds and form the two strands (backbone) of DNA. These two strands twist forming a double helix connected by the nitrogen base pairs, the "stairs" of the helix. These are complex organic groups of one or two cycles: the purine, Adenine (A) and Guanine (G) have two organic cycles; and the pyrimidine, thymine (T) and Cytosine(C) have only one organic cycle. One of the biggest achievements of Watson and Crick was

in determining the constraints of the nitrogen bases to pair: A-T and G-C, joined by two and three hydrogen bonds respectively, forming a similar size cluster which regularises the overall structure, see Figure 3.1.

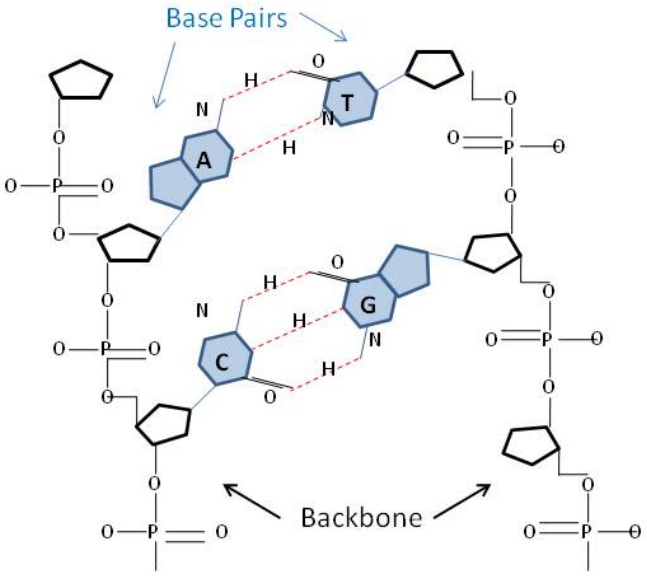

Figure 3.1: DNA structure in its chemical form.

While the primary structure of DNA is determined by the sequence, the secondary structure corresponds to the double helix structure. The resulting helix of the sugar-phosphate backbone gives rise to two asymmetrical grooves, the major and the minor, see Figure 3.2. The former corresponds to the backbones that are further apart, while in the latter they are closer together. As a consequence, proteins bind to specific sequences of the DNA through the major groove.

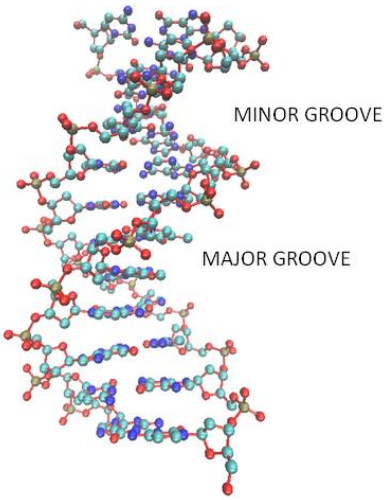

Figure 3.2: DNA double helix showing the minor and major grooves.

The main forces responsible for holding the nucleotides together and stabilising the DNA structure are the hydrogen bonding and the stacking interaction. The latter contributes the most energetically and its origin arises from interatomic contributions: the $\pi - \pi$ stacking which are attractive, noncovalent interactions between aromatic rings(purine, pyrimidine), as a result of overlap of π orbitals of the aromatic molecules; and hydrophobic forces. This is the reason why water molecules are not found between the base pairs, as it is energetically unfavourable [37]. This interaction can be understood as analogous of having big plateaux (base pairs) attached by rigid rods; the distance between consecutive plateaux is well defined by the distance between adjacent phosphate 6 Å(see Figure 3.3). Nevertheless, the "hole" showing in the figure is reduced by acquiring a helical form, so that rotations of the bonding can take place. The differences in bonding, and most importantly, those in stacking, are reflected in the dynamics of the molecule. They define the thermodynamics and physical properties of the molecule: stretch, melting, elasticity, etc.

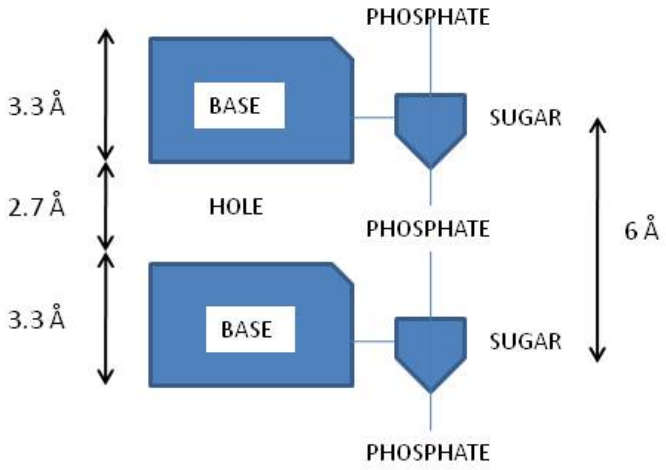

Figure 3.3: Two nucleotides in schematic form, showing key dimensions.

3.2.2 Dynamics

Information for the synthesis of proteins is embedded in the DNA sequence of the base pairs. Accessing the code requires high distortions of the DNA structure since the base pairs are protected by the backbone. The weak interaction of the hydrogen bonds that join the bases together, and at the same time the strong interaction between the sugar-phosphate backbone, allow fluctuations of the molecule at biological temperatures. These consist in the local openings and closing of units of these base pairs. "Breathing", has been the term used by biologists. These sporadic dislocations give rise to a broad range of possibilities for biological applications, since any genetic process is initiated by the exposure of the base pairs sequence to the surroundings.

For instance, the process of transcription which is essential for protein synthesis is led by RNA polymerase which unzips the double helix from 1 to 2 turns by breaking the hydrogen bonds. This open region called the "transcription bubble", comprises the sequence that will become a template for transcription. Additionally, an enzyme called Helicase is responsible to promote replication by unwinding DNA where synthesis will be initiated. The events leading to the reading of the genetic code are complicated since they involve at

least two elements, DNA and enzyme. Although the genetic processes are carried out by external biological particles which exert mechanical forces, thermal fluctuations can also assist in the openings. Understanding the simple process of how the base pairs separate under thermal fluctuations, an effect involving only the DNA molecule, is a first step of a more complex phenomenon.

One can study these localised defects as a pure physical process induced by heat. By increasing the temperature of the system, more and more open regions can be induced, forming bubbles, which will eventually expand to larger sizes, until they become unstable leading to the total dissociation of the double helix, Figure 3.4. This phenomenon is known by the following appellations: DNA denaturing, melting of DNA or helix-coil transition. The temperature at the mid point of the transition is defined as the melting temperature, T_m.

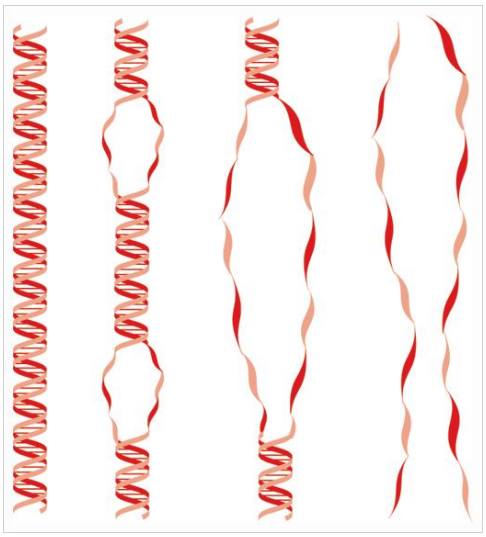

Figure 3.4: DNA melting. Figure reproduced from [38]-Figure. 1

The energetics involved in the melting transition highly depend on the stacking energies. These interactions occurring in a duplex structure depend on the distribution of the bases along the chain, and in particular on the nearest-neighbours bases interaction as established by Breslauer *et al* [39]. They defined the interaction energies $\triangle H$ of the ten different possible nearest-neighbours bases within Watson-Crick DNA model: AA/TT, AT/TA, TA/AT, CA/GT, GT/CA, CT/GA, GA/CT, CG/GC, GC/CG and GG/CC. The values of all the combinations are shown in Table 3.1.

They carried out an investigation into the thermodynamics of the helix to coil transition

Interactions	$\triangle H$	$\triangle S$	$\triangle G$
AA/TT	9.1	24.0	1.9
AT/TA	8.6	23.9	1.5
TA/AT	6.0	16.9	0.9
CA/GT	5.8	12.9	1.9
GT/CA	6.5	17.3	1.3
CT/GA	7.8	20.8	1.6
GA/CT	5.6	13.5	1.6
CG/GC	11.9	27.8	3.6
GC/CG	11.1	26.7	3.1
GG/CC	11.0	26.6	3.1

Table 3.1: Interaction energies of the nearest-neighbour bases resolved from calorimetrically and spectroscopically measurements [39].

(denaturation) on synthetic oligomer and polymers of DNA molecules. This was done using calorimetric and UV spectroscopy. They showed that the overall energies of a duplex structure can be estimated from nearest-neighbours interactions. These data became crucial to obtain information about the stability of the duplex structure predict the temperature of the helix-coil transition and in general, determine thermodynamic transition properties. The theoretical calculations on different DNA structures were compared to calorimetric studies on the same specimens, showing excellent agreement. The dynamics of a few base segments (oligomers) are strongly sequence dependent. In the case of polymers of DNA, where there are of the order of 10,000 base pairs, the effects of the sequence are averaged, and ultimately the dominant effect is the proportion of A-T with respect to G-C.

Chemically, the melting temperature depends upon two main factors: the sequence, and the experimental parameters such as ionic strength of the surrounding medium which acts as a shield for the repulsion between the phosphate groups of the backbone, and hydration. Hence, DNA melting in a salt medium can occur within a broad temperature range, defined between 37 and 137 ° C. But, strictly speaking there are many aspects that can favour or hinder the transition, such as having the system in a crystal structure which limits the degrees of freedom.

The dynamics involved in the opening of the molecule must be described using nonlinear mathematics. A review of some of the models used to characterise this transition will be discussed in the following section.

3.3 Theoretical models describing DNA melting

Melting transition of DNA has raised interest for physicists, as it is an example of a phase transition occurring in a 1-D system. Theoretical approaches based on the nonlinear dynamics of DNA have been developed along lines inspired from condensed matter theory. It has been shown, in this particular nonlinear system, that a phase transition in 1-D is possible without contradicting physical principles[40].

3.3.1 Ising Model

In a helix-coil system, the size of the closed regions (in helical form), is one parameter that can be described by a critical exponent in a continuous phase transition. The analogy of a DNA chain with a well-known ferromagnetic system has made possible the description of DNA denaturing with the crude Ising model [41]. In this scenario, the base pair status is described with two variables: 1 if the base pair is open, and 0 if it is closed, similar to the ferromagnetic Ising model with spins up and down.

The Ising model does not take into account the shape of the open regions to account for collective effects. It does not include nonlinear dynamics, which add a degree of difficulty but permit the description of intermediate states.

3.3.2 PBD Model

A more rigourous model to study the melting transition in DNA is the 1-D Peyrard-Bishop-Dauxois (PBD) model[6]. The simplest form of the model reduces DNA to N base pairs, each one described by a single real variable y_n, and solves the dynamical properties associated to the formation and stability of the bubbles. For non-homopolymers, sequence effects must be included by disorder parameters in order to be able to reproduce the melting curves for different DNA sequences. The phase transition is facilitated by an increase in the entropy of the system when DNA goes from a closed to a denatured state.

The model introduces one degree of freedom per base pair which is the stretching of the base pair from their equilibrium position perpendicular to the axis y_n. It takes values from 0, for a closed pair, to a continuous range up to infinity when the two bases are separated. The model is described by 1-D Hamiltonian in the form of

$$H = \sum_n \frac{p_n^2}{2m} + W(y_n, y_{n-1}) + V(y_n), \text{ with } p_n = m\frac{dy_n}{dt}, \tag{3.1}$$

The first term introduces the kinetic energy; second and third terms correspond to a potential energy. $V(y_n)$ is a Morse potential describing the interaction between the two bases within a pair; while W(y_n, y_{n-1}) accounts for interpair interactions and it incorporates the $\pi - \pi$ orbital interaction of the base pairs plateaux. All the potentials in the Hamiltonian should be understood as effective potentials, since they include different interactions. Figure 3.5 gives a scheme of the dynamical base pair model in the 1-D chain.

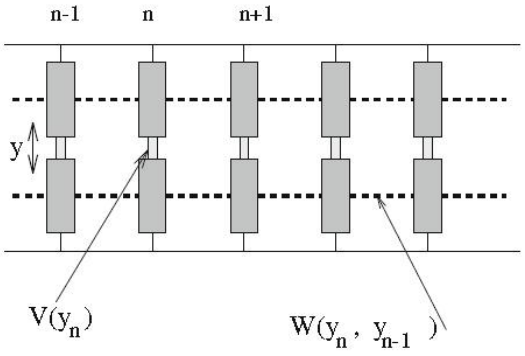

Figure 3.5: Graphical representation of the PBD model. Figure adapted from reference it was adapted from [42]-Figure 10.

Unlike other models, the PBD model describes the evolution of the opening and closing of the base pairs and how these fluctuations occur and their probability. It contains many simplifying assumptions but few free parameters, and they are calibrated from experimental data.

3.4 Experimental Studies in DNA fibre

3.4.1 Static Structure

The secondary structure of fibre DNA can take different forms, also called conformations of DNA. These are: A, B, C, D and Z , shown in Figure 3.6. The first four have right handed helices, the last one is left handed. Among all forms, A and B are the most common, and can be easily induced by changing the ionic nature and concentration of the solution, and/or the hydration level of the molecule. These 3-D structures differ in the helix pitch and the number of nucleotides per pitch; on average, the DNA pitch extends to 28 Å with 11 base pairs for A-form, and 34 Å with 10 base pairs for B-form. Furthermore, the stabilisation of the A-form is provided by an organisation of the cations and water molecules within the major groove of the double helix [43], and a more economic hydration of the phosphate groups [44]. For the B-form the hydration occurs in the minor groove; it is the most hydrated structure of all and is favourable in solution. That is the reason why most of the studies have been centred in this form as it is the state present in the cells. The A-form is less known and less work has been done on it. However, it is believed that when DNA forms transient heteroduplex with RNA during transcription it acquires an A-form [45], which shows its possible interest for biology besides its physical interest to better understand the forces that control DNA structure.

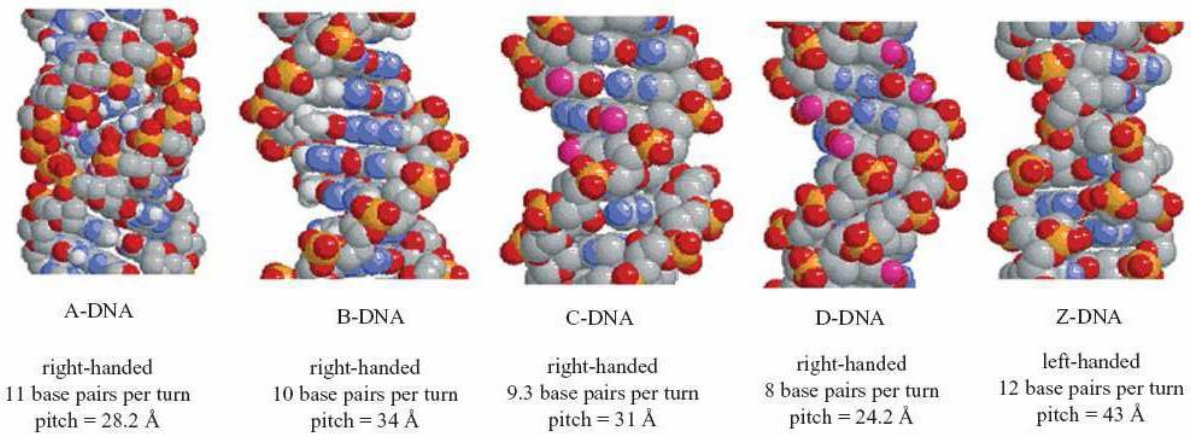

Figure 3.6: Different conformations of DNA, figure adapted from reference [46]-Figure 1.

DNA can exist under different states: solution, crystal, fibre, etc. The possibility of having DNA in fibres opened new opportunities for experimental studies. Fibre samples

are a simple way of having oriented DNA molecules, and moreover these molecules can be assembled within the fibre in the form of a crystalline structure making DNA samples suitable for the investigation of the characteristic length scales: base pair separation, unit cell distances and structure using scattering methods. Furthermore, DNA fibres offer higher configuration flexibility over crystalline DNA, since the weaker confinement in fibres permits the penetration of water, and leaves space to allow DNA to change structure.

Moreover, it was the possibility of having samples of DNA molecules oriented in a fibre structure which allowed Rosalind Franklin to carry out the first structural studies using X-ray diffraction [47]. By a proper interpretation of the X-ray fibre diffraction images, especially "image 52", Watson and Crick enlightened the world with the structure of the double helix [1]. Wilkins became a pioneer in preparing oriented fibres of 50 to 100 μm in diameter [48]. The technique, which demanded the use of a microscope, consisted in the pulling of a fibre from a wet gel with a pointed glass rod. The hydration of the gel and the speed of the pull determined the diameter of the fibre.

It was observed that under different hydrations, depending on the presence of the salt, the DNA molecules were packing together forming different structures, and with different crystallinity. After the discovery of the DNA structure, studies of the effects responsible for DNA conformations in fibres continued on X-ray fibre diffraction. Naming but a few important investigations: Langridge *et al* for their investigations centred in the B-form Li-DNA [49] [48] [50]; and Fuller *et al* for those in the A-form Na-DNA [51]. They investigated the arrangement of the water molecules in the different conformations in order to understand the conformational transitions and stabilisation of the molecules within the crystal system.

In the semicrystalline B-form Na-DNA the neighbouring molecules pack in a 2-D hexagonal/orthrhombic lattice, screwed in or out of the plane by random amounts [46]. It is a high hydration form, in which water is placed between the molecules. By decreasing the hydration, the molecules can be transformed into a crystalline A-form, in which the crystalline regions acquire 3-D order [46]. However, the conversion from the different forms is also salt dependent, and changes from B to A by reducing the hydration only occurs under the presence of Na. On the other hand, when Li salt is used a semicrystalline and a crystalline B-form can be induced by means of the hydration. Moreover, the neighbouring

molecules order within different unit cell packing: hexagonal, orthorhombic and monoclinic for B-semicrystalline, B-crystalline and A-form respectively. Table 3.2 was adapted from [48]. It gives a summary of the different structures in DNA fibres and their main characteristics such as: inclination of bases with respect to the helical axis; presence of salt and optimal relative humidity in which the conformation can be adopted; lattice and crystalline character.

Configuration of Molecule	No. nucleotides/ per helix turn	Salt	Relative Humidity	Lattice	Crystallinity
A-form	11	Na,K,Rb	75%	monoclinic	crystalline
B-form	10	Li	66%	orthorhombic	crystalline
		Li	75-90 %	orthorhombic	semi-crystalline
		Li,Na,K,Rb	92%	hexagonal	semi-crystalline

Table 3.2: Overview of the main conditions under which different DNA forms can be induced in fibre samples [48].

The resulting diffraction pattern for the different conformation is given in Figure 3.7. Subfigures (a) and (b) shows the crystalline A Na-DNA and B Li-DNA forms humidified at 75% and 66% respectively. Subfigure (c) shows the semicrystalline B-form at 92% RH, where each quarter of the image corresponds to a different salt: lithium I), sodium II), potassium III) and rubidium IV).

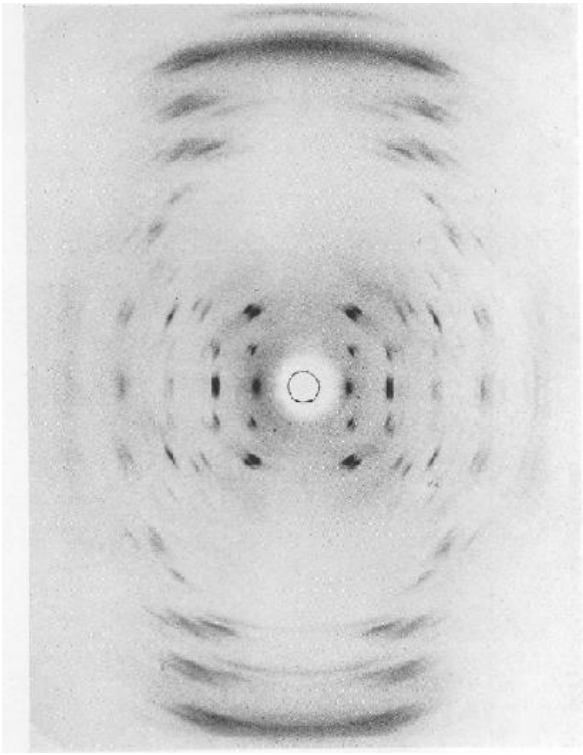

(a) A-form Na-DNA 75% RH

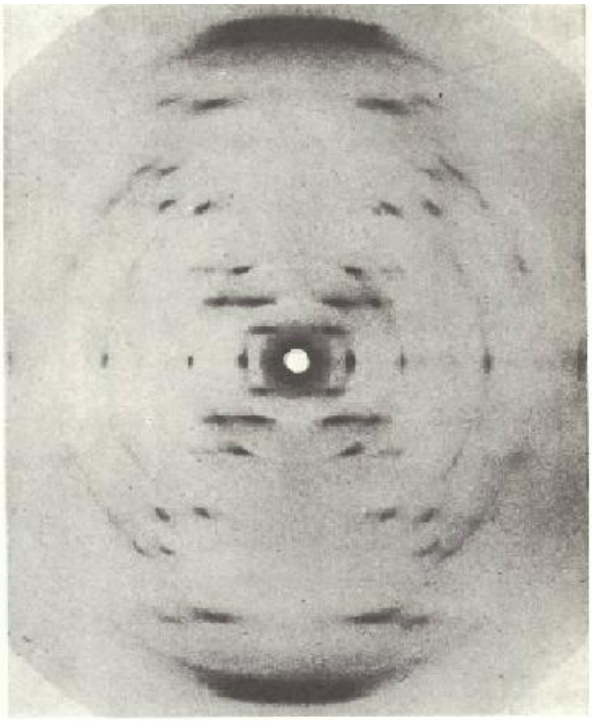

(b) B-form Li-DNA 66% RH

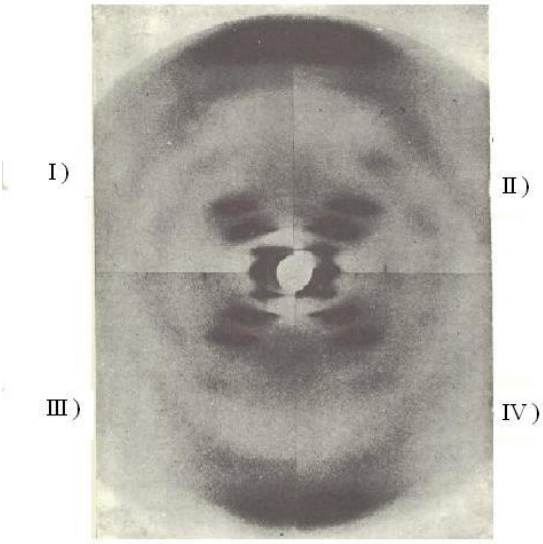

(c) B-form different salts 92% RH

Figure 3.7: X-ray diffraction images of A- and B-form DNA for different salts and relative humidities. The images were reproduced from the following sources: Figure-a from [*W. Fuller, M. H. Wilkins, H. R. Wilson, L. D. Hamilton, Journal of Molecular Biology 1965, 12, 60-80*]-Plate IV; Figure-b and Figure-c from [*R. Langridge, H. R. Wilson, C. W. Hooper, H. F. Wilkins, L. D. Hamilton, Journal of Molecular Biology 1960, 2, 19-37*]-Plate II and -Plate I respectively.

A useful way of comparing qualitatively the different fibre diffraction images is through

the use of layer lines. They correspond to the Miller index reflections (hkl), where each layer line $i-th$ is associated to a reflection $l = i$, being [00l] along the helical axis. It shows again the A and B diffraction patterns with the corresponding layer lines. The A-form presents a highly crystalline pattern (many Bragg peaks). The most prominent features of this form are the three off-axis Bragg peaks displayed on the 6th, 7th and 8th layer lines which are associated to the stacking of the tilted bases pairs. The Bragg peak given by the distance between the base pairs is found at the 11th layer; it is a very weak peak and thus it is out of the limit of the figure. However for the B-form, this feature gives rise to a strong reflection in the 10th layer line. It is important to notice that this layer coincides with the 8th of the A-form. The central part of the diffraction pattern in the A-form or crystalline B-form is associated to the helical form of the polynucleotide chain, as it corresponds to longer distances in real space (recall: $G = \frac{2\pi}{d}$). The most remarkable feature in the B-form is the X-shaped cross rising between 0th-3rd layer, this pattern revealed the double helical structure of DNA.

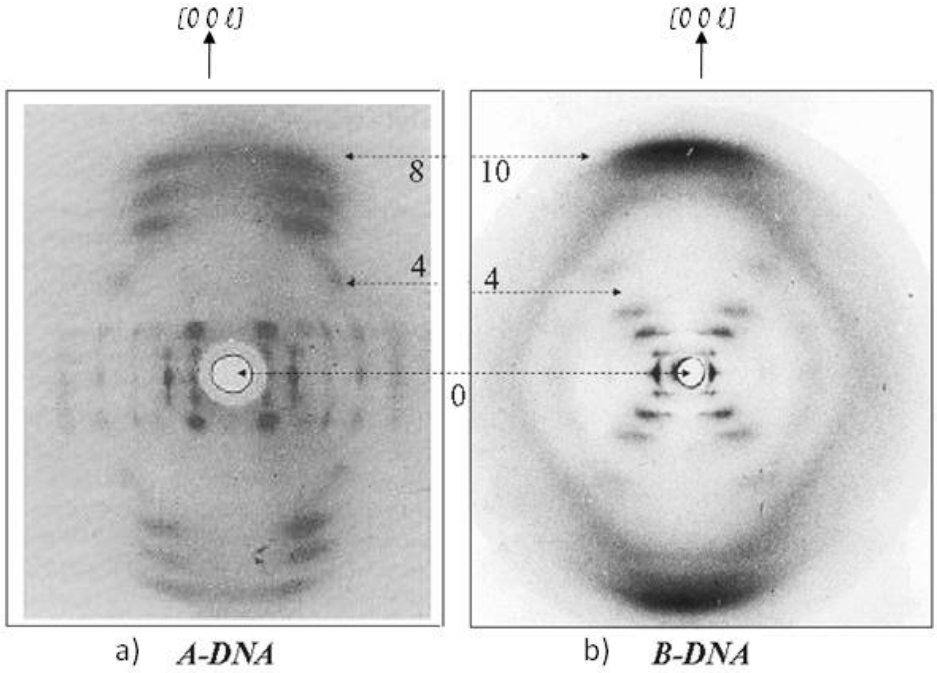

Figure 3.8: X-ray fibre diffraction images for A- and B- forms where the layer lines have been drawn. The figures are represented in the same scale. Figure 3.8 has been taken from [52]-Figure 13.

Under specific conditions hydration stipulates the limits between conformations in fibres

samples. The coexistence of structures, A + B was already proposed by Franklin [53] using X-ray fibres diffraction. Na-DNA fibres in an A-form DNA can undergo a transition to B-form with increasing the hydration. This transition was in detailed investigated by S. Premilat and G. Albiser [54], comparing X-ray fibre diffraction and fibre dimension measurements on fibres of Na-DNA with changes in hydration. The X-ray fibre diffraction images obtained at a fixed relative humidity of 87% at different temperatures: 7, 20 and 37 °C, are shown in Figure 3.9.

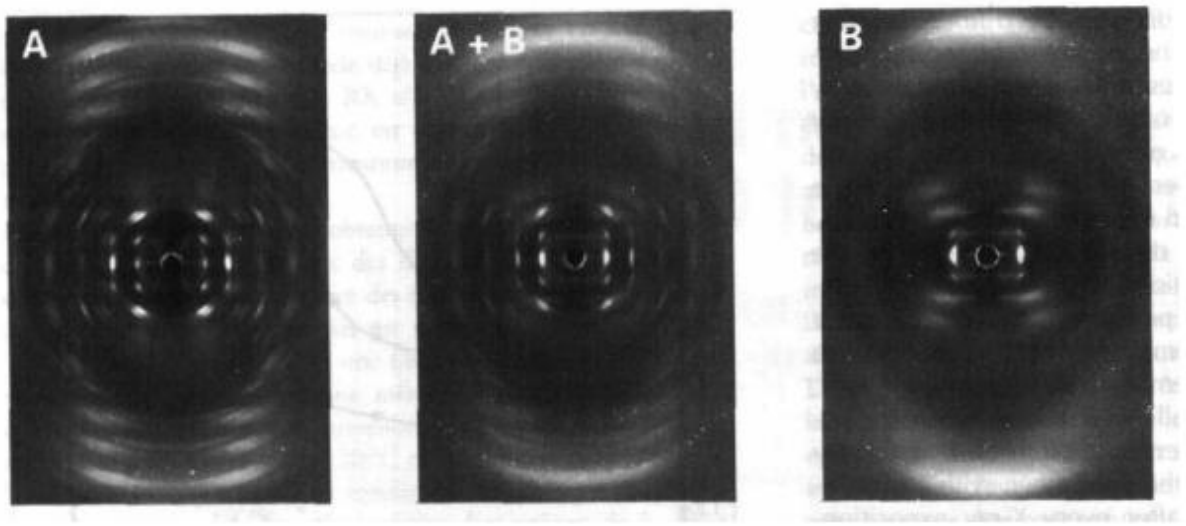

Figure 3.9: X-ray fibre diffraction patterns of a DNA fibre humidified at 87% RH, for different conformations obtained as a function of temperature. The images corresponds to A-form at $37°C$, A+B mixture at $20°C$, and the B-form at $7°C$. Figure reproduced from [54]-Figure 2.

At room temperature and a that high relative humidity, DNA molecules in the fibre organise partly in a B-form and partly in an A-form. From the diffraction images, the most prominent features revealing this A+B phase mixture are: the three off-axis Bragg peaks in the 6th, 7th and 8th layer lines, correspondent to the A-form; and the strong Bragg peak in the 10th layer line from the B-form. At that fixed relative humidity, when the temperature is increased water molecules organised around the DNA are released to the surrounding medium, favouring the A-form. This transition between A to B and vice versa is reversible.

Improvements in the preparation of DNA fibres arrived in 1963, when Allan Rupprecht designed the wet spinning method with which films, of few cm wide, made of oriented DNA fibres became available [2]. With this method, a thin filament of DNA was obtained by precipitation from an ion salt solution in high concentration of ethanol, and wound

around a bobbin. The large size of the samples, their viscosity and molecular orientation made them suitable for the investigation of physico-chemical characteristics with multiple experimental techniques, such as X-ray, NMR or Optic Microscopy, and specially the examination of the dynamical properties of DNA using neutron scattering.

Dynamics

To date, most of the experiments to study the topology and thermodynamics of DNA were carried out in solution, as this is how DNA is found in organisms and therefore attracted most of the attention. Information about these properties were mainly studied through the thermal denaturation of DNA using bulk techniques such as Raman spectroscopy [3], UV absorbance [4][55] and calorimetry [56]. The hyperchromic shift detected with UV absorbance indicates the disruption of the base pairs stacking, hence proving the denaturation of the molecule. This behaviour is also observed using Raman spectroscopy, where its spectrum provides information about specific vibrational modes from the different constituents of the molecule. When the bases unstacked during melting the intensity of the corresponded frequency increases. On the other hand, Differential Scanning Calorimetry (DSC) became one of the most powerful tools to study the effect of temperature upon bio-systems and the exchange of heat yield to a physico-chemical transformation; and furthermore, this technique excels in its flexibility to investigate specimens in different states: liquid, fibre, solid, etc. Thus, DSC became a key technique for the thermodynamic investigation of DNA fibres carried out in this thesis. Attempts were also made to detect the melting transition using UV absorption, but the films were not thin enough to allow any transmittance. Moreover, problems to maintain constant the relative humidity were encountered.

In the early 90's several calorimetry studies carried out by Tsereteli and Smirnova reported for the first time evidence of vitreous behaviour in biopolymer-water systems [57],[58],[59]. They showed for a range of humid macromolecules such as collagen, DNA and proteins, that after heating the samples above their denaturation transition a second heating ramp give rise to a jump of the heat capacity characteristic of a glass transition [60].

The dynamical properties of biological systems were first experimentally studied through Raman and Brillouin light scattering. The Brillouin scattering by acoustic phonons was observed for the first time thanks to the achievement of solid samples of oriented fibres

of DNA [61]; and thus the speed of sound, in both parallel and perpendicular direction to the helical axis, for A- and B- conformations of DNA was determined [61],[62].
Phonon dispersion curves on Oriented fibres of DNA were measured for the first time using inelastic neutron scattering by Grimm [63]*et al*, [64]; later on, inelastic measurements were carried out in different DNA conformations using X-ray scattering (IXS) [65]. This results motivated M. Johnson and co-workers to investigate the longitudinal phonon dispersion along the helical B-form DNA using, instead, inelastic neutron scattering (INS) on a TOF spectrometer [11]. In parallel, the same group developed a computational package to study the longitudinal phonons branches along the double helix. This program, called NMscatt, is based on force-field simulations, allowing the calculation of phonons for large biomolecular system.

Chapter 4

Preparation and Characterisation of Samples of Oriented DNA Fibres

4.1 Foreword

This chapter describes the experimental studies carried out to characterise samples of oriented DNA fibres. Maintaining oriented DNA molecules within a fibre structure stable under the influence of external factors, temperature or hydration, have been crucial to be able to proceed with further studies into their dynamics.

4.2 Sample Preparation

4.2.1 Oriented fibres of DNA

Oriented fibre samples of DNA consist of films of parallel and adjacent fibres oriented along the molecular axis. The molecules organised in a periodic lattice within the crystalline regions of the fibre. These films of any desired dimension on the centimetre scale were made using the wet spinning method, proposed by Allan Rupprecht in 1963[2]. The wet spinning apparatus uses a technique in which a thread of DNA in aqueous solution is stretched as it precipitates in high concentration of ethanol, resulting in a solid fibre. Compared to other methods of fibre solidification such as dry-spinning or melt-spinning[66], wet spinning has proved to be the most efficient in producing big samples.

Ziabicki and co-workers contributed in the 70′s with their studies in fibre spinning [66].

Ziabicki showed that fibre spinning is crucial to achieve molecular orientation [67]. The same group proved the orientation of the samples by negative dichroism in the ultraviolet spectrum and birefringence in the visible spectrum.

DNA molecules are soluble in water and in a medium with low ethanol concentration. The solubility depends on the salts present in the solution. It is highest for Li salt and decreases for K, Cs, Na [68]. At high ethanol concentration DNA aggregates and precipitates. This is due to the low dielectric constant of ethanol compared to distilled water. In the presence of positive ions, as the ethanol concentration increases, the dielectric constant of the medium decreases allowing the positive ions to attach to the DNA molecules. This reduces their negative charge as well as the repulsion between the charged phosphates of the DNA backbone. This allows intermolecular aggregation, exploited in the wet-spinning apparatus. If the resulting sample of aggregated DNA molecules is exposed at lower ethanol concentrations($< 70\%$ for Li-DNA and $< 60\%$ for Na-DNA), the DNA disaggregates and a reversible solution of randomly oriented molecules can be observed.

The raw material consists of an aqueous solution of DNA sodium salt from salmon testes (purchased from SIGMA). According to the product information, DNA has a GC content of approximately 41% and a molecular weight of 1.3×10^6 [69]. The solution is prepared in the presence of a counter-ion: sodium or lithium. DNA is stable in water, with a neutral pH, and under the presence of ions. The choice of the salt will define the accessible conformations of DNA.

The Na-DNA and Li-DNA solution were based from recipes given by Rupprecht [66],[70]:

1. Na-DNA solution: 1.58g of Na-DNA dissolved in 1L of distilled water, with 0.15M of NaCl, 0.003M of Na-citrate and 0.00005M of Na-EDTA. The latter is used for its great affinity for divalent cations such as Mg^{+2}, Cu^{+2}, which are cofactors of many enzymes. It chelates the ions, thereby reducing the activity of enzymes that could cut or digest DNA.

2. Li-DNA solution: 0.6g of Na-DNA were dissolved in 1L of distilled water with a high concentration of LiCl, 0.4 M. Other complementary salts such as 0.2 g/l of sodium azide and 0.02 g/l of EDTA where also added. The former acts as anti-microbial agent.

Dialysis was also explored to obtain Li-DNA and Na-DNA solutions purified from undesired ions or divalent cations that could have been present in commercial DNA. A total of 9 changes during 3 days were carried out. The DNA concentration within a fibre is lower for Li-DNA than for Na-DNA, as the injected solution has a concentration for Li-DNA of 0.9mg/ml and 1.58mg/ml for Na-DNA.

4.2.2 The Wet Spinning Apparatus (WSA)

Figure 4.1 shows a layout of the wet spinning apparatus. The process starts as the DNA solution is extruded from the syringe by a precision pump (spinning pump) at 1 ml/min. It is conducted inside a teflon tube through the spinneret into the alcoholic solution at the top of the glass column. The spinneret acts as a kind of microscopic shower forming fibres with molecules pre-oriented as the solution pass through it. The DNA in a diluted solution of counterion in contact with concentrated EtOH aggregates and consequently precipitates along the glass column. The DNA fibres stretch as they fall down, towards a V-shape wire guide which collects them into a thin fibre which is then wound around a Teflon-coated cylinder; like a thread of silk of tens of microns thick. While the fibre is being smoothly wound, the translational motor of the cylinder is activated, producing a back and forth displacement. The number of sweeps defines the thickness of the film. The process can last between 2h-5h depending on the initial volume of DNA solution, i.e. number of syringes. Throughout the preparation of the film there is a recycling system running. It consists in transferring, via a pump, a higher ethanol concentration solution from the conical flask into a degasser and to the top of the spinneret. At that site the DNA solution is being injected, decreasing the EtOH concentration of the surroundings, so that the injecting of new EtOH avoids disturbing the aggregation of the DNA. Every 10-15 min about 300 ml of solution are pumped out of the spinning bath back to the degasser, preventing an overflow. Air bubbles must be prevented from appearing in the preparation process as they could ruin the film. Thus, the DNA solution and the other liquids are degassed by pumping on them using a vacuum.

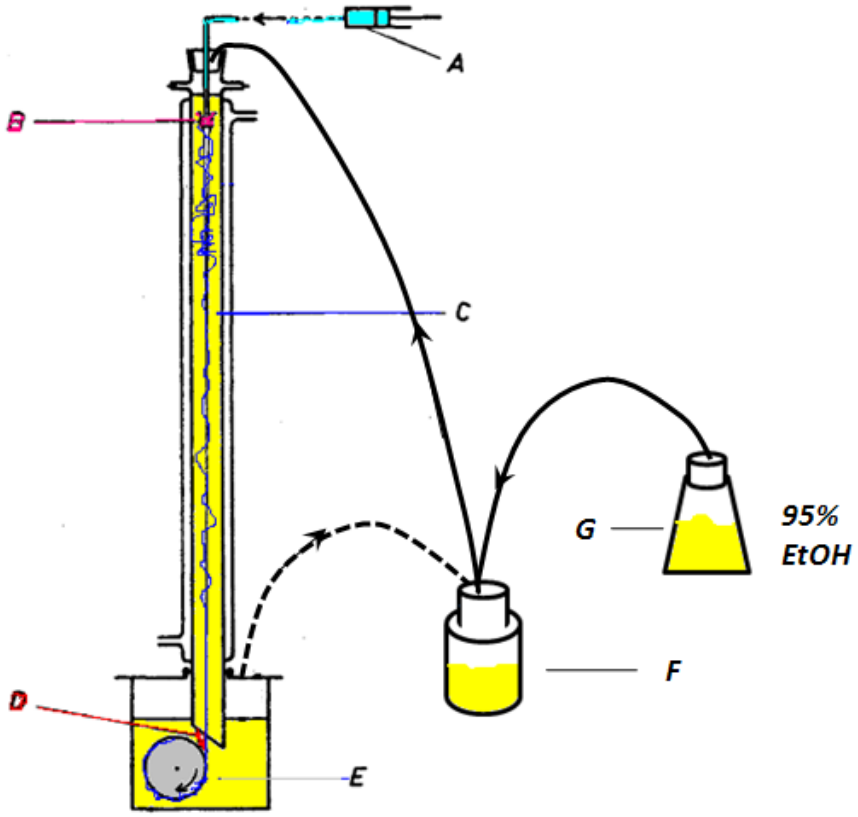

Figure 4.1: Scheme of the wet spinning apparatus. The different letters designate the sequence of steps within the preparation process: DNA is extruded from the syringe (A) into the glass column and through the spinneret (B). The DNA precipitates in contact with alcohol, represented by a yellow colour, down the glass column (C), to the V-guide (D). The DNA thread is finally wounded on a cylinder (E). The recycling system is composed of the following elements: the degasser (F) and the Erlenmeyer flask (G) [66].

Preparation of the equipment

1. The spinning apparatus is operated through a computer program called Labview. Once the program is started, two parameters have to be defined: number of translational sweeps and time per sweep. The time per sweep was fixed to 8 min/sweep for all the samples, providing samples of 3 cm wide. The spinning time (number of sweeps) defining the thickness of the films was established depending on the experimental purpose for which the film was made.

2. The DNA solution is degassed using a vacuum pump to avoid air bubbles throughout the spinning process.

3. A Teflon-coated cylinder is fixed in the metal or glass shaft in the glass vessel. Cylinders of different diameters have been used.

4. The syringes are carefully connected to the spinneret to avoid the entrance of air bubbles in the tubes.

5. The spinning bath and glass column are filled with 7 litres of an EtOH solution: for Na-DNA films 75% EtOH and 0.02 M of NaCl were used; and in the case of Li-DNA films, 83% of EtOH with 0.4M LiCl.

6. A higher concentration of ethanol, 90-100% ethyl alcohol, was poured into the Erlenmeyer flask connected to the top of the spinning glass column and to a recycling pump.

7. The motor of the cylinder was activated to provide a slow rotational motion.

The following images, 4.2 and 4.3 are photographs of the front and side views of the apparatus, in which the main parts have been marked.

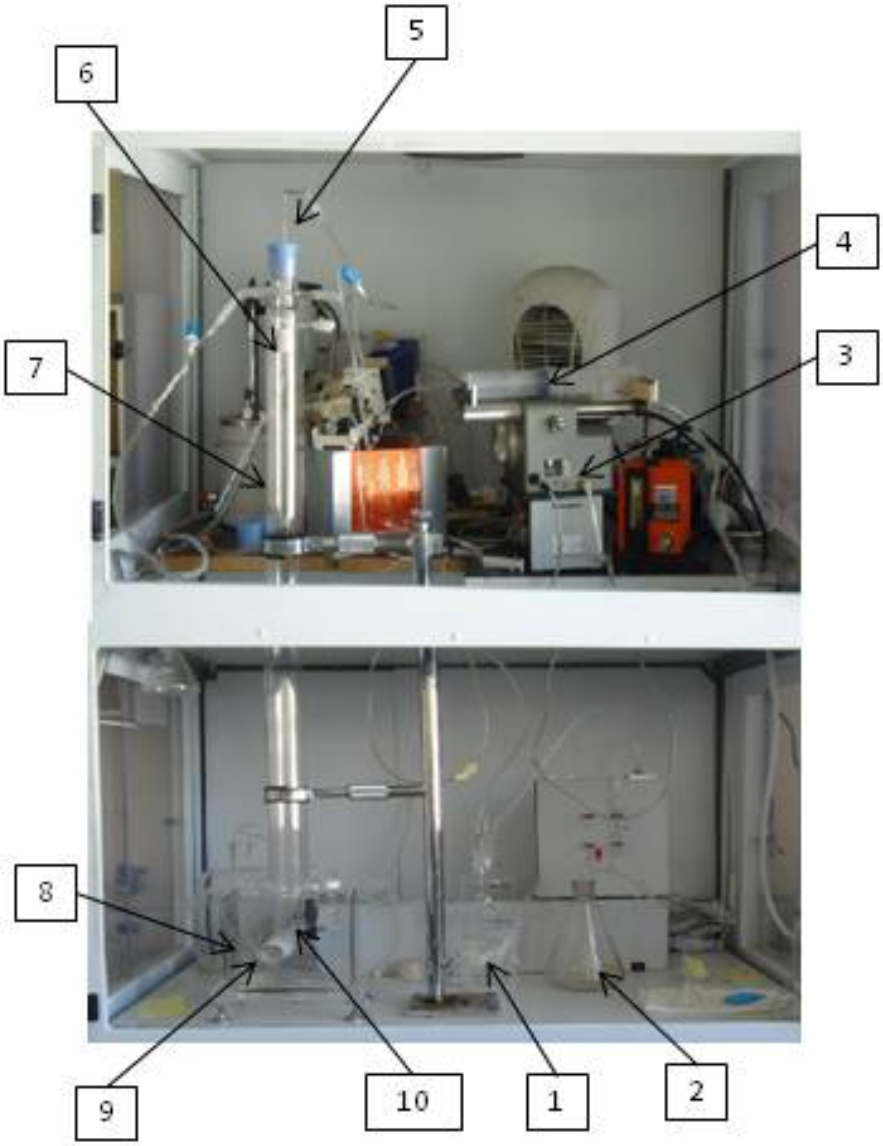

Figure 4.2: Front view of the Wet spinning apparatus. (1) Degasser; (2) Erlenmeyer flask with 99.5% ethyl alcohol; (3) spinning pump; (4) disposable syringe containing DNA solution; (5) spinneret holder glass capillary, spinneret and stopper assembled together at the top of the glass column; (6) spinneret; (7) glass column (i.d. = 0.045 m, l. = 1 m); (8) glass vessel (0.2×0.15×0.2 (m^3); (9) glass cylinder coated with Teflon tube; (10) V-shape guide made of Teflon coated wire.

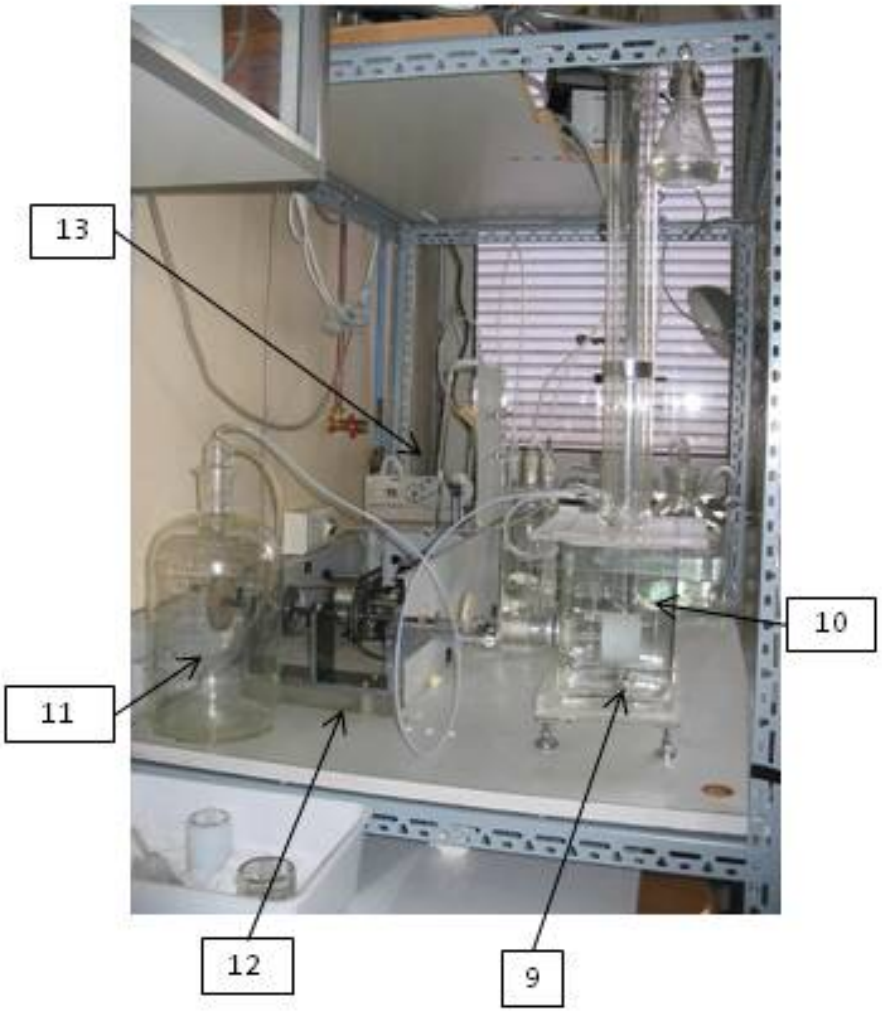

Figure 4.3: Side view of the Wet spinning apparatus. (9) glass vessel; (10) V-shaper guide; (11) bottle containing excess spinning bath; (12) screwed shaft and driving shaft, which are operated by a driving motor. This motor permits a rotational and translational motion of the shaft; (13) alcohol-pump.

One of the most important elements of the WSA are the position of the V-guide with respect to the cylinder and the spinneret. The surface of the V-guide needs to be smooth to avoid the fibre getting stuck and thus the complete loss of the film. Figure 4.4-left shows a picture of the V-guide within the instrument and the fibre passing through it; on

the right hand side figure we can see the film covering part of the surface of the cylinder. In the case of the spinneret, it is crucial to clean it properly before using it, as well as making sure that there are no air bubbles on its surface before starting the DNA spinning pump. Figure 4.5 shows a picture of the spinneret.

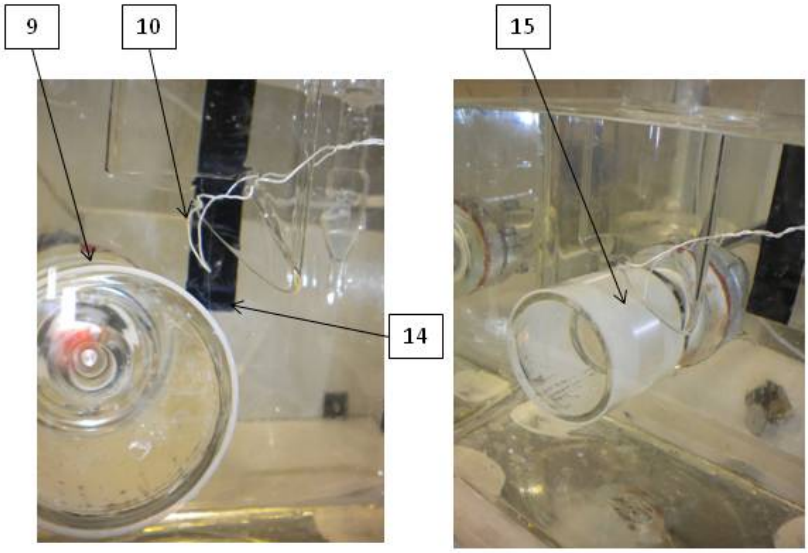

Figure 4.4: Zoom into the V-guide [10], and cylinder [9] of the WSA. The DNA fibre [14] is falling from the V-guide down to the cylinder. The DNA film [15] can be seen on the right image. [9]

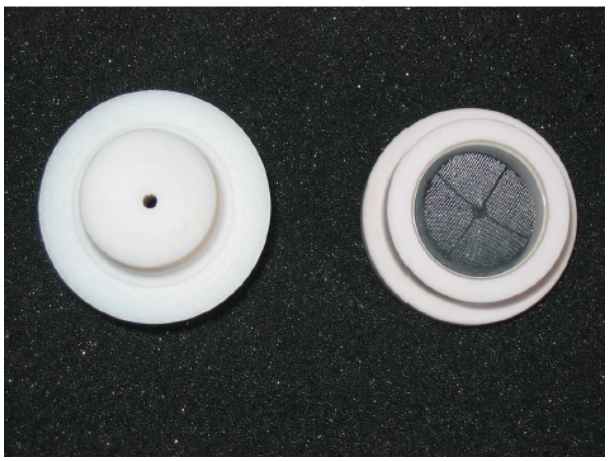

Figure 4.5: From left to right: teflon plug and spinneret.

Details of the method and equipment were given elsewhere [2], [66], [71] and [70].

Film treatment

Once the films are made, they are put through a process of cleaning, drying and humidifying, each step requiring at least 24 hours.

The cleaning process consists in a bathing process, or dialysis of the spun DNA deposit, in which the content of the electrolyte is adjusted by a predetermined concentration. In our case this is: 77% ETOH and 0,03M NaCl for Na-DNA films; and 80% EtOH and 0.25M of LiCl for Li-DNA films.

The resulting DNA fibres contain water, alcohol and electrolyte. To finally acquire an homogeneous DNA film, the DNA deposit goes through a **drying process** to eliminate excess of alcohol and water. This is done by inserting the cylinder in a desiccator with silica gel. This should be a slow process to avoid cracking of the films.

The last step, **humidification**, is crucial to determine the final conformation of DNA. This is done by placing the samples inside vacuum desiccators with a defined relative humidity (at room temperature) provided by an over-saturated salt solution in deuterated water (D_2O) for samples made for neutron scattering purposes, or in protonated water (H_2O) for the rest of the experiments (calorimetry, X-ray, etc.). The range of relative humidities obtained with the correspondent oversaturated salt have been presented in table 4.1.

Relative humidity (%)	Saturated Salt
dry	Silica gel
56	Sodium Bromide
75	Sodium Chloride
84	Potassium Chloride
92	Potassium Nitrate

Table 4.1: Different relative humidity provided by an oversaturated salt solution.

Each sample consists of a film of 2.5×9 mm^2, of around 20 μm thick, with a weight of 50 to 100 mg. They were stored in a vacuum desiccator with an specific humidity to provide the desired conformation.

The following table is a summary of the different solutions needed throughout the stages in the preparation of an oriented film: preparing the solution, spinning the solution and cleaning the final film.

Table 4.2: Values of variable to prepare DNA films by the wet spinning method

	Na-DNA film	Li-DNA film
DNA concentration	1.58 mg Na-DNA/ml	0.9 mg Na-DNA/mg
Electrolyte concentration	0.15M NaCl	0.4M LiCl
Bath sol concentration	75% EtOH with 0.02M NaCl	83% EtOH with 0.4M LiCl
Cleaning sol concent	77% EtOH with 0.03M NaCl	80% EtOH with 0.25M LiCl

The wet spinning apparatus became accessible to the ILL in 2004 when it was donated by H. Grimm to the Institut Laue Langevin, and re-installed in one of the labs by Fabian Fontaine-Vive and Mark Johnson. Maintenance and improvements of the WSA have been necessary to achieve a more efficient performance of the instrument and the preparation of higher quality samples. The apparatus is capable of working with 3 syringes with a volume capacity of 140 ml each. These allow to obtain higher mass samples in one spinning operation.

4.3 Sample Characterisation with different techniques

4.3.1 DNA conformations in oriented fibres DNA

As discussed in Chapter 3 the different conformations in fibre DNA can be obtained by changes in the ion nature and concentration, and the hydration level of the samples. However, due to the preparation method of samples, the ethanol concentration at which DNA aggregates to form the fibre also acts as an influential factor.
According to the preparation conditions of the samples, A- and B-forms can be induced within the following limits:

1. A-form DNA is favoured when spinning the solution in high ethanol levels around 77%. Spinning at lower ethanol levels may cause the coexistence of A and B forms, since decreases of the ethanol level is equivalent to increasing the water content (relative humidity) [72],[73]. Within these conditions the spun films have to be rehumidified between 32-84% relative humidity.

2. For the B-form Li-DNA, the ethanol levels are within the range $82 - 83\%$. The crystalline B-form has been established for Li-DNA samples at 75% RH; while for Li-DNA at higher than 75% RH, B-form is semicrystalline. In the case of Na-DNA, B-form DNA can be induced at high hydration levels, $86\% - 94\%$ RH.

Figure 4.6 shows the phase diagram presenting the conditions, relative humidity and counterion, needed to achieve the different DNA conformations of interest, as accepted from the literature [46].

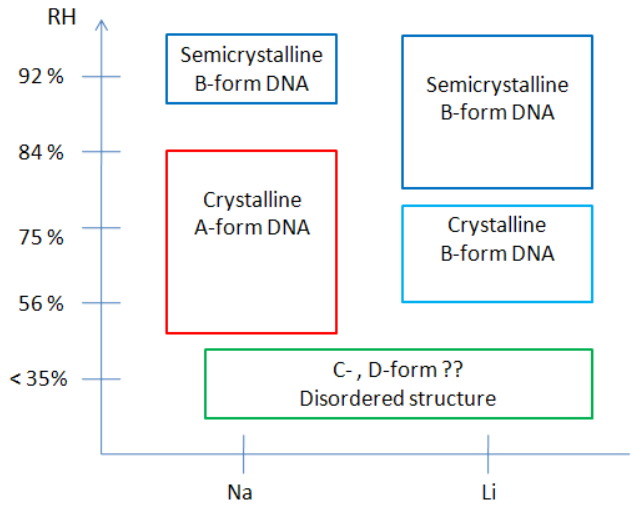

Figure 4.6: Phase diagram, relative humidity *vs* counterion, defining the different DNA forms

The following images in Figure 4.7 represent the theoretical diffraction peaks of a 1-D system composed of a DNA molecule with N base pairs within two turns of the double helix. The layer lines have been also represented. Conventionally, the vertical axis of the diffraction images is defined in the $l-direction$ coinciding with the fibre axis, as described in Chapter 3. But for experimental reasons, the fibre axis has been defined along the $H-direction$, and this definition will be held for the rest of this thesis; moreover, we will be working in inverse Angstroms and not in Miller indices.

A fibre diffraction image is the result of the structure factors of thousands of DNA molecules within a chain, but the theoretical calculation for such a big system would require long computational time. To overcome this problem a method was applied analogous to obtaining the diffraction intensity of a DNA molecule as it rotates about the helical axis. Before describing the method the scattering vector needs to be designated. It was defined as a cartesian coordinate system (Q_H, Q_K, Q_L) with $\mathbf{Q}_\theta = \mathbf{Q}_H + Q_\perp \cos\theta\hat{\mathbf{k}} + Q_\perp \sin\theta\,\hat{\mathbf{I}}$, where $Q_\perp = \sqrt{Q_K^2 + Q_L^2}$ corresponds to the components perpendicular to the helical axis. The method consisted in calculating the structure factors for twelve different $Q_\perp$ vectors in intervals of 30° covering 360°, at each Q_H position. And then averaging

over the twelve combinations.

This is expressed by the following mathematical expression,

$$I(\mathbf{Q}) = \frac{1}{12}\sum_{\theta} I(\mathbf{Q}_\theta), \tag{4.1}$$

$$\text{with } I(\mathbf{Q}_\theta) = \left|\sum_i b_i \exp(i\mathbf{Q}_\theta \mathbf{R}_i)\right|^2, \tag{4.2}$$

where $I(\mathbf{Q})$ is the total intensity at each $\mathbf{Q}$ position, $\mathbf{Q}_\theta$ is the scattering vector obtained for each value θ, $\mathbf{R}_i$ is the position vector in cartesian coordinates of each atom in the system, and b_i is neutron scattering length of each atom. The positions of the atoms were obtained from a Protein Data Bank (PDB)[74] file for an idealised B- and A-DNA oligomers.

These images show very similar features as the diffraction patterns for the A- and semicrystalline B-forms (Figures 3.7-(a) and -(c)), noticing that less peaks are present since the calculation does not consider the crystalline structure of the molecules in the fibre. Intense peaks in the 6th, 7th and 8th layer line, as well as strong peaks at low-Q are present. In the case of the B-form DNA, the most distinguishable spots are those at the 10th layer line, part of the famous X-shaped is also shown. It is important to notice that in the A-form there is almost no intensity between the symmetrical peaks at the 8th layer line. This point will become relevant when analysing X-ray and neutron diffraction patterns of oriented samples in both forms.

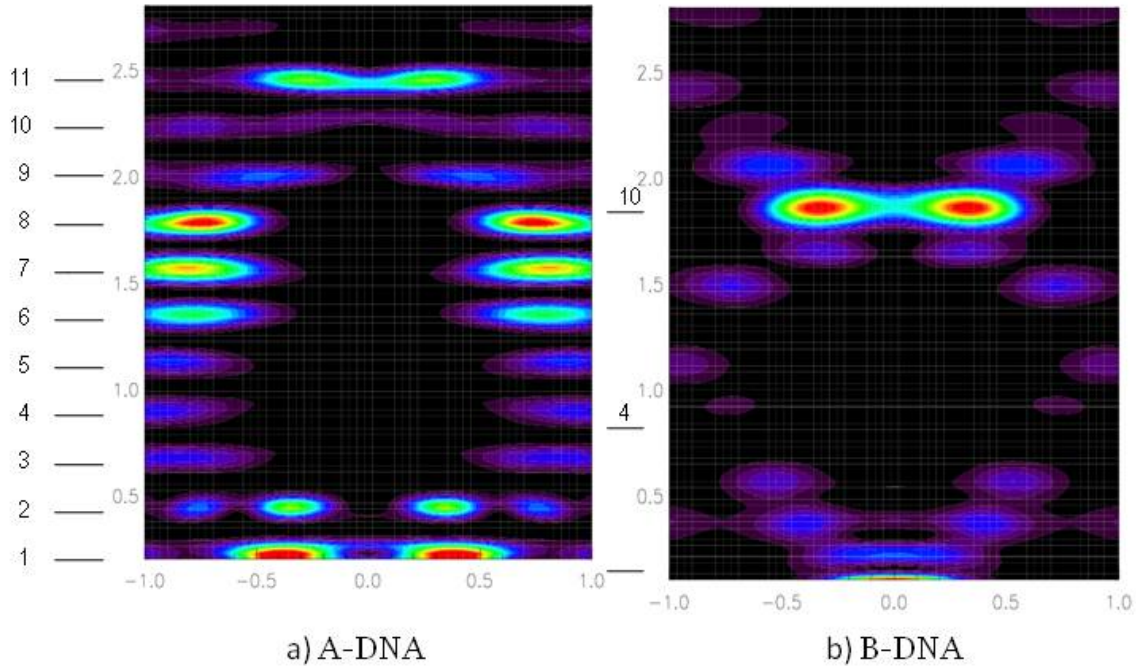

Figure 4.7: Structure factor calculations for A-form (a) and B- form (b).

Moving away from the simplest system of single molecule in a chain to a more complex system of a collection of molecules within the fibre puts the X-ray and neutron diffraction images into context.

The X-ray fibre diffraction patterns of oriented fibre DNA samples were part of the results presented in a paper by M. Krisch *et al* [65]. The samples investigated were made with the WSA, and the DNA solution was prepared and spun under similar conditions as the samples made for the purposes of this thesis. A-form Na-DNA was induced under 75% relative humidity, while B-form was obtained through the exchange of Na^+ counterion against Li^+ by dialysis, and rehumidified under 75% RH. Figure 4.8 is reproduced from reference [65]. The most distinguishable feature is that impurity phases of B-form were detected in A-form samples as a broad peak between the 8th layer features at around 1.85 $Å^{-1}$; C-form contamination Bragg peak is also present at a higher Q-position of 1.95 $Å^{-1}$. In these A-form samples, 10% of B and C contamination was estimated, Figure 4.8-(a). Figure 4.8-(b) corresponds to B-form DNA in a crystalline phase as the numerous black spots denote.

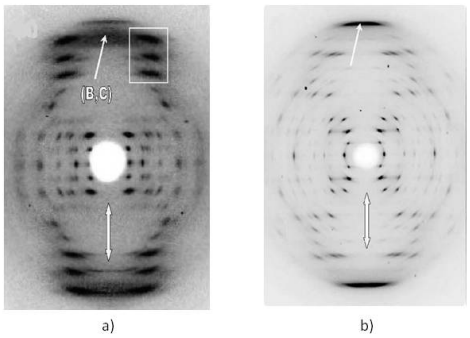

Figure 4.8: Figure adapted from article [65]-FIG. 1. Figure-(a): crystalline A-form Na-DNA at 75%RH. Figure-(b): crystalline B-form Li-DNA at 75%RH. The double arrow indicates the direction of the molecular axis. These images are not in scale.

It is important to notice from the diffraction images that the molecular arrangement in the fibres does not correspond completely to that of a single crystal. The fibres are better described as a combination of crystallisation and amorphous states. Since we are discussing macromolecules, the degree of molecular orientation in the films is not uniformly distributed, and inhomogeneities give rise to regions with a higher crystallinity than others, as well as small regions with high order but variations in their local alignment.

The width of the Bragg peaks perpendicular to the fibre axis is given by the mosaic spread of the crystal. Figure 4.9 proposes a cartoon of different crystal alignments, in real and reciprocal space, of a 1-D system composed of base pairs. The figure gives a comparison between the Bragg peaks from a 1-D perfect crystal to that of a system subjected to dislocations and mosaic spread.

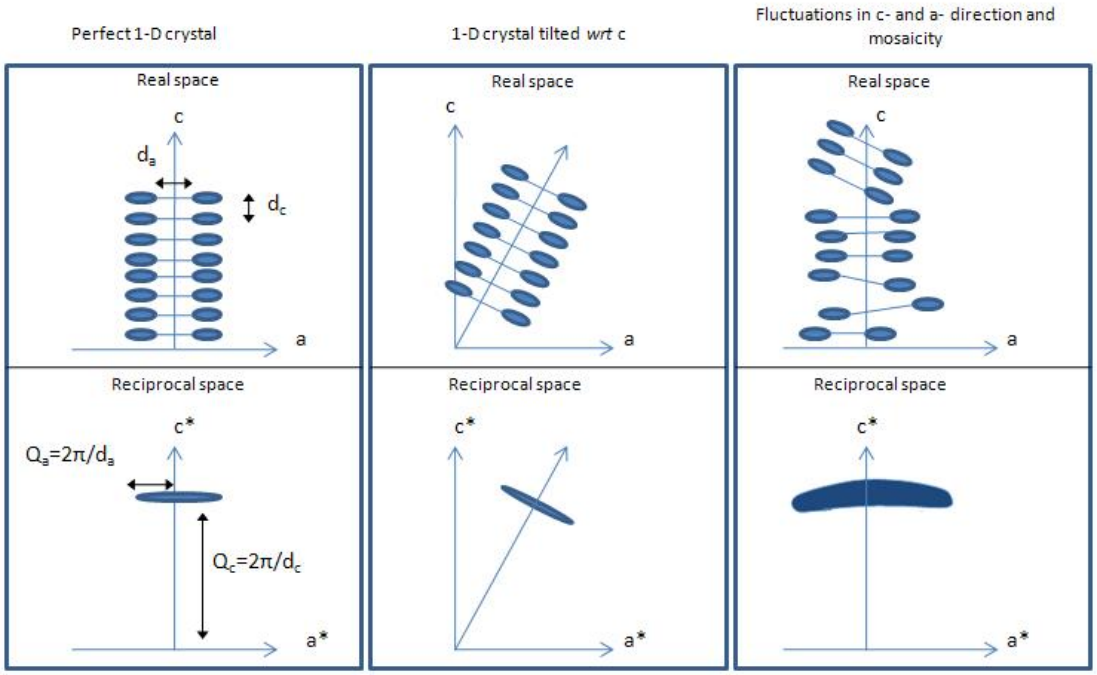

Figure 4.9: Comparison of a 1-D crystal made of base pair planes in real and reciprocal space. Left and middle images show in real space a 1-D perfect crystal; in reciprocal space this results in Bragg peaks with a determinant width in c*- and a*- direction. Right image: It is a more realistic representation of a biological crystal such as is the case of DNA base pairs.

In the proposed perfect 1-D crystal, the periodic distributions of the base pairs gives rise, in reciprocal space, to infinite sheets which are separated by Q=$\frac{2\pi}{d_c}$ (one base pair per unit cell). The intensity in each sheet will be modulated by the diffracting elements within the plane in real space.

One now has to consider the case in which the system is no longer a 1-D perfect crystal, but consists of domains which are tilted with respect to the molecular axis, i.e. mosaic spread. The distribution of these misaligned crystals will result in a broad Bragg peak at the same position but with an arc-like shape comprising the angle dispersion with respect to the molecular axis.

The widths of the Bragg peaks must be analysed in two directions: one along the c*-direction, which is the result of spatial fluctuations of the base pairs along the c-axis; and the one in the a*-direction, which is associated to the dimensionality of the crystal and mosaic spread.

We have studied the nature of the Bragg peaks, the characteristic features of the different conformations, and the transitions between DNA forms using X-ray and neutron fibre diffraction, calorimetry and optic microscopy. Changes in the relative humidity of the samples can have a relatively quick effect on the stability of the conformation. That is the reason why, for all our experiments, we have subjected the sample to a controlled humidity environment.

4.3.2 X-ray fibre diffraction

Experimental method

The experiment was done using the macromolecular crystallography diffractometer ID14 eh2 (ESRF, Grenoble), which provides a wavelength of 0.933 Å. See 2.3.4 in Chapter 2.

A piece of Na-DNA sample was cut into nine 1mm x 3mm samples, and two pieces of the same dimensions of a Li-DNA sample were also prepared. The films were glued to the edge of a pin, then left in different containers with different relative humidities between 56% and 92%, until the sample was placed on the beam.

The sample set-up consisted of a liquid nitrogen exit located a few centimetres away from the sample. The nitrogen flow freezes the sample, ensuring a fixed conformation during the exposure time. The fixed beam was on one side, while on the opposite side there was a movable detector located at around 183 mm from the sample. The alignment of the sample and the focus of the beam were controlled with a computer program. The image exposure time was set between 10-20 seconds.

Results

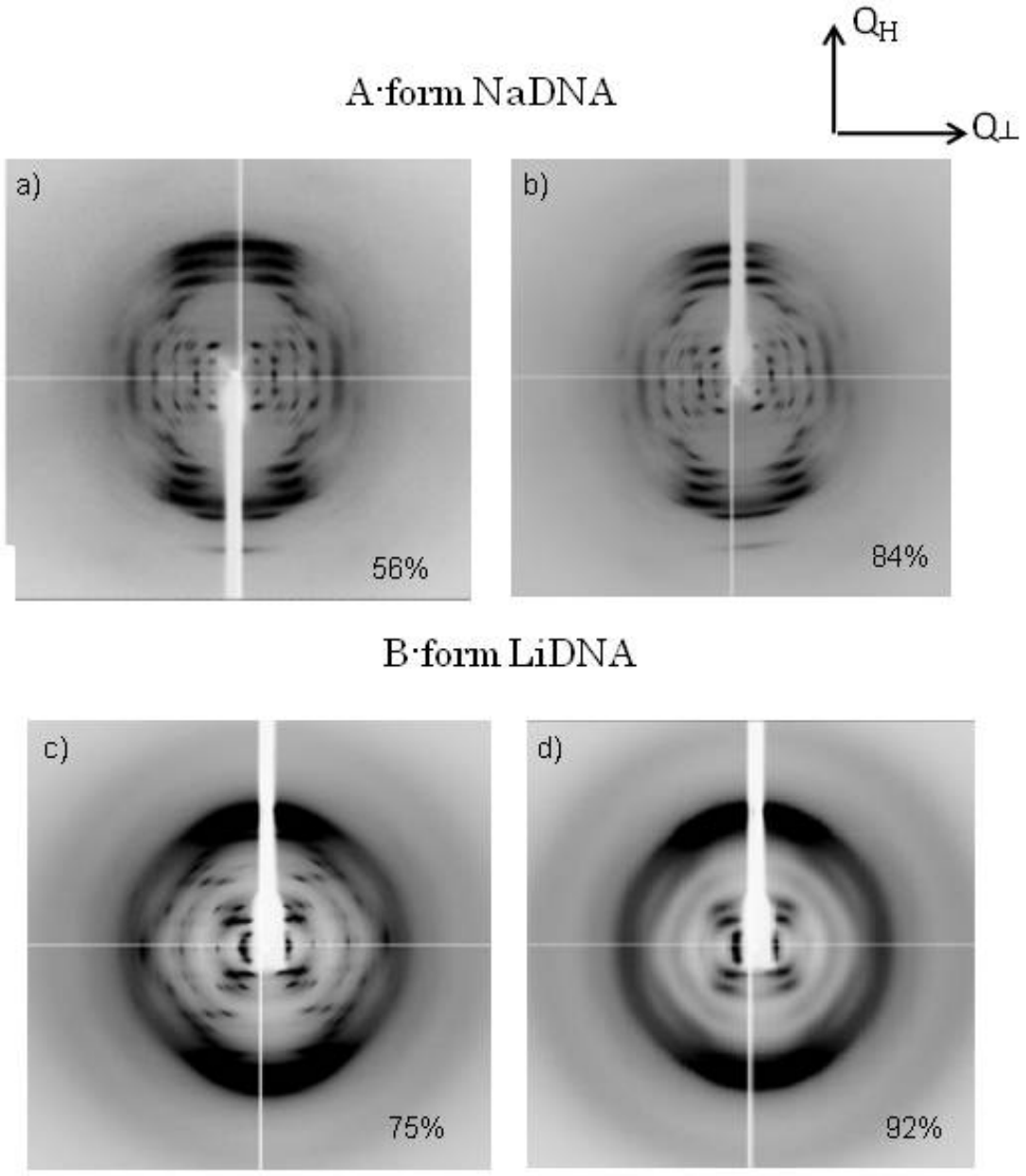

Figure 4.10: Figures (a) and (b) shows the crystalline A-form Na-DNA at 56%RH and 84%RH. Crystalline B-form Li-DNA at 75%RH (c), and semicrystalline form at 92%RH (d). The momentum coordinates system is defined by Q_H *vs* $Q_\perp$, where Q_H is parallel to the molecular axis, and $Q_\perp$ perpendicular to it.

The resulting 2-D X-ray images in Figure 4.10 map the reciprocal space (in Q) of DNA samples.

The X-ray fibre images proved an A-structure of oriented fibre Na-DNA with hydration levels between 56% and 84% RH. From the A-form image (a) and (b), it can be seen that the Bragg peak at the 11th layer is only visible at the bottom of the images and is seen at Q_H = -2.45Å^{-1}. Again very prominent three-off axis Bragg peaks appear at the $6th$, $7th$ and $8th$ layer lines.

In the case of B-form Li-DNA, the samples are semicrystalline at high hydration levels of 92% RH, and crystalline at 75% RH as expected from literature.

Figure 4.11 also shows that for Na-DNA samples at very high hydrated levels, 92% RH, the molecules undergo a transition from a less hydrated and compact A-form, to a B-form which presents the same diffraction pattern as the semicrystalline B-form obtained with Li-DNA.

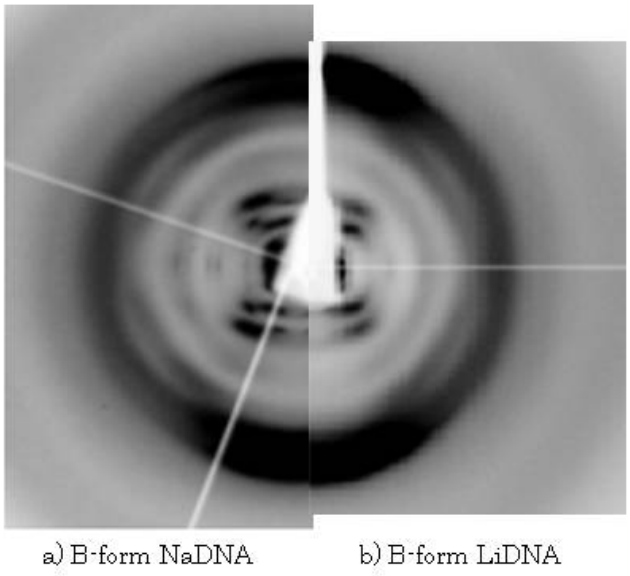

Figure 4.11: B-form DNA obtained under the presence of two different ions, Na and Li. The first half of the image, (a), was obtained with Na-DNA, and the other half with Li-DNA (b).

From the A-form diffraction patterns, it is noteworthy to mention the broad peak bridging the symmetrical peaks of the $8th$ layer line, associated to the B-form. These results do not confirm the general accepted phase diagram in Figure 4.6, which does not stress the mixture of A- and B- forms in Na-DNA samples at the relative humidities optimised for

an A-form. This will be discussed in detail further in this chapter as it will have important consequences for our experiments.

4.3.3 Neutron diffraction

We have carried out a stricter characterisation study of the samples obtained directly from the wet spinning apparatus using neutron diffraction. As in the case of X-ray fibre diffraction the samples were exposed to the optimal humidity conditions to induce A- and B- form, but no further treatment was carried out. The aim of these measurements was to map regions in reciprocal space of interest and compare to those obtained using X-ray fibre diffraction. We expected to detect and learn more about the existence of B-form in the A-form Na-DNA samples.

A preliminary study of the Bragg peaks, along and perpendicular to the fibre axis, was carried out for both structures. The study was carried out as a primary step in the study of the melting transition described in Chapter 5. An intense and well defined Bragg peak along the DNA molecule is needed to determine the static correlation length which is inversely related to the width of the Bragg peak (see later in Chapter 5). The aim of exploring the perpendicular orientation was promoted by the desire to study transversal phonons. The nature of the Bragg peaks, whether they correspond to powder rings or single crystal reflections was also tested.

Experimental Method

The characterisation of the different DNA structures, A- and B- forms, via neutron diffraction, took place on the triple axis spectrometer IN3 and IN8 at the Institut Laue-Langevin. The samples were stored under different relative humidities from 56% for Na-DNA samples, and 75% for Li-DNA films. The hydration was provided by an oversaturated salt solution in D_2O, which was used to reduce the incoherent scattering.

Each sample was composed of about eight films for a total of around 4 grams of DNA. The films were folded in concertina fashion, maintaining the fibre orientation. The ensemble of the films were placed in a thin niobium envelope, and then inside an aluminium cassette. Niobium is used because it does not react with DNA while aluminium does. The aluminium cassette was sealed using a lead wire joint, and screwed. The sealing process took place inside a humidity chamber to prevent changes in the water content.

This ensured that the number of water molecules in and around the sample remained constant throughout the experiments.

IN3 and IN8 were configured with a pyrolytic graphite (PG) monochromator. A PG analyser was used for IN3 while no analysis was used for IN8. For both instruments the wavelengths were set to 2.36 Å. 60 min collimation was placed before and after the sample for IN3, and 40min collimation for IN8. A PG filter to suppress higher order wavelengths was also located before the sample. Scheme of both instruments were given in Chapter 2. Figure 4.12-(a) shows the scattering triangle where the instrumental axis (X, Y, Z) have been represented. Figure 4.12-(b) shows the the configuration of the sample axis relative to the aluminium cassette.

Before introducing the specifics of the measurements, one must describe the relation between the DNA fibres and the instrument. This is solved by considering two decoupled coordinate systems, one for each entity: the instrument is defined by (X, Y, Z) where (X, Y) are in the scattering plane, and Z is perpendicular to it; and the DNA sample is defined by (Q_H, Q_K, Q_L), where Q_H is defined along the helical axis, and (Q_K, Q_L) are in the perpendicular plane.

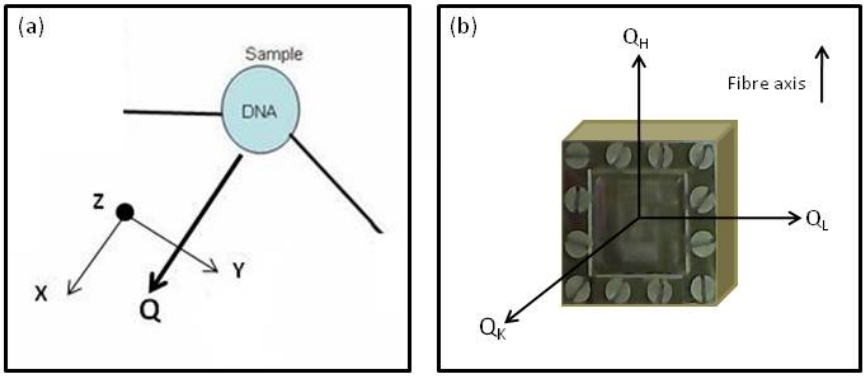

Figure 4.12: Figure-(a) shows the instrumental axis (X,Y,Z) with respect to the scattering vector **Q** aligned with the fibre axis. Figure-(b) corresponds to the DNA reciprocal coordinate system with respect to the sample cassette.

Figure 4.13 shows the configuration of the reciprocal vectorial-space of the sample (Q_H, Q_K, Q_L) with respect to the instrument, (X, Y, Z).

Measurements were carried out with two different alignments to access different Bragg peaks: longitudinal in $Q_H - Q_K$ space; and transverse in $Q_K - Q_L$ space.

In the first type of measurements, the samples were aligned with the fibre axis in the scattering plane, such that (Q_H,Q_K) were in the (X,Y) plane and $Q_L \parallel Z$. The ultimate goal of these measurements is to explore the reciprocal space along the molecule, and thus Bragg peaks in that direction. This orientation is hereafter defined as longitudinal. The set up is shown in Figure 4.13-(a).

In the second type of measurement, the samples were turned 90° so that the X is perpendicular to the fibre axis, Figure 4.13-(b). This allows the study of the transversal properties of the samples, related to the intermolecular orientation of the DNA molecules within the fibre.

Figure 4.14 shows the 3-D reciprocal space in (Q_H,Q_K,Q_L) of a DNA sample using examples of the two types of measurements discussed.

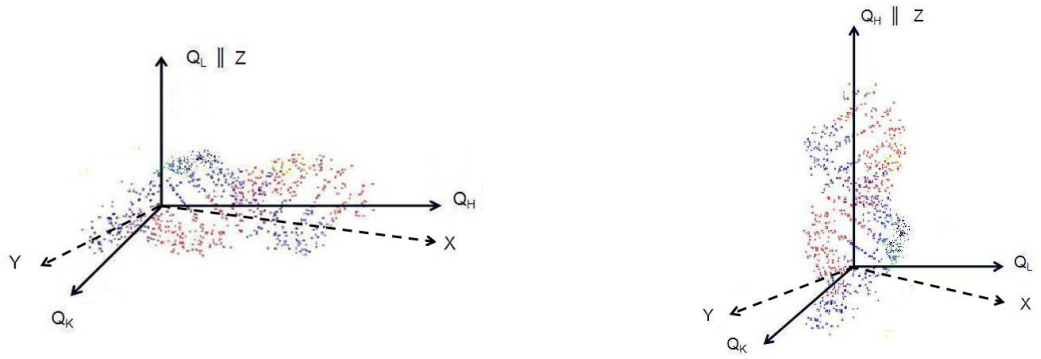

(a) Longitudinal Bragg peak configuration

(b) Transverse Bragg peak configuration

Figure 4.13: Description of the instrumental axis (X, Y, Z) with respect to the reciprocal plane of the sample (Q_H, Q_K, Q_L). The choice of vectorial-space has been arbitrary, with the only restriction that Q_H is parallel to helical axis.

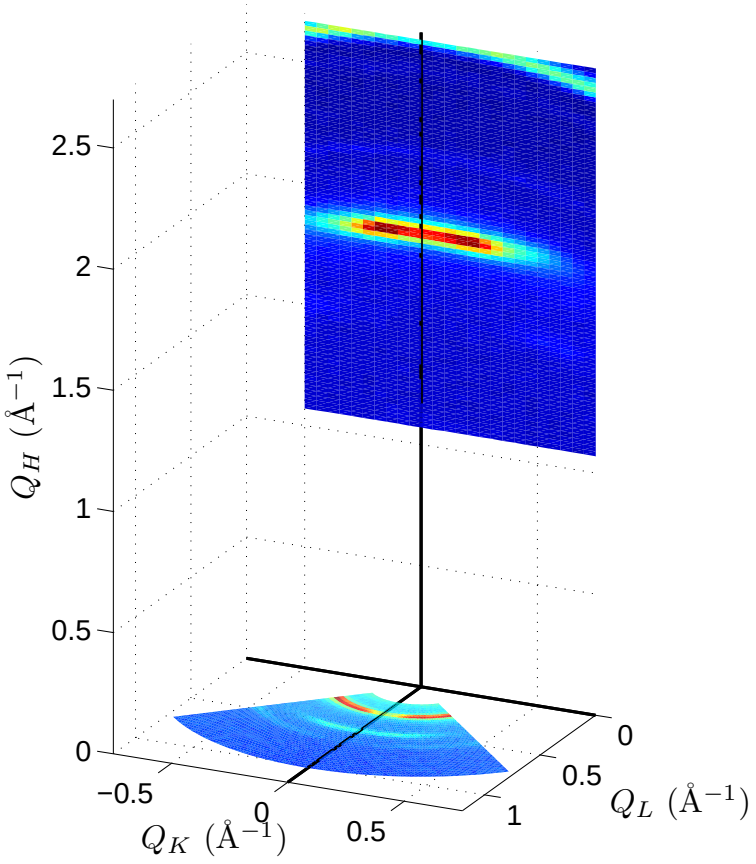

Figure 4.14: Reciprocal space maps obtained in the (Q_H, Q_K) plane and (Q_K, Q_L) plane for a DNA sample, plotted in a 3-D coordinate system.

Bragg Peaks of Different DNA Structures

Reciprocal space maps (RSM) were measured on samples that were directly obtained from the WSA and humidified for several weeks, and are presented as contour maps.
The following images consist of RSM of the Q-regions comprising the main features of the different DNA structures. They were measured at room temperature.

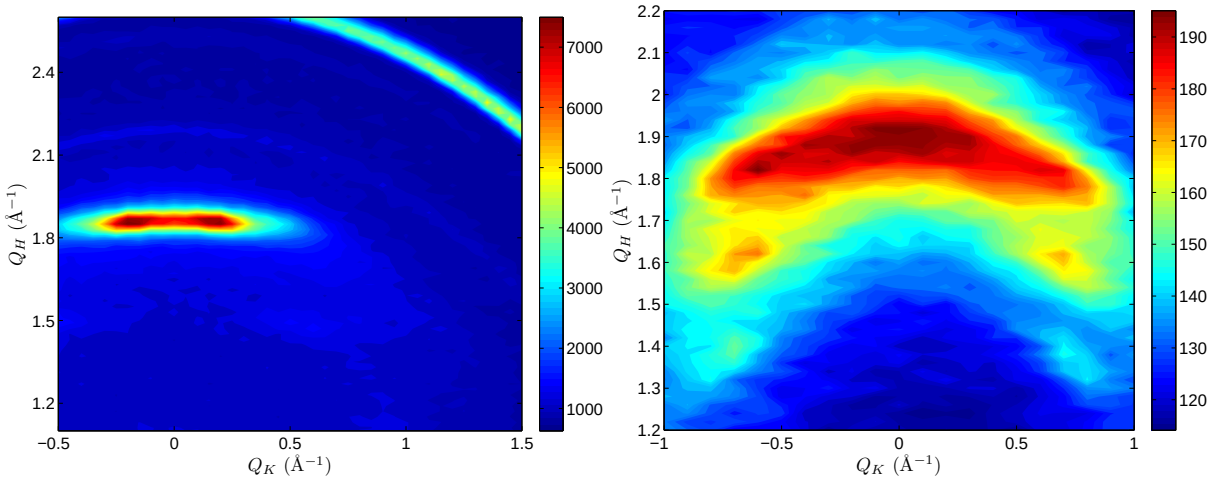

(a) B-form (b) A-form

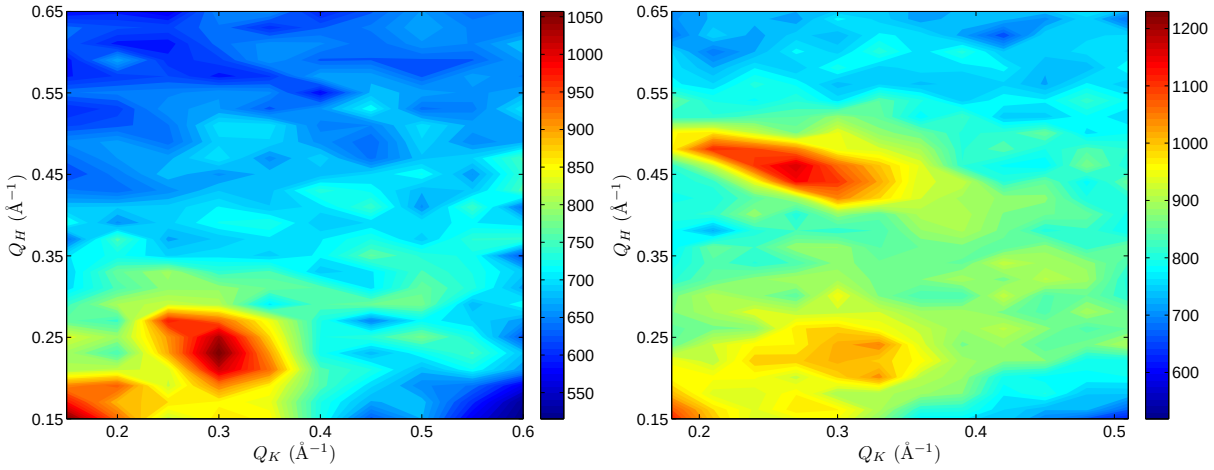

(c) B-form (d) A-form

Figure 4.15: a) and c) corresponds to the B-form Bragg peaks of Li-DNA, humidified under 92% RH; (b) and (d) show the Bragg peaks of the A-form, humidified at 56%RH.

For the B-form, image (a) shows an intense Bragg peak due to the base pair stacking on the $10th$ layer line, centred at (1.87,0,0)Å^{-1}. There is also a low-Q Bragg peak present at (0.25,0.2,0) Å^{-1}, shown in figure (c).
In the case of the A-form samples, image (b) does not show the Bragg peak of the $11th$ layer line at around 2.5 Å^{-1}. The data for this value of Q_H was purposely excluded

as it is a very weak peak. Instead, the RSM was centred on the three off-axis peaks corresponding to the 6th, 7th and 8th layer lines, displayed along the molecular axis at $Q_K = \pm 0.7$ Å^{-1}. A Bragg peak at (1.87,0) associated with the B-form Bragg peak is extremely conspicuous, and even making the off-axis Bragg peaks in the $8th$ layer line indistinguishable.

Figure (d) shows two peaks. The intense peak at (0.45,0.25,0) Å^{-1} from the A-form, and a less intense peak at the same position as in the B-form, (0.25,0.3,0)Å^{-1}, consequence of B-form contamination. This feature was not identified in the X-ray fibre diffraction images.

Nature of Bragg Peaks

In the process of winding the fibre threat around the cylinder during sample preparation, naively one could think that the fibres are randomly oriented with its neighbours. In reciprocal space this will lead to a cylindrical symmetry in the $Q_K - Q_L$ plane (perpendicular to the fibre axis). Henceforth, the most straightforward analysis to learn more about the molecular arrangement within the sample is via measurements perpendicular to the helical axis in the $Q_K - Q_L$ plane. They not only demonstrate the existence of transversal Bragg peaks, associated to an intermolecular arrangement, but also how this arrangement is occurring.

Figure 4.16 shows the RSM of the $Q_K - Q_L$ plane for both DNA conformations.

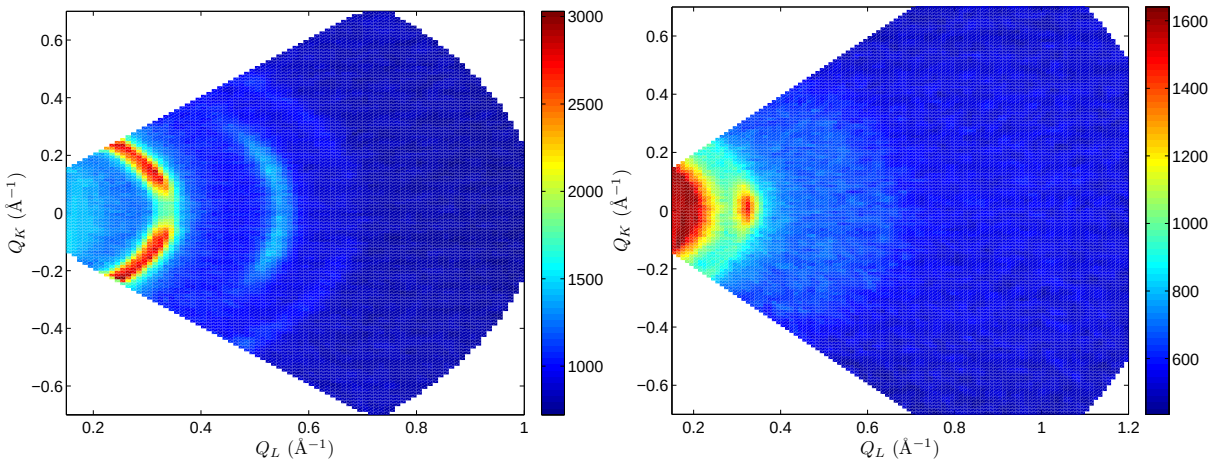

(a) B-form (b) A-form

Figure 4.16: (a)B-form transversal Bragg peak, (b) A-form transversal Bragg peak. peaks

The RSMs proves that there is a crystalline arrangement of the molecules perpendicular to the helical axis for both structures. In the Li-DNA films, Figure 4.16-(a), the Bragg peaks have a curvature more like a mosaic spread in each peak. The peaks are in a powder-like position as a result of a preferred orientation of the sample, but the intensity is not homogeneous, i.e. spherically averaged. There is a clear dim spot at (0,0.34) Å^{-1}. Peaks with similar behaviour were detected at larger Q_L. In the case of the A-form Bragg peak, Figure 4.16-(b), its single crystal nature is even clearer, with a very broad peak centred at (0,0.32) Å^{-1}. No other peaks were detected in the RSM.

For a better appreciation of the intensity of the Bragg peaks as a function of rotation angle, rocking curve scans across the Bragg are shown in Figure 4.17. These results are astonishing since they reveal that not only the molecules are oriented so that there is a periodic order of the bases along the helical axis; but that molecules are coaxial in a fibre and have similar orientation between fibres. This perpendicular order is stronger for the A-form than for the B-form.

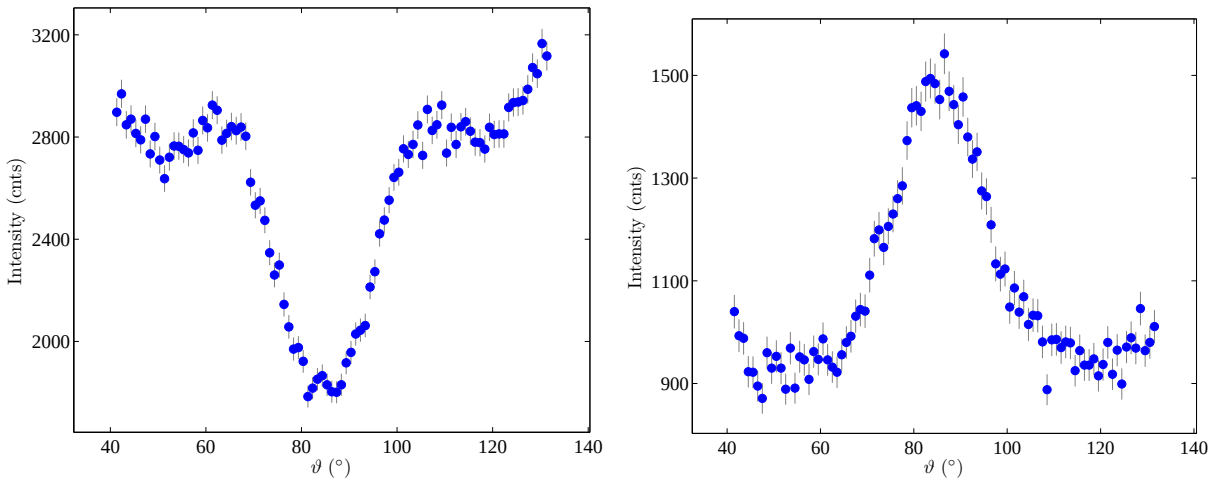

(a) B-form (b) A-form

Figure 4.17: Angular scans through the Bragg peak with a radius $Q_L = 0.34$ and $Q_L = 0.32$ for B- and A- form respectively.

Another way of testing the crystalline nature of the DNA samples is by studying the Bragg peaks in the longitudinal configuration as they are tilted out of the scattering plane. A goniometer allowed a tilt of the sample, gu, up to 20 degrees around the Y axis. Measurements of the Q_K separation of Bragg peaks will distinguish between sheet-like and powder-like scattering.

Figure 4.18 provides a graphical representation of two different measurements made of a Bragg peak along the molecule. Figure 4.18-(a) shows no inclination of the reciprocal space of the sample with respect to the instrument (gu=0); while Figure 4.18-(b) presents a tilt angle (gu> 0).

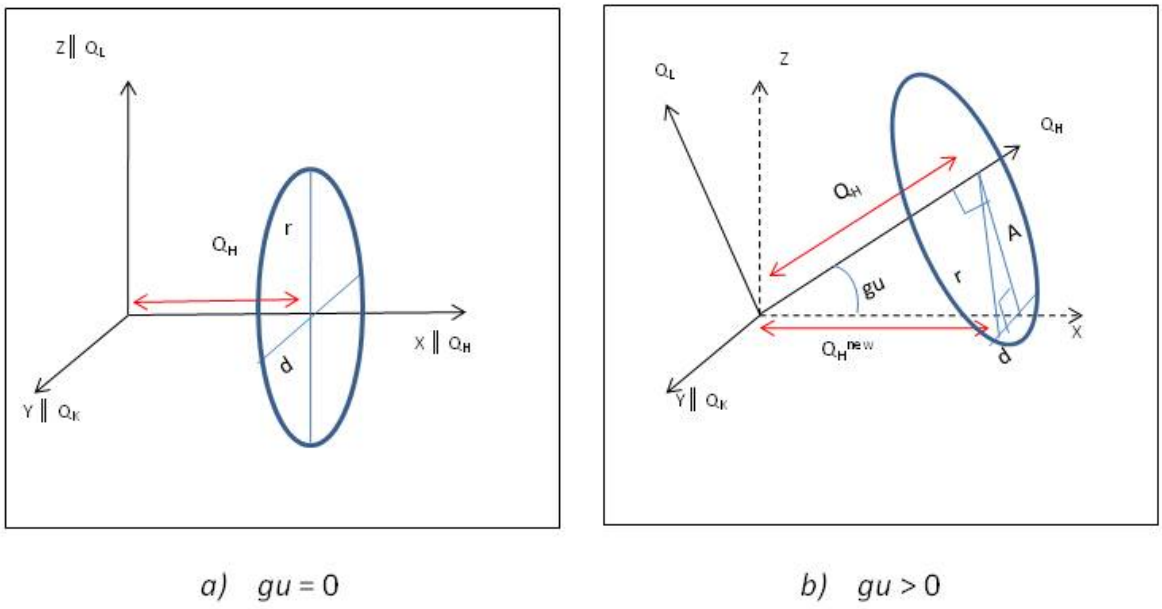

Figure 4.18: Definition of gu measurements. (a): the scattering coordinate system (Y, X, Z) is parallel to the reciprocal coordinate system of the sample (Q_H,Q_K,Q_L). The circle on blue represent the powder ring, of radius r=d. The intersection of the ring with the (Q_H,Q_K) plane is given in scalar units by (Q_H,d). (b): sample and instrument reciprocal coordinate system does not coincide as the sample is subjected to an angle with respect to $Y - X$ plane, this tilt is given by the angle gu. The radius of the ring is given by r, differing from d which still is the Q_K coordinate; and Q_H^{new} is the Q_H coordinate as a function of the angle. The length A is orthogonal to Q_H, and thus A=$Q_H \cdot \tan(gu)$.

The study was carried out for A-form for two Bragg peaks: one at high-Q associated to the base pairs stacking centred at (Q_H,Q_K)= (1.65, ±0.7) Å^{-1}, and a second one at lower-Q centred at (0.44, ±0.3) Å^{-1}. The samples were aligned with the fibre axis parallel to the scattering plane, Q_H.

Figure 4.18 represents the case in which the Bragg peaks are powder rings in Q_K-Q_L plane. At zero inclination, both reciprocal coordinate system, instrumental and sample, coincide. The positions of the Bragg peaks in $X - Y$ plane correspond to the intersection of this ring with that plane, and the distance between them is the diameter of the ring ($\frac{1}{2}D$=d=r) as shown in Figure 4.18-(a). As the tilt angle (gu) was scanned from 0 to 15 in steps of 5°, a Q_L component appears, X component increases (Q_H^{new}), and the distance between the spots where the powder rings are intersecting with the scattering plane should

become smaller, Figure 4.18-(b).

To see this effect, scans along Q_K comprising the distance between peaks, from -0.4 to 0.4 Å^{-1} and from -0.8 to 0.8 Å^{-1} for the low-Q and high-Q Bragg peaks respectively were measured at Q_H^{new} which is given as a function of the tilt. The $Q_H^{new}(gu)$ coordinate was calculated using the following relation, $Q_H^{new} = \frac{Q_H}{cos(gu)}$.

The distance between intersected points was compared with equation 4.3.

$$d = 2\sqrt{r^2 - tan^2(gu)Q_H^2} \tag{4.3}$$

Results

The three off-axis Bragg peak structure had a Q_K spacing that could be resolved with the instrument Q-resolution.

Q_K scans centred at $Q_H = 1.65$ and 0.44 Å^{-1}, for the high and low-Q Bragg peaks for each gu inclination, were fitted with 2 Lorentzian functions, one for each symmetrical peak. Figures 4.19 and 4.20 show the resulting fits. The distance between peaks was plotted as a function of gu angle, see Figure 4.21.

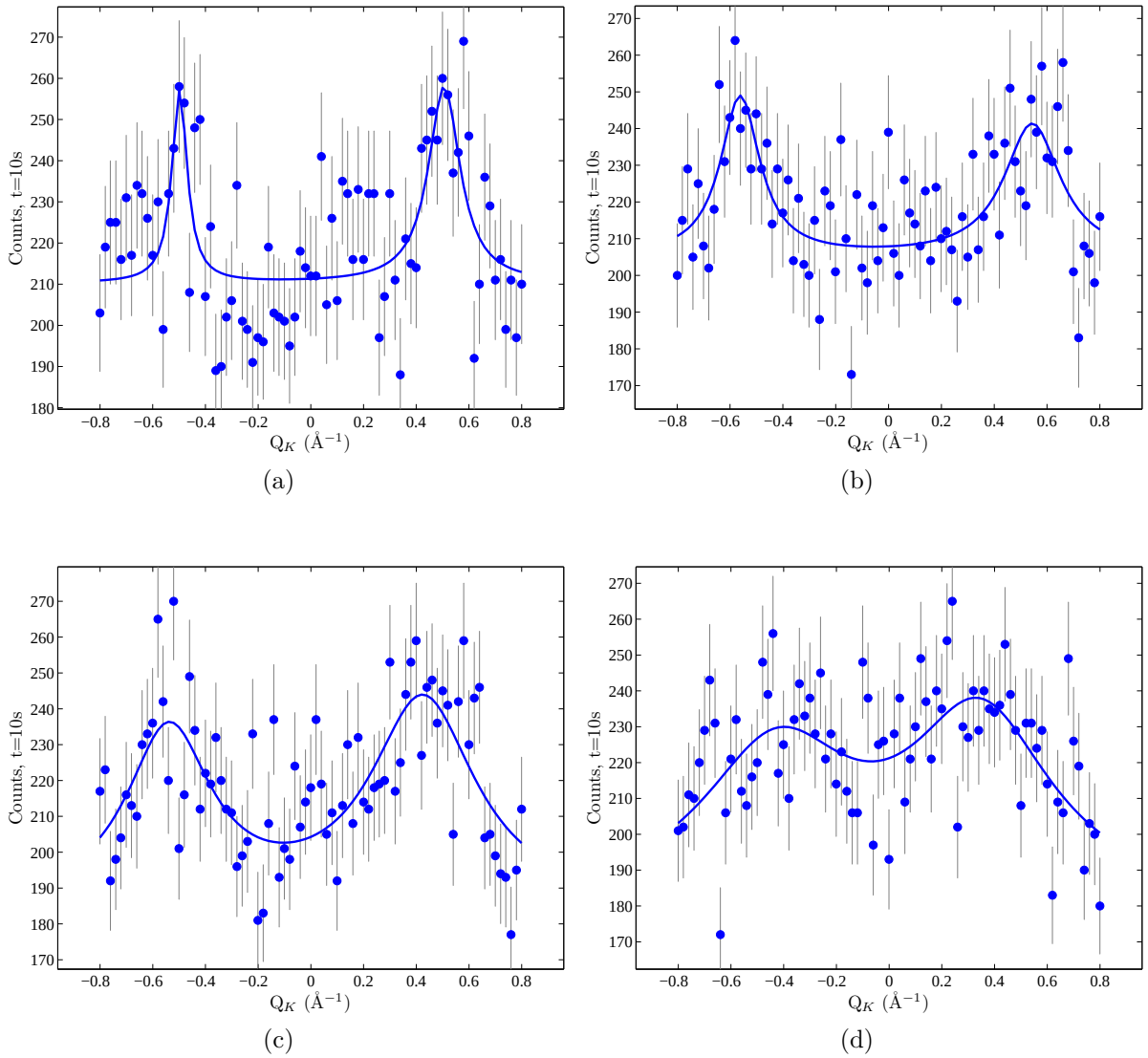

Figure 4.19: The images correspond to the Lorentzian fits of Q_K scans centred at the Base pair Bragg peak of the A-form Na-DNA, at different *gu* angles: 0° (a), 5° (b), 10° (c) and 15° (d).

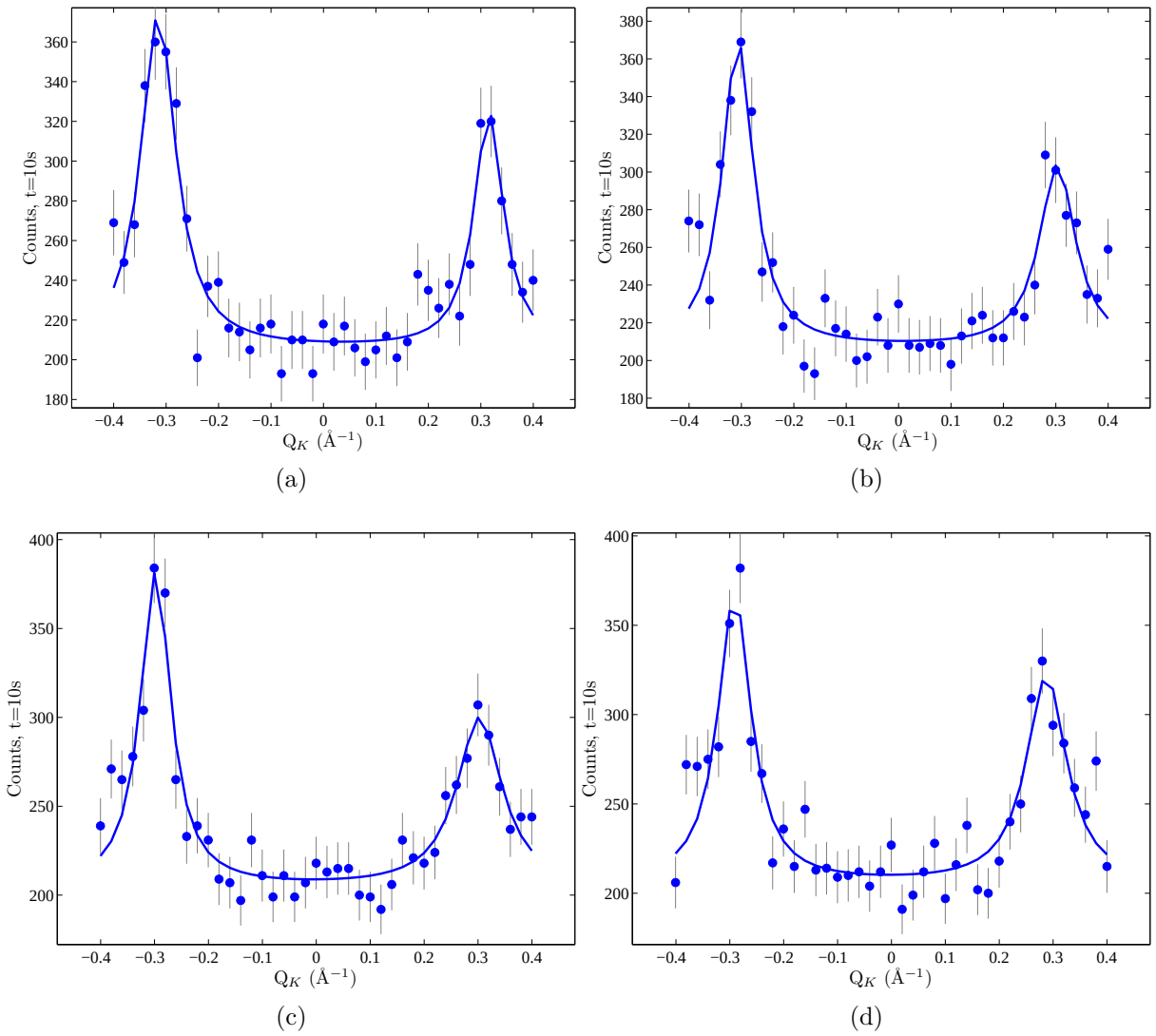

Figure 4.20: The images correspond to the Lorentzian fits of Q_K scans centred in the low-Q Bragg peak of the A-form Na-DNA, at different *gu* angles: 0° (a), 5° (b), 10° (c) and 15° (d).

From the Lorentzian fits, the peak position of the symmetrical peaks was defined, and hence the distance between them was calculated. Using equation 4.3, the theoretical distance as a function of the tilt (*gu*) was also calculated. Figure 4.21 gives a comparison between the measured distances at each angle (dots), and the theoretical distances expected for powder ring Bragg peaks (continuous red lines).

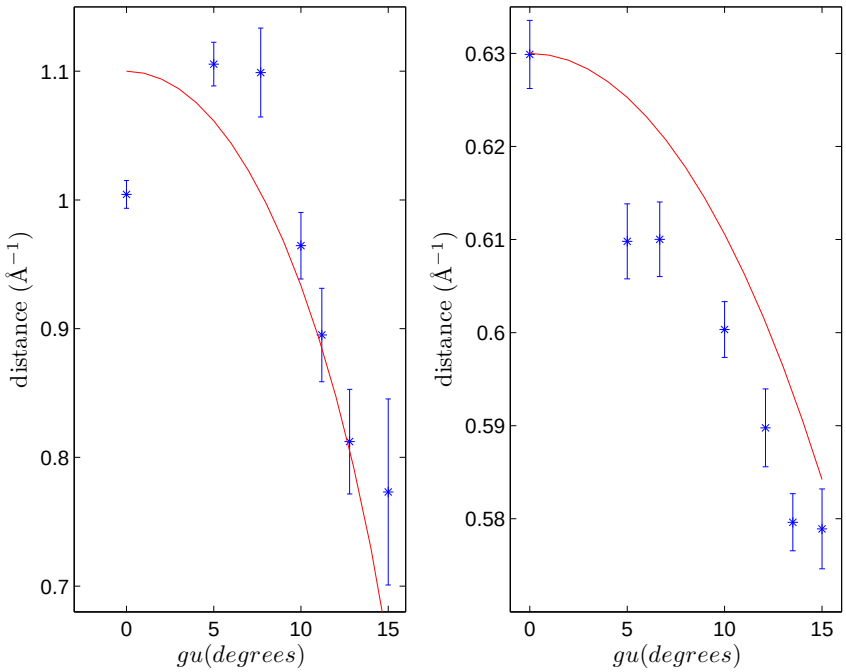

Figure 4.21: Distance obtained from the Lorentzian fits *wrt* the tilt angle (dots with error bars); fitted to the theoretical distances expected for a powder ring behaviour as a function of angle (continuous red lines). The image on the left corresponds to the fits of the high-Q Bragg peak, while that on the right is for the low-Q peak.

Discussion

The X-ray fibre diffraction images of oriented fibre DNA show the expected pattern for the two possible conformations, A- and B-, that one can induce when samples, directly obtained from the wet spinning apparatus, are humidified to 56%-84% RH for the A-form and 92% RH for semicrystalline B-form in Na-DNA, and 75% RH for the crystalline B-form in Li-DNA. We also showed that the B-form base pair Bragg peak is always present in the A-form images despite the humidity used. A further characterisation of these samples was carried out using neutron diffraction, the different scattering properties compared to X-ray diffraction provide complementary information of the specimen under study. And indeed, not only the B-form base pair Bragg peak was detected in the A-form samples, but also a low-Q peak which had not been identified from the X-ray images.

Other methods like ^{2}H-NMR previously reported evidence of contamination of B-form DNA in A-form Na-DNA. Those measurements estimated that Na-DNA contains typically amounts between 30% to 57% of B-form DNA [75]. The amount of $B_{residue}$ will be linked to the conditions under which the samples are prepared, like for example the ethanol

concentration in which the DNA precipitates.

Regarding the nature of the Bragg peaks, we showed that they are not powder rings since their intensity is not cylindrically averaged, although they do have strong texture or preferred orientation. The reason of the orientation of molecules between fibres may be associated with a macroscopic shape of the actual fibre, giving rise to some sort of self-organisation of the fibres with their neighbours.

4.3.4 Purification of A-form samples by removal of B-form residues

Our goal is to obtain samples of the most pure and stable secondary structures of A- and B-forms DNA upon changes in temperature. The A-form can only be adopted for Na-DNA and we have seen that the fibres always contain a contamination of the B-form. This led us to study in detail the B to A transition and to look for a protocol that could allow us to prepare a sample of pure A-form DNA. Brandes and co-workers refined two methods to reduce the B-contamination: hydration and addition of ethanol [72]. We have explored the effect of temperature on conformational transitions, and hence examine if the phase diagram in Figure 4.6 is temperature dependent.

Figure 4.6 shows that the A-form is preferentially observed at low hydration. This is understandable because it is a more compact form of DNA, which leaves less space for the water molecules. As discussed, other agents such as ethanol or ionicity can influence the transition during the preparation of the samples, but once the films are made they cannot be easily manipulated through those agents. This section presents our investigations of this transition as a function of temperature.

Water molecules and hydrated ions are located between parallel DNA double helixes. As the temperature is raised these molecules are released to the outer hydration layers and surrounding medium. This induces changes in the secondary structure of the DNA.

While most of the studies in fibre conformation have been developed using X-ray diffraction, binocular microscopy has become a powerful tool to prove the conformation of DNA via the length of the fibre. This measurement infers the length of the molecule and so the axial rise per nucleotide. In other words, it confirms in real space the structure of DNA fibres [76]. A reversible shortening of the fibre due to a B$\rightarrow$ A transition as a consequence of changes in the axial rise per base pair, was reported by Zimmerman *et al.* [77] and [73], driven by a decrease in the concentration of ethanol with respect to water.

We have studied the effects of temperature on the macroscopic and microscopic properties of the samples, and whether the detected changes could be attributed to the transition between B to A-form DNA. Based on the fact that A-form samples always contain a low percentage of unstable B-form (highly hydrated form), the increase of temperature will have a higher impact in those regions most sensitive to changes in hydration.

In our neutron and calorimetry experiments the water content within the sample and its surroundings was fixed as it is captured inside the sample holder. As the temperature changes the dew point changes, and thus the relative humidity, but the available number of water molecules stay constant.

Calorimetry and Optic Microscopy

The conformational transition was also observed with physico-mechanical experiments, in which the fibre diameter decreased as the temperature increased [76] due to the loss of hydration. This was expected, since the molecules take an A-form in the lower hydrated system, compacting themselves to fill the space the water has left. This shortening of the fibres was observable with optic microscopy at around 320 K, and thermodynamically detected in calorimetry.

Calorimetry Two experiments were carried out using Differential Scanning Calorimetry. The data are shown in Figure 4.22. The first experiment corresponds to an increasing temperature ramp and is shown by the black curve. The sample, treated with temperature from 278 K up to 368 K, undergoes two transitions: one centred at 318 K; and another at 351 K. The first transition is associated to a configurational change within the secondary structure of the DNA. It was previously discussed by S.Lee and co-workers as an endothermic process due to the loss of ordered structure driven by dehydration [78]. Our studies, based on structural studies using neutron diffraction (see next section) suggest that it is instead a conformational change of some DNA molecules, that switch from the B-form of DNA to the A-form of a part of the sample that was in the B-form in spite of the long period of storage of the sample at a relative humidity of 56% RH, which tends to favour the A-form.

The second transition which occurs in the temperature range in which DNA denaturation is observed in solution can be assigned to the melting transition of the DNA and the film

together. There is no possibility to differentiate among DNA denaturing and melting of the film since calorimetry provides the global energy involved. When another sample was heated up to 321 K (red curve), cooled down to 278 K, and subsequently heated up to 368 K (blue curve) only the second transition was visible, and the sample remained thermally stable until it reached the melting transition. The small bump present at 330 K may be associated to the configurational transition from remains of B-form, which could have been prevented by treating the sample at slightly higher temperature.

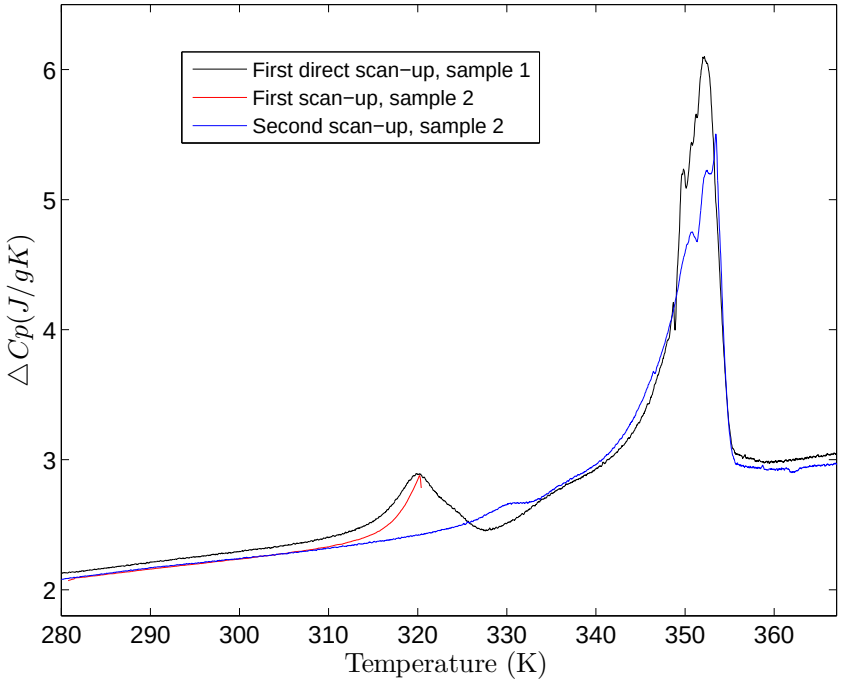

Figure 4.22: DSC curves of two pieces of the same A-form sample rehumidified under 56%RH. Sample 1 was heated up from 278 K to 368 K directly; while sample 2, went through a pre-heating process from 278 K up to 318 K, cooled down and heated again up to 368 K.

This would be consistent with an irreversible B to A transition occurring below 320 K. The first heating turns the fibre into a "pure" A sample, so that the second heating only records the melting transition. This analysis is confirmed by neutron diffraction and optic microscopy studies.

Optic Microscopy Each sample corresponded to a 2×2 cm^2 piece of the same film. The pieces were exposed to 56% RH during 3 days prior to the optic microscopy measurements. A sample was extracted from its humidity chamber and placed between two glass plates sealed with adhesive tape to preserve the hydration. The temperature was increased at

a rate of 5°C/min. The melting profile of each sample was recorded, while pictures every $10°C$ were taken.

The following picture shows the optical observation of a fibre structure of the DNA sample. The black features correspond to the space between fibres, while the "orangy" colour in the background is due to the copper base where the glass plates, with the film in between, were placed.

(a) 323 K (b) 333 K

Figure 4.23: Optic Microscopy image of an A-form DNA humidified at 56%RH at 323 K, before the $B_{residue}$ to A transition (a); and after the transition at 333 K. A black line between two features present on the film have been drawn to see the fibre shortening occurring between 323 K and 333 K. The line in figure (b) is shorter than that in figure (a).

At around 328 K there is a collective shortening of the fibres which is visible until 333 K. A black line was drawn to represent the distance between two features, the same in both images. The figures show that the two features have approached at 333 K as the line is shorter compared to that before the transition at 323 K.

At a higher temperature, 343 K, a second transition occurs which culminates in the complete destruction of the film at around 358 K. The transition temperature cannot be qualitatively compared with those observed with neutrons or calorimetry, because of the differences in the experimental apparatus. Nevertheless, within the order of the temperature at which the optical transition occurs, the detection of fibre shortening supports the hypothesis of a B to A transition; while the second optical transition occurring at high temperatures is associated to the melting of DNA and the destruction or collapsing of the film.

A proper visualisation of the optical transition associated to the $B_{residue}$ to A transition can be better discerned from the videos (see CD attached in Appendix).

Neutron as the probe

DNA structures via the Bragg peaks were studied at different temperatures.
The samples were placed inside an orange cryofurnace. Scans of A-form samples at Q_H centred at the position of the B-form Bragg peak were taken at different temperatures, from 295 K to 324 K, which is well below melting. The scans were fitted with Lorentzian functions keeping all parameters free. Figure 4.24-(a), shows the fitted scans for different temperatures. For a better appreciation of the temperature dependence of the amplitude of the B-form Bragg peak, and thus the transition temperature, Figure 4.24-(b) are shown. It corresponds to the Lorentzian amplitude and background fitting parameters as a function of temperature. The free background is plotted to show that it stayed flat up to the transition temperature.

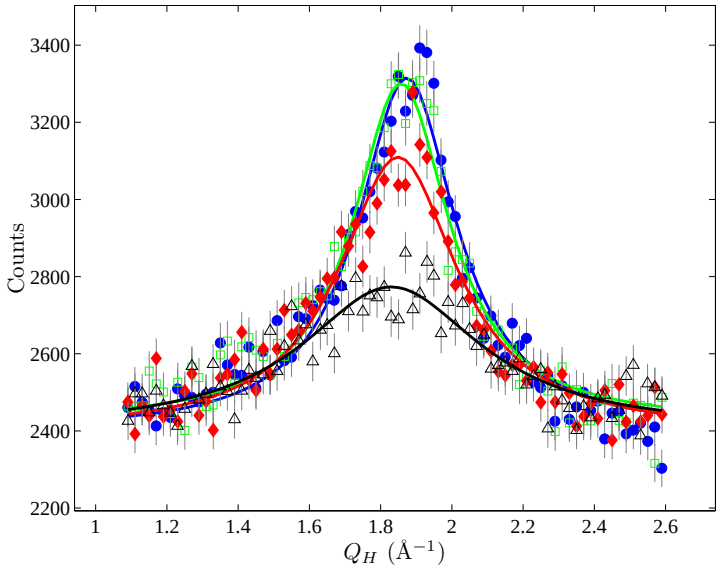

(a)

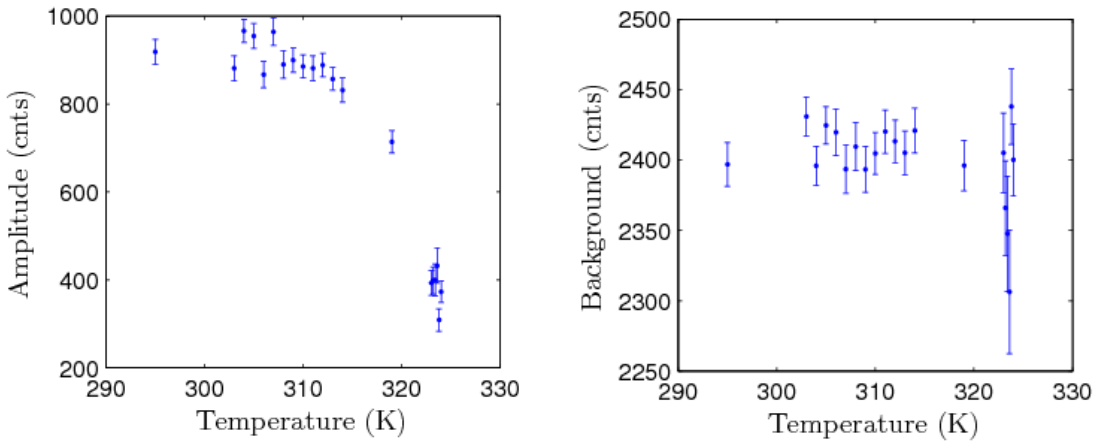

(b)

Figure 4.24: Figure (a): Scans centred at the residual B-form Bragg peak in an A-form DNA sample, taken at different temperatures: 295 K (blue curve), 311 K (green curve), 319 K (red curve) and 324 K (black curve). Figure (b): Lorentzian fitting parameters: peak intensity and background.

From the temperature scans it appears that the peak is very susceptible to temperature. From the study of the behaviour of the Lorentzian intensity, we can conclude that a thermally induced transition marked by a drop of the intensity of the Bragg peak of the B-form due to the loss of diffracting elements (base pairs), occurs at around 318 K. Figure 4.25 shows the RSM of the B-form Bragg peak contamination and the three-off axis A-

form Bragg peaks, i.e. features of the "impure" A-form. Figure 4.25-(a) was measured at 300 K. The sample was then heated to 320 K, and left at that temperature for 8 hours as the reciprocal space map was measured, Figure 4.25-(b). The images show a collective broadening of the peaks and a decrease of the intensity, as we saw from the individual scans. This effect can be explained by a global disordering of the crystalline fibre structure.

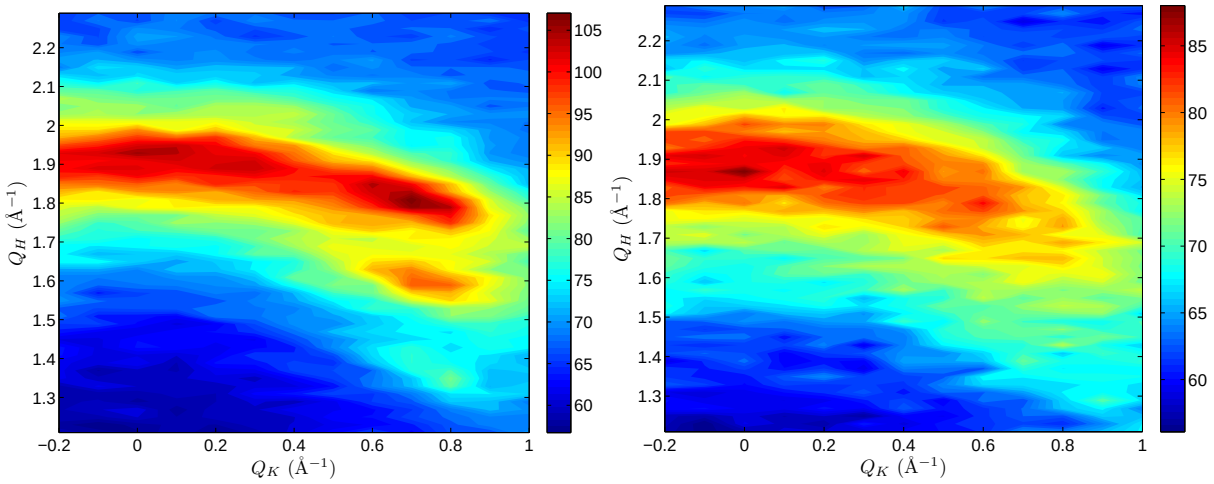

(a) 300 K

(b) 320 K

Figure 4.25: High-Q RSM of the "impure" A-form measured at 300 K (a), and 320 K (b).

Then, the sample was cooled down to room temperature and rehumidified at 56% RH for several weeks before being remeasured. The three-off axis Bragg peaks in Figure 4.26-(a) appeared to be stronger and the B-form Bragg peak at Q=(1.89,0,0) Å^{-1} was no longer present. This shows that the crystalline structure may be recovered and that the sample has almost a pure A-form structure. This is expected since the sample was exposed to temperature much lower than the melting temperature.

Figure 4.26-(b) corresponds to the low-Q features of an original "impure" A-form sample that was heated to 320 K in an oven for 8 hours, cooled down to ambient temperature, and left at that temperature for 12 hours. The B-form Bragg peak at (0.25, 0.3,0) Å^{-1} as seen in Figure 4.15-(d) has practically disappeared, while the A-form Bragg peak (0.5,0.25) Å^{-1} appears even more localised and intense. When the sample was heated the water molecules released to the surrounding media, partly from the water molecules between DNA molecules and partly from the B to A transition, were contained within the sample. We believed that at room temperatures those molecules are available and can

be reincorporated to the DNA molecules, if enough time is left the fibre structure can be recovered, as it occurs during rehumidification.

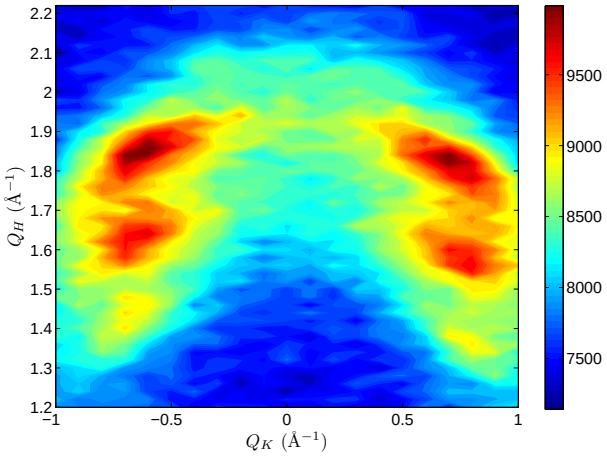

(a)

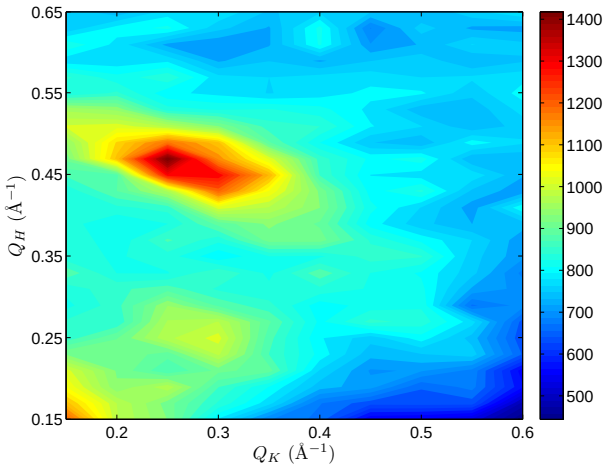

(b)

Figure 4.26: The Figures show the RSM of the pure A-form diffraction pattern, after annealing, i.e. heating to 320 K and rehumidifying to 56% (a), and with the available water molecules within the sample (b). These should be compare with Figure 4.15

Discussion

The combination of neutron scattering technique, calorimetry and optic microscopy have provided the global picture of the B to A transition, i.e. the key to determine a purification method for A-form DNA.

The neutron scattering described above gives understanding of the phenomenon occurring at 320 K. We believe that the loss of hydration from the DNA molecules upon heating to 320 K comes from the rearrangement of these B-form segments, i.e. transformation

from B- to A-form. As the A-form of the molecule is shorter than the B-form, the B to A transition is accompanied by a distortion of the fibre structure as seen by optic microscopy and by the loss of the intensity of the Bragg peaks in the neutron images. However, the complete structure and orientation of the DNA fibres is not lost, and this is why an ordered and oriented sample can be recovered after a sufficiently long relaxation and rehumidification at room temperature.

When the sample was cooled down to 278 K in the calorimetry experiment we expected that there were no remains of the B-form and hence an endothermic peak associated to B to A transition was scarcely observed in the second DSC heating scan. For this experiment, no aging was needed, as this technique is not sensitive to the periodic structure.

In the case of the neutron experiment, the proper rehydration of the sample to favour an A-form, results not only in the recovery of the orientation of the DNA molecules in the fibre but provides what we call a "pure A-form" which the structure is stable up to melting temperatures. This has been a very important discovery for our study, since good quality and stable A-form samples upon heating have been essential to proceed with the study of the melting transition of A-form DNA.

Figure 4.6 shows the phase diagram of the A- and B-forms of DNA that was generally accepted before our study. What was missing on this picture was the existence of a contamination of the A-form in domains which are marked as A on the diagram. We have shown that, if one increases the temperature to 320 K the stability of the B-form that coexisted with A-form decreases and it converts to A (Figure 4.27). As a result, after this thermal treatment the diagram of Figure 4.6 becomes actually correct, the area marked A are indeed pure A-form

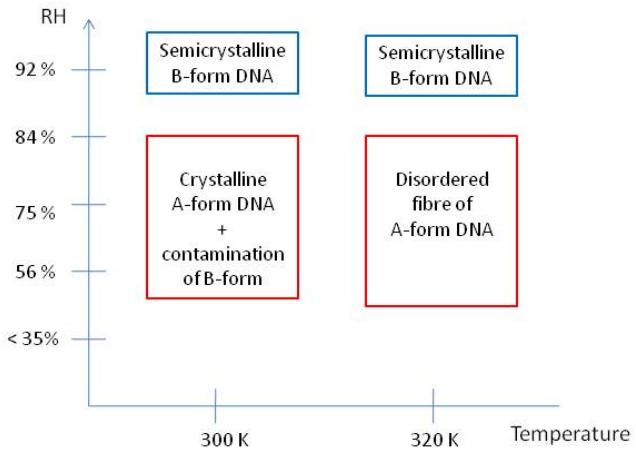

Figure 4.27: Corrected phase diagram for Na-DNA films, relative humidity as a function of temperature.

Chapter 5

Melting Transition of Oriented DNA Fibres

5.1 Foreword

This chapter describes investigations of the thermal denaturation transition of oriented DNA fibres in the A- and B-forms. A thermodynamical analysis was obtained using calorimetry, and complemented using neutron scattering in order to access the structural information of the transition. The results were completed using electrophoresis and optical observation data. The neutron scattering results were analysed in terms of a one-dimensional mesoscopic model of DNA (Peyrard-Bishop-Dauxois).

5.2 Introduction

The thermal denaturation of DNA can be analysed as a physical phenomenon. In this context it appears as a first order phase transition in which domains in the double helix form coexist with regions where the two strands are separated ("bubbles") which grow when the temperature increases, until they extend over the whole molecule. Theoretically it can be described by statistical physics.

A phase transition describes any structural change, and it is represented by a thermodynamic macroscopic quantity whose behaviour describes the transition. This is called the order parameter. A discontinuity in its lowest derivative as the system goes through a boundary regime determine the order of the transition. Examples are: magnetisation for magnetic materials, density difference in liquid-gas phase, helix base pairs in an helix-coil system,etc. The first order transition differs from a second order by the presence of a

latent heat during the transition. At the phase boundary both phases coexist and their Gibbs free energies *G(P,T)* are equal, but the entropy and volume exhibit discontinuity. In the case of a second order phase transition, or more properly named a critical phase transition, the first derivative of the Gibs free energy is continuous throughout the phase transition. The transition takes place at the critical point $T = T_c$, without a latent heat. The order parameter experiences a symmetry breaking when going through the critical temperature, from zero at $T > Tc$ to nonzero at $T < Tc$. The dimensionality plays an important role on the properties of phase transitions. On approaching the transition, close to the critical point there are microregions of both phases fluctuating at characteristics length scales. The thermal correlation length, describing the length at which the fluctuation will be still felt by the system, diverges, as do their time scales. At this stage, all thermodynamic quantities are described by a power law characterised by critical exponents.

To date, most of the experiments to study DNA melting transition have been carried out in solution using bulk techniques such as, Raman spectroscopy, UV absorbance and calorimetry. The latter provides a general overview of the macroscopic behaviour of a system, whereas other methods give more insight into the microscopic behaviour of the system, and gives direct access to thermodynamic data.

To understand a phase transition it is important to characterise its macroscopic properties, such as its thermodynamic data, but this is not enough. Measuring spatial correlations is essential. This cannot be done in solution because the molecules are diffusing and are not oriented in space. It is necessary to fix the molecules and orient them in space. This can be done for a single DNA molecule in a solvent using for instance optical tweezers [79], but this does not allow the observation of its structural fluctuations. An alternative is to look for a solid phase made of oriented DNA. As discussed in the previous chapters such samples can be produced in fibre form and characterised. This raises however further questions: how does the proximity of the molecules in the solid phase influence the fluctuations and denaturing of DNA? One could even wonder whether denaturing is possible in this highly confined environment. This is why we have investigated DNA melting by two complementary approaches:

1. Bulk calorimetry to confirm the existence of the melting transition in fibres and films and study its main features, such as the effect of hydration.

2. Structural studies, using neutron scattering, to get the precise structural information needed to understand and model the denaturing transition.

5.2.1 Calorimetry

A qualitative characterisation of melting curves for different structures and their variants in oriented DNA samples was obtained. In the case of the A-form, as it was proved earlier on Chapter 4, impure A-form fibre samples contain residues of a B-form, so pure and impure samples of this conformation were investigated. B-form in fibre samples can be adopted under different counter-ions, Na and Li, when exposed at different hydration levels, so both structures have also been explored. In resume, the following samples were measured: pure A-form and impure A-form Na-DNA rehumidified at 56%, B-form Li-DNA hydrated at 56% and 75% RH, and B-form Na-DNA rehumidified at 92% RH.

A quantitative study of the thermodynamic quantities at the transition temperature was investigated as a function of hydration, counter-ion and consequently, structure. These quantities were: the heat capacities of native (helix) and denatured (coil) states, named as Cp^{nat} and Cp^{denat} respectively; the enthalpy absorbed during the transition $\triangle H$; and the transition temperature, T_m. Hydration has a main role in DNA stability, and thus can contribute to the breakdown of this stability upon heating. The effects of hydration in the transition of DNA solution are reflected in the changes of the heat capacity from native to denatured state. Here we have also checked if this is the case in oriented fibres DNA.

All samples were made using natural DNA extracted from salmon testes (purchased from SIGMA), so it is assumed that the average sequence (A-T:G-C ratio) of the DNA macromolecules are the same in all samples. This means that the difference in the thermodynamic quantities as well as in the shape of the melting curves for the different samples can only be dependent on hydration and counter-ion and not on DNA sequence.

However, a calorimetry investigation does not provide any spatial information, and it is not possible to obtain it either having DNA in a solution state, or with a bulk measurement. This is why we completed these measurements by structural investigations.

5.2.2 Structural Studies

In films of oriented DNA fibres [71], the molecules are orientated along the fibre axis. The system is analogous to having 1-D chains of diffracting planes along the helical axis. In the B-form the base pairs stack perpendicular to the helical axis, and the periodic distance of these planes give rise to a very intense Bragg peak. In the case of the A-form, the planes are tilted with respect to the helical axis. The structure becomes more complex. The fibres arrange with each other in a crystalline lattice structure. It was found that while B-DNA forms a semicrystalline structure, A-DNA arranges in a higher crystalline way. Bragg peaks with a component along the helical axis can easily be detected. (See Chapter 4).

Structural information can be extracted from a Bragg peak from the width along the helical axis, since our interest is in the study of the correlation length along that direction. The correlation function is considered to be exponential characterised by a correlation length, ξ, corresponding to the distance over which the closed base pair correlation takes place. Due to the structure of the sample, and the DNA sequence in particular, the correlation length as seen from neutrons accounts for two aspects: the number of closed base pairs and the geometric contribution due to the sequence disorder of natural DNA. The former is very temperature dependent. The structure factor introduced by the latter limits the maximum number of closed base pairs observable and the effects of temperature on it can be negligible. This limit is of the order of 20-50 base pairs. As a consequence we have made the assumption for the experimental and theoretical analysis that the temperature effects on the fibre are negligible. However, in the case of the B-form this aspect needed to be revised at very high temperatures. This assumption is validated by the calorimetric studies which show the specific heat characteristic of the transition. Observing denaturation are therefore possible by structural studies as a function of temperature until the DNA melts. These effects can be monitored via the width and integrated intensity of the measured Bragg peaks. The width is inversely related to the closed region size (correlation length), while the integrated intensity accounts for the number of elements, i.e. diffracting base pairs. These concepts will be better explained in further sections.

The aim of the neutron scattering experiments presented in this chapter was to measure the correlation length along the DNA molecules as the temperature approaches the transition (melting) temperature, to be able to test statistical mechanics models such as the

PBD model. The method used was based on similar experiments that measured the magnetic correlation length around an order-disorder phase transition in a low-dimensional magnetic material. Neutron scattering data was obtained for B-form [7] [8] and pure A-form DNA.

The neutron scattering results of the B-form DNA were analysed using the PBD model, and both experimental and theoretical results will be described in this chapter. In the case of the A-form, although only the experimental results were completed, a first "fit" of a theoretical analysis will be also presented. Due to the complexity of the structure the theoretical model has encountered additional difficulties compared to those for the B-form. Nevertheless, these difficulties as well as a preliminary comparison of the model for both DNA structures will be discussed.

5.3 Melting Profiles by DSC

5.3.1 Experimental method

The samples were prepared using the WSA by spinning solutions of Na-DNA and Li-DNA in order to obtain films of oriented fibres of the respective ion-nature. (See Chapter 4).

In order to explore different DNA conformations, Na-DNA and Li-DNA films were re-humidified at different hydration levels given by an oversaturated salt solution in H_2O. Table 5.1 gives a summary of the DNA structures of the analysed samples.

Table 5.1: Values of variable to obtain the DNA-forms of interest.

DNA conformation	A-form	B-form		
counter-ion	Na-DNA	Na-DNA	Li-DNA	Li-DNA
Relative humidity (%)	56	92	56	75

A Setaram Micro DSC III calorimeter was used for the measurements. The principles of this apparatus and its characteristics have been described before; please refer to Chapter 2 for a better understanding.

For each of the DSC experiments, one hydrated film with a mass between 80 and 100 mg was rolled up and placed in an hastelloy tube. It was then left inside the desiccator for a day to allow the tube to attain the same relative humidity as the surroundings. Once this was accomplished, the tube was sealed with an O-ring to fix the water content

throughout the experiment. The films inside the tubes were in contact with the cylindrical wall ensuring a good thermal contact.

Before placing the sample inside the DSC, the temperature of the water regulator bath was set to 293 K for the A-form DNA measurements, and 296 K for B-form. The melting transition for the B-form occurs at a higher temperature, so the temperature of the bath needed to be increased to be able to reach to high enough temperatures to include the transition. Once the temperature of the regulator bath was stable, the samples were put in the DSC and held at 293 K isothermally for 10 mins to allow thermal equilibrium. The reference tube was left empty.

The sample was cooled down to 268 K at a rate of 1.2 K/min, kept at that temperature during 10 mins and then heated to 368 K (for the A-form) and 383 K (for the B-form) at 0.6 K/min. After 5 mins of stabilisation at the highest temperature, the sample was cooled down again to 268 K at the same rate of 0.6 K/min. The heating-cooling cycle was repeated twice to check reversibility. The experiment was finished by a final heating ramp from 268 K to 293 K at 1.2 K/min.

The DSC output data was given as heat flux $\triangle P$ as a function of temperature. The data was corrected from instrumental resolution using equation 2.63, 2.62 in Chapter 2 in the form,

$$\triangle Cp = \triangle Cp_{raw} + \tau_{ins}\beta\frac{d(\triangle Cp_{rau})}{dT}, \tag{5.1}$$

where $\triangle Cp_{raw} = \triangle P/\beta$ is the uncorrected specific heat and $\triangle Cp$ is the corrected one, β is the scanning rate and τ_{ins} is the thermal time constant of the instrument, and was given by the supplier as τ_{ins}=60s.

As previously described in Chapter 2, the deconvoluted data, $\triangle Cp$, corresponds to the difference in heat capacity between the DNA and the reference cells; since the latter was kept empty, the measured signal comes from DNA only. The data was normalised by the mass of each sample, so it is given in (J/gK) units. The DSC presented in this thesis were smoothed after being corrected for the instrumental resolution, to avoid effects introduced by the numerical derivative.

The correction of the data involves the derivative $d(\triangle Cp_{raw})/dT$ which has to be included to the measured data. This requires some care as a direct numerical derivative is strongly affected by the noise of the measurement as shown in Figure 5.1. The corrected signal for

the instrumental time constant of τ_{ins}=60s is also represented in the figure.

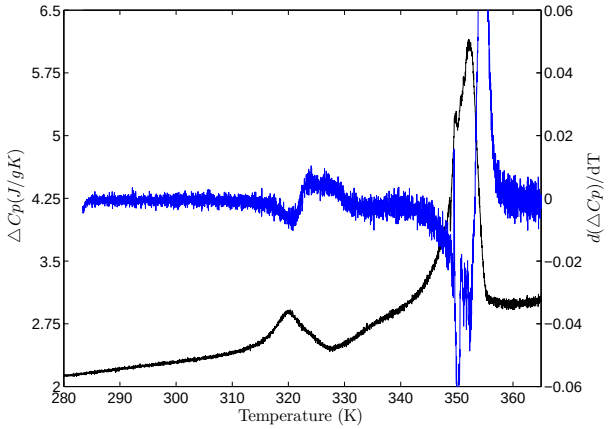

Figure 5.1: Example of a DSC curve, $\triangle Cp$ *vs* Temperature, corrected for a calorimeter time delay τ_{ins} = 60 and smoothed (black); compared to its derivative dCp/dT *vs* Temperature (red).

To avoid this problem, the experimental data must first be smoothed, by using a function in *Matlab* called 'smooth', which performs a local polynomial regression on N experimental points. Increasing N gives more smoothing but care must be taken not to lose information. With N=50 we still get some unphysical spikes in the derivative. The value N=150 appeared as a good compromise. Once we have a reliable calculation of the derivative we can proceed to the correction of the time lag of the calorimeter according to equation 5.1.

5.3.2 Results

Melting Profile for Different DNA conformations Figure 5.2 shows the first and second DSC heating scan for the two standard DNA forms obtained directly from the wet spinning apparatus: "impure" A-form Na-DNA humidified at 56% RH, and B-form Li-DNA humidified at 75% RH. The curves are presented in heat capacity as a function of temperature. The nonappearance of the transition peak on the re-heating scan shows that the transition from double helix to a random coil single stranded in fibre samples is irreversible, contrary to what is observed in solution. The reason, as discussed in the introduction, is believed to rely in the confinement of the DNA molecules in the fibre. Furthermore, the second heating scan shows a typical glass behaviour denoted by the step-like ascent in the heat capacity. The glass properties of our denatured samples will be discussed in detail in the next chapter (See Chapter 6).

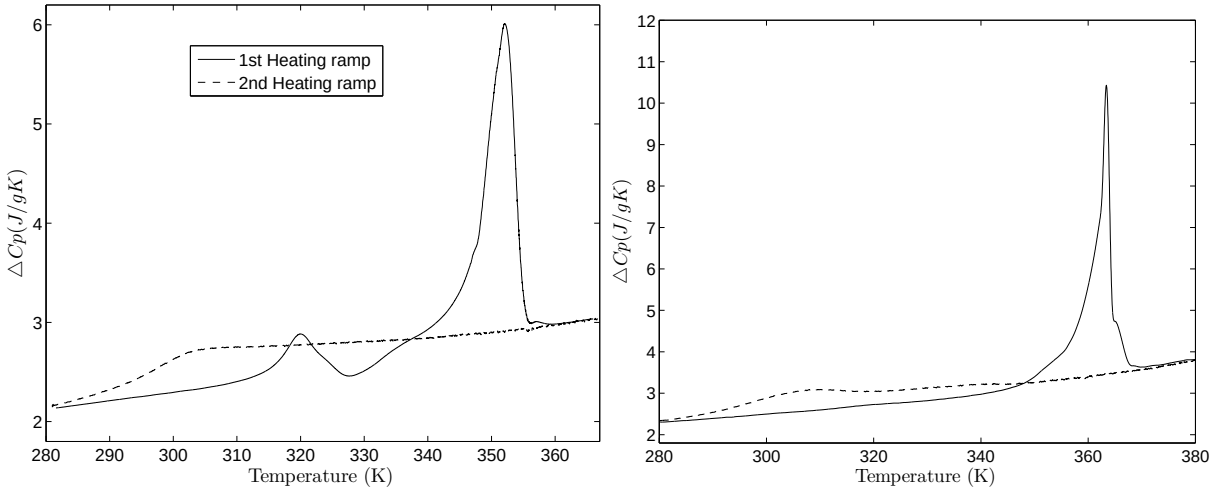

(a) A-form (b) B-form

Figure 5.2: First (continuous line) and second heating ramp (discontinuous line) of two DNA conformations: impure A-form Na-DNA (a), and B-form Li-DNA (b)

Figure 5.3 shows the configurational transition of an impure A-form (a) and pure A-form (b). Both samples belong to the same film, which was cut into two pieces of comparable mass, and humidified for 5 and 10 days respectively. This reduces the influence of sample preparation when comparing the melting profiles and the thermodynamic quantities at the transition of both structures.

The first heating curve for the impure A-form sample shows two endothermic process, one at 320 K and a more prominent one centred at around 350 K. The first one is associated to a conformational change of some DNA molecules, that switch from the B-form of DNA to the A-form which was described in detail in Chapter 4. Recall that, in order to obtain the melting profile of a pure A-form, the sample has to be pre-heated to 320 K, cooled down and heated again all the way through to the melting transition.

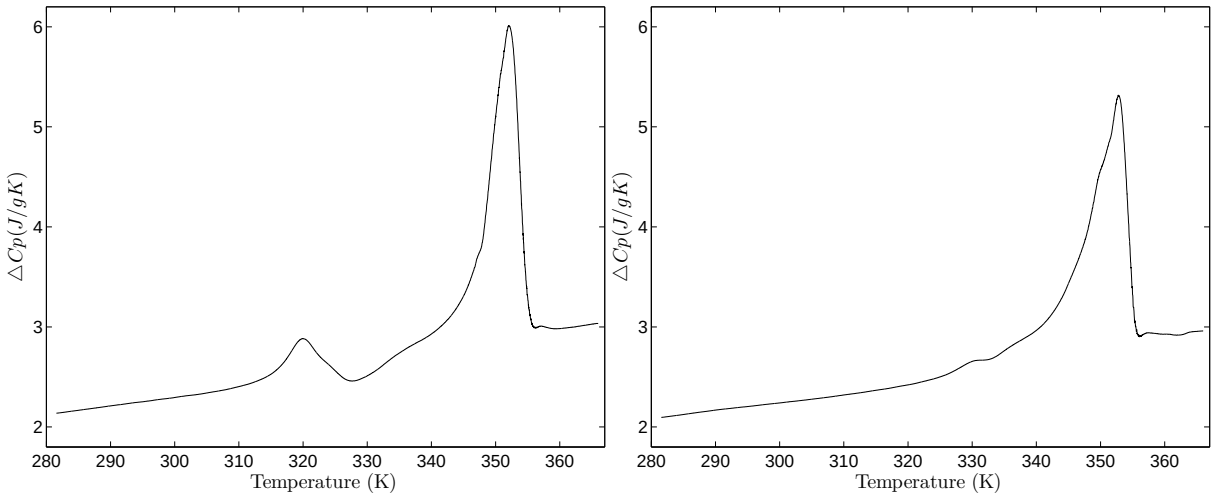

(a) native A-form (b) pure A-form

Figure 5.3: Melting profile of two DNA conformations obtained from two pieces of the same film sample: Impure A-form Na-DNA (a), and pure A-form Na-DNA (b)

Both figures have been plotted together in Figure 5.4 for better comparison. The effects of a previous heating in an impure sample seem not to affect the shape of the melting transition and its temperature. The endothermic peak of the A-impure rises to a higher heat capacity than for the A-pure. But also, the specific heat of the native Cp^{nat} and denatured state Cp^{denat} appears slightly lower in the A-pure.

Although the small peak at 320 K has disappeared in the A-pure form, a small endothermic bump is still visible at a higher temperature, suggesting that a very small B-contamination remains.

The specific heat involves many contributions: the fluctuation of the DNA molecules themselves (internal to a molecule) but also the inter-molecular interactions, i.e. it depends on the structure of the film. Therefore, as discussed in Chapter 4, the thermal effects of the pre-heating process will have an effect in the structure of the fibres in the sample, leading to a loss of part of the orientation of the fibres. Small differences between the melting curves of both samples are therefore not surprising.

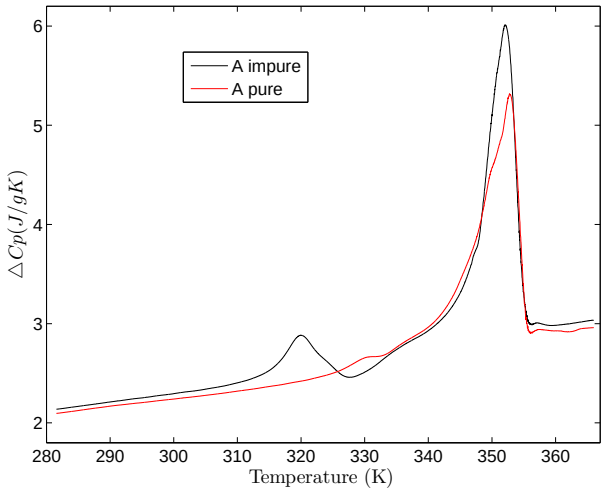

Figure 5.4: Combined DSC heating scans of impure A-form Na-DNA (black curve), and pure A-form Na-DNA (red curve).

Figure 5.5 shows the denaturing transition in B-form Li-DNA samples at two different hydrations: 56% and 75% RH; and in a B-form Na-DNA hydrated at 92% RH. For B-form DNA, the samples do not suffer any configurational transition until the melting temperature is reached; the peaks are narrower than those of the A-form, and the transition starts at higher temperatures. In the case of Li-DNA films, the decrease in hydration from 75% RH to 56% RH shifts the transition about 7 K to lower temperatures, and makes it narrower. Since both samples were prepared in the presence of Li and both are in a crystalline form, this effect can be attributed mainly to hydration. It is well known that hydration is a crucial component of DNA stabilisation, higher hydration implies higher stability and thus higher T_m. On the other hand, the comparison between the melting curves of Li-DNA film at 56% RH and Na-DNA film at 92%, becomes more complex as the ionic strength is different in both samples. They present a very similar profile, the transition occurs at the same T_m and have similar width. The role of the Li and Na in the stabilisation and crystallisation of DNA is not fully understood at present. However, using Li^+ over Na^+ provides a higher stabilisation of the DNA molecule [68].

The width of the peak is associated to the degree of cooperation of the helix-coil transition. The narrower peak of the B-form indicates that the transition in this structure is more cooperative than in the A-form DNA.

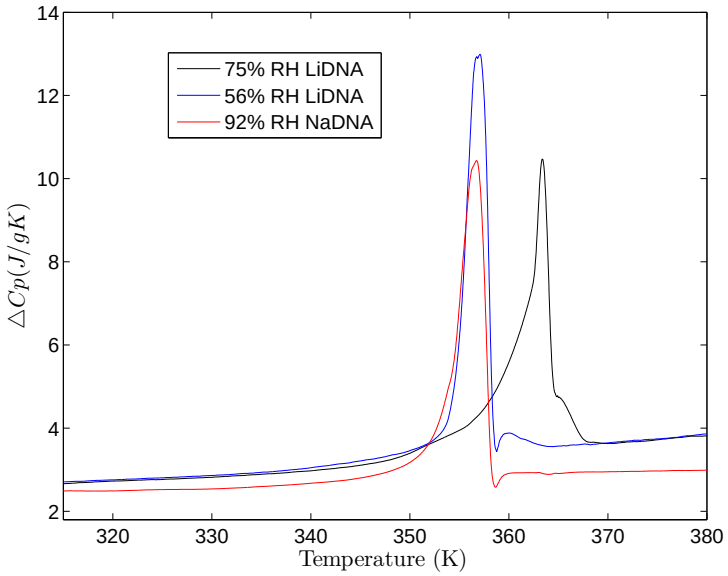

Figure 5.5: Melting profile of B-form DNA. Comparison of the melting curves with different counter-ion solutions and hydrated at different relative humidities: 56% (blue curve) and 75% (black curve) for Li-DNA; and 92% (red curve) for Na-DNA.

Determining the transition thermodynamic quantities Changes in the system as a function of temperature are described by the heat capacity. As a first order transition, thermal denaturation occurs with a latent heat, and therefore this energy can be accessed by calculating the area under a DSC curve (see equation 2.54 in Chapter 2).

First of all, the transition temperature was obtained by fitting the DSC curves with a Lorentzian function with a sloping background, followed by the determining the C_p^{nat} and C_p^{denat} curves and their values at the peak temperature T_m. They were described by linear functions and extrapolated to the transition temperature. The difference between both states at that temperature was obtained, $\triangle C_p(T_m)$. The limits of integration were defined by the intersections between the melting curve and the baselines. Finally, the area under the curve limited by the heat capacity functions at this midpoint, T_m, was calculated. Furthermore, $\triangle S$ was obtained by calculating the area under the curve $\frac{C_p}{T}$ *vs* T. Figure 5.6 shows a diagram showing how the different thermodynamical quantities were defined.

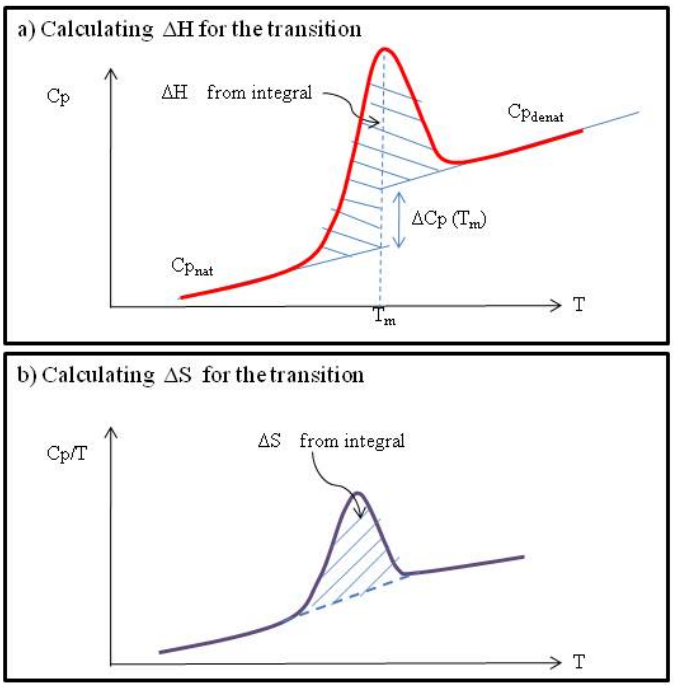

Figure 5.6: Figure (a) represents a typical calorimetric curve C_p as a function of T. The temperature transition at the maximum has been marked, T_m, to which the base lines, Cp_{denat} and Cp_{nat}, were extrapolated. The difference between the heat capacity of both states at that temperature corresponds to $\triangle C_p(T_m)$. Figure (b) shows the curve $\frac{C_p}{T}$ as a function of T, the area under which corresponds to the entropy $\triangle S$.

As discussed earlier, the melting transition is sensitive to the ionic strength, and to the sequence: G-C over A-T content, and stacking interactions between nearest neighbours. The duplex DNA stability from the base sequence was investigated in detailed by Breslauer and co-workers based on the nearest neighbour (NN) interaction. They reported thermodynamic transition quantities $\triangle S$ and $\triangle H$ for different DNA oligomers and polymer sequences [39]. However, heat capacity effects due to denaturation were not considered until late 90′s [80],[81] due to experimental limitations. The noise in the background of the curves did not allow $\triangle C_p$ to be resolved. Figure 5.6 shows that both $\triangle H$ and $\triangle S$ quantities do depend on the increase of the heat capacity from a native to a denatured state. Rouzina and Bloomfield carried out studies to analyse previous published data on $\triangle C_p$, $\triangle S$ and $\triangle H$ for DNA denaturation in solution. Within this scenario, they investigated the effects of the ionic strength and sequence composition in the melting temperature in order to prove the presence of $\triangle C_p$ as a consequence of the dependence of $\triangle H$ and $\triangle S$ on T_m. Furthermore, recent studies on $\triangle C_p(T_m)$ stressed the influence of base pair stacking, and how residual stacking in the single-stranded state can minimise

the manifestation of this quantity[82].

Table 5.2 summarises the accepted values of DNA solution per base pair of the investigated quantities: $\triangle C_p(T_m)$, $\triangle H$ and $\triangle S$ during the transition. The thermodynamic quantities are given in units of cal/mol, which were converted into J/mol in order to compare them with our experimental results. Since the molecular weight of DNA base pairs is almost equal for AT and GC base pairs, independently of the AT/GC fraction, the unit conversion can be made by using the average base pair molecular weigh of 618 g/mol and 1 cal=4.18 J.

Thermodynamic Quantities	Experimental values of DNA in solution per base pair [cal/mol]	Conversion units [J/g]	Reference
$\triangle C_p(T_m)$	30 - 100 cal/mol/K	0.2 - 0.67 J/g/K	[80]
$\triangle H$	5.6 - 11.1 kcal/mol	37 - 75 J/g	[39]
$\triangle S$	12.9 - 27.8 cal/mol/K	0.087 - 0.188 J/g/K	[39]

Table 5.2: Summary of thermodynamical quantities obtained for the melting transition of DNA in solution as given by different references.

It has been difficult to estimate errors in the respective quantities due to the variety of variables involved to their calculation. In the case of the enthalpy, the area under the curve was calculated for different limits of integration within a range of 1 K, and for shifts in T_m of ± 2 K. The values obtained differed from what was considered the optimal enthalpy value by ± 1 J/g.

The thermodynamic transition quantities obtained for each of the explored structures are presented in Table 5.3.

As discussed before, hydration and ionic strength play a important role in DNA stabilisation, and hence changes in both quantities will have an effect in the transition temperature, T_m, and denaturation peak area.

As all samples were made using the same DNA product, so the comparison of these results are sequence independent. Recall from the product information of natural DNA used for our samples (see Chapter 4) that there is 41% GC content. For a given sequence, the value of $\triangle H$ at melting depends on the GC content because GC pairs have 3 hydrogen bonds and AT pairs have only 2 hydrogen bonds; and in the stacking interaction, which is also higher between the nearest neighbours G-G/C-C/G-C [39]. From Table 5.2 one can get an order of magnitude of an average value of $\triangle H$ per base pair of 37 - 75 J/g. Although this

DNA oriented samples	C_p^{native} (J/gK)	C_p^{denat} (J/gK)	$\triangle C = C_p^{denat} - C_p^{nat}$ (J/gK)	$\triangle$ H (J/g)	T_m (K)	$\triangle$S (J/gK)
A-impure Na-DNA 56% RH	2.75	2.90	0.15	21	351.5	0.058
A-pure Na-DNA 56% RH	2.85	2.70	0.15	21	351.2	0.055
B-form Na-DNA 92% RH	2.76	2.90	0.13	26	356.3	0.07
B-form Li-DNA 56% RH	3.12	3.38	0.26	31	357	0.075
B-form Li-DNA 75% RH	3.15	3.46	0.32	34	363.5	0.078

Table 5.3: Values of thermodynamic quantities obtained during DNA melting for the following DNA samples exposed to different hydration levels and counter-ions.

method to calculate the enthalpy is not rigourous, the values that we obtained within the experimental errors are at least two times smaller than the expected ones. The reason for this missing enthalpy could lie in the confinement of the DNA in the fibres. The thermal denaturation of the DNA molecules has a strong effect of the whole structure of the fibres and films. DNA is fairly rigid in its double helix form, with a persistence length of about 500 Å, whereas the two single strands formed after denaturation are very flexible, with persistence lengths of the order of 10 Å. In solution, at high temperature this leads to a sample in which the strands are fully disordered and free to move. Contrary in the films, even if hydrogen bonds are broken between base pairs, the lack of free space could prevent some small segments to unstack. The melted sample appears to be in a quasi-liquid state. By "quasi" we mean two important differences with the melted DNA in solution: the reversibility of DNA denaturation in aqueous solution relies in the fact that the bases can move in space to form hydrogen bonds, while in fibrous sample there are much less water molecules available; and secondly, the confinement of this quasi-liquid state does not allow the bases to move freely. The DNA strands themselves have difficulties to move in the kind of polymer melt made by the film at high temperature. Hence, the transition is irreversible. In addition, the increased elasticity of small, single stranded sequences and viscosity of the state upon raising temperature could contribute to their local re-stacking, and a decrease in the latent heat involved.

It can be seen that for the same counter-ion, increasing the hydration level of the sample shifts the transition temperature to higher values, and the enthalpy is also higher. Despite the hydration variable, $\triangle H$ and T_m are clearly higher for samples made using Li-DNA. However, Na-DNA samples at the highest hydration levels show a transition occurring

almost at the same temperature as Li-DNA samples at a lower hydration. This suggests that, despite the ionic strength differences, hydration can contribute to the DNA stability and hence shift the transition to higher temperatures.

5.4 Structural correlations via Neutron Scattering

5.4.1 Experimental method

Apparatus

The measurements of Bragg peaks as a function of temperature for both DNA structures were carried out on a three axis spectrometer (TAS) in an energy integrating mode, in order to attain the static approximation throughout the experiments.

B-form DNA measurements were carried out on the IN8 TAS at the ILL (France). A-form measurements were performed on IN8 and the TAIPAN TAS at ANSTO (Australia). A description of both instruments was given elsewhere, section 2.2.4 in Chapter 2.

Experiments on IN8 used a cryofurnace, while those carried out on TAIPAN used a heater chamber. For both instruments the analyser was removed and they were configured with a graphite monochromator with k_i fixed at 4.1 Å^{-1} for the B-form, and 2.662 Å^{-1} for A-form. The Q-resolution was defined by 40' collimators before and after the sample. A PG filter was also placed before the sample to remove higher order wavelengths.

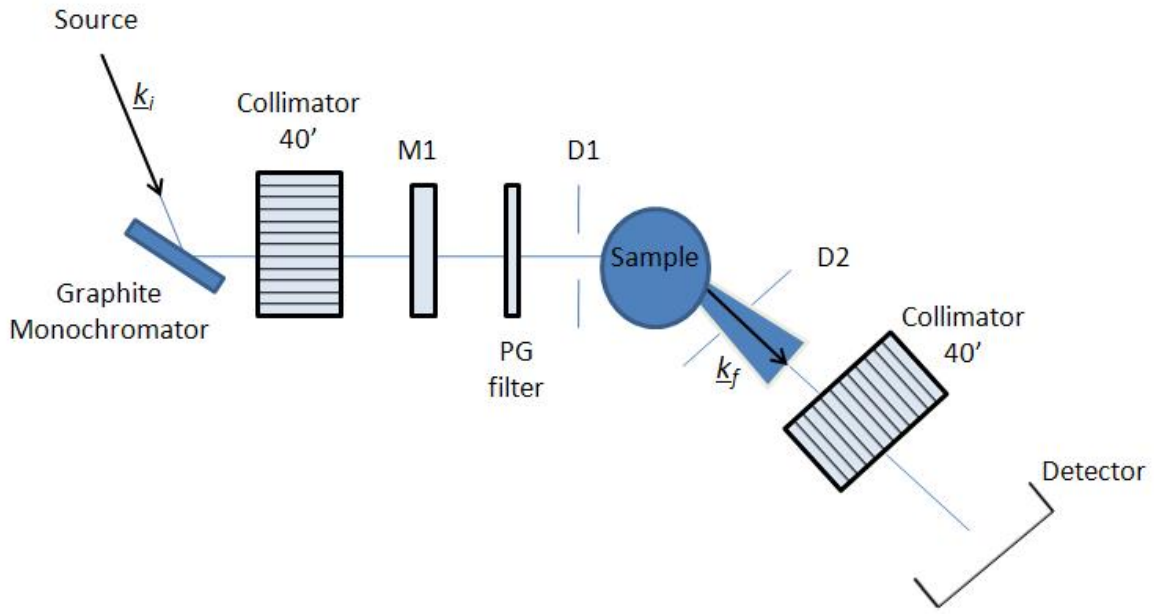

Figure 5.7: Layout of a triple axis spectrometer in energy integrating mode, i.e. no analyser axis.

Sample

The study of thermal denaturation was carried out on B-form Li-DNA humidified at 75% RH, and the purified A-form Na-DNA (see Chapter 4) rehumidified at 56% RH. The samples were humidified in a D_2O saturated salt solution. Each sample consisted of 10-15 films each of 100 to 300 mg in weight. The samples were folded in a concertina form, placed between aluminium plates and sealed using lead wire inside a humidity chamber to ensure the conservation and control of water molecules within the sample (see Chapter 4).

Measurements

The samples were aligned with the fibre axis in the scattering plane, such that Q_H was defined parallel to the fibre axis, and Q_K was perpendicular. Both sample environments, liquid helium cryofurnace on IN8, and a heater chamber on TAIPAN, allowed a temperature control of 0.1 K. The measurements covered a temperature range from 295 K to 360 K.

Throughout measurements the temperature was increased by choosing a temperature step size of 3 K for the first temperatures, and reduced to 0.2-0.1 K as the melting transition

was approached, in order not to overshoot the critical transition temperature. Scans at a given temperature were repeated to ensure thermal equilibrium and reproducibility. Once the critical transition temperature is surpassed the sample is destroyed, the transition is not reversible, as shown on the DSC results.

After each of the experiments was completed the instrument resolution was measured by making a reciprocal space map of the (111) Bragg peak from a silicon single crystal.

B-form DNA The measurements were performed with k_i fixed at 4.1 Å. They were centred on the intense Bragg peak at a position in reciprocal space given by the longitudinal component of the scattering vector $Q_H = 2\pi/d = 1.87$ Å^{-1}, associated with the average distance d=3.36 Å between consecutive base pairs.

The evolution of this Bragg peak as a function of temperature was monitored by the means of two types of scan performed at each temperature:

1. Scan 1: A scan along Q_H, centred at (1.854,0,0). This corresponded to a Q scan along the helical axis through the centre of the base-pair Bragg peak.

2. Scan 2: A scan along Q_H, centred at (1.854,0.443,0), corresponding to a Q scan along the helical axis at a position where k_f was perpendicular to the fibre axis at the centre of the scan. This scan provides two pieces of information: by scanning with a component perpendicular to the helical axis, we obtained information about the transverse displacement of the base pairs; and secondly we satisfy the static approximation for a one dimensional lattice.

The respective scans are shown on the reciprocal space map of the B-form DNA, Figure 5.8.

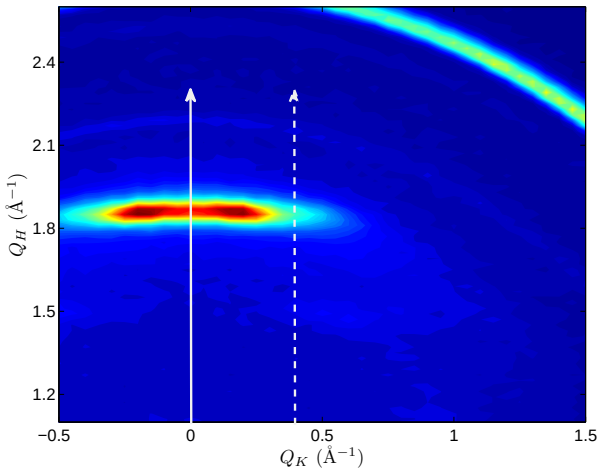

Figure 5.8: Contour plots of reciprocal space map of B-form Li-DNA. The axes correspond to the scattering vector parallel (Q_H) and perpendicular (Q_K) to the helical axis. The lines mark the two type of scans: scan 1 (solid line) and scan 2 (broken line).

A-form DNA Contrary to the experimental method applied to the B-form DNA, due to the complexity of the A-form Bragg peaks a Q scan with k_f perpendicular to the fibre axis at the centre of the scan, as Scan 2 in the B-form, was not carried out on this DNA structure. Nevertheless, as the A-form Bragg peaks are off-centre, i.e. having a **Q** component perpendicular to the molecular axis, displacement of the base pairs in the transverse direction can also be probed. The static approximation still holds but it is not ideal for the energy integration of a 1-D system.

The standard scans performed on a A-form sample were chosen to include some interesting features in reciprocal space. These correspond to the three-off axis Bragg peaks near Q_H=1.7 Å^{-1}, and the low-Q Bragg peak centred at (0.25, 0.5) Å^{-1}.

Contrary to the B-form measurements, in order to be able to access low-Q values, the momentum wavevector had to be lowered to k_i=2.662 Å^{-1}. The compromise of this configuration is in the loss of flux and that the integration of energy over a lower neutron energy loss can exclude phonon excitations of higher energy transfer. Since the evolution of the correlation length along the molecule can be studied from measuring any Bragg peak in the Q_H-direction, a single intense peak, as in the B-form, provides the necessary data for our study.

Figure 5.9 shows the reciprocal space maps comprising the main features. The arrows denote the direction of the measured scans.

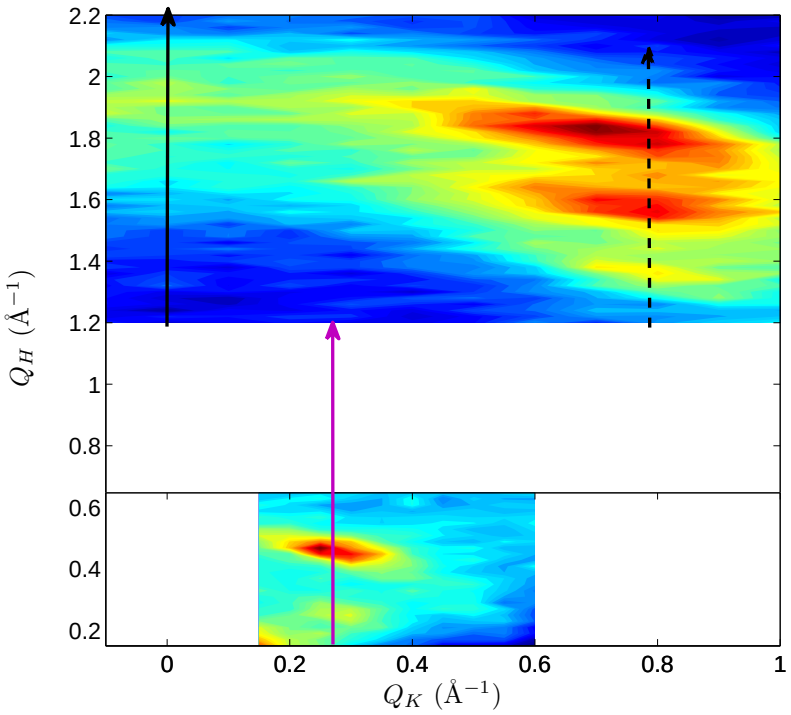

Figure 5.9: Colour contour plots of reciprocal space map of A-form DNA with k_i=2.662 Å^{-1}. The direction of the three cases are represented with arrows: scan along the fibre Q_K=0, at high Q (solid black line); scan along the three-off axis Bragg peaks Q_K=0.6 (broken line); and scan along the low -Q Bragg peak Q_K=0.25 (solid violet line)

Measurements of the three-off axis and the low-Q Bragg peaks were made by the means of three types of scan. Both low and high-Q Bragg peaks were scanned at all temperatures, from 295 K to 359 K. The aluminium powder ring was also measured after changing the temperature, to allow thermalisation time and as a check on instrument alignment.

1. Scan 1: A scan along Q_H, centred at (0.5,0.25,0). This corresponded to a Q scan through the centre of the low-Q Bragg peak.

2. Scan 2: A scan along Q_H, centred at (1.8,0.6,0). This corresponded to a Q scan of the three Bragg peaks specific to A-form.

3. Scan 3: A scan along Q_H, centred at (2.7,0,0). This corresponded to a Q scan of the powder peak of aluminium, again to account for any changes in the instrument configuration as a function of temperature.

5.4.2 Data Analysis

It has been previously assumed that the correlation function can be described by an exponential. Since the Fourier transform of this exponential function is a Lorentzian, the DNA Bragg peaks were fitted using Lorentzians. Thus, the Lorentzian width is the inverse of the correlation length determined by the number of closed base pairs and inhomogeneities of the DNA structure. The measured spectrum is broadened by the instrumental resolution, and hence the model to fit the data consists of a convolution, i.e. the data was fitted with a function that calculated the convolution of the Lorentzian with the instrumental resolution at each position in Q. The fitting routine has been used for both DNA conformations, and it is described in three steps: fitting method, determining the Q-resolution function; and convolution.

Fitting method

The scattering from the sample was treated as a combination of different components: Bragg peaks, background from the sample and powder rings given by the different materials of the sample holder. Functions to fit the scattering processes of interest were defined. As discussed before, the DNA Bragg peaks were described by Lorentzians. The measured aluminium powder ring was assumed to have a Gaussian behaviour, in which the width is associated to the instrumental resolution. This scan is essential when testing the stability of the instrumental configuration, where the width and amplitude of the aluminium Bragg peak should be stable upon changes in temperature.
Treatment of the background is a more complicated aspect to fit due to its nature, whether it is incoherent scattering from the sample or coherent scattering from the disordered states within the DNA, is uncertain. The background did not change much as a function of temperature, so it could be left free or fixed. In order to fit the three-off axis Bragg peaks, the background was fixed to reduce free parameters; in the case of the low-Q Bragg peak, all fitting parameters were left free to be analysed as a function of temperature.

B-form The Bragg peaks associated to the base pairs were fitted with the Lorentzian function given in equation 5.2. The second peak at $Q_H = 1.5$ Å^{-1} was also fitted with a Lorentzian, as it corresponds to a DNA Bragg peak. The amplitudes for these two peaks were free parameters, however, their widths were set to be equal in the fits since we

assumed that the evolution of the correlation length as a function of temperature affects collectively the DNA structure along the helical axis. Examples of the fits are given in Figure 5.10.

$$S(Q_{\parallel}) = \frac{I_0}{\pi}\left(\frac{\Gamma/2}{(\Gamma/2)^2 + (Q_{\parallel} - Q_0)^2}\right) \tag{5.2}$$

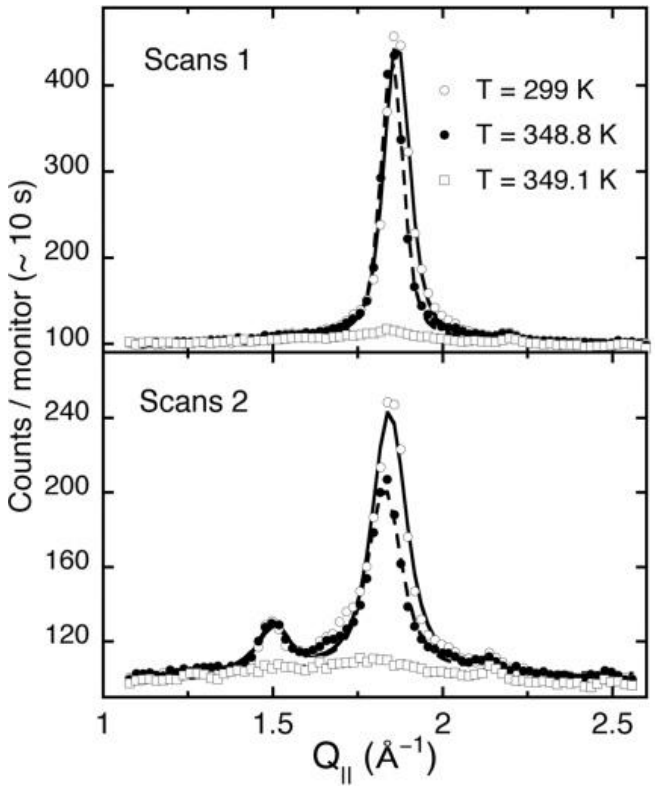

Figure 5.10: Examples of the two type of scans shown in Figure 5.8. The first temperature scan taken at 299 K, and the last one at 349.1 K are shown. The figure shows the fits obtained using equation 5.2 convoluted with instrumental resolution.

A-form Despite the study of the different features of the A-form, only the analysis of the low-Q Bragg peak was completed by fitting the data with a convoluted model in order to obtain fit parameters as a function of temperature. However, fits of the three off-axis Bragg peaks are shown below for comparison, and the non-deconvoluted fitting parameters as a function of temperature are also shown.

The data corresponding to temperatures from 298 K to 351 K were fitted using equation

5.3.

$$S_2(Q_H) = Backg + \sum_{i=1}^{3} A_i \frac{\gamma^2}{(\gamma^2 + (Q_H - Q_{0i})^2)}, \tag{5.3}$$

where *Backg* corresponds to the flat background, A_i and Q_i are the amplitude and centre of each peak, and γ is the width. The three Lorentzian widths were defined by the same parameter, γ, and the Lorentzian peak positions were fixed parameters, as it was assumed that the distance between consecutive base-pairs in the closed regions does not change. The *Backg* was also fixed to reduce the number of free parameters and facilitate the fitting. The integrated intensity is equal to I_0=A$\pi\gamma$.

However, at the highest temperatures (>352 K) the three peaks had vanished and the fit gave incongruities. The three Bragg peaks became indistinguishable, resulting in a broad featureless signal. For that reason, a Gaussian to model the data from 352 K to 354 K was used instead,

$$S_1(Q_H) = Backg + A \exp\left(-\frac{1}{2}\left(\frac{Q_H - Q_0}{\sigma}\right)^2\right), \tag{5.4}$$

where A and Q_0 are the amplitude and centre of the peak respectively, and σ is the standard deviation. The *Backg* was also fixed to the same value as for the Lorentzian fits.

Figure 5.11 shows the Lorentzian fits at different 298 K, 346 K and 352 K, as well as the Gaussian fit at 354 K. One can see that the fits of the Bragg peaks at the lowest temperatures are already not ideal.

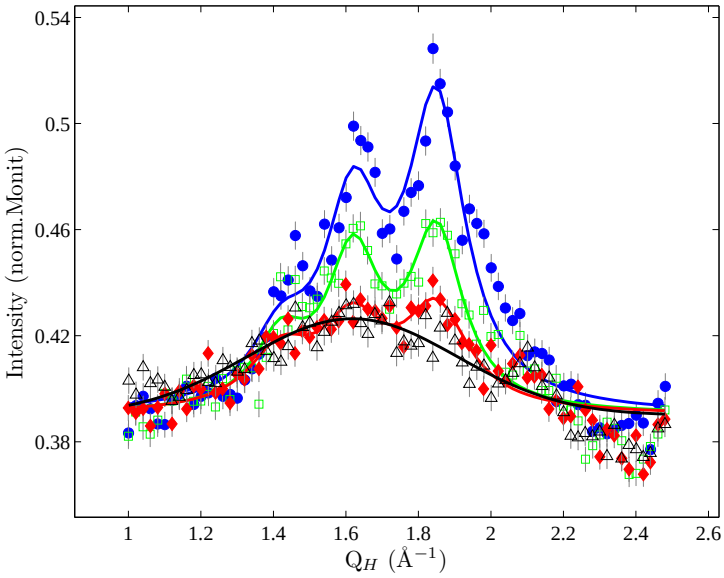

Figure 5.11: Lorentzian fits of the three off-axis Bragg peaks at three different temperatures: 298 K (blue), 346 K (green), 352 K (red), and 354 K (black).

In the case of the low-Q scans, as the temperature was increased a clear broadening and decrease of the intensity of the peak was detected until the highest temperature was reached where only a broad and diffuse peak remained.

Along the same line of thought as for the B-form, the Bragg peak was fitted with one Lorentzian with the form of equation 5.3. All parameters were kept free at all the temperatures. Data for Q <0.4 Å^{-1} could not be used as the intensity decreases dramatically due to a rapid increase in the path length through the aluminium plate sample cassette. Figure 5.12 shows the data with fits, and even for the scans at the highest temperatures the fits show good agreement with the data.

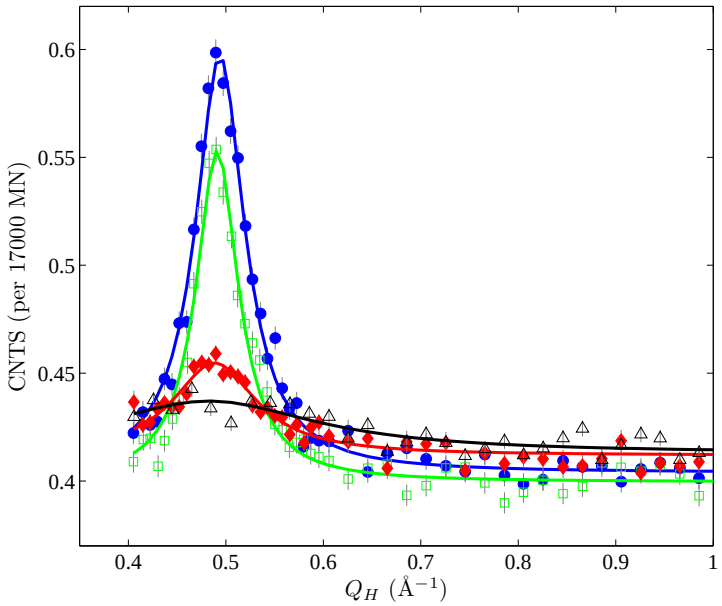

Figure 5.12: Lorentzian fits of low-Q scans taken at different temperatures.

Q-Resolution Function

The resolution function was calculated for the two scans of the B-form data, and to the low-Q data of the A-form. The general method was explained in Chapter 2. For our specific case of a triple axis in energy integrated mode, the resolution function (equation 2.45 in Chapter 2) is given by a 3x3 matrix where χ corresponds to the Q-vector = (Q_H,Q_K,Q_L). The mathematical treatment was carried out in *Matlab* where only the momentum resolution was considered, excluding the energy resolution.

The aim of this section is to match the measured resolution with experimental values, to compute a more realistic resolution matrix. Henceforth, to be able to obtain the most accurate Q-resolution function to finally fit the data at each measured Q-point with a convoluted model.

Optimising in-plane resolution parameters from Si(111) measurements The resolution matrix [M] is calculated with respect to the instrumental parameters at a Q-vector space. The Q-vector coordinates are given by the silicon scattering vector defined as $Si(111) = (\frac{2\pi}{3.3135}, 0)$ in Å^{-1}.

The output from applying our *Matlab* resolution function is the 3x3 [M], from which the

reduced 2x2 matrix [M$_{reduced}$]=

$$\begin{pmatrix} M_{11} & M_{12} \\ M_{21} & M_{22} \end{pmatrix} \tag{5.5}$$

can be extracted to consider only the $Q_X - Q_Y$ resolution ellipsoid. This ellipsoid was compared to that measured for the Si-map under the same experimental conditions. There are some values of the spectrometer parameters that accept some manipulation, and thus allow a better match between the contour lines of the Si-map and the calculated ellipsoid to be obtained. These values are the horizontal collimation before and after the sample, which were nominally defined by 40′ collimations.

In the calculation of $[M_{reduced}]$ the values for the horizontal collimation (before and after) were varied between 30′ and 40′. Consequently, the resolution matrix was obtained for each value and the resolution function was calculated for each $[M_{reduced}]$.

Figure 5.13 shows that the calculated resolution ellipsoid that best matched the measured instrumental resolution occurred at a horizontal collimation of 34′ before and after the sample .

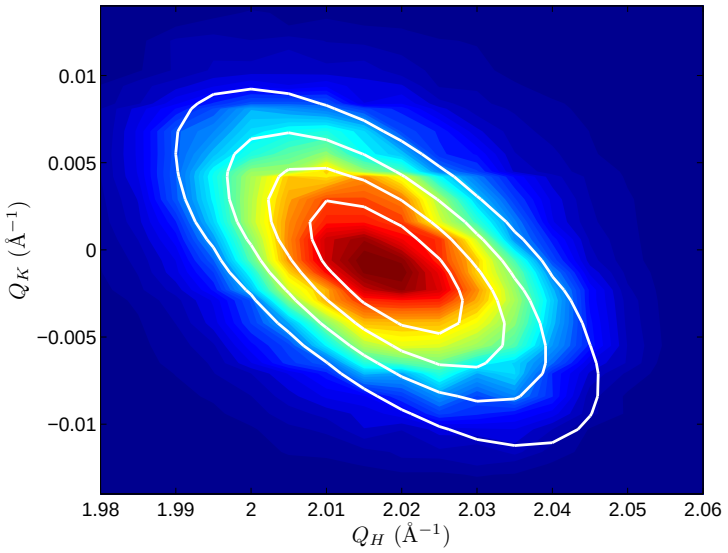

Figure 5.13: Measured contour reciprocal space map for the Si Bragg peak (111), superimposed with the calculated resolution Ellipsoid in Q$_K$ and Q$_H$ direction for a horizontal collimation (pre- and post sample) of 34' instead of 40'.

Optimising out-of-plane resolution (Q_L) from Si(111) Another spectrometer parameter that can be calibrated is the vertical collimation. This affects the resolution matrix

at the element M_{33}, which can be related to the resolution function in the following way,

$$R_L = R_0 \exp\left(-\frac{1}{2} M_{33} Q_L^2\right) \tag{5.6}$$

The FWHM can be calculated as a function of M_{33},

$$FWHM = 2\sqrt{\frac{2ln2}{M_{33}}}. \tag{5.7}$$

.

M_{33} was obtained from measuring the $Si(111)$ Bragg peak centre as a function of tilt about the Q_K axis. This measurement consisted in a tilt scan over a range of six degrees, as seen in Figure 5.14. The data was fitted with a Gaussian. The fitted width gave FWHM = 0.2059 radians = 0.4154 Å^{-1}. The conversion to reciprocal was done by applying the circle arc equation using the Silicon Bragg peak coordinate Q_H=2.017 Å^{-1} as a radius. The resolution matrix was then calculated using 60x5.0114 ° for the spectrometer parameter of the vertical collimation.

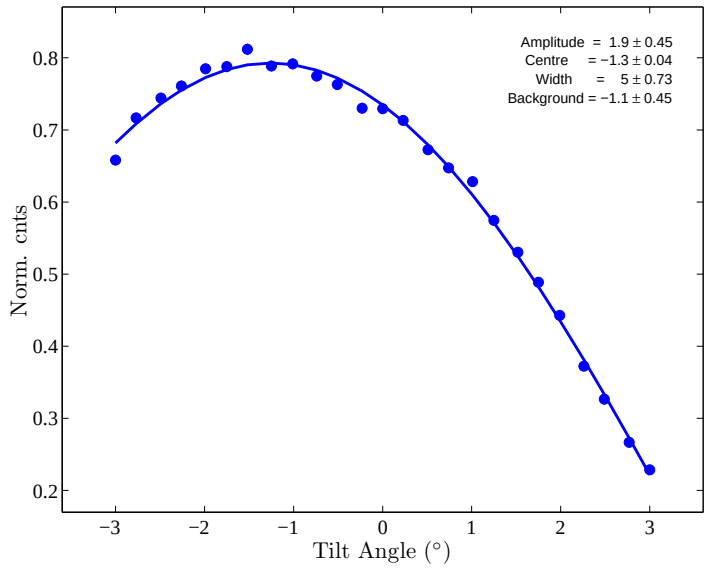

Figure 5.14: Gaussian fit of a tilt scan, intensity *vs* angle, measured at the $Si(111)$ Bragg peak centre (2.017,0)

.

Once the final spectrometer parameters were defined, the resolution function was calcu-

lated for each type of scan. For A-form, Q_H scan centred at Q_K=0.23 Å^{-1}. For B-form, there were two scans to analyse: type 1 scan centred at Q_K=0, and type 2 scan at Q_K=0.4552 Å^{-1}.

Convolution The Lorentzian function was convoluted with an estimate for the instrument resolution obtained from the previous section. A function script was used in *Matlab* for this calculation. The output Lorentzian parameters are independent of the resolution function.

The dimensionless widths are given with respect to a=3.36 and 2.545 Å which is the step along the helix obtained for B and A-DNA respectively.

5.4.3 Results

B-form DNA, k_i = 4.1 Å^{-1}

Figure 5.15 illustrates the evolution of the Lorentzian parameters of the B-form DNA. The integrated intensity of the Bragg peaks stay constant from room temperature to about T = 346 K. At this temperature they start to show a small decrease, occurring in a temperature range of about 3 K, followed by an abrupt drop. A more careful examination of this figure reveals the following results.

1. The intensity of the peak observed in scan 1 is higher than that of the off-centre peak in scan 2, as expected, but its evolution versus temperature is remarkably similar in both scans. The drop of the intensity is extremely sharp in temperature. Although the DNA thermal denaturation can occur in a narrow temperature range, for natural DNA the transition is widen by sequence effects, so that the temperature drop appears to be sharper than what one would expect. Alternative mechanisms for a further investigation of this phenomenon were considered. It was suggested as a possible explanation that the nature of the sample undergoes a change leading to a disappearance of the Bragg peaks, and this is why macroscopic observations were performed and will be described in the next section. They revealed that, besides the thermal denaturation of DNA, the last stage of the transition is accompanied by destruction of the film in which the ordered fibre structure collapses, i.e. the DNA denaturation as seen by neutrons is hindered by this phenomenon, as the diffracted

regions become part of a quasi-liquid state before DNA denaturation has completed. We investigate some of its consequences in Chapter 6. In the present discussion we shall focus our attention on the phenomena that occur prior to this collapse of the film.

2. The width of the off-centre peak (scan 2) is significantly larger than the width at the centre of the diffraction spot.

3. In the 300 K to 340 K temperature range the width of both peaks is essentially constant and even shows a slight decrease, which can be attributed to an annealing of the sample. This consists of a better alignment of the DNA molecules in the sample, and hence a better arrangement of the base pairs along the helical axis, i.e. increases the number of diffracting elements in that direction.

4. For scan 1, the figure shows that, in the vicinity of the transition, where the annealing has been completed, the width of the Bragg peak is remarkably constant even when the intensity of the mode starts to decrease in the temperature range 346 $< T <$ 349 K. On the contrary, for scan 2 (off-centre) the width of the peak shows a gradual increase in this temperature range, which appears to mirror the decrease in the intensity of the peak.

5. A small deviation in the data at $T \approx 345$ K was due to the discovery of an alignment issue that was found and rectified before reaching the melting transition.

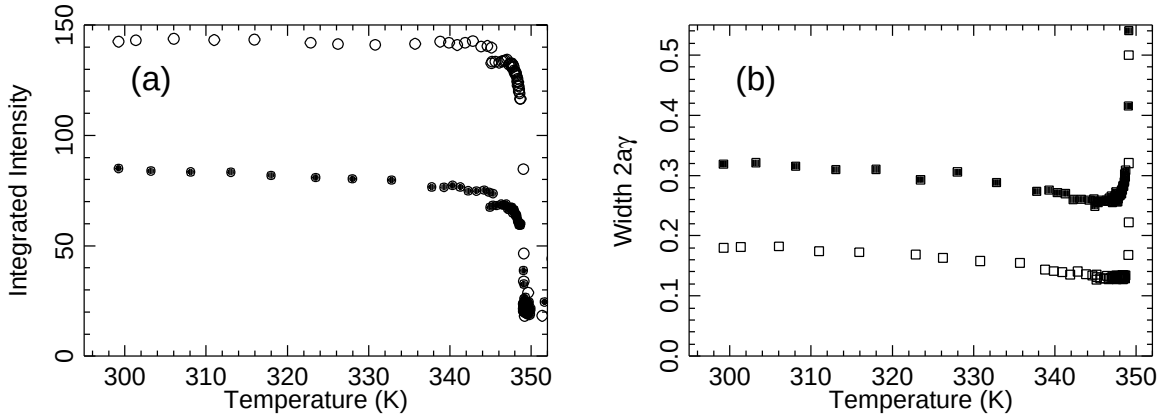

Figure 5.15: (a) Integrated Intensity and (b) width 2aγ (dimensionless) of the Bragg peaks versus temperature. Results for scan 1 are shown by open symbols, while results for scan 2 are plotted with filled symbols.

A-form DNA, k_i = 2.662 Å^{-1}

High-Q data These measurements allowed us to study the different Bragg peaks along the molecule as a function of temperature. Due to the lower quality of the fits for the three off-axis Bragg peaks compared to that of the low-Q Bragg peak convolution with the resolution function was not carried out.

Figure 5.16 shows the evolution of Lorentzian parameters, amplitude and width, of the three off-axis Bragg peaks. The Gaussian amplitudes for the highest temperatures have also been included. Finally, the integrated intensity I_0 ($I_0 = 2\pi\gamma$) under the spectra has been plotted for each temperature.

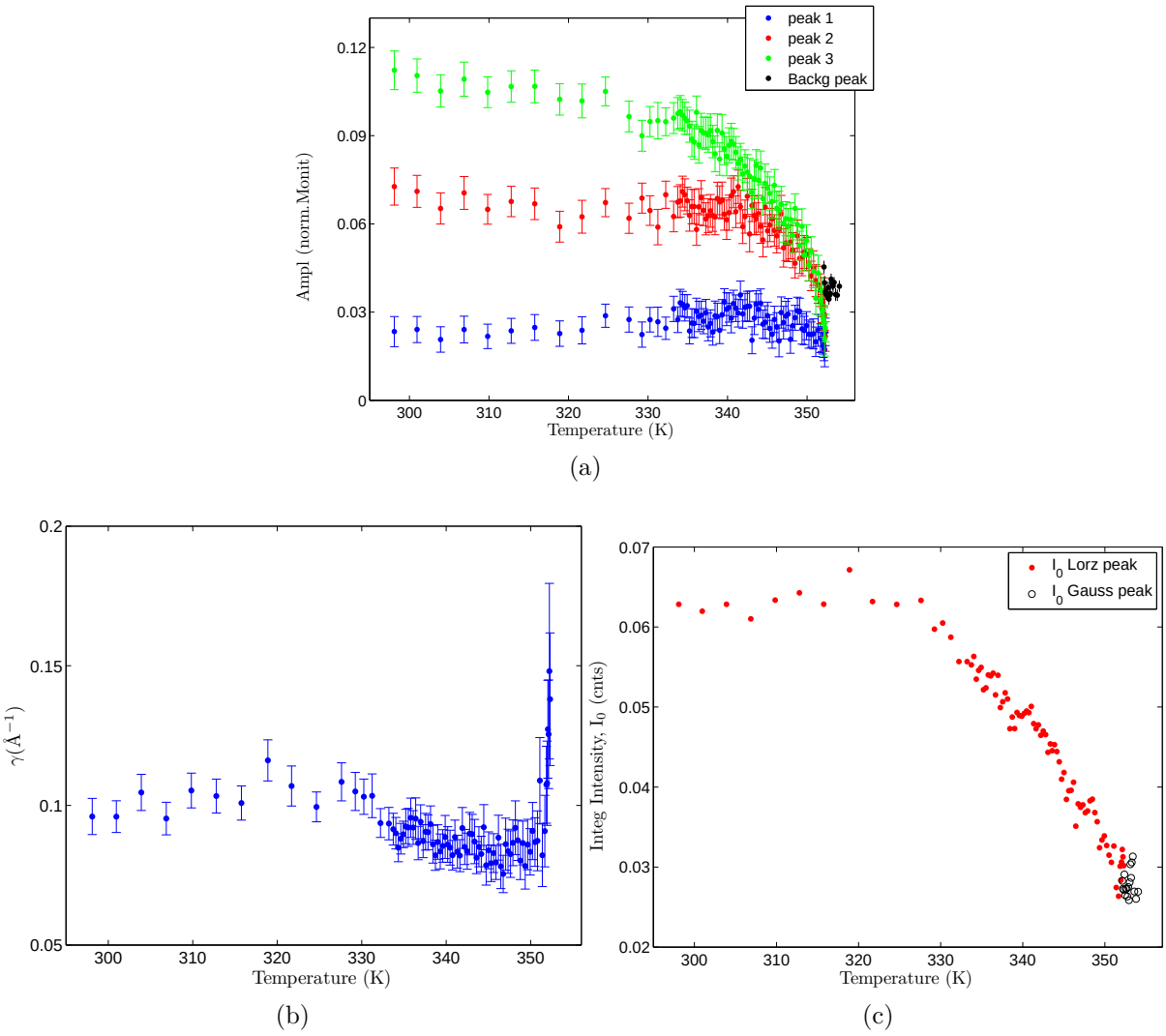

Figure 5.16: Fitted parameters of the three off-axis Bragg peaks. Temperatures from 298 K to 352 were fitted with three Lorentzians, while at the highest temperatures, 352-354 K, the remained intensity was plotted using one Gaussian. The amplitudes of each of the functions are plotted as a function of temperature (a). Peak 1 to 3 are designated with respect to the lowest to the highest Q_H value. Image (b) shows the Lorentzian width (γ); Figure (c) shows the integrated intensity I_0 for the three Lorentzians as function of temperature (red), and that for the Gaussian (black).

From Figure 5.16-(a) the amplitudes start to decrease at a different temperature: 350 K for *peak* 1, 340 K for *peak* 2 and 335 K for *peak* 3. The integrated intensity over the three peaks I_0 drops at 330 K, while changes in the width γ do not occur until higher temperature, 350 K. The small decrease of γ between 330 - 345 K could be associated to an annealing effect as seen in the B-form. Large discrepancies between the data and the fit arise at the transition temperatures, so that a proper analysis of the fitting parameters as a function of temperature up and through the melting transition could not be carried

out.

Low-Q data This was not the case of the low-Q Bragg peak. Figure 5.17 illustrates the evolution of the fit parameters of low-Q A-form DNA, where instrumental resolution was included in the fit. The examination of this figure reveals the following results:

1. In the 300 to 333 K temperature range the width and integrated intensity are essentially constant. The integrated intensity starts to drop at 330 K, while the width stays stable up to temperatures higher than 350K.

2. The integrated intensity of the Bragg peaks shows a progressive decrease within a temperature range of about 20 K. At around 355K the integrated intensity is at its minimum, and it is at that temperature when the width increases abruptly.

3. The increase of the integrated intensity at the highest temperature is an artefact of the poor quality of the fits at those temperatures, as shown by the error bars.

4. We discussed that the drastic drop of the intensity of the B-form Bragg peak is associated to a loss of the fibre structure, which collapses before the transition has completed. On the contrary, for the A-form the broader temperature range of the transition is what is expected from natural DNA denaturation. The collapse of the fibre structure occurs at much higher temperature, so that the last stage of the transition is dominated by the loss of order along the DNA molecule. The effects of temperature in the fitting parameters can be monitored throughout the transition temperature. Optic microscopy measurements clarified the interpretation of the results, and will be discussed in the next section.

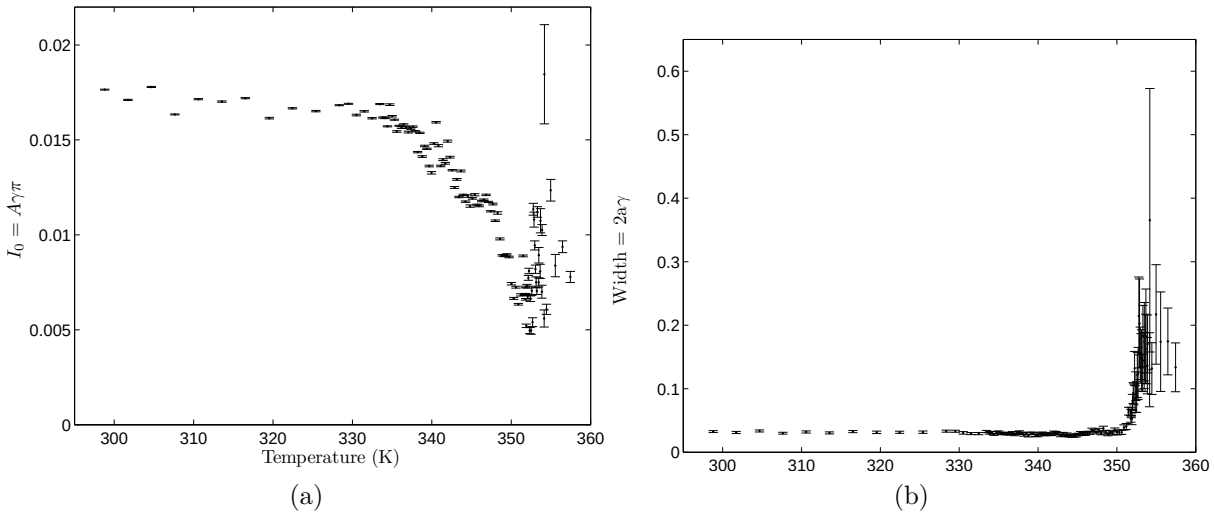

Figure 5.17: Fit parameters as a function of temperature for the low-Q Bragg peak: the integrated intensity I_0 (a), and the Lorentzian width = $2a\gamma$ (b).

5.5 Complementary techniques to study thermal denaturation

5.5.1 Optic Microscopy

Optical microscopy observations provide information about the fibre structure of the film, and how it changes as it is heated until the denaturation temperature is reached. The neutron scattering results of the melting transition for B- and A-form were not fully understood, but it was suspected, as discussed in previous section, that some differences in the melting profiles of both conformation could lie in the fibre properties rather than the experimental parameters. Studying the macroscopic changes in the fibre during the melting transition can give information by inference about the microscopic behaviour. This is why we carried out optical observations of the film melting.

Experimental Method

This experiment consisted of a qualitative study of the melting character of the fibre structure for the two different DNA conformation: "impure" A-form Na-DNA humidified at 56% RH and B-form Li-DNA humidified at 75% RH.

Each film was exposed to the indicated relative humidity 3 days prior to their optic

microscopy measurements. Each sample was extracted from its humidity chamber and sealed between two glass plates to conserve the water content, while it was heated on a copper base below an optical microscope. The temperature was increased at a rate of about 5 K/min. The melting behaviour of each film was recorded from the top, while pictures at the different temperatures were taken.

Results

Figure 5.18 and Figure 5.19 show the fibre structure of an A- and B- form DNA samples at two different temperatures: well below the transition, and after the transition. The images show that at very high temperatures, once DNA melting is completed, as seen from calorimetry data, the fibre environment of the sample has been considerably damaged in the B-form, compared to that of the A-form. On the contrary, for the A-form DNA samples, raising the temperature seems to have a smoothing effect in the macroscopic structure of the fibres. Due to the differences of the technique with respect to neutrons or calorimetric observations, the transition temperature cannot be quantitatively compared.

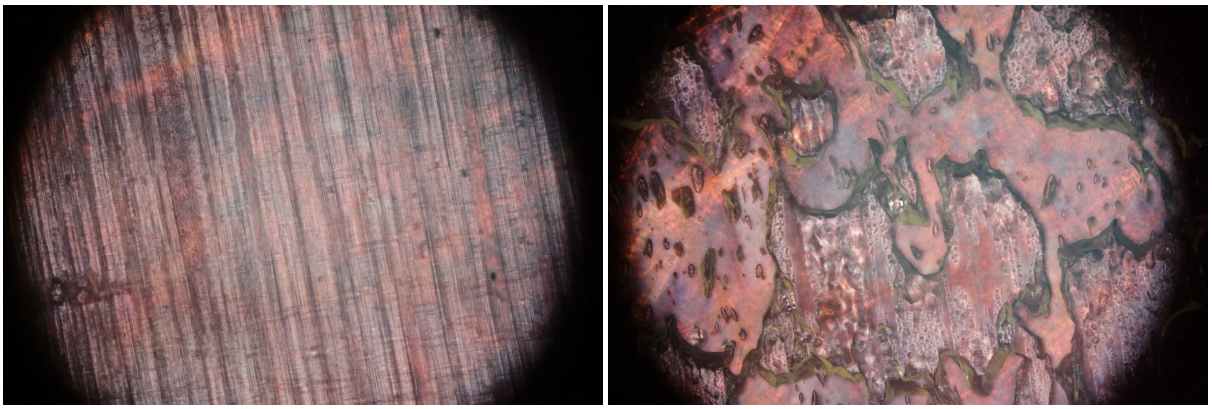

Figure 5.18: Optic microscopy observation of a piece of a B-form Li-DNA film, at 297.5 K (left) and 371.5 K (right).

B-form

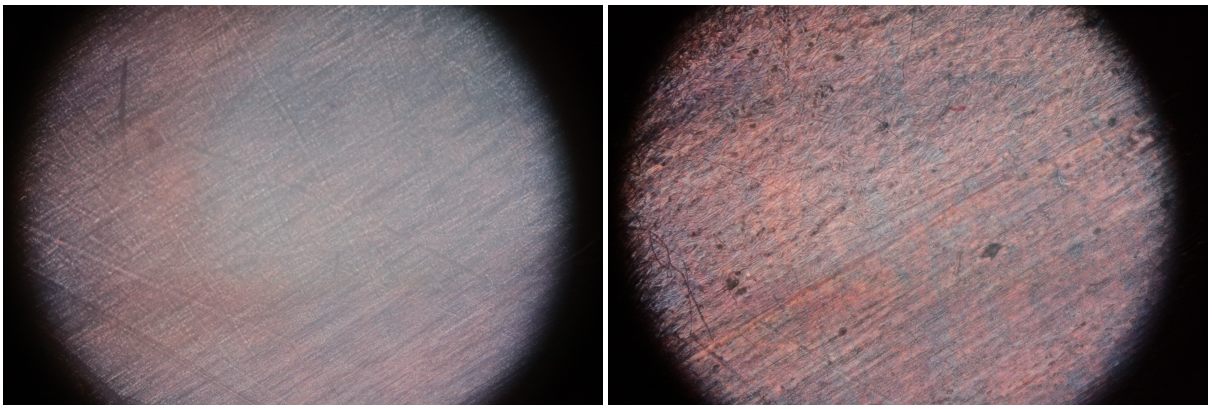

Figure 5.19: Optic microscopy observation of a piece of an A-form DNA film, at 314 K (left) and 367.9 K (right).

A-form

5.5.2 Electrophoresis

By running a gel electrophoresis experiment one can determine the length of the DNA molecules of the solution used to prepare the films. This is important when studying the effects of the thermal denaturation of DNA in the original molecules.

Experimental method

A small piece of a Li-DNA sample (0.01 g taken before and after heating in the neutron scattering experiment) was dissolved in water. The solution was used to run a standard gel electrophoresis experiment, using a 1% nondenaturing agarose gel and staining with ethidium bromide. Comparisons with DNA mass ladders were used to measure the length of the DNA fragments in the sample. A similar experiment was performed with the solution used to prepare the DNA fibres to probe the state of the DNA molecules prior to any treatment.

Results

Gel electrophoresis shows that the length of DNA molecules in the solution of a Li-DNA, or in a dissolved piece of film which was not heated, is of the order of 20 kb or larger. This suggest that the molar mass given by the DNA provider (2000 base pairs) [69] is underestimated. However, the same measurements performed on a piece of film which

was heated up to DNA denaturation and film collapse, and subsequently cooled to room temperature, only detects DNA fragments of a few hundreds of bases, indicating that the molecules have been chopped in the thermal cycle.

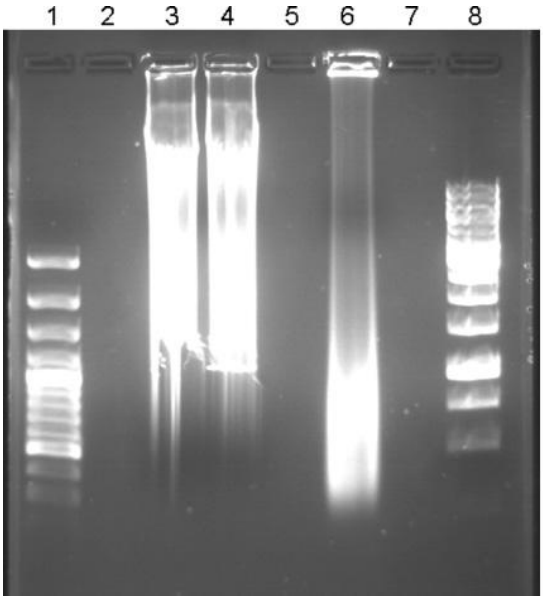

Figure 5.20: Gel electrophoresis image showing the length of the molecules before and after heating of the film. From left to right: DNA mass ladder SM0321 (100-3000 base pairs, lane 1); solution used to prepare the DNA film (lane 3); solution prepared from a piece of film that was not heated (lane 4); solution prepared from a piece of film after heating (lane 6); DNA mass ladder SM0311 (250-10000 base pairs, lane 8). Lanes 2, 5 and 7 were not used.

5.6 Theoretical Analysis of experimental data

A theoretical analysis was completed for the neutron scattering data of the B-form DNA. In the case of the A-form, only preliminary analysis were carried out, the added complexity of the system demands a more rigourous examination, which will take some time.

The theoretical model consists of two steps: first, a theoretical calculation of the structure factor of 1-D lattice including some disorder in the parameters, due to effects in the DNA sequence and thermal fluctuations; second, a statistical physics theory of DNA denaturation using the PBD model to obtain the average size of the closed regions at temperature T.

5.6.1 Structure Factor of a closed DNA segment

The sample is described by the structure factor of a long 1-D DNA chain made of consecutive M closed base pairs. The structural deviation parameter to account for sequence effects is given in both directions, longitudinal $\sigma_{\parallel}$ and transversal $\sigma_{\perp}$ to the molecule. The former is defined from the deviation of the average distance, a, between successive sites, jth and $(j+1)th$; where the equilibrium position between two sites in the chain, m and n, differ by $(m-n)a + \sum_{j=N+1}^{m} \sigma_{\parallel,j}$. The structural disorder in the transverse direction is similarly expressed, the deviation is defined from the transversal distance between consecutive sites. Figure 5.21 gives a representation of the system, where the sites in the equilibrium position have been symbolised with light-blue squares, and their actual positions with a darker blue. The disorder parameters in the two directions are also represented.

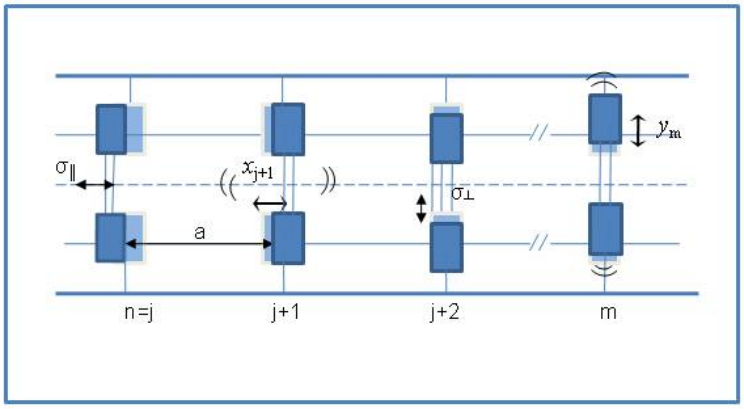

Figure 5.21: Cartoon representing the following elements of the model: a DNA chain made of M closed base pairs; the longitudinal and transverse structural deviation parameters, $\sigma_{\parallel}$ and $\sigma_{\perp}$; and the longitudinal and transverse displacements, x and y.

The structure factor of such a finite chain segment is given by,

$$S_M(\mathbf{Q}) = \frac{1}{M} \sum_{m,n=1}^{M} e^{iQ_{\parallel}a(m-n)} \langle e^{i\sum_{j=n+1}^{m}(Q_{\parallel}\sigma_{\parallel,j}+Q_{\perp}\sigma_{\perp,j})} \rangle \tag{5.8}$$

$$\times \quad \langle e^{iQ_{\parallel}(x_m-x_n)+iQ_{\perp}(y_m-y_n)} \rangle, \tag{5.9}$$

where x_m and y_m represent, respectively, the longitudinal and transverse displacements of the mth site from its position at thermal equilibrium, and $\mathbf{Q}$ is the scattering vector, having the component $Q_\parallel$ along the helical axis and $Q_\perp$ orthogonal to it. The first term in the angle braces corresponds to the average effect of the structural disorder, and the second to thermal motion. Equation 5.9 is a generalisation of the profile for a 1D paracrystal of finite size [83]. A simplified form of this equation can be obtained by making the following assumptions:

1. The structural disorder can be characterised by Gaussian displacement, along and perpendicular to the helical axis $\sigma_{\parallel,\perp}$. These values can be obtained from conformational analysis: $\langle\sigma_\parallel^2\rangle^{1/2} = 0.18$ Å; and $\langle\sigma_\perp^2\rangle^{1/2} = 0.55$ Å [84].

2. Whether the transversal and longitudinal structural disorder parameter are correlated is determined by the parameter χ. Values of $\chi = 0$ for uncorrelated or $\chi \neq 0$ were explored in the calculations.

3. The thermal fluctuations are described by the $\kappa_{\parallel,\perp}$ terms. Along the molecule, $\kappa_\parallel$ is defined by the Debye Waller correction at any temperature T, $\kappa_\parallel^2 = k_B T/\mu c_0 a^2$, where $\mu = 618$ a.m.u is the total DNA mass per base pair; $c_0 = 2830$ m/s is the speed of sound [65]; and k_B is the Boltzmann constant.

Giving rise to,

$$S_M(\mathbf{Q}) = M + 2\sum_{n=1}^{M-1}(M-n)cos(Q_\parallel na)e^{-n\triangle}, \tag{5.10}$$

where

$$2\triangle = Q_\parallel^2(\langle{\sigma_\parallel}^2\rangle + \langle{\kappa_\parallel}^2\rangle) + Q_\perp(\langle{\sigma_\perp}^2\rangle + \langle\kappa_\perp^2\rangle) + 2Q_\parallel Q_\perp\chi(\langle\sigma_\perp^2\rangle\langle{\sigma_\parallel}^2\rangle)^{1/2}. \tag{5.11}$$

5.6.2 Statistical physics of the closed regions of DNA

Henceforth, in order to obtain a more realistic structure factor calculation for the sample, the probability of having a closed cluster of size m at a given temperature $P(m)$ needs to be incorporated, and then the total structure factor must combine all the possible sizes

of the cluster.

$$S(\mathbf{Q}) = \sum_{m=1}^{\infty} P(m) S_m(\mathbf{Q}), \tag{5.12}$$

where S_m is given by equation 5.10, and the size of the DNA molecule has been extrapolated to infinity.

The statistical physics of these m sites are developed via the PBD model, in which the size distribution of the closed segments is analysed. The model can be applied to short (few hundred base pairs) or genomic DNA with no free parameters, as they are established from the sequence information. These are necessary to describe the DNA molecule of N base pairs in terms of the Hamiltonian,

$$H_y = \sum_{j=1}^{N-1} W(y_j, y_{j+1}) + \sum_{j=1}^{N} V_j(y_j), \tag{5.13}$$

The configurational energy is composed of two terms: an anharmonic potential describing the stacking interaction $W(y_j, y_{j+1})$,

$$W(y_j, y_{j+1}) = \frac{1}{2} C \left[1 + \rho e^{-b(y_j + y_{j+1})}\right] (y_j - y_{j+1})^2, \tag{5.14}$$

and a Morse potential describing the combined effects of hydrogen-bonding, electrostatic interactions between the charged phosphate groups, and solvent effect on the jth base pair, $V_j(y_j)$,

$$V_j(y_j) = D_j \left[1 - e^{(-\alpha_j y_j)}\right]. \tag{5.15}$$

Both the stacking interactions W and the the intrapair potential V are affected by the sequence of bases. However, for long DNA chain (thousands base pairs) the sequence effects can be incorporated into the intrapair potential only, reproducing accurately the melting curves. And hence, the stacking interaction is considered homogeneous. The parameter y_j represents the stretching of the jth base pair, due to the transverse displacements of the bases; to provide a more complete definition of a closed base pair, it is defined within $y_j < y_c$, where y_c is a reference stretching chosen to be 1.5 Å.

The statistical weight Z can be calculated within stretching limits, i.e. for opened base pairs ($y_c < y_j < +\infty$), or closed base pairs ($-\infty < y_j < y_c$), defining different con-

figurations of the molecule at a given temperature T. It is expressed in terms of the Hamiltonian. Hence, this allows the calculation of the probability $\mathcal{P}(m,i)$ that m adjacent sites, starting at site i, are closed. Furthermore, for a specific configuration of a closed region with open ends, existing at site i, the probability is given as $P(m,i)$, from which the probability of having a closed cluster of size m in a DNA segment of N_0 base pairs is simply,

$$P(m) = \frac{1}{N_0}\sum_{i=1}^{N_0} P(m,i). \tag{5.16}$$

And the average size of a cluster of closed base pairs is then,

$$l_c = \frac{\sum mP(m)}{\sum P(m)} = \frac{h}{1-h-P_0}, \tag{5.17}$$

where h is the helix fraction and P_0 is the statistical weight of two consecutive bases being in the closed state.

In practice $P(m,i)$ is computed up to clusters M of $\sim 10^2$ base pairs, while natural DNA contains $\sim 10^6$ base pairs. It has been shown that $P(m)$ can be scaled exponentially with m by $P(m > M) = P_0\zeta^m$ [85], so that the calculation of $S(\mathbf{Q})$ in equation 5.12 becomes,

$$S(\mathbf{Q}) = \sum_{m=1}^{M} P(m)S_m(\mathbf{Q}) + \sum_{m=M}^{M_0} P_0\zeta^m S_m(\mathbf{Q}) + \mathcal{S}'(\mathbf{Q})P_0\zeta^{M_0+1}\left[\frac{M_0}{1-\zeta} + \frac{1}{(1-\zeta)^2}\right], \tag{5.18}$$

where typically $M = 150$ and $M_0 = 1000$. Equation 5.10 can be expressed by a limiting case where $m \to \infty$, for sufficiently large clusters,

$$lim_{m\to\infty}[S_m(\mathbf{Q})/m] \approx \mathcal{S}'(\mathbf{Q}) = \frac{sinh\triangle}{cosh\triangle - cos(Q_\parallel a)}. \tag{5.19}$$

and hence this approximation can be used to compute the third term in equation 5.18. The sum includes 3 points: from 1 to M the exact value of $P(m)$ is used; then from M to M_0 the exponential extrapolation of $P(m)$ but still the full expression of $S(\mathbf{Q})$ are considered; and finally the third contribution is an analytical evaluation of the sum up to infinity, using the exponential extrapolation of $P(m)$ and an approximate expression for $S_m(\mathbf{Q})$.

The same method can be used to compute the average cluster size l_c (equation 5.17).

The final step is to fit the structure factor with the same Lorentzian expression as the one used to analyse experimental data to determine the integrated intensity I_0 and width (Γ or γ) of the diffraction peak (equations 5.2 and 5.3).

5.6.3 Model Parameters

To analyse the neutron scattering experiments, in principle, we would need to know the base-pair sequence of the sample. As the experiment requires a significant amount of sample, it can only be performed with natural DNA. The salmon testes DNA that we use is provided without its sequence [69], and even its GC content is only approximately known. It is estimated to be 41.2%. The theoretical analysis has been tested on different DNA sequences from the genome of Danio rerio (zebrafish)[74] and Pyrococcus abyssi [74],[86]. The results presented were obtained with a sequence of 280 000 bases, part of the full genome of Pyrococcus abyssi, chosen based on the B-form results as the theoretical analysis was first developed for this form. This sequence was used as it gave the closest denaturation profile as that measured by DSC. The GC content of this fragment is 44.08%. Model parameters were obtained from an extensive study of DNA denaturation in various sequences [87], which determined a set of parameters allowing the prediction of melting curves of various DNA sequences to a good accuracy.

Model Parameters	Values for B-form	Values for A-form (attempt 1)/(attempt 2)
C (eV/Å^2)	0.00045	0.0009 / 0.00025
ρ	50	50 / 30
b (Å^{-1})	0.2	0.50 / 0.2
α_{AT} (Å^{-1})	4.2	4.2
α_{GC} (Å^{-1})	6.9	6.9
D_{AT} (eV)	0.12905	0.11244
D_{GC} (eV)	0.16805	0.14666
a (Å)	3.36	2.545

Table 5.4: Model parameters used for the theoretical analysis of the melting transition of B- and A-form DNA.

Figure 5.22 shows the theoretical curves for B- and A-form. For the latter, values of ρ=50 and b=0.5 were used.

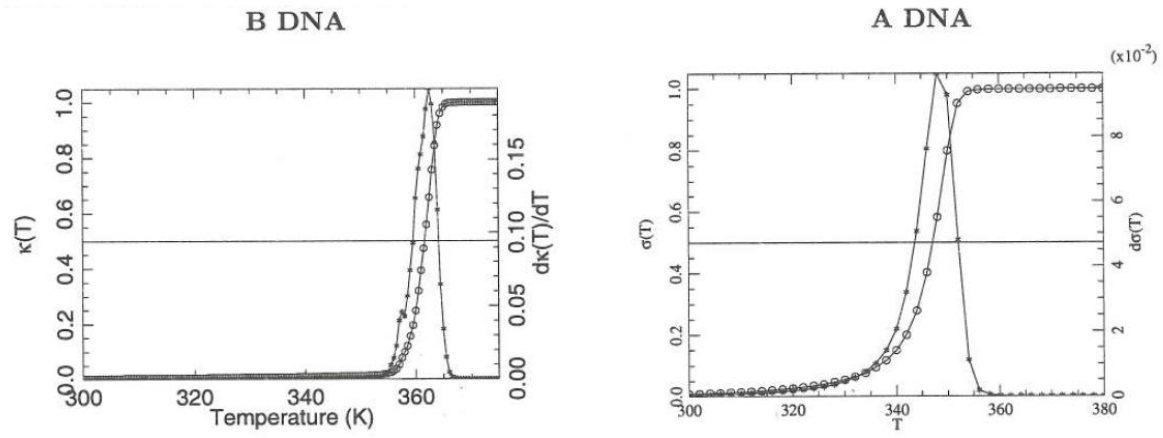

Figure 5.22: Theoretical results. Melting curve of a reference DNA segment of 280 000 base pairs, part of the genome of Pyrococcus abyssi: circles show the fraction of open base pairs versus temperature, and stars correspond to its derivative to get the melting profile. The B- and A- melting curves differ in the parameters: ρ =50, b=0.18 and C=0.00045 (a); and ρ =50, b=0.5 and C=0.0009.

5.6.4 Results

B-form

As the actual melting temperature is very sensitive to experimental parameters, such as ionicity and hydration. The comparison between theory and experiment was done with a reduced temperature $\theta = T/T_c$, where T_c is defined as when 50% of the base pairs are open.

Figure 5.23 provides a comparison between theoretical (curves) and experimental (points) results. The theoretical analysis (curves) show the variation versus temperature of the integrated intensities and widths of the Bragg peaks in scans 1 and 2. As expected, the intensity shows a sharp drop near the denaturation transition. It reflects the openings of the base pairs that break the clusters of stacked pairs, and therefore reduces the number of scattering sites. As a result, the integrated intensity of the peak almost provides a quantitative measure of the helix fraction of DNA because, as shown by equation 5.18, for sufficiently large clusters, the structure factor is proportional to the number of sites in a cluster. Moreover, the curve shows that the size of the clusters drops significantly only in the last stage of denaturation. Theory and experiment are very well matched until $\theta \approx 1$, in particular, for the integrated intensities where the agreement is almost perfect. The intensities are almost constant with increasing temperature until $\theta \approx 0.97$, due to there being a very low fraction of open base pairs in this temperature range.

There are no free parameters in the calculation of the widths for scan 1, where $Q_\perp = 0$. While scan 2, with $Q_\perp \neq 0$, require the introduction of χ. They provide the spatial information and it is strongly sensitive to the distribution of the sizes of the diffracting clusters. The rise in the average size of open regions in the last stage of the transition (circles in Figure 5.22-a) is reflected in the large increase in the width of the Bragg peak as predicted from theory (solid line in Figure 5.23). For scan 2, with a nonzero transverse component Q_K of the scattering vector, the width of the peak is also affected by the transverse structural disorder due to the effect of the sequence (variables $\sigma_\perp$) and by their correlations with the longitudinal structural disorder (variables $\sigma_\parallel$), measured by the coefficient χ. The statistical properties of $\sigma_\perp$ and $\sigma_\parallel$ have been obtained by conformational analysis [84] but their correlations have not been determined. We show results with $\chi = 0$ (no correlation) and $\chi = 0.35$ corresponding to moderate correlations.

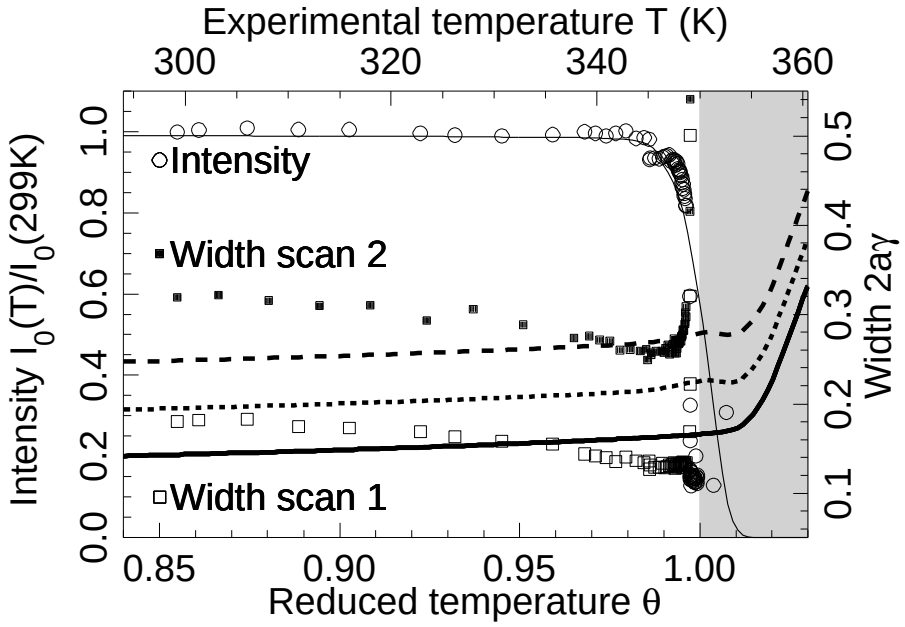

Figure 5.23: Comparison between theory and experiment. Points are experimental results, while curves plot theoretical results. A reduced temperature, $\theta = T/T_c$, is used, where T_c is the temperature at which 50% of the bases are open. Circles show the integrated intensity of the Bragg peak, rescaled to 1 at low temperature. After rescaling, the results for scans 1 and 2 follow exactly the same curve. The thin line is the calculated integrated intensity. Open squares show the experimental width of scan 1 and the thick solid line is the theoretical value for this width. Filled squares show the width of scan 2. The dotted line shows the theoretical width of scan 2 calculated by assuming that the longitudinal and transverse structural disorders due to the sequence, determined by conformational analysis [84], are uncorrelated ($\chi = 0$), while the dashed line is the theoretical width of scan 2 calculated by assuming a partial correlation between the longitudinal and the transverse structural disorders ($\chi = 0.35$). The shaded area shows the temperature range in which the experimental observations are hindered by collapse of the sample film.

A-form DNA

Contrary to the B-DNA case where model parameters could be determined from conformational analysis, our work on A-DNA presents the first melting curve of this form. Therefore the model parameters had not been calibrated earlier and we must estimate them to analyse our results. The results that we present here are only preliminary, but the idea of our approach is to say that the main difference between A and B comes from the stacking interaction. And thus, only the parameters concerning the stacking interaction, particularly ρ, b and C, (see equation 5.14) have been changed to try to get an approximate fit of the experimental data.

Figure 5.24-(a) shows the comparison of using the B-form model parameters on the A-form experimental curves. These parameters do not show agreement with the experimental curves for the A-form, i.e. the DNA melts differently, and moreover the behaviour of the correlation lengths as a function of temperature is also different.

The A-form theoretical curves were obtained from a description of the denaturation transition with two sets of values for ρ, b and C: first attempt with 50, 0.5 and 0.0009 respectively; and second attempt with 30, 0.2 and 0.00025. These results are shown in Figure 5.24-(b) and -(c). The aim of varying these parameters is to obtain a broader transition than for B-DNA, as it can be done by decreasing ρ and/or increasing b. Changes in the well depth of the Morse potential, D_{AT} and D_{GC}, compared to the values used for the B-form were done to get a reasonable transition temperature. The strength of the stacking interaction W can be controlled by the prefactor C, which also changes the value of T_m.

The integrated intensity I_0 is rescaled in the range [0,1] as the experimental intensity does not fall to 0 after melting.

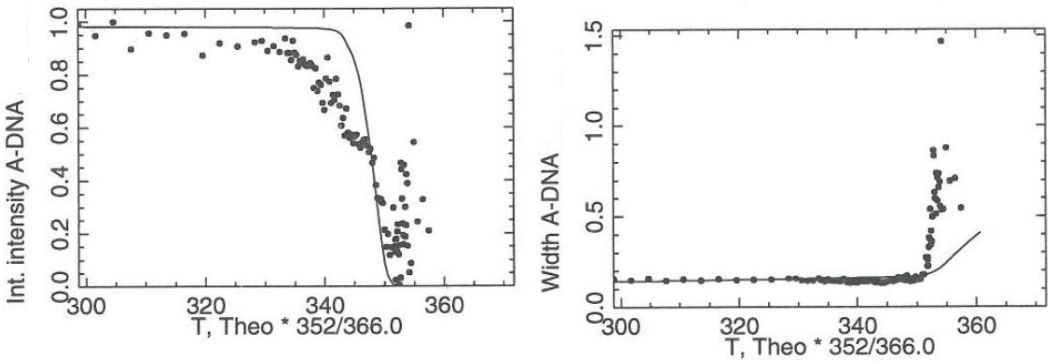

(a) B-form parameter: ρ=50, b=0.2 and C=0.00045

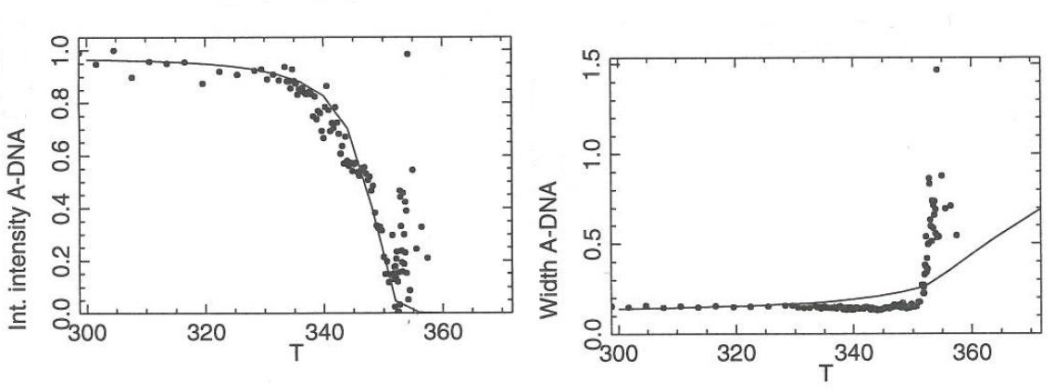

(b) attempt 1:ρ=50, b=0.5 and C=0.0009

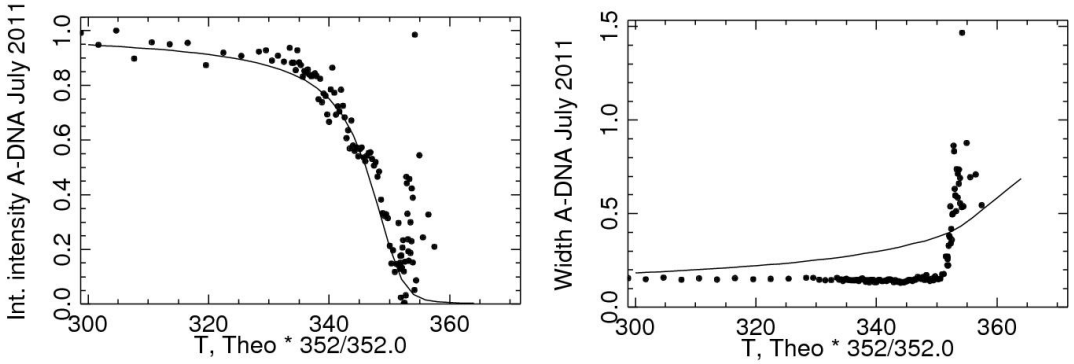

(c) attempt 2:ρ=30, b=0.2 and C=0.00025

Figure 5.24: Comparison between theory (continuous line) and experiment (points) using different values for ρ b and C. Left images correspond to the integrated intensity versus temperature. Right images give the width as a function of temperature. Figure (a) corresponds to the theoretical parameters established to analyse the experimental results of the B-form.

For both attempt 1 and attempt 2 parameters, an acceptable description of the variation of the integrated intensity as a function of temperature is obtained, better than that

showed with the B-form model. Both rely on a change in the base stacking interactions with respect to B DNA, which seems justified as the distance between the base pairs and their relative positions are very different between A and B. However, while the parameters could be considered as equivalent for the intensity, they are not when one considers the width of the peaks. The measured width shows a much more abrupt transition than the theory. Figure (b) gives a much better agreement with experiments, although it is still not perfect.

This shows that recording the denaturation curve (or the intensity) is not sufficient to characterise DNA denaturation. Observing spatial correlations, through the width of the Bragg peaks, brings an important additional information, and allows us to distinguish among theoretical models.

There are probably several reasons for the discrepancies between experimental and theoretical results:

1. The parameters of the model require a better adjustment

2. The structure factor is not adapted to the low-Q peak that we observe, since it is computed for a 1D system which centre is defined at $Q = \frac{2\pi}{a}$, where a is the distance between the particles (base pairs). The low-Q peak is a higher order peak due to a repeated distance of around $5a$.

3. Although the film does not fully melt, there is probably a partial disorientation which could explain the sharp increase in width.

Therefore, the analysis of the experimental data for A-DNA requires further investigations.

5.7 Discussion

Calorimetry data provides an overall macroscopic picture of the melting behaviour of the different studied DNA structures within a fibre environment. The melting curves cannot be attributed only to denaturation of DNA since they are the result of a collective thermodynamical phenomena mainly between DNA denaturing and fibre melting. For that reason obtaining information of the initial and final temperatures, and thus the width, of the melting transition of the entire sample, has been essential for our understanding of

how DNA melts. Complementary information such as the binding enthalpy can contribute to the characterisation of the effects of conformation to the melting behaviour of DNA. Neutron experimental results give two pieces of information: integrated intensity and width of the Bragg peak as a function of temperature. The integrated intensity indicates the number of scatters in the system, and hence it reflects the number of closed base pairs. The shape of the DSC melting curves can be compared with the integrated intensity curve obtained in the neutron experiment since changes in both are strongly driven by increases of the open base pairs.

1. In the case of the B-form, the theoretical model predicts that low fraction of open base pairs are occurring close to the vicinity of the transition at around 347 K. This is consistent with the temperature at which the rise of the endothermic calorimetric peak and the decrease of the integrated intensity. Although, the calorimetric and neutron experiments were carried out on a B-form humidified at 75% RH, the samples were prepared under different conditions (salt concentration), which needs to be taking into account when comparing T_m, the mid point of the transition. Moreover, both experimental techniques are sensitive to different phenomena and thus this can have an effect to the temperature at which the transition is completed. The endothermic processes occurring during the melting of the DNA sample are completed at around 368 K, as shown in the DSC curve; while, the Bragg peak intensity shows a discontinuous drop at 349 K. It is not surprising that the DSC melting curve is broader as it does not only consider DNA melting, which ultimately neutrons are only sensitive to, but bulk thermal effects of the film. From the neutron experiment, the complete loss of the intensity of the Bragg peak suggests two possible scenarios: the first one considers that there are no longer closed regions in the sample, and hence DNA has completely denatured; while in the second scenario, the remained closed regions are no longer highly oriented along the molecular axis, but they are part of a disoriented and flexible segments immersed in a quasi-liquid state. As shown in Figure 5.23, the theoretical curve follows the experimental decay of the intensity until the immediate vicinity of the transition. This discrepancy is a sign that another phenomenon, not included in the theoretical description, could have occurred, which then corroborates the second scenario. We believe that at higher temperatures the sample is no longer a good approximation of a one-dimensional

crystal but is more an ensemble of disoriented, short-length DNA. This phenomenon is also referred to as "collapsing" of the film, and it is indicated in Figure 5.23 by the shaded area. It is also included in the DSC melting curve.

2. For the A-form DNA, the raise in the endothermic peak and the descent of the integrated intensity occur at the same temperature, and within the same temperature range 334 K to 354 K. Furthermore, the theoretical melting curve obtained using modified values for the anharmonic potential W with respect to those used for the B-form, is consistent with the calorimetric observations. The Bragg peak integrated intensity does not fall abruptly as it does in the B-form DNA. Besides the difference in the molecular structure between B- and A-form, the intermolecular arrangement of the molecules within the fibre also differs for both forms. The combination of these factors is responsible for the dependence of DNA melting on the conformation of the samples. The A-form sample appears as a more crystalline and less hydrated form than the B-form. The proximity of the molecules results in a strong confinement which introduces local energy barrier for inter-molecular motions. Under this confinement we expect that even if the single strands DNA gain flexibility, they will be subjugated to strong effective forces between molecules moderated by the Na ions. The evolution of the average size of the open regions within this scenario does not provide enough freedom to the rigid double-helix segments to allow them to lose their spatial orientation. The shape of the width suggests that the closed regions stay large until the last stage of the denaturation which is where the theoretical attempts shown in Figure 5.24, present inconsistencies with the experimental results.

Optical observations support our hypothesis. The evolution of the images of the B-form sample during heating indicates that, at high temperatures, the film itself shows a considerable damage, or "collapse", characterised by a disorganisation of the oriented fibre structure. While in the A-form DNA the film seems to maintain its structure even at temperatures higher than the transition.

How does the correlation length evolve as a function of temperature for the different DNA structures? As discussed in the introduction, this can only be answered by studying the evolution of the width of the Bragg peak as a function of temperature.

1. For the B-form, the two measured scans provide different pieces of information

about the correlation along the molecule with (Q_H,Q_K=0) (scan 1), and between the longitudinal and the transverse structures (Q_H,$Q_K \neq 0$) (scan 2). For scan 1, the width of the peak is remarkably constant until 350 K and the collapse of the film. Theory predicts that the domination of the base-pair openings at θ=T/T$_c$=0.98, is responsible for the sharp increase of the open cluster fraction until denaturation has occurred, Figure 5.22-(a). In the case of scan 2, the transverse component introduces the correlation between the longitudinal and transverse structural disorder due to sequence. The experimental width increases significantly in the range $0.99 < \theta < 1$, which was not predicted by the theory. For that reason and to be consistent with our melting scenario in the B-form, we attribute this behaviour to the misalignment of the molecules. It is very likely that the collapse of the film is preceded by increased fluctuations in the orientation of the helix fragments. We expect that this would have a stronger influence on the width of the Bragg peak in scan 2 than in scan 1 since it includes a transversal component. In resume, the PBD model successfully describes the experimental results up to the collapsing of the film with only one free parameter, χ.

2. For the A-form. Recall that the scan of the low-Q Bragg has a transverse component, so that the same principles are applied as for scan 2 in the B-form. The theoretical attempts to fit the experimental curve were not yet successful. A significant increase in the width is detected only in the vicinity of the transition, where the integrated intensity has almost vanished. Again, contrary to the B-form, the curve proves that in the A-form the film has not collapsed, but it will probably occur at a higher temperature.

There is an aspect that has not been discussed yet. The electrophoresis analysis of the length of DNA fragments in the film before and after heating, indicate that, after film melting, the DNA molecules that were more than 20,000 base pairs long at low temperature are chopped into segments of a few hundreds of base pairs. We believe that these regions are entangled in a viscous state, in which the lack of space have prevented their unstacking, even if the hydrogen bonds are broken, and thus not all the enthalpy expected is recovered. This phenomenon could be responsible for the "missing" value of the transition thermodynamical quantities in DNA films compared to those in DNA in solution. These values are also lower for the A-form than for the B-form, this is coherent with our

discussion, since the increase of water and/or the reduced size of Li^+ over Na^+, liberates space between the molecules and gives them more flexibility.

It can be concluded from these results that DNA denaturation in a fibre sample is very dependent on the DNA conformation, whether it is in a crystalline A- or semicrystalline B-form, and hydration. The fibre environment contributes to maintain the orientation of the molecules along the molecular axis, which seems to be enhanced in the A-form. Complete melting DNA in a fibre medium is probably more possible in highly hydrated (92% RH) B-form Li-DNA, than in crystalline (56% RH) A-form Na-DNA. Nevertheless, the complete observation of DNA melting in the B-form is obstructed by the film collapsing.

Chapter 6

Glass Transition in denatured DNA

6.1 Foreword

This chapter describes the glassy properties of films of oriented DNA fibres heated above the thermal denaturation temperature using Differential Scanning Calorimetry.

6.2 Introduction

The loss of the double helical structure of DNA as a consequence of thermal denaturation has a strong effect of the whole structure of the fibres and films. While DNA is fairly rigid in its double helix form, when the two single strands dissociate after denaturation they become very flexible, with persistence lengths of the order of 10 Å, 50 times smaller than that in a double helix form. At high temperature this leads to a sample in which the strands are fully disordered and entangled, in a quasi-liquid state.

A glass transition is a phase change in which an amorphous system on rapid cooling undergoes a transition from liquid (equilibrium) to glass (non-equilibrium) without being able to crystalise. As the temperature of an homogeneous vitreous system in a liquid state is lowered, the system experiences thermal heterogeneities due to its disordered nature; their inter and intramolecular motions become too slow to be detectable experimentally. The liquid is impeded from reaching structural equilibrium described by a relaxation time parameter τ_{sys}. Its conformational modes are understood to be kinetically frozen. For DNA films, even though the stacking of the base pairs is broken, the intermolecular confinement is still present and influences the relaxations in the glassy state. The transition

is observed within a temperature interval centred at a characteristic temperature, called glass temperature T_g, at which relaxation time of the system becomes of the same order as the observation time. In the glassy region the non-equilibrium state evolves towards equilibrium by structural relaxation (aging). In cooling this is too slow to be detected experimentally. During aging or slow cooling the system evolves towards metastable states with lower and lower enthalpy. Conversely, when the system is heated up after aging, it can absorb the corresponding enthalpy, which shows up as a peak in the heat capacity.

The rate of temperature variation defines the timescales at which the system is allowed to change. The dependence of the glass transition temperature on the cooling rate can be described by the limiting fictive temperature, T'_f [88]. It is the frozen value of the so-called "fictive temperature" defined long ago by Tool and co-workers [89]. The fictive temperature can be defined as the temperature at which a property p of a system in a glass state is extrapolated to intersect the liquid line. It has become a useful quantity to investigate the phenomenology of the glass transition, but discussions about its physical significance are still a current issue [90]. In general, the glass transition of non-crystalline materials and soft matter, studied for decades, is still an open problem. There are numerous approaches dealing with the glass transition process. Some are rather based on microscopic models, such as the Adam-Gibbs theory [91]. These theories start from the microscopic or molecular structures of the glass-former, and they attempt to explain at this fundamental level why certain liquids crystallise while others fail and become glassy. Another angle of attack proceeds rather by macroscopic approaches dealing with thermodynamics and the phenomenology of the glass transition process, an example of this is the Tool-Narayanaswamy-Moynihan (TNM) model [92].

The glass character of DNA have been studied previously. Tsereteli's group [60] presented many published reports in the glass character of DNA in solution. Observations of the glassy behaviour in fibres were made [78] but the relaxation character of these glass-like systems was never quantitatively analysed.

In this chapter, we report a detailed calorimetric study of the glassy behaviour of films made from DNA fibres. We show that after the first irreversible thermal denaturation of the molecules when the sample is reiteratively heated, it reaches a disordered state in which it shows a typical glass behaviour during successive cooling and heating scans. Our investigation of the relaxation of melted DNA as a glass includes: the determination

of the activation enthalpy by means of the fictive temperature obtained after cooling at different rates; and access of its recovery enthalpy (as well as fictive temperature) after aging. A direct comparison of the before-mentioned glass properties between DNA and the well-known polyvinyl acetate (PVAc) glassy polymer [93] will also be presented for better understanding. This study shows that glasses can be obtained directly and easily from fibres of oriented DNA macromolecules.

6.3 Theory of the glass transition

The kinetics of a liquid are expressed as the combination of molecular vibrations and structural relaxations. The latter is strongly dependent on temperature and inversely proportional to viscosity. Generally, glasses are better understood when their properties are defined relative to equilibrium liquids. The relaxation time can be used to describe the three different regions:

1. In liquids the relaxation processes occurs very quickly, in which the relaxation time τ_{liq} is shorter than the observation time t_{obs}.

2. At the glass transition, $\tau_{sys} = t_{obs}$, the relaxation properties of the non-equilibrium state become detectable.

3. When the system has become a glass, it takes longer for the non-equilibrated system to relax. The process timescales are much longer than the maximum time accessible to the observation, $\tau_{sys} \gg t_{obs}$.

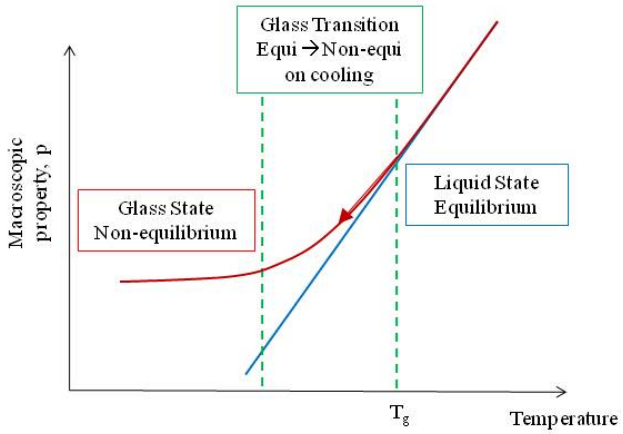

Figure 6.1: Diagram of the thermodynamic property as a function of temperature of a liquid-glass state.

When the equilibrium can no longer be reached, the molecules enter the glass region where they mainly experience vibrational motions. The higher viscosity of this region compared to that of the liquid state limits the structural relaxation. As can be seen from Figure 6.1, the departure of the property p of the system from liquid equilibrium to non-equilibrium state is commonly defined by a glass transition temperature, T_g or more phenomenologically by a fictive temperature T_f.

The geometrical description of T_f in terms of a macroscopic property p is given in Figure 6.2. Both cooling and the subsequent heating path have been represented. When a system is cooled down, T_f corresponds to the temperature of intersection between a curve of slope α_g, where $\alpha_g = \frac{dp}{dT}$ is the slope of the p_a curve in the glassy state, extrapolated from any point in the non-equilibrium p curve to intersect the equilibrium liquid curve. From the figure, T_{fa} corresponds to the fictive temperature at a point a. If the system is further cooled, it will reach the glass state curve at T^*, where the intersection with the liquid line is given by a limiting value of the fictive temperature, T'_f.

In heating from the low temperature T^*, the property p of the system attempts to rejoin the liquid equilibrium line at higher temperatures through a different path than in cooling.

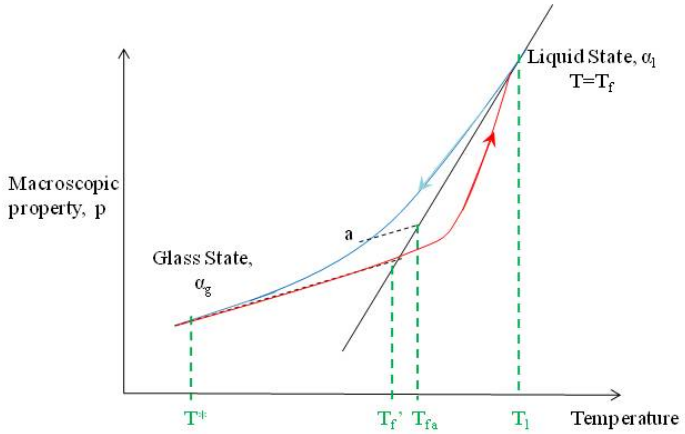

Figure 6.2: Representation of the cooling and subsequent heating curves of a glass system in terms of property p *vs* temperature. The fictive temperature and limiting fictive temperature has been also marked.

where T_l is a temperature in the domain of the liquid state.

From the cooling cycle in figure 6.2 it can be shown a simple mathematical relation between the property p of a system in the glassy state, $p(T^*)$, and that of the liquid equilibrated at T_f, $p(T_f)$,

$$p(T*) = p(T_l) - \alpha_l(T_l - T_f) - \alpha_g(T_f - T*). \tag{6.1}$$

For each cooling rate β_n, all the states of the glass will have one value of T'_{fn} below the glass transition region, which is a characteristic feature of the thermal history of the sample, as shown in Figure 6.3.

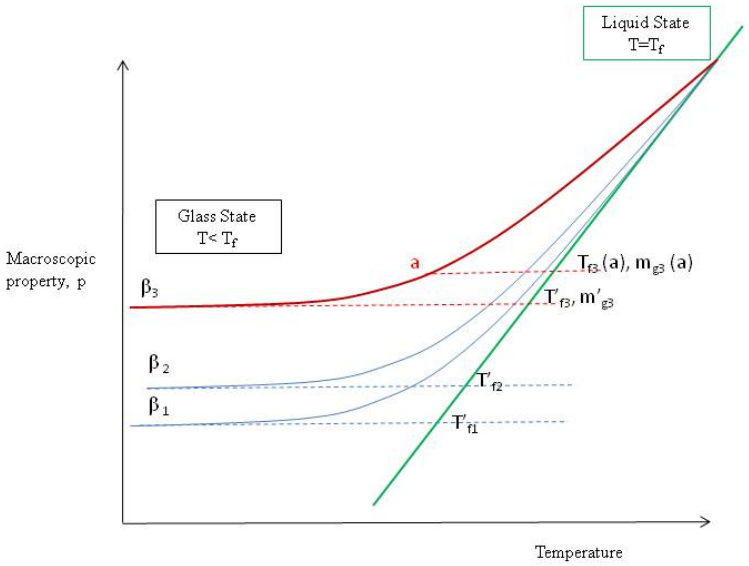

Figure 6.3: Schematic of glass curves at different cooling rates, β_n, with the correspondent T'_{fn}.

This concept implies that the glassy state can be described by a single parameter, which depends on a particular property p, such as enthalpy. In this particular case, it follows from equation 6.1 that the corresponding limiting fictive temperature can be obtained from the relation,

$$\int_{T*}^{T_l}(Cp - Cp_g)dT = \int_{T_{f'}}^{T_l}(Cp_l - Cp_g)dT, \tag{6.2}$$

where T_l and T* are the limits of integration defined at positions in the liquid (l) and glass (g) region further from the transition, and C_p is the specific heat.

Structural relaxation is usually described by the evolution of order parameters towards equilibrium. The Tool-Narayanaswamy-Moynihan (TNM) model is based on a simplified model to describe the relaxation time associated with each order parameter, τ_i, having the same temperature dependence. This is known as "temperature-independent spectrum of relaxation times" [88],[94]. Equation 6.3 gives the mathematical expression for τ_i,

$$\tau_i = A_i \exp(\frac{\triangle h}{RT}x + \frac{\triangle h}{RT_f}(1-x)) \text{ for } 0 \leq x \leq 1, \tag{6.3}$$

where $\triangle h$, A_i and x are constants, and R is the ideal gas constant. More properly: x is the fraction of the degree of freedom or modes in equilibrium, while $(1-x)$ is the fraction of the degrees of freedom in non-equilibrium; the activation enthalpy, $\triangle h$, defines

the barrier height that the system has to overcome for relaxation; and A_i is defined for each order parameter. The first term relates to an Arrhenius behaviour and the second introduces a T_f dependence.

Physically this is understood in the following way: below the glass transition the system relaxes slowly and it is said to be kinetically arrested. The glass system results in a mixture of modes. The regions with slow modes, $(1-x)$ will thermalise slower and at a higher temperature T_f, than those regions x, governed by faster modes. Eventually, slow regions will reach $T_f{}'$, in which they will relax to achieve the equilibrium temperature of the rest of the system, T_{equi}. This may even require an infinite time to be reached. See Figure 6.4.

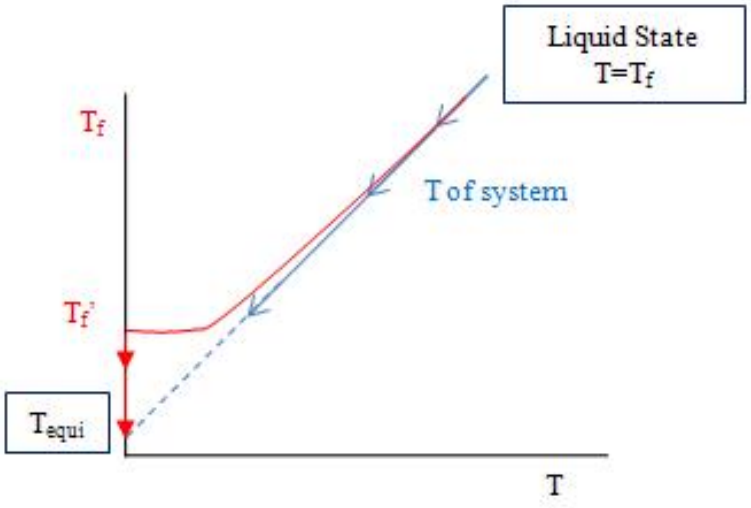

Figure 6.4: Representation of T_f vs T when the breakdown of equilibrium takes place. The red curve constitutes the slow modes, while fast modes follow the blue profile.

The departure from Arrhenius-like behaviour occurs when we consider that the activation energy depends on temperature $\triangle h(\mathrm{T})$. This topic is out of the scope of this chapter.

Despite glasses being in a non-equilibrium state, from the TNM model we can make the assumption that the relaxation time can be described using an Arrhenius law within the window of time observed by calorimetry experiment which is very small (1-0.1 K/min). Near equilibrium the TNM equation becomes,

$$\frac{d}{d(\frac{1}{T})}(lim_{T_f \to T} ln(\tau)) = \frac{\triangle h}{R}. \tag{6.4}$$

And further expansion of previous equations yields the Arrhenius expression, giving a linear relation between limiting fictive temperature T'_f and scanning rate β.

$$\frac{d}{d(\frac{1}{T_f{}'})}(ln(\beta)) = -\frac{\triangle h}{R}. \tag{6.5}$$

From equations 6.4 and 6.5 we can state that the scanning rate and the relaxation time are inversely proportional, and thus

$$\tau \propto \frac{1}{\beta} \propto exp(\frac{\triangle h}{T'_f}). \tag{6.6}$$

In a glass transition region, as was discussed in the introduction, the thermal-change rate established experimentally starts to differ from the rate at which the system actually changes. As seen from Figure 6.3, for instance, the faster the system is cooled down the faster the observation window loses the ability to see the changes in the sample, and the property p of the glass curve appears at a higher value. Slow cooling allows us to observe the phenomena that occur on a longer time scale, therefore the domain of observable τ broadens when β decreases. By measuring the system at different cooling times, it allows us to map the behaviour of τ as a function of temperature

Another property that plays a crucial role in this process and is conceptually related to the relaxation time is the recovery enthalpy, or also called relaxation enthalpy. As the temperature of the glass is driven down through the glass transition at different scanning rates, the structural relaxation effects will manifest themselves as an endothermic processes at the subsequent heating ramp. The slower the system is cooled down the longer the system relaxes, and thus the higher the endothermic effect is observed upon heating.

The relaxation enthalpy can also be revealed by another method: aging. Analogous to the previous consideration, when the sample is cooled down to a temperature, $T_a < T_g$, and is maintained at that temperature during time, t_a, the system relaxes by lowering its internal energy (enthalpy) towards equilibrium in the liquid state (t$\rightarrow \infty$). The longer t_a, the higher the enthalpy recovered when the system is reheated. This quantity corresponds to the difference of the initial and final energy states between the annealed and non-annealed states. It is important to consider the temperature at which the aging is allowed T_a. The lower it is compared to T_g, the longer the system will take to reach equilibrium.

Figure 6.5 gives a graphical interpretation of the concept of recovery enthalpy in both processes. So far we have introduced relaxation effects in terms of enthalpy versus temperature. As discussed previously, a DSC measurement provides direct access of the heat capacity of the system, and thus all our experiments have been presented and analysed using this property. Recall that the heat capacity is the temperature derivative of the enthalpy, $\triangle C_p = \frac{d\triangle H}{dT}$. Therefore, figure 6.5 includes the relaxation behaviour in terms of both the heat capacity and the enthalpy as a function of temperature.

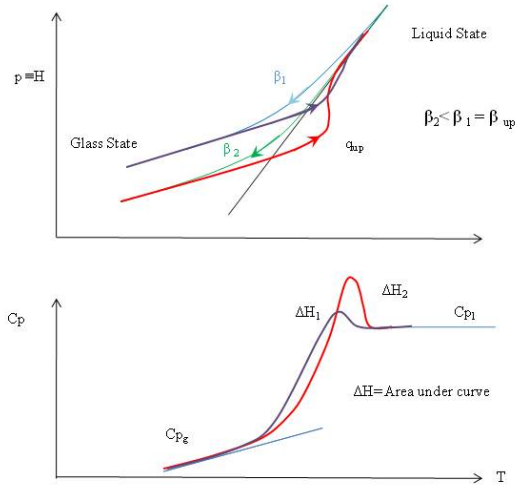

(a) Specific heat and recovery enthalpy for different β

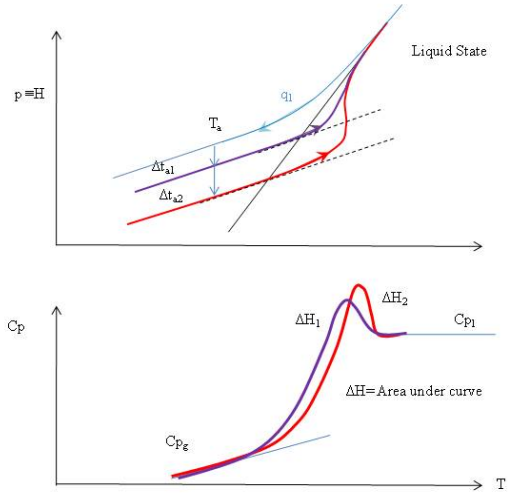

(b) Specific heat and recovery enthalpy for different t_a

Figure 6.5: Definition of specific heat and recovery enthalpy for different cooling rates β (a), and for different aging times t_a (b). Figure(a) shows the effect of cooling at different rates. Top (a): the blue and violet curve correspond, respectively, to the cooling and heating ramps taken at β_1, while the green and red ramps were taken at a slower rate β_2. Bottom (b): using a slower cooling rate gives rise to a higher recovery enthalpy, $\triangle H_2 > \triangle H_1$. Figure (b) represents annealing the sample at different t_a at a fixed temperature, T_a. Top (b): the cooling ramp is represented with a blue curve, while the heating ramps after different t_a are shown in red and violet; the latter curve corresponds to a higher aging time $t_2 > t_1$ resulting in a more prominent recovery enthalpy, $\triangle H_2 > \triangle H_1$ (bottom (b)).

6.4 Experimental Method

6.4.1 Sample Preparation

Preparation of DNA films

Oriented fibres Na-DNA samples were prepared using the WSA [2]. The spun films were dried for 24 hours and placed in desiccators with an oversaturated solution of NaBr in H_2O for a number of weeks, providing a relative humidity of 56%. This hydration level insures a predomination of A-form conformation in the samples, although a low fraction of B-form always remains (see Chapter 4).

For each of the DSC experiments one or several hydrated films with a mass between 80 and 100 mg were rolled up and placed in an hastelloy tube. It was then left inside the desiccator for a day to allow the tube to attain the same relative humidity as the surroundings. Once this was accomplished, the tube was sealed with an O-ring to fix the water content throughout the experiment. The films inside the tubes were in contact with the cylindrical wall ensuring a good thermal contact. In most cases the space occupied by the films in the tube reached up to 3/4 of the total volume.

Vitrifying DNA

The film was then subjected to an appropriate thermal treatment to obtain the DNA glass. The hastelloy tube containing the sample was inserted in the DSC at 293 K and left 10 min for stabilisation. For the reference tube, 345 mg of polyimide trademark VESPEL was used. This polymer does not exhibit a glass transition within the measured temperature range, but a linear baseline.

The sample was first cooled down to 268 K, where it was stabilised for 10 min. This initial sequence was followed by first increasing and decreasing DSC temperature ramps. The increasing temperature scan was performed at 1.2 K/min, from 268 K to 368 K. The sample is stabilised for one hour at this high temperature. Then a decreasing scan was performed at the same rate, from 368 K to 268 K. The results are shown in Figure 6.6.

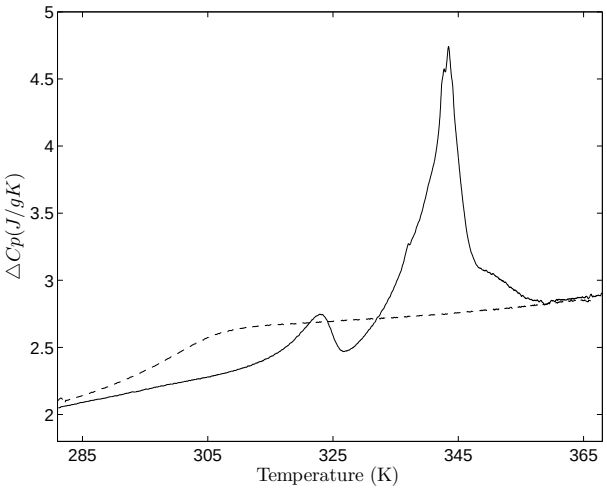

Figure 6.6: DSC heating scan of oriented fibres DNA measured at 1.2K/min (continuous line), followed by a cooling scan at the same rate (discontinuous line).

As discussed earlier, the cooling scan shows that the denaturation of the double helix is not reversible. On cooling, we observe a step-like descent in heat capacity, which is typical of a glass transition. Subsequent heating and cooling do not show the two endothermic peaks observed on the first heating, but instead show features which are characteristic of a glass.

Before proceeding with each of the experiments to study the glass behaviour of melted DNA, a protocol composed of a series of cooling-heating ramps (pre-experiment) was performed to ensure a stabilisation of the glass structure and to erase any previous thermal history. After placing the sample inside the DSC for the first time, or after finishing a DSC experiment, the sample was held isothermally at 293 K for at least 10 min. This was henceforth the initial temperature of the pre-experiment. The sample was then cooled down to 268 K and left at that temperature for 10 min, heated to 363 K and held isothermally for 1 hour. This was followed by cooling back to 268 K, maintaining this temperature for 10 min and heating thereafter to 363 K and stabilising the sample at this temperature for 20 min. This was the initial state for the different experimental procedures detailed below and summarised in Table 1. These cooling-heating ramps were performed at a scanning rate $\beta = 1.2$ K/min.

Preparing the polyvinyl acetate (PVAc) samples

The PVAc samples were provided by Jean-Luc Garden and Jacques Richard (CNRS, Néel Institute, Grenoble).

PVAc is a polymeric glass former that is a reference in glass science. Its major advantage is that it does not crystallise during cooling, and its glass transition temperature is around room temperature. Consequently it has been extensively studied by various techniques and particularly by DSC, and useful data can be found in the literature [93],[95]].
The samples consisted of small balls of about 100 mg, given by Pr. G. Mckenna (Department of Chemical Engineering, Texas Tech University, Lubbock, TX 79409-3121). The average molecular weight is of 157 kg/mol and its polydispersity index (PDI), which indicates the distribution of individual molecular masses in a polymer, is 2.73. The PVAc was first put in an oven under vacuum at a temperature of 105°C, well above Tg, for 24 hours in order to remove all the water from the melt. After a rapid mass measurement, the sample was put in the micro-DSC sealed Hastelloy tube for DSC measurements that follow exactly the same protocol as for the DNA sample.

6.4.2 DSC experiment

A Setaram Micro DSC III was used to perform the experiments (see Chapter 2). The temperature of the water regulator bath was fixed to 288 K.

Thermal lag and deconvolution of the data from the instrumental response

As DSC scans involve a temperature variation, one must consider two effects in the analysis of the data. First a bad thermal contact between the sample or reference and the calorimeter probes, or the low value of the thermal diffusivity of some samples, could lead to spurious temperature gradients; and second the calorimeter has a finite response time that must be taken into account.
A preliminary experimental check was carried out to prove that the measurements did not accounted for any thermal lag. Indeed, general DSC instruments work with rather high-weight samples (about 1 g) at scanning rate around 10 K/min or more. It induces the presence of temperature gradients inside the volume of the sample, or at the interfaces between the sample and the vessel. These unwanted gradients can deform the shape of the measured heat capacity curves and provide data with high inaccuracies. In the present case, the samples masses used were between 50 and 100 mg, and we have taken advantage of the very low scanning temperature rates range of the Setaram microDSCIII calorimeter (between 10^{-3} and 1.2 K/min) to assume that such effects do not cause parasitic effects

in our experiments. A second unwanted effect than can occur is the presence of an external thermal time constant of the microcalorimeter. In the case of the glass transition study, neglecting such an effect can completely suppress heat capacity overshoots during heating scans as is well described in [36]. To account for this time constant effect, a protocol consisting of a series of cooling/heating cycles at different scanning rates but with constant cooling rate/heating rate ($\beta_c/\beta_h = 0.833$) ratio has been used.

The protocol consisted of temperature cycles of: a cooling ramp from 363 K to 268 K; 10 min of equilibration at that temperature followed by a raise in temperature from 268 K to 363 K; and again a 20 min pause at constant temperature to allow the sample to stabilise. The cycles were repeated 7 times.

The data were deconvoluted from instrumental resolution using equation 2.63 in Chapter 2.

The deconvoluted data, $\triangle Cp$, corresponds to the difference in heat capacity of DNA and VESPEL cells. In order to isolate the DNA contributions, the VESPEL component must be accounted for in the total signal. The data were normalised by the sample mass, and finally presented in the form of Cp_{DNA} (J/gK). These can be summarised by the following mathematical expressions,

$$\begin{aligned} \triangle Cp &= m_{DNA}Cp_{DNA} - m_{VES}Cp_{VES}, \\ Cp_{DNA} &= (\triangle Cp + m_{VES}Cp_{VES})/m_{DNA}, \end{aligned} \tag{6.7}$$

where m_{DNA} and m_{VES} are the DNA and VESPEL masses respectively.

Figure 6.7 shows the heating ramps for the same ratio of *cooling rate* to *heating rate*. The deconvoluted data for the instrument response of τ_{ins}= 60s (left image) are compared to those without deconvolution τ_{ins}=0 (right image). The image on the left shows all peaks at the same amplitude [36]. This effect can only be attained when the data is deconvoluted with the right time constant, and no thermal lag due to a bad thermal contact of the sample within the pans occurs. Therefore the comparison of both images indicate that the sample was properly thermalised, without significant internal gradient, in our experiments and that the proper calorimeter time constant was used to analyse the data.

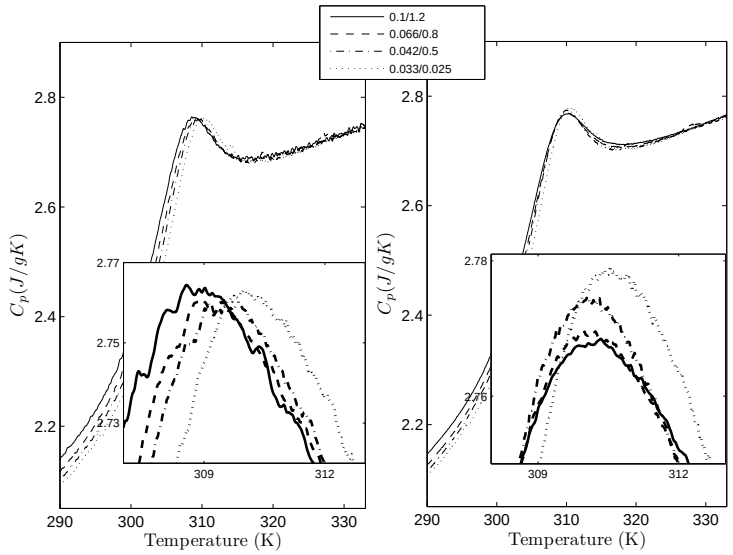

Figure 6.7: DSC heating scans at different heating rates, maintaining the ratio of cooling rate/heating rate β_c/β_h constant. The image on the left shows the deconvoluted data for τ_{ins}=60 s; the data on the second image have not been deconvoluted.

Experimental Protocol

As discussed with the presentation of the protocol to get the DNA glass, each series of measurements was preceded by a "pre-experiment" to achieve a well defined starting state of the sample. Two series of experiments were carried out with the same sample to study the structural relaxation behaviour of melted oriented fibres DNA via two methods:

1. **Different cooling rates.** This consisted of a succession of temperature ramps. Starting from the initial state at 363 K, the sample was cooled down at a rate β from 363 to 268 K; left for 5 mins for equilibration; and heated to 363 K at 1.2 K/min. It was then stabilised for 20 min at this highest temperature before the next cooling ramp, which was recorded as a DSC scan. The cooling rate was modified at each ramp in the following order, β= 1.2, 0.4, 0.2, 0.1, 0.05, 0.033, 0.01 and back to 1.2 K/min. The heating rate was kept fixed.

2. **Annealing at different ageing times.** The procedure consisted on cooling at 1.2 K/min from 363 K to the aging temperature T_a below the glass transition temperature, annealing the sample for a period of time t_a, and then cooling down to 268 K before recording the DSC signal on heating from 268 K to 363 K. All temperature ramps were programmed at a rate of 1.2 K/min. The relaxation of the system was studied at fifteen different aging times, t_a= 84, 78, 72, 66, 60, 54, 48, 42, 32, 20,

10, 6, 3, 1 and 0 hours. The last corresponds to an experiment without annealing. However by simply taking into account the minimal response time of the calorimeter one can consider that the effective minimal aging time is actually equal to 10 min.

DSC runs relevant to the paper have been summarised in Table 6.1.

Analysis thermal lag	Different cooling rates	Annealing at T_a at different t_a
363 $\rightarrow$ 268 $\rightarrow$ 363 $D_n \rightarrow M_n$ at β_n	363 $\rightarrow$ 268$\rightarrow$ 363 $D_n \rightarrow M_n$ at β_n	363 $\rightarrow$ T_a (t_a^n)$\rightarrow$ 268$\rightarrow$ 293 for t_a
$\beta_1(D_1/M_1)$= 0.1/1.2 $\beta_2(D_2/M_2)$= 0.0833/1 $\beta_3(D_3/M_3)$= 0.066/0.8 $\beta_4(D_4/M_4)$= 0.416/0.5 $\beta_5(D_5/M_5)$= 0.033/0.4 $\beta_6(D_6/M_6)$= 0.025/0.3	$\beta_1(D_1/M_1)$= 1.2/1.2 $\beta_2(D_2/M_2)$= 0.4/1.2 $\beta_3(D_3/M_3)$= 0.2/1.2 $\beta_4(D_4/M_4)$= 0.1/1.2 $\beta_5(D_5/M_5)$= 0.05/1.2 $\beta_6(D_6/M_6)$= 0.033/1.2 $\beta_7(D_7/M_7)$= 0.01/1.2 $\beta_8(D_8/M_8)$= 1.2/1.2	84, 78, 72, 66, 60, 54, 48, 42, 32, 20, 10, 6, 3, 1, 0

Table 6.1: Table of scanning rates for the different experimental procedures. The temperatures are given in K; the scanning rate in the ratio between the decreasing (D_n) and increasing (M_n) ramps, $\beta(D_n/M_n)$, in K/min; and the annealing times, t_a in hours.

6.5 Results

6.5.1 Different cooling rates

Let us first consider a series of experiments in which the sample is cooled at different rates β, as indicated in column 2 of Table 6.1 and then heated at the rate of 1.2 K/min. Figure 6.8-(a) shows the specific heat *Cp(T)* measured during each of the heating scans. As expected for a typical glass [96] it shows a fast rise in the glass transition temperature domain, and even a peak when the cooling has been sufficiently slow. This peak becomes more pronounced as the cooling rate decreases. In the case of DNA one can notice that the highest peak (for the cooling rate $\beta_7 = 0.01$ K/min) appears shifted towards a higher

temperature compared to the other measurements. After this measurement with a very low cooling rate, we again performed a ramp with a cooling rate $\beta_8 = 1.2$ K/min, i.e. identical to the cooling rate β_1 of the first experiment. This last ramp gives a curve *Cp(T)* which is different from the curve recorded in the first ramp under the same conditions, indicating that, after the series of experiments involving a very slow cooling, the DNA sample has evolved.

It is also useful to introduce the normalised specific heat, Cp^N(T) which is plotted in Figure 6.8-(b).

$$Cp^N(T) = \frac{\triangle Cp(T)}{\triangle Cp^{eq}} = \frac{Cp - Cp_g}{Cp_l - Cp_g}, \tag{6.8}$$

where Cp^{eq} is the equilibrium heat capacity.

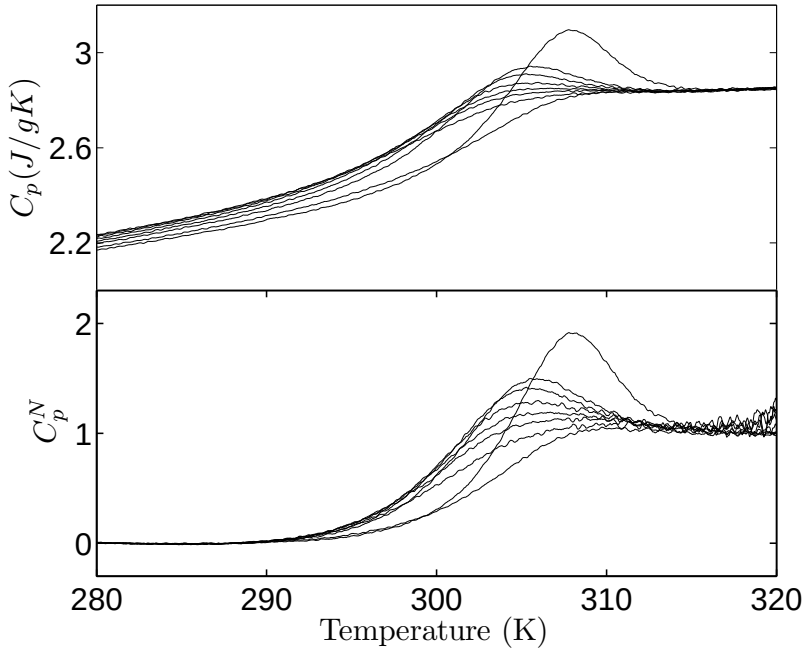

Figure 6.8: (a): DSC enthalpic response on heating at 1.2K/min after cooling at different rates, (q), the data is expressed in heat capacity versus temperature. (b): Normalised heat capacity (C_p^N) versus temperature.

T_f' was calculated for each normalised curve using equation 6.2. In order to calculate $Cp^N(T)$ the value of Cp_g obtained for each particular glass (i.e. particular cooling rate) must be used.

In Figure 6.9 the log of the cooling rate versus the corresponding $1000/T_f'$ value for a denatured sample of DNA has been plotted. The curves show that T_f' decreases with cooling rate, as expected; and that, for β=1.2 K/min down to β=0.05 K/min equation

6.6 is well verified as the data follows a straight line. Its slope corresponds to $\triangle h_{DNA}$ = 79 kK.

However, for the slowest cooling rates $\beta_6 = 0.033$ and $\beta_7 = 0.01$ K/min, the experimental points show a systematic deviation from the Arrhenius curve, suggesting some evolution of the sample, facilitated by a process in which the system has been staying a very long time at high and moderate temperatures. A new measurement with $\beta_8 = 1.2$ K/mn after the sample has passed through this step of extremely slow cooling leads to a point on Figure 6.9 which does not coincide with the first point, obtained with the same cooling rate β_1 = 1.2 K/mn. This attests of an irreversible evolution in the DNA sample. The slope of the line connecting the last two points β_7 =0.01K/min and β_8 = 1.2 K/min corresponds to $\triangle h$ = 68.8 kK, a bit lower than the value found before the sample evolved.

Similar analysis in polymer samples such as PVAc led to $\triangle h_{PVAc}$ = 99 kK, which is a value comparable to the one obtained for DNA. The interpretation of these results from the observations on a polymer like PVAc for which the Arrhenius plot is valid for all the cooling rates, will be given in the discussion.

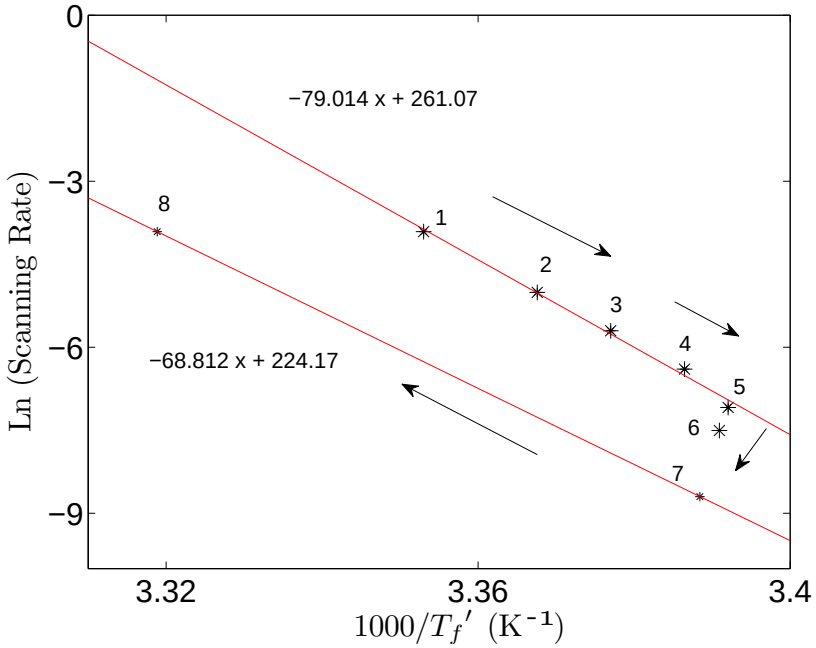

Figure 6.9: Dependence of $T_f{}'$ on the cooling rate β. The symbols represent the values $T_f{}'$ calculated with equation 6.2, while the solid line corresponds to a linear fit. The top fit includes the five points lying on it, which corresponds to the fastest cooling rates (β= 1.2, 0.4, 0.2, 0.1 and 0.05). The point corresponded to β=0.033 was excluded. The line below was obtained with the last cooling scans, β=0.01 and β=1.2 K/min arising at a higher $T_f{}'$. The slopes for each of the fits are also showed on the plot. The arrows indicate the time-evolution of the system, also marked by numbers. Between the first measurement (number 1) and the last one (number 8), there was a period of ten days, corresponding to the cumulative time of the experiments.

6.5.2 Annealing at different ageing times.

As discussed when we introduced the experimental protocols, a second series of experiments was carried out to investigate the time evolution of the sample submitted to aging in the glassy state. The study was compared with a similar set of measurements for PVAc. The samples were annealed at a temperature T_a of 293K and 297K for DNA and PVAc respectively, for a series of aging times (relaxing times), t_a (hours) = 84, 78, 72, 66, 60, 54, 48, 42, 32, 20, 10, 6, 3 and 1. T_a were chosen to be 15 K below the inflexion point of their respective specific heat curves measured during the cooling run at 1.2 K/min. $T_{a,DNA}$ and $T_{a,PVAc}$ were chosen to be low enough to ensure that the samples were in the non-equilibrium state. By selecting the same temperature drop of 15 K below the glass transition temperature of each sample, we expected the relaxation times to be comparable for the DNA and PVAc annealing studies. It turned out not to be the case.

Figure 6.10 shows the DSC scans obtained by heating two samples at 1.2 K/min above the annealing temperature: denatured DNA (red) and PVAc (black). Non-annealed (continuous line) and 72h annealed (discontinuous line) scans were chosen to compare the glassy behaviour of these samples upon aging. From the curves we can conclude that both samples behave in a similar way: the annealed scans show a prominent peak at a temperature T_p higher than T_a. However for PVAc a peak is visible during reheating even without aging, while for DNA there is no peak in the absence of aging. This suggests that underlying relaxation mechanisms for the two glass-formers do not obey the same laws. The comparison of the two heating-scan peaks after the same period of aging is more difficult because the aging temperatures are different. This is the object of the experiments described below.

Again, after the sample was annealed it was cooled down to 268 K at the rate of 1.2 K/min, stabilised for 10 min at this temperature and then a DSC scan was recorded while heating from 268 K to 363 K. The measurement actually characterises a system which has been frozen in its glassy state after aging.

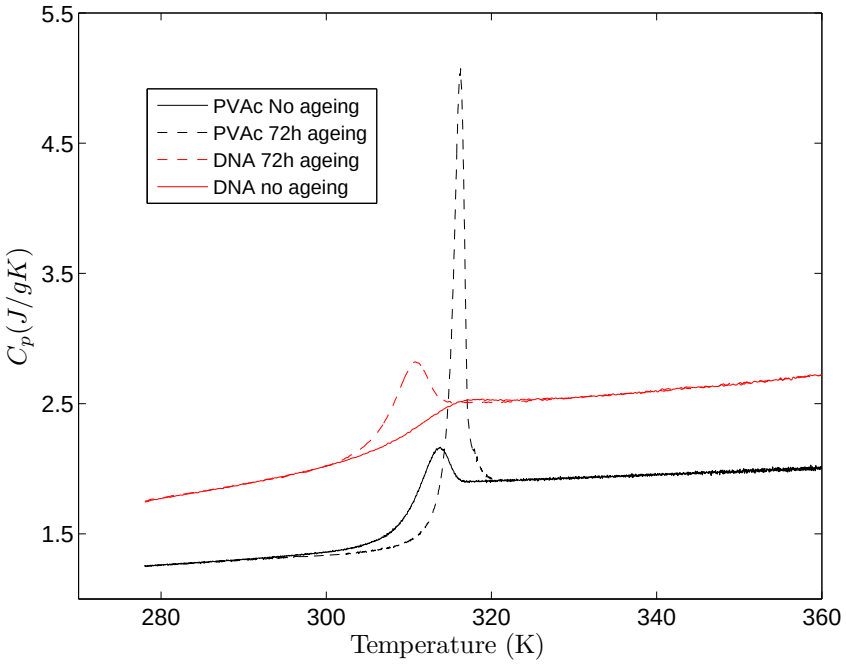

Figure 6.10: Comparison of the effects between non-annealed and annealing for 72 hours of two different samples, denatured DNA and PVAc.

Figure 6.11-(a) shows DSC heating scans for melted DNA annealed for different annealing times t_a. The image clearly shows a progressive growth of the endothermic peak with t_a. Figure 6.11-(b) shows the difference curves of the annealed scans with respect to the non-annealed one, t_a=0, also called reference curve. The effects of the increase of the peak as well as the change in the peak position are very distinguishable on the image.

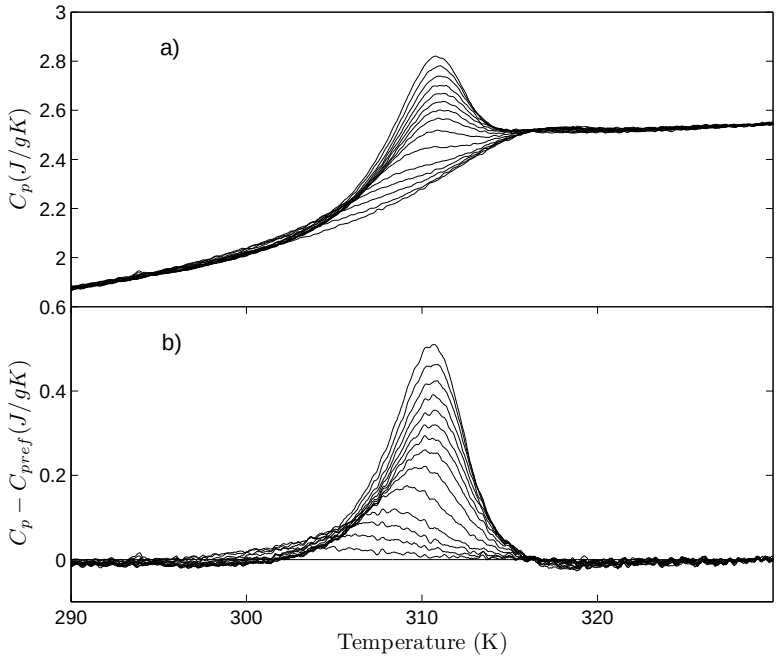

Figure 6.11: (a): Heat capacity versus temperature of denatured DNA annealed at 297K for different t_a (in hours)= 84, 78, 72, 66, 60, 54, 48, 42, 32, 20, 10, 6, 3, 1 and 0; the latter corresponds to that of non-annealed. (b): Heat capacity versus temperature for the corresponding DSC difference curves(Cp-Cp_{ref}) for each t_a.

The state of the sample after annealing can be characterised by two quantities. First: the difference of area under the annealed and non-annealed curves which accounts for the enthalpy recovered, $\triangle H$. As discussed in the theory section, the enthalpy of the system decreases as it relaxes during aging. The lost enthalpy is again absorbed by the system upon heating to reach the liquid equilibrium state. It characterises the annealed glassy state from the energetic view point. Second: the notion of fictive temperature, that we used in the previous section to characterise glassy states obtained at different cooling rates can also be used to characterise the states after aging. Since our DSC heating ramps were recorded from a frozen state lower than T_a, we can also apply equation 6.2 to the specific curves of figure 6.11 to calculate T_f'.

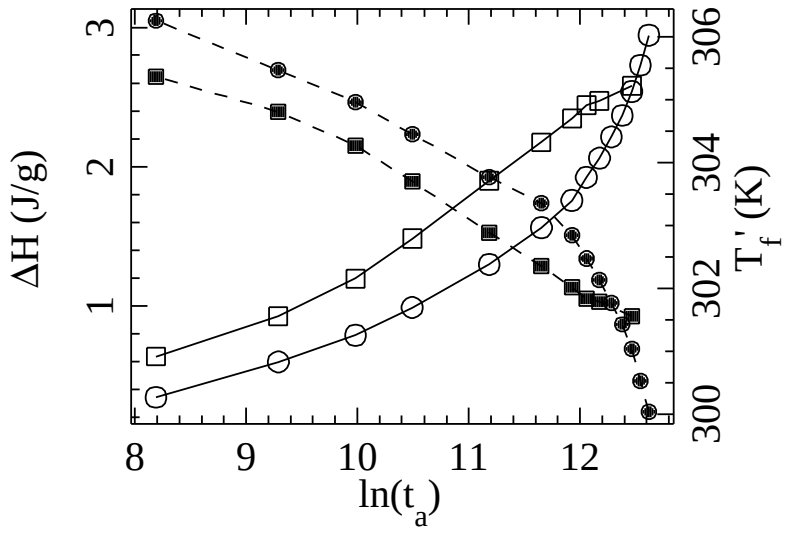

Figure 6.12: Aging of the DNA and PVAc samples. The circles refer to DNA results and the squares to PVAc. Open symbols and full lines: enthalpy recovery $\triangle$H as a function of the logarithm of the aging time (in seconds). Filled symbols and dash lines: fictive temperature T'_f as a function of the logarithm of the aging time (in seconds)

As expected the enthalpy recovery increases with the aging time, while the effective temperature decreases, as shown in Figure 6.12. The curves for DNA and PVAc, however, show a difference. For PVAc, for the longest aging times, one can notice the beginning of a saturation, as the variation of $\triangle H$ and T'_f appears to slow down. This suggests that the longer waiting time used in our experiment, 84 hours, approaches the relaxation time of the PVAc glass. This is not the case for DNA. Even for the longest aging times the evolution of the glass continues, without a sign of a saturation.

Furthermore, one can try to determine how the relaxation time evolves during the aging process for the two different systems. It seems reasonable to assume that, at the beginning of its aging, a system evolves faster because it explores the "easy paths" for relaxing. Then, once those paths are exhausted, the relaxation becomes harder. We cannot measure this directly, but, as we determine the fictive temperature $T'_f(t_a)$ as a function of the aging time, and if we assume the validity of Equation 6.6, we can write:

$$\tau(t_a)/\tau(t_a = 0) = \exp\left[\Delta h \left(\frac{1}{T'_f(t_a)} - \frac{1}{T'_f(t_a = 0)}\right)\right]. \tag{6.9}$$

Figure 6.13 shows the calculated evolution of the ratio $\tau(t_a)/\tau(t_a = 0)$ as a function of aging for DNA and for PVAc. The relaxation time grows faster for PVAc than for DNA

in the initial stage of aging, but then for long aging periods, while the relaxation time for PVAc tends to stabilise, the value of τ for DNA increases drastically. In terms of a free energy landscape, it would mean that, for DNA, after an initial period during which the glass can rearrange, the system falls into deep metastable minima from which it is very hard to exit. This can be related to the decrease of the enthalpy for DNA for the longest aging times.

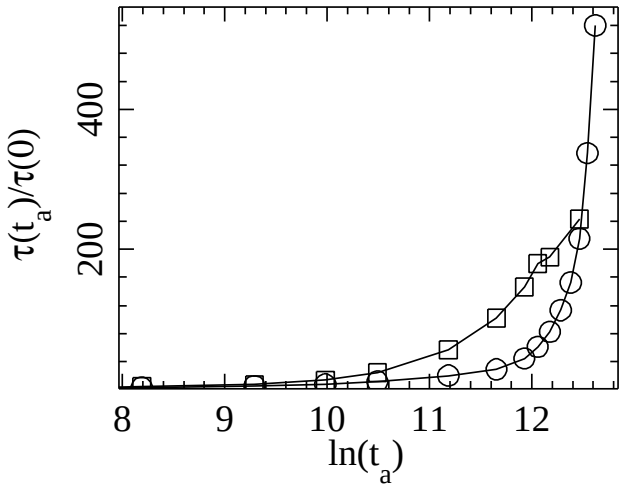

Figure 6.13: Evolution of the relaxation time versus aging. This figure shows the ratio of the relaxation time after an aging during t_a (in seconds) to the relaxation time without aging $\tau(t_a)/\tau(t_a = 0)$, assuming that the relaxation time follows the Arrhenius law, equation 6.6. The circles correspond to DNA and the squares to PVAc.

6.6 Discussion

Our calorimetric study of a DNA film has shown that, after the thermal denaturation of the double helix, this system has properties which are very similar to those of a polymer glass, such as PVAc, with noticeable differences

1. an irreversible evolution of the DNA sample is observed when it is cooled extremely slowly,

2. when it is annealed at low temperature, the DNA sample shows a very long relaxation time. Even after 84 hours of annealing, 15 K below the glass transition temperature, the DNA sample still evolves significantly while PVAc starts to show some saturation.

These two effects are probably linked and related to the particular structure of DNA. The denatured strand of DNA is made of a sugar-phosphate backbone that carries large side groups, the A,T,G,C bases which have the shape of flat single or double organic rings. The presence of these bases may affect the relaxation of the DNA glass in several respects: (i) by making the reptation of the polymer more difficult, (ii) because the bases tend to stack on top of each other, or may form hydrogen bonds with complementary bases.

Our experiments show that the enthalpy barrier $\triangle h$ associated to the relaxation in the DNA film is of the same order of magnitude (79 kK) as the enthalpy barrier measured for PVAc (100 kK). This suggests that the slow relaxation in DNA come from kinetic factors, due to the confinement effect in the fibres. In the slow cooling experiments the system stays a long time at high temperature, which allows a faster exploration of the phase space. This could explain why its irreversible evolution is only observed in this case. The microscopic origin of this evolution is difficult to assert, but it could be associated to a partial stacking of the bases in some regions of the sample. In double stranded DNA the stacking interaction is known to contribute significantly to the stabilisation of the double helix structure. Moreover, even in solution, the bases tend to stack, so that a partial stacking is plausible within the fibres too. But, as it requires large amplitude motions of big organic groups in a very confined environment, it is certainly a very slow process unless it can be assisted by thermal fluctuations. Moreover, a slow stacking of the bases occurring in the last stage of a long relaxation of the DNA sample would be associated to an enthalpy gain. This would be consistent with our observation that the enthalpy recovery for the DNA sample exceeds that of PVAc for the longest aging times (Figure 6.12).

We cannot rule out other phenomena to explain the irreversible evolution of the DNA samples, in particular the role of the hydration water. Water could be expelled from the bulk of the film during the slow cooling and accumulate in the part of the sample holder which is not fully filled by the DNA film. However, the lack of an exothermic peak, due to the crystallisation of water when the sample is cooled down to 268 K, suggests that the water molecules might instead reorganise in the fibres, probably in the external hydration layers.

This investigation has shown that the fibre form of DNA, prepared in the form of a film, has interesting physical properties which pose some questions for their understanding.

DSC calorimetry is a useful tool to investigate the physical properties of this system, provided it is completed by some quantitative analysis. Using the fictive temperature allows further explorations of the relaxation processes, in particular because it gives an estimate of their enthalpy barrier. For a complete microscopic understanding this method has nevertheless to be completed by other approaches, such as structural studies with neutron scattering[8], or perhaps spectroscopic investigations.

Chapter 7

Transversal and Longitudinal Phonons in Oriented DNA Fibers

7.1 Foreword

This chapter gives an overview of preliminary and incomplete studies in the measurement of the coherent inelastic modes, acoustic and optical, in oriented fibres of DNA using IXS and INS techniques. We have revealed that controlling the humidity of the sample can become a challenge when carrying out IXS experiments, especially when increasing temperature.

7.2 Introduction

Base pair stacking is not simply one of the forces that maintains stable the DNA double-helix structure, but it is also partly responsible for its flexibility. And thus bubble formation upon heating, for example, will be affected by the stretching elasticity as it involves increasing the base pair distance. This mechanical property plays a crucial role in the biological functionality of DNA. A direct way to measure the stacking interaction along the helical axis is via acoustic phonons. Again, changes in the stacking will affect the propagation of the phonons.

Over the last decades there have been several experimental attempts to measure the parameters describing mechanical properties of DNA, but the results have been shown to be technique-dependent, and hence no consistency between the results has yet been

established.

Investigations using inelastic neutron scattering (INS) [64], [63] and inelastic X-ray scattering (IXS) [65] have measured phonon excitations on highly oriented fibre samples of DNA[71]. Their measurements concluded that inelastic excitations along the helix show liquid-like phonons in the base pair length-scales. The sound velocities obtained for the acoustic curves for INS and IXS were 1.85 km/s and 2.84 km/s respectively.

These experiments became the precursor of the research project started by M. Johnson, L. Van Eijck (ILL) *et al.* They resolved the phonon dispersion curves on B-form DNA using INS technique on a time-of-flight spectrometer (IN5)[11]. The results were compared with atomic scale force field based phonon calculations [97], which became essential to interpret the INS data. INS measurements mapping the acoustic dispersion curves around the base-pair Bragg peak (0,0,10) were measured at temperatures from 70 K up to 335K, just below the melting temperature. The average inter-base pair force constant defining DNA elasticity was obtained to be 83 N/m, and a sound speed of 4.3 km/s. Figure 7.1 shows the INS results at two temperatures, 70 K and 335 K. The plots corresponds to constant-Q scans extracted from the $S(Q, E)$ plots.

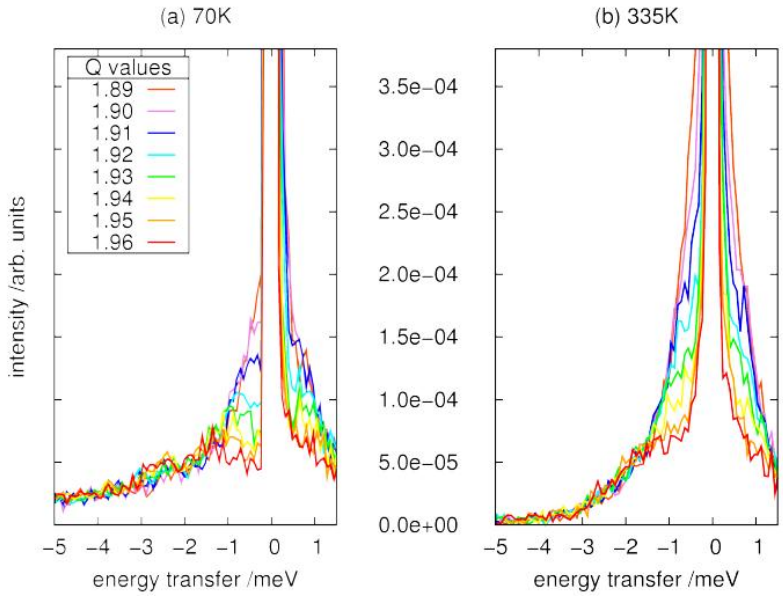

Figure 7.1: Constant-Q scans of the $S(Q, E)$ plots measured at (a) 70 K and (b) 335 K on IN5. Figure reproduced from [11]-FIG. 3.

These vibrations became the proof that there is a long range order along the molecular axis prevalent even at temperatures very close to the melting transition, typical of a

crystalline-like system; and that their dispersion curve goes to ω=0 at the Bragg peak position, unlike that corresponding to a liquid-like system as previous IXS results reported [65].

Figure 7.2 shows a global compilation of the phonon dispersion investigations using different techniques on wet-spun oriented films. It includes the early INS and IXS results that were interpreted to have a liquid-like behaviour; and the most recent INS and simulations results obtained by M.Johnson and co-workers.

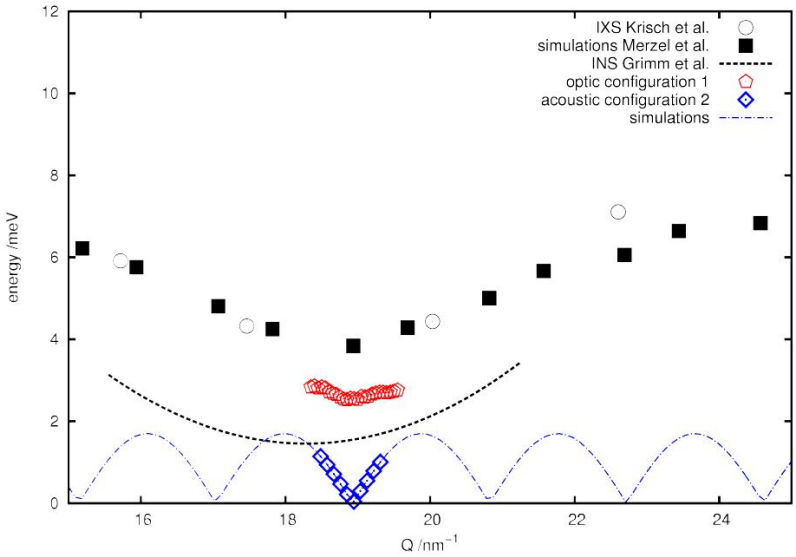

Figure 7.2: Experimental and molecular dynamics calculations of the longitudinal phonon dispersion curves of B-form DNA. The experimental data corresponds to: IXS by open circles [65] and INS with dashed parabola[64]; while the calculations are shown by filled squares. The most recent INS measurements obtained by M. Johnson's group for the acoustic and optic mode, (red pentagons) and (blue diamonds) respectively, are present, together with their simulations (dashed blue line). The sound speed obtained from the acoustic dispersion curve at the base-pair Bragg peak is 4.3 km/s. This figure was reproduced from [11]-FIG. 2.

Based on Figure 7.2, they argued that the results obtained from different techniques are complementary if a proper interpretation is considered. This was possible thanks to the simulations, as they probe the optical and acoustic longitudinal dispersion curves associated to a crystalline DNA structure, whose Brillouin zone is defined by the helix-turn period $\triangle BZ_{Ht} = 2\pi/3.4$ (nm)$^{-1}$. In conclusion, the comparison between previous reported dispersion curves and their studies revealed the following:

1. The dispersion curve reported using IXS [65] does not correspond to the intensity of a single acoustic mode but a combination of optical modes. And thus, B-form of

oriented DNA fibres should not be considered as a liquid-like system.

2. The dispersion curve reported using INS [64],[63] is probably a combination of optical and acoustic modes that could not have been resolved within the resolution of the measurements.

We continued the study of the modes associated to long correlation length along the molecular axis in collaboration with Mark Johnson at the ILL. The purpose of the research project was to resolve the acoustic and optic dispersion curves of the B-form DNA in the low-Q limit using IXS; and to map the acoustic dispersion curve along a high symmetry direction by INS using triple axis spectrometry.

In parallel, we developed an interest for transverse phonons in oriented DNA due to their role in bubble formation. The forces responsible for bubble forming would have their origin in the sliding of the bases on each other. Theoretical models of the DNA thermal denaturation, including the PBD, have given special attention to the analysis of these transversal fluctuations [10]. It was clear that, in order to understand the melting transition better, we needed to investigate the vibrational modes polarised perpendicular to the helical axis. The ultimate goal was to study the effects of temperature on these modes, and consequently to test the statistical mechanical models for thermal denaturing.

Unlike the previous experiments on melting, which required the samples to be a very good approximation to a one-dimensional system, the sample for this experiment needed to be as crystalline as possible in order to have Bragg peaks with significant intensity in a direction perpendicular to the fibre axis. This was accomplished by A-form DNA samples, which have sharper Bragg peaks and hence are more crystalline than B-form samples. The energy and momentum transfer ranges were appropriate for triple axis measurements, so the project started using this technique. These type of modes had never been measured before.

Depending on the orientation of the scattering vector with respect to the phonon propagation, longitudinal or transverse phonons can be detected. Figure 7.3 shows the diffraction pattern of the crystalline A-form DNA. The vector configuration to measure longitudinal and transverse phonons have been represented with coloured arrows, red for longitudinal and green for transverse. In both cases the phonon propagates along the molecular axis (vertical). (See equation 2.37 in Chapter 2).

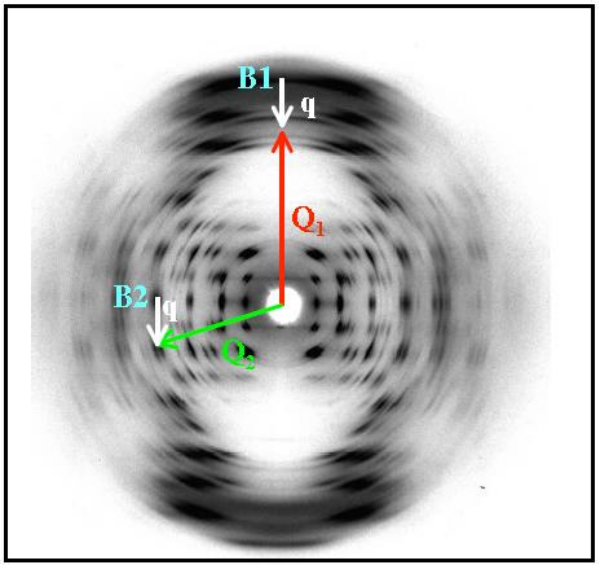

Figure 7.3: Fibre diffraction pattern from A-form DNA, with superimposed momentum vectors. The neutron momentum transfer, **Q** in the direction of the red arrow corresponds to the configuration to detect longitudinal phonons; while that with **Q** in the direction of the green arrow will measure transverse phonons.

7.3 Vibrations of DNA as a linear model

We will consider DNA using a simple model formed by 2 chains of nucleotides, each joined to its neighbour by an harmonic potential, and with the interaction between the two strands as given by a Morse potential [98], see Figure 7.4. The transversal displacement vectors are given by u_n and v_n where the subindex corresponds to the position of the nucleotides on its respective backbone. The model does not incorporate the longitudinal displacements since their amplitudes are considered negligible relative to the transversal ones.

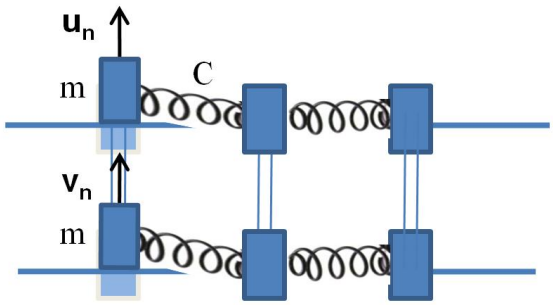

Figure 7.4: Representation of the linear model of DNA, where the transversal displacement vectors from equilibrium for each of the chains are denoted u_n and v_n, where n corresponds to the index of nucleotide along the chain. And m is the mass of the nucleotide.

We can define the Hamiltonian of the model as,

$$\begin{aligned} H &= \sum_n \Big[\frac{1}{2}m(\dot{u}_n^2+\dot{v}_n^2)+\frac{C}{2}[(u_n-u_{n-1})^2+(v_n-v_{n-1})^2] \\ &+ D(e^{-a(u_n-v_n)/\sqrt{2}}-1)^2\Big] \end{aligned} \tag{7.1}$$

The Morse potential can be treated within the linear approximation by transforming the displacement coordinates into normal coordinates in the linear limit, $x_n = (u_n + v_n)\sqrt{2}$ and $y_n = (u_n - v_n)\sqrt{2}$.

From these assumptions we can construct the equations of motion for each of the chains including the Morse potential, yielding

$$m\ddot{x}_n = C(x_{n+1}+x_{n-1}+2x_n) \tag{7.2}$$

$$m\ddot{y}_n = C(y_{n+1}+y_{n-1}+2y_n)+2Da(e^{-ay_n}-1)e^{-ay_n}, \tag{7.3}$$

The second term in equation 7.3 corresponds to the Morse potential where a is the distance between nucleotides. In the linear approximation it reduces to $-2Da^2y_n$. These equations have a wave solution, $x_n = Ae^{i(qna-\omega t)}$ and $y_n = Be^{i(qna-\omega t)}$, where A and B are constant. By solving the equations of motion for this solution, equation 7.3 becomes,

$$\begin{aligned} -m\omega^2 A &= CA(e^{iqa}+e^{-iqa}-2) = -2CA(1-\cos(qa)) \\ \omega^2 &= \frac{4C}{m}\sin^2(\frac{qa}{2}), \\ \omega &= \sqrt{\frac{4C}{m}}\sin(\frac{qa}{2}). \end{aligned} \tag{7.4}$$

Recall the standard identity, $\cos x = \frac{1}{2}(e^{ix}+e^{-ix})$; and the trigonometry identity, $(1-\cos x) = 2\sin^2(\frac{1}{2}x)$.

Equation 7.4 corresponds to the phonon dispersion relation of the acoustic branch.

Similarly, the dispersion relation for the y_n wave solution gives,

$$\begin{aligned} -m\omega^2 B &= CB(2\cos(qa) - 2) - 2Da^2 B, \\ \omega^2 &= \frac{4C}{m}\sin^2(\frac{qa}{2}) + \frac{2Da^2}{m}. \end{aligned} \tag{7.5}$$

This corresponds to the optic branch.

When nonlinearity is taken into account (the linear expansion of the Morse potential is no longer valid), the lower edge of the optical band $\sqrt{\frac{2Da^2}{m}}$ is replaced by the oscillation frequency in the Morse potential which tends to decrease to 0 when the amplitude grows. This is mode softening behaviour.

7.4 Longitudinal phonons

The investigations of longitudinal modes were carried out on a B-form Li-DNA sample provided by A. Rupprecht. It is many years old, which allows a complete relaxation of the structure and is a guarantee of its molecular orientation and quality. As shown in figure 7.3, the samples must be aligned with the fibre axis in the scattering plane, where Q_H is defined along the helical axis.

7.4.1 Longitudinal Modes with IXS

The advantage of measuring phonons with IXS is that energy and Q are decoupled, hence large energy transfers at low Q values are accessible, and the flux is high. This signifies that measurements within the first BZ can be performed as a function of temperature up to melting. Furthermore, the small amount of sample needed becomes a considerable advantage since above the melting the sample is destroyed.

The measurements aimed to resolve the acoustic and optic dispersion curve in the first BZ to compare the molecular simulations with experimental data. The dependence of the dispersion curves on temperature were investigated. Previous IXS measurements on the same DNA conformation studied the acoustic dispersion curve from 2.5 to 27 nm^{-1}, for which a speed of sound of 2.84 km/s was obtained [65]. Figure 7.5 reproduced from [65] shows these results obtained by M. Krisch *et al*, as well as those measured by Grimm *et al* using INS.

Our experiments were designed to measure lower-Q values, to also check the value of the speed of sound for the crystal-like acoustic phonons.

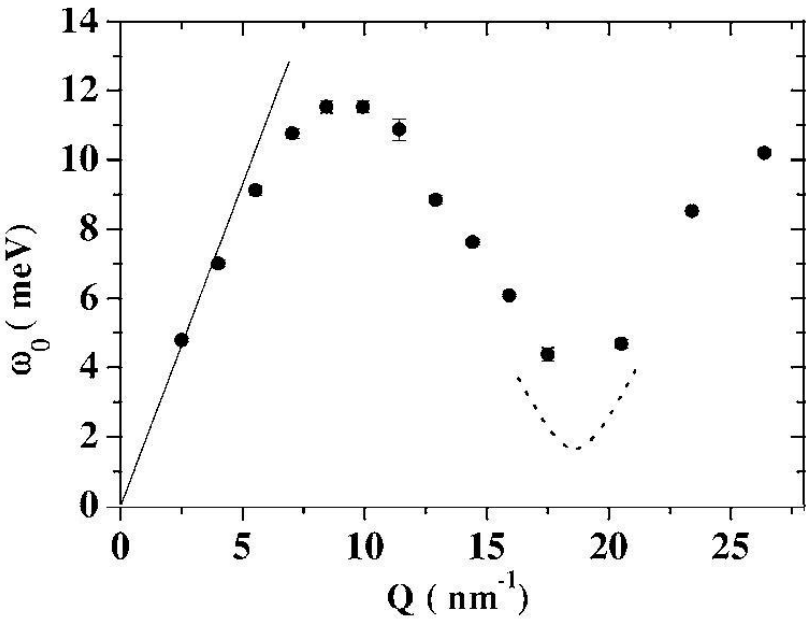

Figure 7.5: Dispersion of the eigenfrequency ω_0 of the DHO for B-form DNA at ambient temperature. The slope, corresponding to a sound velocity of 2.84 km/s, is indicated by the straight line. The dotted parabola represents results obtained by neutron scattering [63]. The figure was reproduced from [65]-FIG. 4.

Experimental Method

The sample consisted of a piece of an oriented film of Li-DNA, a few μm thick. It was humidified for several days in a humidity chamber at 75% RH. The sample was mounted in the sample holder inside the humidity chamber to preserve the humidity and hence the DNA structure. The sample holder was sealed and placed in the beam. Figure 7.6 shows the sample cell with the different elements and the location of the DNA within the cell. The X-ray beam path has been drawn, and the orientation of the fibre on the DNA film (black line).

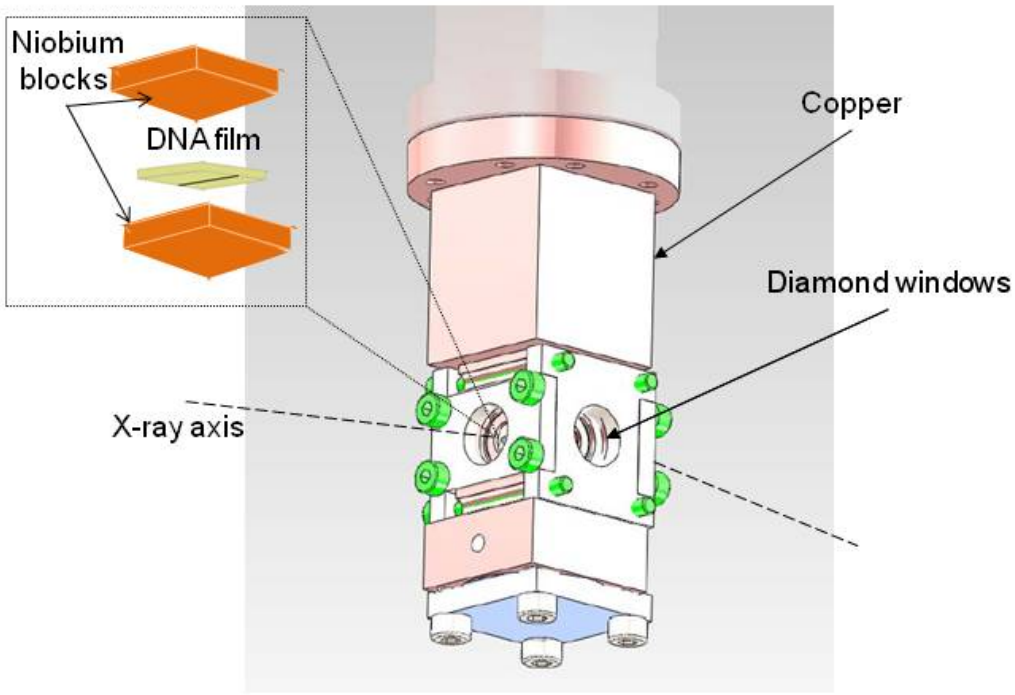

Figure 7.6: Original sample cell for ID28 apparatus. The various elements are listed on the figure and shown with arrows. The cell is made of copper, with four very thin diamond windows, through which the X-ray beam goes. Diamond is used as carbon atoms cause very little attenuation of X-rays. The insert shows the content of the cell. There are two niobium blocks pressing the thin DNA film. The direction of the fibre has been drawn with a black line.

The IXS measurements were carried out on ID28 at the ESRF (Grenoble). The instrument was previously described in section 2.3.4, Chapter 2.

The Si(12,12,12) monochromator was used, providing the maximum flux 5.85 x 10^9 photons/s/200mA. With this configuration, the wavelength is defined as 0.522598 Å(E_i=23.725 keV) with an energy resolution of $\triangle E$=1.3 $\pm$0.1 (meV). The accessible Q-range was $0.1 \leq Q \leq 11.1$ Å^{-1}, with a momentum resolution, $\triangle Q$ of 0.324 Å^{-1}. A layout of the instrument was given in Figure 2.11 in Chapter 2.

Our experiments focused on the acoustic modes of the first BZ for Q_H = 0.9, 1, 1.5, 1.8, 2.5, 2.64, 3.1, 3.4 and 4.2 nm^{-1} covering a range from -30 to 30 meV. Some of the measurements were repeated at different temperatures, from 297 K up to 356 K, to investigate phonon softening.

A second series of the same type of measurements were carried out using a humidity control cell designed for the experiment. It had an entrance for nitrogen gas humidified through a bubble chamber for the DNA, and an exit also through a bubble chamber. In both bubble chambers there was a solution of NaCl in distilled water, providing a relative humidity at room temperature of 75% RH. The aim of the humidity chamber was to achieve a constant humidity flow of 75% RH throughout the DNA sample, to maintain a constant B-form DNA. The humidity was measured during the whole experiment with a hygrometer connected to the effluent bubble chamber, see Figure 7.7.

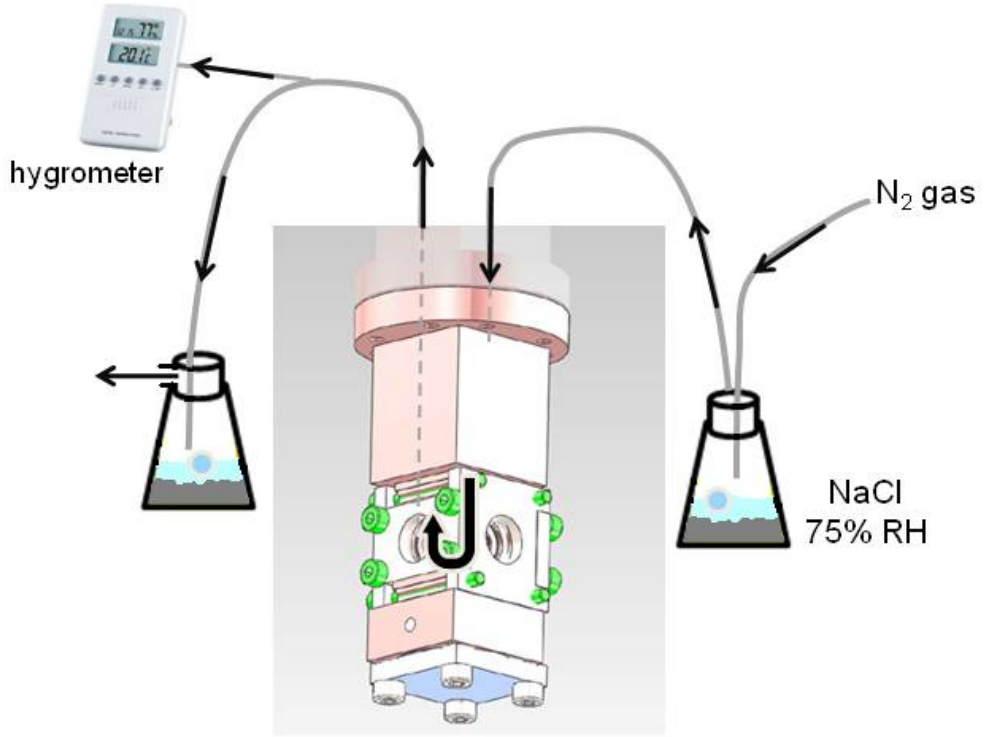

Figure 7.7: The sample cell shown in Figure 7.6 was modified to incorporate a humidity flow of N_2 gas providing 75% RH into the sample. The humidity flow has been marked with black arrows, from the first bubble chamber containing an oversaturated salt solution of NaCl, to the hygrometer connected to the effluent gas tube.

Only four Q-values were measured with this cell Q_H=1, 2.64, 4.2 and 5.83 nm^{-1}, repeated at increasing temperatures 298, 318, 333, 343, 353, 358, 365 and 371 K. The final temperature was expected to be well above melting. No measurements were taken within an hour and a half after each temperature change, to ensure thermal stabilisation of the sample. At each new temperature, before and after the inelastic measurements, an S($\mathbf{Q}$) scan comprising the Bragg peak was taken to check the structure stability of the sample. Once the experiment finished the sample was removed and measured using DSC to obtain the melting curve and check if it had denatured as expected.

In order to investigate the phonon correlation as a function of temperature through the melting transition, inelastic scattering measurements must be performed with samples that are stable upon heating. This can only be achieved by having the sample under controlled humidity, which has become the challenge of these measurements.

The IXS spectra can be characterised by the combination of two responses: a delta function for the elastic line at zero energy transfer; and a "damped harmonic oscillator" (DHO) describing the inelastic modes. A standard fitting routine may be used to model the main features of the spectra which requires a minimum of parameters.
The data were fitted with a the DHO convoluted with the resolution function which was described by a Lorentzian.
From the DHO fit, the frequency ω of each mode measured at the different Q-values was obtained. And thus, at each temperature the resulting dispersion curve was mapped.

Results

Figure 7.8 shows the IXS measurements obtained where the sample was not subjected to a humidity control. The spectra show the elastic line with fitted excitations for the different momentum transfers, Q = 0.9 to 4.2 nm^{-1}, taken at 297 K.

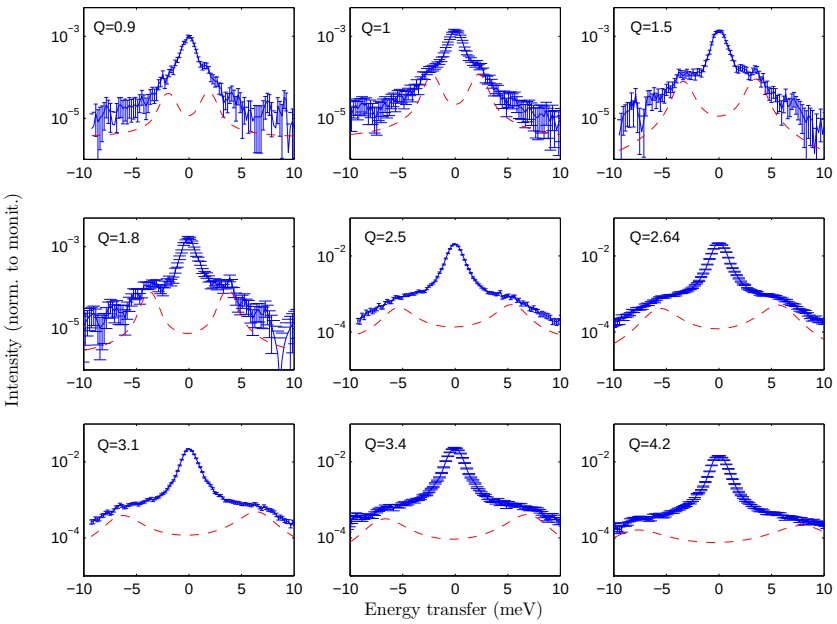

Figure 7.8: IXS spectra with fitted excitations for each Q at T=297 K.

The DHO model gives a good fit of the inelastic phonon excitations. Their energy position increases with increasing Q, due to a phonon dispersion. The width of the mode broadens with increasing Q, the phonons become more damped resulting in a decrease of their amplitude. Figure 7.9 shows the phonon dispersion curve at T =297 K for all measured Q-values. Due to the energy resolution we could not resolve $\triangle E < 2$ meV, so that at this

point we can not conclude whether the dispersion is liquid-like or crystal-like. A linear fit was applied to the data for which the slope is related to the sound velocity v_s=2 km/s of the dispersion.

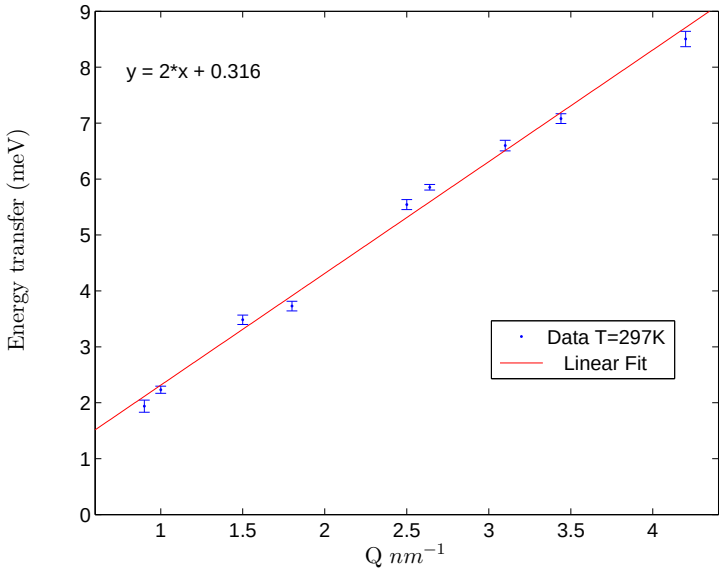

Figure 7.9: Dispersion curve of the eigenfrequency ω obtained using the DHO model at T=297 K for Q = 0.9, 1, 1.5, 1.8, 2.5, 2.64, 3.1, 3.4 and 4.2 nm^{-1}. The data (dots) was modelled with a linear fit (red line), whose slope is given by v_s=1.998 km/s.

The following results were obtained with the use of the humidity control flow cell. IXS measurements were taken at different temperatures, as well as elastic scans through the Bragg peak to determine the stability of the DNA form. Figure 7.10 shows the IXS spectra with the fits of the inelastic excitation at 298, 318 and 353 K. Measurements were taken at higher temperatures, up to 371 K, in which inelastic excitations were still detected. However the fitting model did not show a good agreement with the data at those high temperatures, and thus only IXS results measured at temperatures up to 353 K are presented. As observed from calorimetry data, the B-form Li-DNA undergoes a melting transition at temperatures between 355 K(56% RH) and 365 K (75% RH). And thus, at 371 K we expect the sample to have melted. In that disordered state phonons should no longer be detected, but they were.

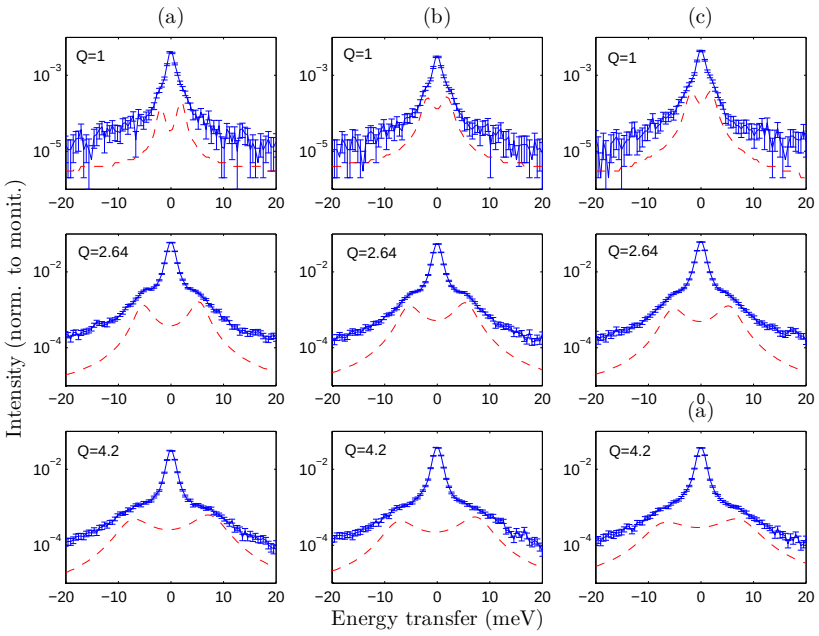

Figure 7.10: IXS spectra with fitted excitations as a function of Q at each temperature. Each column corresponds to a temperature: 298 K (a), 318 K (b) and 353 K (c).

Figure 7.11 shows the elastic scans of the Bragg peak measured at different temperatures. At the two lowest temperatures the structure seems stable, but it undergoes a considerable decrease in intensity and broadening of the Bragg peak at higher temperatures $T > 320$ K. Despite the humidity flow, it seemed that the sample was drying. It is known that Li-DNA acquires a B-form within a broad range of hydration levels, but at extreme low levels, the sample is no longer in a stable B-form, and even leading to a loss of the molecular orientation. The decrease of the Bragg peak intensity is associated to the loss of the B-form base pairs long range order, but not to the thermal denaturation.

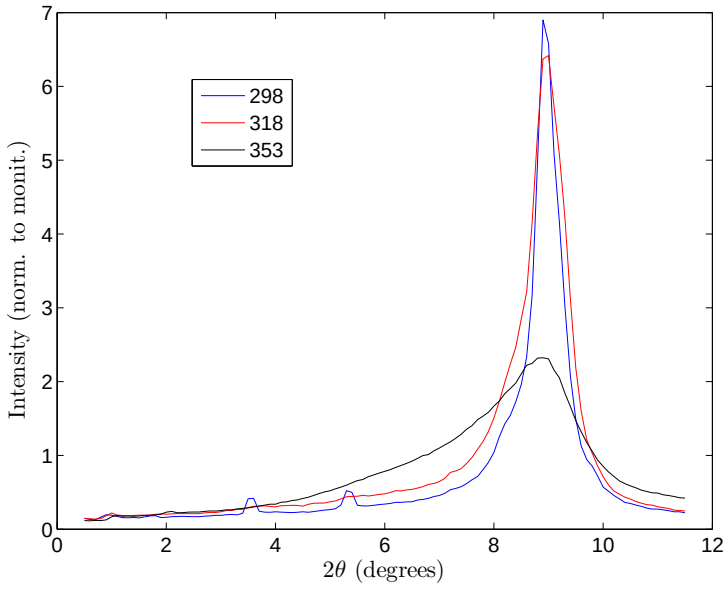

Figure 7.11: Elastic spectra comprising the B-form base pair Bragg peak, taken at different temperatures: 298, 318 and 353 K.

The dispersion curves for the latest measurements at each temperature, 298 K, 318 K and 353 K, are plotted in Figure 7.12. No softening mode behaviour is observed. A linear fit was applied to the data, whose slope corresponds to the speed of sound, $v_s = 1.89 km/s$. While at higher temperatures, $> 353K$, it cannot be stated that the modes correspond to a B-form oriented sample, the $S(\mathbf{Q})$ maps proved that this was the case for the two lowest temperatures.

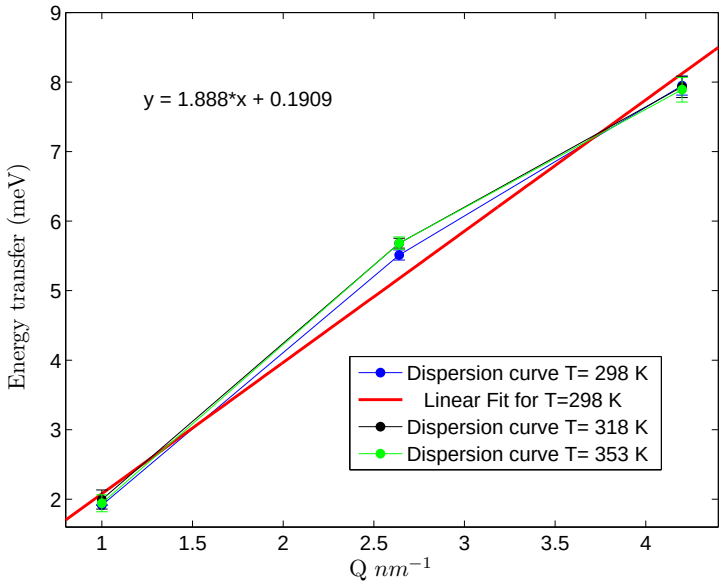

Figure 7.12: Dispersion of eigenfrequency ω obtained using the DHO model at three temperatures, 298 (blue curve), 318 (black curve) and 353 K (green curve). The linear fit applied to the data is shown (red curve). The sound velocity given by the slope corresponds to 1.89 km/s.

Both IXS measurements, without and with humidity cell, give a similar value for the speed of sound at room temperature, 2 km/s and 1.9 km/s, respectively. The differences may lie in the fact that the second set of measurements were obtained with a better humidity control of the sample at room temperature. These values are still lower than that reported in previous IXS experiments [65] of 2.83 km/s, which never measured inelastic excitations at $Q < 2.5$ nm^{-1}.

Once the experiment was finished the sample was removed from the humidity cell. It was then confirmed by direct observation that the sample had dried out, as it looked very rigid and brittle. It was placed in a plastic tube which was not sealed, so the sample could have been exposed to ambient humidity. Calorimetry measurements were then carried out on the sample to investigate why at temperatures of 371 K, phonons were still present. Figure 7.13 shows the first and second DSC heating ramps. In the first ramp, two transitions are observed. The low temperature one could be associated to a conformational change. The second peak corresponds to DNA melting at around 340 K. The second heating ramp shows a glass-like behaviour as expected. The figure proves that the sample never melted on ID28, since we know that the transition is not reversible in fibre samples. The transition temperature appears at a lower temperature, which is consistent with a sample

rehydrated during its exposure to the atmosphere relative humidity, to a level lower than that at 56% RH.

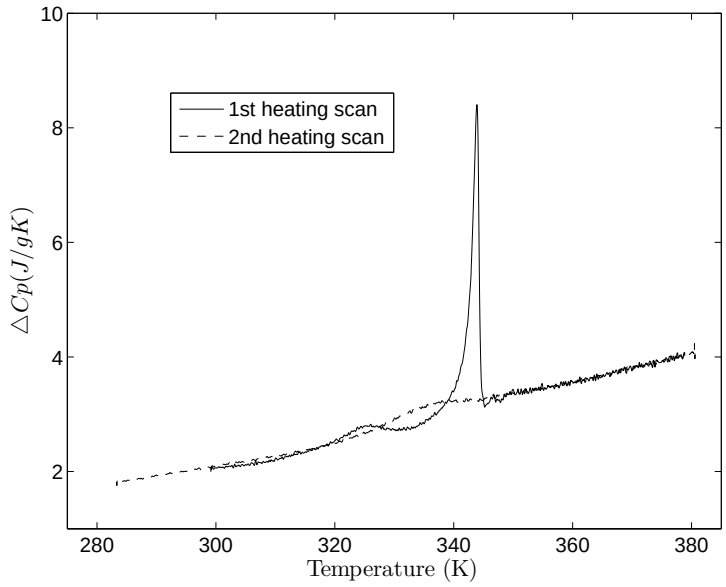

Figure 7.13: First (continuous line) and second (discontinuous line) DSC heating scans of dried DNA oriented sample measured at 1.2K/min. The sample was previously exposed to IXS measurements at different temperatures, from 298 up to 353 K.

In order to investigate the melting transition of a completely dried sample, as we believe is the case for the IXS sample at the high temperatures, another set of DSC measurements were carried out with a dried and a humid sample. The following figure shows the melting profile of two pieces of the same Li-DNA sample subjected to two different hydration conditions: dried, by leaving the sample in a silica gel desiccator during 1 day; and humid to 75% RH during 2 days. The figure shows the first and second heating DSC scan of both samples. The dried sample shows no melting transition within the measured temperature range, which it is present in the humid sample. This concludes that the dry sample could have been exposed to such high temperatures without undergoing a melting transition.

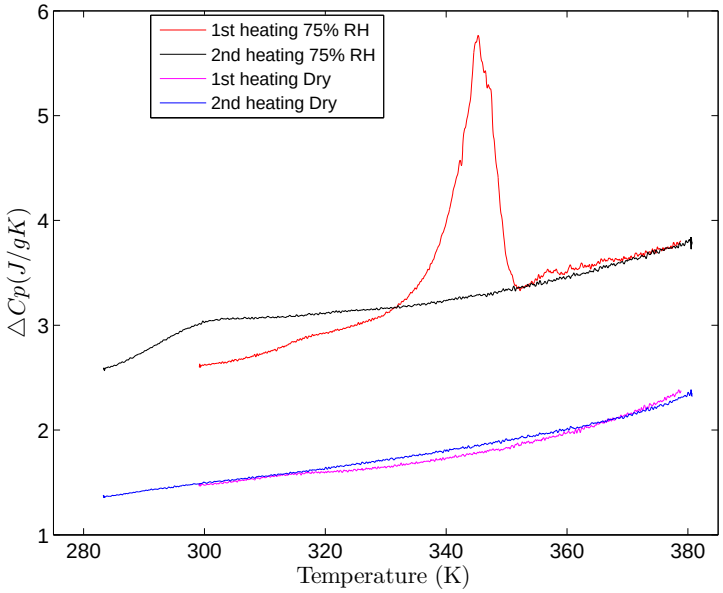

Figure 7.14: DSC heating scans of two pieces of a Li-DNA sample: one exposed to a dry atmosphere (blue and magenta curves), and the other to 75% RH (red and black curves). The first heating scan shows the melting transition in the humid sample (red), and a flat baseline for the dried one (magenta). The second heating scan shows the known glass transition in the humid sample (black), and again a flat baseline for the dried one (blue).

7.4.2 Longitudinal modes with INS (TAS)

Experimental Method

The purpose of using a three-axis spectrometer is to complement the previously published data [11] by resolving the eigenvectors for the low energy acoustic and optic phonon branches. This allows the determination of the elastic constant along the helical axis. The measurements aimed to map the same region as IN5, i.e. the base pair Bragg peak centred at (0,0,10).

The IN14 TAS instrument was used (referred to 2.2.4 in Chapter 2 for complemented material on the TAS technique). Several measurements were made under different configurations in order to identify the acoustic dispersion. As a first approach the instrument was configured with a flat PG analyser, and a 40' collimation before and after the sample. For the first set of measurements k_f was chosen to be 1.5 Å^{-1}. The sample was cooled to 70 K and a number of constant-Q scans were made at various points between 1.85$\leq$ Q_H $\leq$1.955 Å^{-1}. The background was measured by misaligning the momentum transfer with respect to the fibre axis.

Higher resolution measurements were made using three 40' collimators, one before and

one after the sample and the third between analyser and detector. The sample was cooled to 2 K, and constant energy scans at $\triangle$E= -0.7, -0.5, 0.5 and 0.7 meV were performed. Measuring both sides of the energy spectrum at low temperature was done to eliminate suspicions of an spurious signal. At those temperatures the signal is expected to be much weaker at negative energy transfers because there are so few thermally excited phonons to give energy to the neutron.

The sample was heated to 70 K and Q-scans were measured at constant $\triangle E$= 0.34, 0.5 and 0.6 meV.

Figure 7.15 gives examples of constant Q- and E- scans carried out during these measurements.

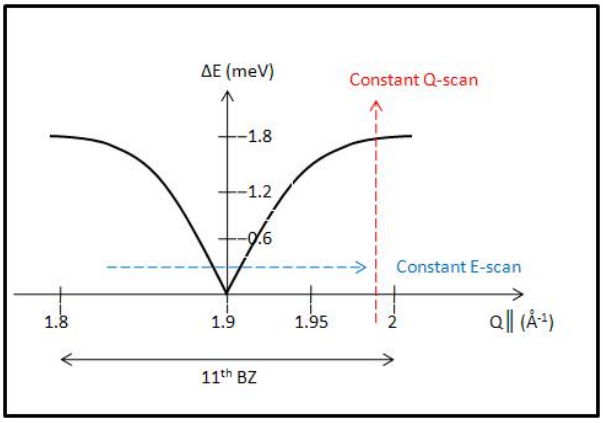

Figure 7.15: Representation of the studied dispersion curve corresponded to the 11th BZ, where constant E- and Q- scans have been drawn.

Results

Figure 7.16 shows the constant-Q measurements (energy scans) for three different momentum transfers, Q_H, at 70 K.

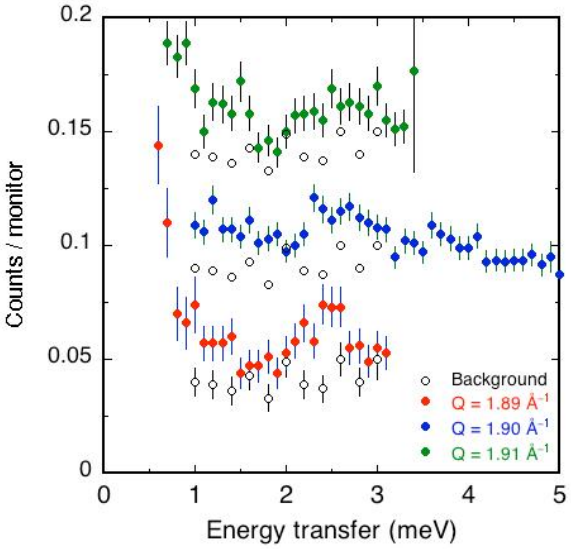

Figure 7.16: Examples of the constant Q_H scans carried out on the B-form oriented sample at 70 K. The background was measured by misaligning the sample such that the momentum transfer was no longer along the fibre axis. The Bragg peak is found at Q_H = 1.89 (Å)$^{-1}$. These measurements were made with k_f = 1.5 (Å)$^{-1}$.

The data show a possible feature at an energy transfer of around 2.5 meV. This corresponds to the position of the optic mode that was previously observed on IN5. There are signs of inelastic scattering at smaller energy transfers that could be associated to an acoustic mode but nothing definitive can be stated. Measurements were made with k_f = 1.3 Å^{-1} which significantly improved the resolution, however these measurements were also not able to clearly show the acoustic phonon.

The constant energy measurements carried out using and a open-40'-40'-40' collimation configuration showed clear evidence of acoustic phonons in the positive energy part (phonon creation) of the spectrum at two temperatures, 70 K and 2 K. A Gaussian function was used to fit the inelastic excitations. Figure 7.17 shows constant-E scans at E= 0.34, 0.5 and 0.6 meV at T=70 K. The modes with the correspondent fits have been plotted as a function of energy transfer (right y-axis), as well as an estimation of the dispersion curve with a slope v_s= 0.9 km/s (discontinuous red lines). The dispersion curves obtained by M. Johnson *et al* on IN5 [11], with a slope = 4.3 km/s (solid black lines), have been superimposed. The values of the speed of sound obtained on a TAS compared to those reported on a ToF are very different, and a further interpretation will be given in the discussion. The intensity of the modes, given on the left y-axis, were off-set for a better representation of the dispersion curve.

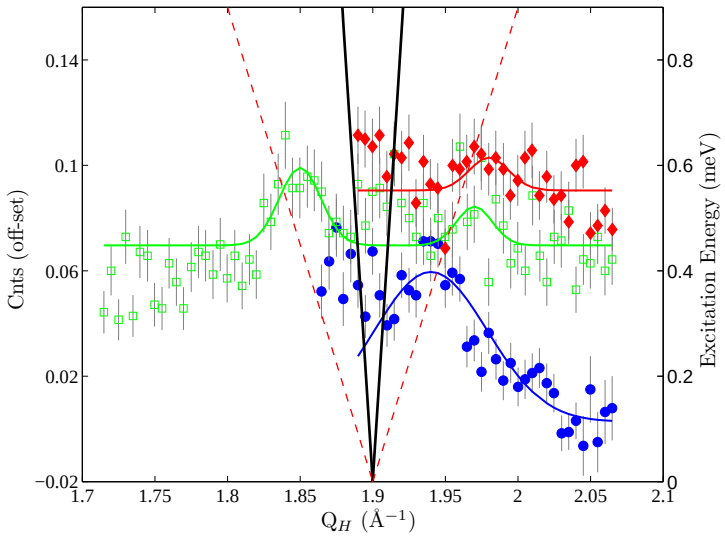

Figure 7.17: Constant energy scans carried out on the B-form sample at 70 K. The spectrum corresponds to the energy transfers: 0.34 meV (blue), 0.5 meV(green) and 0.6 meV (red). The first and the last have been off-set by -0.0095 and +0.03 respectively. The Gaussian fits are also shown for a better distinction of the modes. Their dispersion curve was estimated with a slope of 0.9 km/s (discontinuous red line). The dispersion curves associated to the results obtained on IN5 by M.Johnson *et al* are also presented (solid black lines), whose energies are indicated on the right hand side y-axis.

Figure 7.18 shows the constant-E measurements in the positive energy part of the spectrum (phonon creation) at T=2 K.

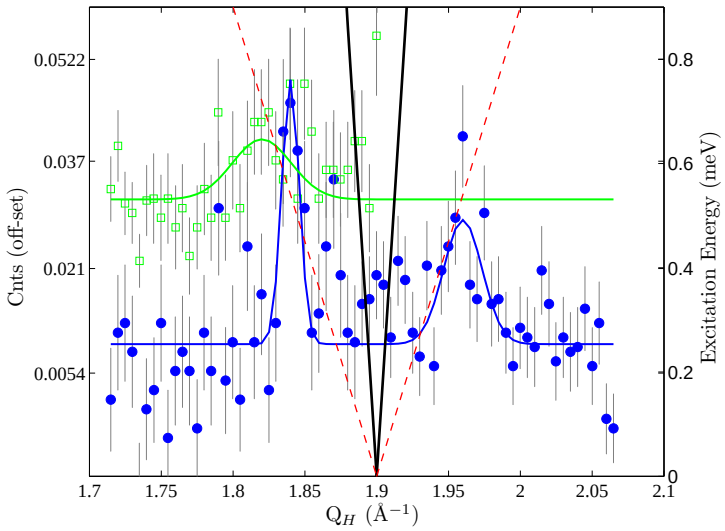

Figure 7.18: Constant Energy scans carried out on the B-form oriented sample at 2 K. At E= 0.5 meV (blue) and E=0.7 meV (green). The 0.5 meV modes were off-set by -0.04. Their dispersion curve was estimated with a slope of 0.9 km/s (discontinuous red line). The dispersion curves reported by M.Johnson *et al* are presented with continuous black lines, whose energies are indicated on the right hand side y-axis.

7.5 Longitudinal Modes in the Transversal Configurations using INS

These measurements were motivated by the role of transversal phonon in bubble formation. With increasing temperatures one expect the optical modes to increase in amplitude and intensity, as well as a soft mode behaviour close to the melting temperatures. The aim when the project started was to detect the dispersion curve of transversal phonons and study its behaviour as a function of temperature up to melting transitions. But as the temperature increased, the DNA signal was more difficult to resolve from the background. Transversal optical phonons from the base pairs were expected at 10 meV, according to Raman Scattering [99], [100].

As discussed in the introduction, the A-form is a more crystalline structure than the B-form, allowing to explore phonon excitations in the vicinity of different Bragg peaks perpendicular to the fibre axis. However, our characterisation of samples of both forms, impure A- (not heat treated) and B-form, in the $Q_K - Q_L$ plane detected broad transversal

features associated to Bragg peaks spread in space due to a preferred orientation (as shown in Figure 4.16 in Chapter 4). Moreover, the texture of these peaks is more prominent in the B-form, so that our first attempts were carried out on the A-form.

7.5.1 Sample Configuration

The B-form films were prepared from a Li-DNA solution and humidified at 56% RH in D_2O, and the A-form films were humidified under 56% RH in D_2O. The films were folded and enclosed in a niobium envelope inside an aluminium cassette to preserve the water content. The samples were placed with the fibre axis perpendicular to the scattering plane, such that the momentum transfer was aligned with the Bragg peak associated to an interhelical distance perpendicular to the helical axis. Reciprocal space maps of the $Q_K - Q_L$ plane show several Bragg peaks perpendicular to the molecule axis, detected at (Q_K, Q_L) =(0.32,0) Å^{-1} for both Li-DNA and Na-DNA samples; less prominent but relevant Bragg Peaks at further Q_K were mapped in Li-DNA, at 0.56, 1.2, 2.4 Å^{-1}(Figure 4.16 Chapter 4).

7.5.2 IN8, Triple-Axis Spectrometer

Measurements

The first experimental approach was to search for optical phonons at a zone centre with eigenvectors perpendicular to the fibre axis. Measuring in the vicinity of the transversal Bragg peaks (in the $Q_K - Q_L$ plane), with $\mathbf{Q}$ along Q_L, probes longitudinal phonons propagating transversal to the fibre axis. The aim was to detect any inelastic excitation and then tilt the sample about Q_K to introduce a Q_H component (which is along the helical axis), and thus have access to transverse phonons propagating along the fibre.
The experiment was configured with a fixed $k_f = 2.662$ Å^{-1}. Due to the limitation in the instrument geometry it was difficult to reach the required high energy transfers at low Q. For the A-form sample, energy scans were taken at fixed Q_L= 0.32, 0.64, 0.96, 1.28, 1.60 and 1.65 Å^{-1}, at a temperature of 80 K. Only scans higher than $Q_L \geq 0.96$ Å^{-1} covered an energy range high enough to comprise the expected optical mode, $\triangle E$= 0 to 12 meV. Kinematic limitations to reach 10 meV at small scattering vectors were encountered.
Since B-form Li-DNA has Bragg intensity at higher momentum transfer Q_L, measure-

ments carried out on this form at higher momentum transfer were able to access a wider energy transfer range.

Due to variations of the incoherent background as a consequence of the shape of the sample (plate) relative to the detector, inelastic energy scans were measured by fixing the sample and analyser angles. Within this configuration, the scattering vector at the elastic position is referred to as Q-nominal (Q_{nom}). INS measurements were taken at Q_{nom}= 1, 1.2 and 4.4 Å^{-1} comprising the expected optical mode at $\triangle E$= 10 meV, at 80 K. Inelastic energy scans were also performed for Q_{nom}= 1.2 and 4.4 Å^{-1} at 10 K.

The same measurements at both temperatures were repeated for an empty sample holder. The sample holder spectra was subtracted to the total inelastic spectra for both Q_{nom} data for each temperature.

Results

Figure 7.19 is a comparison of the energy scans taken for A-form DNA at 80 K at different values of Q_L= 0.96, 1.28, 1.60 and 1.65. It could be argued that there is an inelastic signal at around 9.5 meV, but the signal to noise ratio is very low.

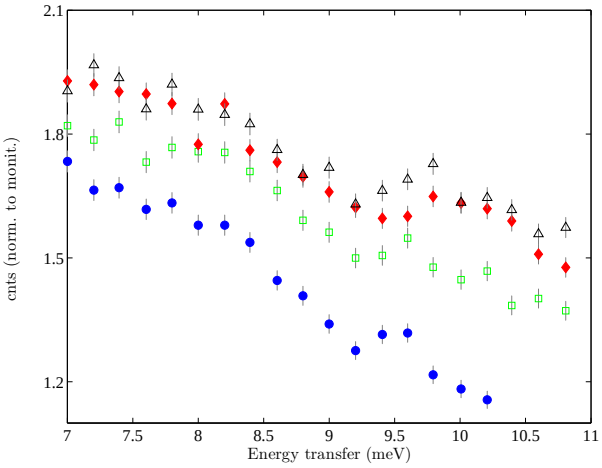

Figure 7.19: Energy transfer versus intensity, corresponding to the energy scans measured for different Q_L= 0.96 (blue), 1.28 (green), 1.60 (red) and 1.65 Å^{-1} (black) at 80 K.

No clear evidence of transversal phonon excitation was found on A-form DNA. Thenceforth, inelastic neutron scattering (INS) measurements were concentrated on a B-form DNA sample.

INS constant-Q scans for Q_{nom}=1.2 and 4.4 Å^{-1}, were measured at 80 and 10 K, as well as an empty can at the two temperatures. Figure 7.20 compares the inelastic scans at a

each Q_{nom} measured at each temperature, where 80 K is represented by blue points and 10 K by green squares. The sample holder contributions have been subtracted.

Figure 7.20-(a) shows at 80 K two inelastic signals, a very broad one centred at 5 meV and a narrower one at 8 meV. At the low temperature of 10 K, the intensity of the signal decreases showing no remains of the signal at the lowest energy transfer (given by phonon population, (n+1)). Figure 7.20-(b) plots the results measured at higher Q-values (Q_{nom}=4.4), so that we expect the inelastic intensity to increase due to the Debye Waller factor ($I \propto Q^2$ for low-Q)). Again by comparing the data at both temperatures a signal at 5 meV is still detected. Referred to equation 2.37 in Chapter 2.

Although the background is still high, due to the temperature dependence we can conclude that inelastic scattering is being detected, and it is stronger at 5 meV. However we cannot assert whether this signal is coherent or incoherent, since dispersion was not probed.

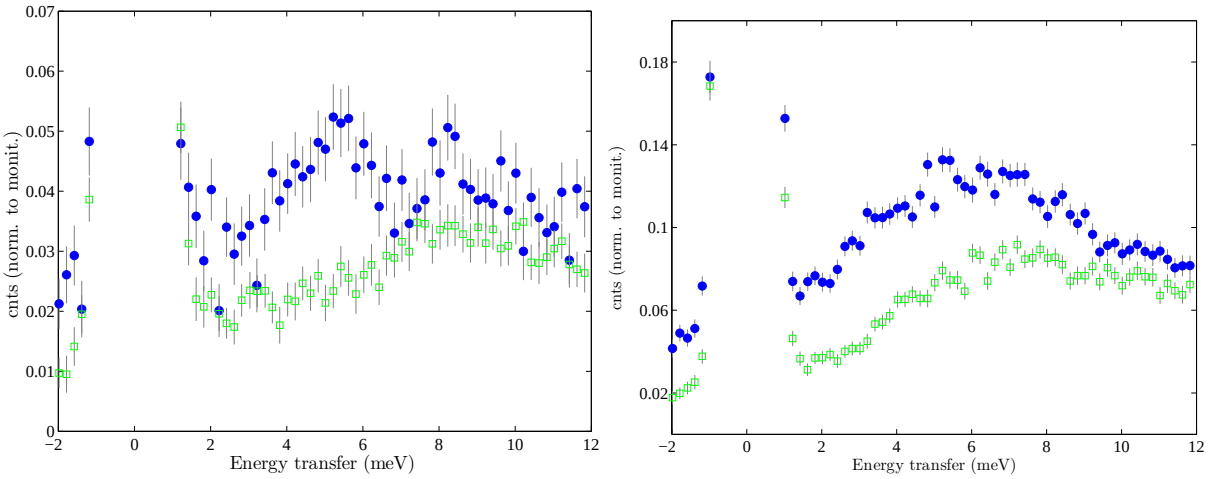

(a) Q_{nom}=1.2 Å^{-1} (b) Q_{nom}=4.4 Å^{-1}

Figure 7.20: a) INS of only DNA contribution for Q_{nom}=1.2 Å^{-1} at two temperatures, 80 K (blue) and 10 K (green);b)Q_{nom}=4.4 Å^{-1}.

7.5.3 IN5, Time-of-flight

Measurements

In order to select the experimental conditions to optimise the energy and momentum transfers of interest on IN5, one must find a compromise between energy resolution, the portion of S(Q,ω) probed and flux. High energy resolution measurements are required to detect low energy excitations, but due to the high incoherent contribution of our sample high flux is also necessary. For these reasons, inelastic measurements were performed at

$\lambda = 4.7$ Å, near to the maximum instrumental flux of 5 Å, with a chopper speed of 8667 rpm. This configuration accessed a momentum transfer range of $0.3 < \mathbf{Q} < 3.62$ Å^{-1}, at the elastic line, and energy transfers -9.9$< \triangle E < 2.2$ meV. This wavelength permits higher $\triangle E$ range to be accessible at lower Q (kinematic condition).

Inelastic measurements were carried out for A-form sample at two temperatures, 75 and 250 K.

The INS data was treated with the computer program "LAMP" (Large Array Manipulation Program). The raw data were corrected by subtracting the empty can data, and finally corrected for detector efficiency by normalising to vanadium. By proceeding with the pertinent unit conversions, from ToF channel and scattering angle to energy and scattering vector, the final spectra are presented in the form of *S(Q,ω)* plots.

Results

Figure 7.21 shows the $S(Q, \omega)$ spectra of A-form DNA in a transversal configuration. The strong Bragg peak at $Q_L = 0.3$ is in the limit of the accessible inelastic region, even so there are no signs of an acoustic branch merging from the Bragg peak, away from the elastic line $\triangle E = 0$. The plots show a possible inelastic signal at around -5 meV displayed along the whole Q-range at both temperatures. As expected from the Debye Waller Factor, its intensity increases with temperature. In these plots the signal appears almost flat in Q, and no dispersion is seen. This probably indicates that the mode is incoherent. The strong intensity feature at positive 2 meV is probably an spurious signal from multiple scattering.

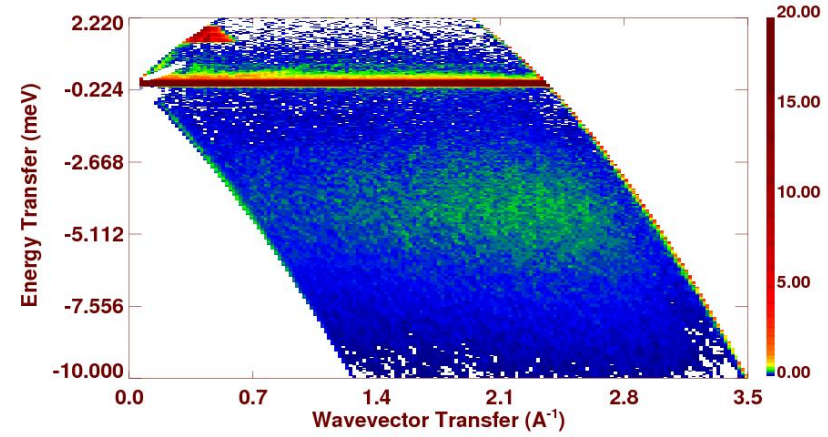

(a) T = 75 K

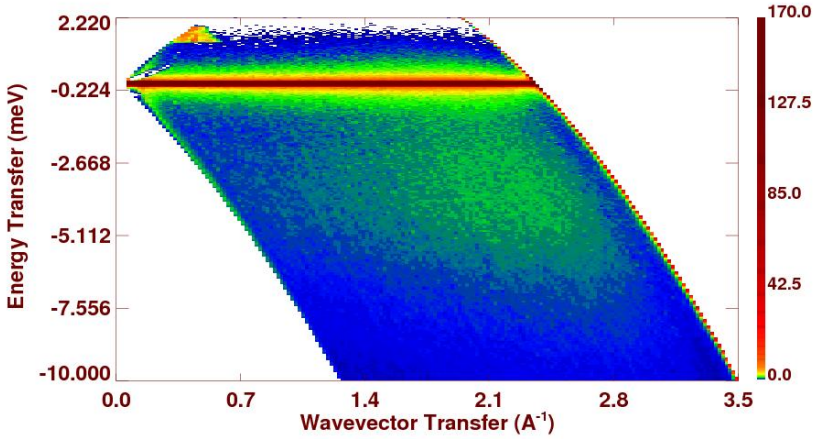

(b) T = 250 K

Figure 7.21: S(Q,ω) plots at two temperatures, 75 K (a) and 250 K (b).

There are two main concerns: resolving the incoherent scattering input by hydrogen onto the total signal; and measuring in a configuration of high resolution in momentum and energy transfer, in the vicinity of Bragg peaks at higher Q-values so that the kinematic condition can be satisfied for higher energy transfers.

7.6 Discussions

7.6.1 Longitudinal Phonons

Measuring the longitudinal acoustic dispersion curve within the 1st BZ for very low-Q values ($0.9 < \mathbf{Q} < 4.2$ nm^{-1}) using IXS, has shown some discrepancies with respect to previous reported values. The acoustic dispersion estimated previously by M. Krisch and co-workers corresponded to a sound velocity of 2.84 km/s being obtained from values

where $Q \geq 2$ nm^{-1}. We believe, previously supported from structural studies, that films of oriented fibres of DNA give rise to crystalline-like phonons as shown with molecular simulations, Figure 7.22. Our IXS results correspond to a sound velocity of 1.89 km/s (with humidity cell) and 2 km/s (without humidity cell), the differences in which may be associated to small changes of the structure due to loss of hydration. At room temperature, elastic scans proved that the structure was stable while inelastic measurements were performed using a humidity cell, so these results are considered to be more accurate. The lowest energy transfer values that could be resolved with IXS were 2 meV.

The comparison between our results and those previously reported were made with the reference to the molecular dynamic simulations obtained by M. Johnson and co-workers. Figure 7.22 was adapted from reference [11]. It shows a contour map of the calculated scattering intensity given as a function of BZs and energy transfer in a B-form. The BZ size is defined by the DNA helix turn. The acoustic dispersion curves for $\triangle E < 2$ meV can be clearly seen in each BZ. At higher energy transfers, the inelastic modes become indistinguishable. But one can see variation in intensity due to the dynamical structure factors. We have used this figure to interpret our results compared to those reported by M. Krisch *et al*, where white lines have been drawn on the figure to indicate the respective acoustic slopes. The broad arc comprising the whole reciprocal space was expressed by M.Johnson *et al* to correspond to the modes seen by M. Krisch *et al*. In this context, ours results show a lower slope (shorter white line).

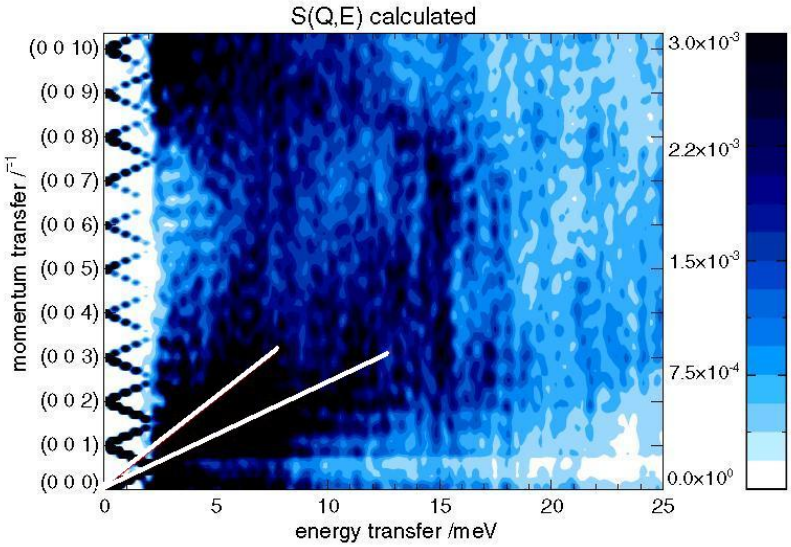

Figure 7.22: A contour map of the calculated scattering intensity (logarithmic scale) versus energy transfer and Q (labelled in terms of the Brillouin zones of the helix) from phonon calculations [97]. The longer white line was drawn to represent the dispersion curves obtained from [65], while the shorter corresponds to our values obtained with IXS. The figure has been adapted from [11]-FIG.4.

We have not been able to investigate changes in the phonon correlation along the molecule on a stable B-form DNA as a function of temperature, due to the lack of control of the humidity. The free volume in the IXS sample holder was larger than in the neutron case, allowing the hydration of the sample not only to decrease but become completely dry; revealed by a considerable loss in intensity of the base-pair Bragg peak. In the dry state, the molecular orientation and B-form can no longer be guaranteed, and the sample does not go through a melting transition within the characteristic temperature range (Figure 7.14). An alternative solution to the problem, apart from introducing modifications to the humidity cell, is to increase considerably the amount of sample to reduce the free space in the cell, as it will resemble to the scenario accomplished in a neutron experiment.

INS measurements on the triple axis spectrometer IN14 showed modes probing the acoustic longitudinal dispersion curve centred at the (0,0,10) Bragg peak. From Figures 7.17 and 7.18 an estimation of the speed of sound gives a value of 0.9 km/s. These results differ significantly from those performed by M. Johnson *et al* using IN5, obtaining a value of 4.3 km/s. Furthermore, our results cannot be interpreted using the phonon calculations in Figure 7.22. The reason for the discrepancies could lie on the way the measurements were done. While on IN14 (triple-axis) the eigenvectors were obtained measuring in a high symmetry direction; on the time-of-flight measurements the sample was treated as

a powder, and thus the dispersion obtained could have been the result of a combination of eigenvectors. Furthermore, the Q-resolution on IN5 was also considered for a powder system, while the sample has a crystalline nature. This may also have had an influence on the energy values.

Table 7.1 summarises our obtained values with those previously reported for the speed of sound measured with different technique , IXS and INS.

Technique	Speed of Sound, v_s	Reference
IXS	1.89 / 1.998	Our values
IXS	2.84	[65]
INS (Triple axis)	0.9	Our values
INS (Time-of-flight)	4.3	[11]
INS (Triple axis)	1.85	[64]

Table 7.1: Summary of the speed of sound v_s, previously reported and measured by us, of the longitudinal acoustic phonon on samples of oriented fibres of B-form Li-DNA. The scattering techniques with which the measurements were carried out and the references are also given.

7.6.2 Transversal Phonons

Our inelastic neutron scattering investigations into the inelastic excitations in the transversal configuration of the crystalline A-form and crystalline B-form DNA has not been conclusive. If present, inelastic excitations within this configuration seem to be weaker than the longitudinal modes and incoherent scattering from hydrogen hinders their observation. Furthermore, the kinematic conditions impeded the measurement of large energy transfer (10 meV) at small scattering vectors, $|Q| = 0.3$ (Å)$^{-1}$.

However, a broad inelastic signal was detected for the B-form DNA sample for Q_{nom}=1.2 and 4.4 Å^{-1} centred at around 5 meV energy transfer using triple axis INS. The modes are detected in the positive energy transfer part of the spectra (phonon creation) at high temperatures 80 K, and as expected the inelastic signal decreased considerably at 10 K, providing additional evidence of the mode. At the same energy transfer a very broad inelastic signal was detected using time-of-flight INS for the A-form DNA sample, which lack of dispersion (flat-Q) indicates that the signal it is likely to be incoherent scattering.

7.6.3 Future Prospects

INS measurements on a time-of-flight instrument (IN5) were recently carried out by M.Johnson. These were centred on a transversal Bragg peak $Q_L = 0.34$ Å^{-1}, of the B-form Li-DNA to detect transverse phonons. The experimental conditions were not optimal with an incident wavelength of 5 Å, as the low-Q Bragg peak was in the limit of the $S(Q, \omega)$ accessible region, using a higher wavelength will allow the low-Q Bragg peak to be accessed. Moreover, the measured sample did not represent the hydrated B-form studied in previous experiments as it was never rehumidified on time for this test experiment. Finally vanadium was never measured in the same configuration.

Figure 7.23 consists of transfer energy cuts versus intensity at different $Q_L = 0.3$, 0.32, 0.34, 0.36, 0.38, 0.4, 0.42 and at 0.6 Å^{-1}. The latter refers to a position far from the Brillouin zone centre, where inelastic signal is not expected. Despite these limitations the results shows shoulders on the elastic line which could be an indication of transversal acoustic phonons.

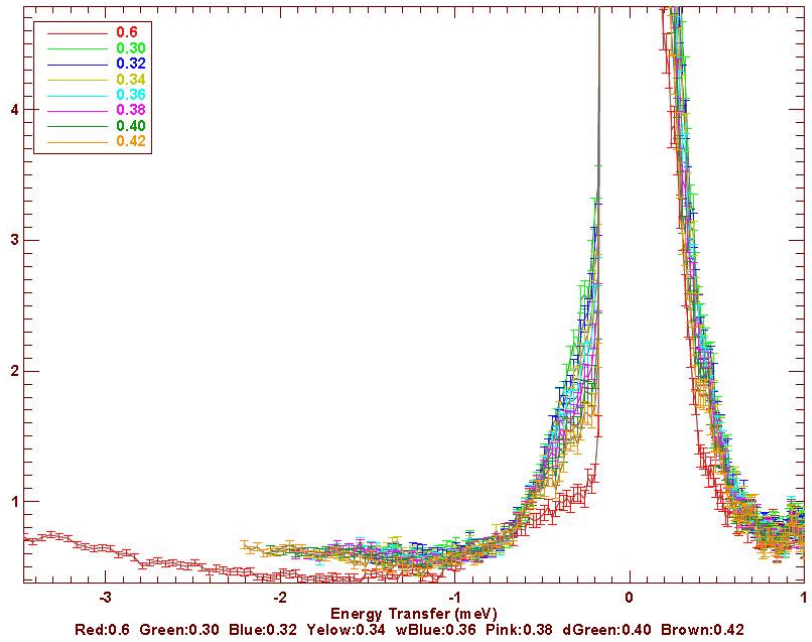

Figure 7.23: INS measurement of the transverse phonons on B-form DNA using TOF technique (IN5). The figure plots intensity *vs* energy transfer at different $Q_{\perp}$ showing in the legend. The image have been provided by M. Johnson obtained during a test experiment in December 2011.

This gives us confidence to proceed with future experiments to look for transversal phonons on the B-form DNA, especially for the acoustic mode, under improved experimental conditions.

With respect to the A-form DNA samples, we must consider atomic scale force field based phonon calculations which will assist in where to look in reciprocal space.

Later diffraction experiments on the pure A-form DNA showed a strong Bragg peak in the $Q_H - Q_K$ plane at (0.5,0.25) Å^{-1} (see Figure 4.26-(b) in Chapter 4) which has a transversal Q-component. This Bragg peak of higher Q-magnitude, permits to accomplish the configuration described in Figure 7.3 to detect transversal phonons propagating along the helical axis, and to explore higher energy transfers. INS measurements in the vicinity of this Bragg peak introduces better conditions to detect phonon dispersion curves.

In addition, to complete the transversal and longitudinal spectra for both studied DNA conformations on oriented DNA, further experiments have been programmed to study longitudinal phonons on the A-form.

Decreases in the hydration of a Na-DNA sample in a B-form leads to a transition into an A-form. This transition on wet-spun films was determined using Raman spectroscopy to cause a mode softening at 25 cm^{-1} (3 meV) [101]. We proved that spun A-form samples

always contain some contamination of B-form that can be eliminated by heating the sample to 320 K. It will be interesting to investigate using neutron scattering if during this heat treatment there is mode softening behaviour, which would support our theory that a B to A transition is occurring at that temperature.

Conclusions

The static structure of the DNA double helix was captured for the first time in a fibre diffraction image. Subsequently investigations on DNA were centred in the characterisation of the structure and the different conformations of the molecule by means of fibre samples. However, DNA is a very dynamical system, which at biological temperatures is subjected to constant fluctuations of the double helix strands. As the temperature increases these sporadic openings and closings of the base pairs, become localised forming "bubbles", that at higher temperatures can lead to the complete denaturation of the molecule. These fluctuations are of a great interest for biologists since they allow the reading of the genetic code by exposing the DNA sequence to the surroundings. For that reason, they have been extensively investigated, but, prior to this thesis, the studies were only made in solution. As a consequence of this, experimental techniques that actually posses sensitivity to spatial resolution, such as scattering techniques, can not be used to resolve the spatial information of DNA in a liquid medium.

The aim of this work has been to obtain structural data on the fluctuations of DNA to characterise the thermal denaturation transition. For this purpose we have worked with DNA fibres, which provide a simple mean to get oriented molecules, and thus are suitable to be investigated using neutron scattering.

In order to proceed dynamical studies high quality samples are necessary, and thus an exhaustive characterisation of the samples has been a considerable part of our research. Two different structures of the DNA double helix, A- and B-form, were investigated. For the first time we have observed the thermal denaturation of A DNA, and proved that it is significantly different from the melting of the B-form. Furthermore, investigations on the reversibility of the transition, unexpectedly showed that DNA can turn into a glass

state after being heated to the denaturation temperature.

In Chapter 4 we carried out static investigations to characterise the structure of oriented DNA fibres in the A- and B-forms. The studies were mainly carried out using neutron diffraction but complemented with X-ray fibre diffraction and calorimetry. From the early discovers of the double helix, both conformations were intensively investigated using X-ray fibre diffraction. There were established the optimal conditions (phase diagram), ionicity and hydration, in order to induce different DNA conformations. Additionally the contamination of B-form in A-form fibre samples in the presence of Na had also been investigated. However, the removal of these B-form residues that seemed to be always present in Na fibres samples up to now has not been the focus of much attention. We found a method which allowed us to get pure A-form samples for our studies. Neutron diffraction measurements made in the B-form Bragg peak of an A-form sample as a function of temperature showed that the intensity dropped considerably at around 320 K, until the total extinction of the peak at around 325 K. Reciprocal space maps on the A-form showed that at such temperatures the features along the fibre, belonging to both conformations, have become diffuse and decreased in intensity. A subsequent rehydration of the sample proved that the A-form features were recovered and traces from the B-form were not present. This transition was consistent with the small endothermic peak observed with calorimetry and a shortening of the fibres as seen by optic microscopy. Therefore, our studies lead us to the determination of a method to obtain pure and stable A-form samples by the removal of B-form contamination, and hence to redefine the accepted phase diagram in order to include the temperature dependence on the DNA forms.
We also investigated the nature of the samples associated to their organisation in the direction perpendicular to the fibre. Within the Wet Spinning method each fibre is wound on a bobbin. One would expect a random orientation of the fibres with respect to each other, which should had appear in the diffraction images as a cylindrical averaged intensity of the Bragg peaks. Surprisingly the diffraction images revealed otherwise. The Bragg peaks in the direction perpendicular to the fibre show a preferred orientation, i.e. not only the molecules are oriented within the fibre, but that the fibres themselves are correlated with their neighbours.

In Chapter 5 we carried out a comparative description of the melting properties of both A- and B-forms of DNA and the effects of having DNA in a fibre confinement.

The first step was to determine melting profiles of different DNA forms using DSC technique. The qualitative description corroborated that samples in the presence of Li-ion have a higher T_m than those of Na-ion, i.e. are more stable; and that a decrease in hydration reduces the molecule stability as seen from a decrease of T_m. We also showed by the transition width that despite the hydration, the B-form is always more cooperative than the A-form. The effects of having DNA in a fibre structure were addressed by a quantitative comparison with DNA in solution of the transition thermodynamical properties: enthalpy, specific heat between native and denatured state, and entropy. Our results revealed deviation within these values by up to a factor of two. We believe that this energy deficiency is associated to the remaining short segments, as seen by electrophoresis, that did not have space to unstack during melting due to the confinement of the fibre.

The preparation of samples that were structurally stable upon heating above the melting transition was crucial for our structural studies of the phase transition using neutron scattering. This permitted us to probe the temperature dependent correlation length associated mainly to the closed base pairs, through the melting transition. At such high temperatures we saw that the fibre nature of the samples can limit the full observation of the transition. This was the case of the B-form film, in which at the reduced temperature θ= 0.99, the fibre seems to "collapse" resulting in the complete loss of the Bragg peak and hence the impossibility to probe the correlation length all the way through the transition. However, this was not the case for pure A-form films which stability upon heating enables monitoring the Bragg peak throughout the transition, and obtaining a complete characterisation of the correlation length as a function of temperature.

The width of the Bragg peak can be described by a simple nonlinear model for DNA at the scale of base pairs, with no free parameter. For the B-form, the satisfactory agreement between theoretical and experimental curves up to the collapsing temperature validates the model. Beyond that temperature the model do not consider the consequences of temperature on the fibre structure. In the case of the A-form only preliminary theoretical analysis have been presented. Due to the complexity of the structure and the fact that the parameters used in the model have never been established, this will require further investigations. The analysis will provide for the first time a description of the melting transition in A-form DNA.

We believe that the main differences in the thermal behaviour of the correlation length

between A and B structures lie in their stacking. Although fibre confinement differs significantly among the structures, it plays a crucial role in the thermal stability of the molecules in the reseaux. The fact that collapsing does not occur in the A-form indicates that in a more confined structure the molecules are less flexible preventing disorientation. The Q-transversal component of the scattering vector in the A-form provides extra information about transverse fluctuations of base pairs. Since no collapse of the fibre occurs, large scale fluctuations important in many biological processes are better investigated in this form.

In Chapter 6 our DSC studies showed that DNA denaturing is not reversible beyond the melting transition. Instead the samples present properties very similar to those of a standard polymer glass, such as PVAc. The glass was characterised by one property, T_f, which allowed the investigation of the relaxation of DNA films and the derivation of the enthalpy barrier $\triangle h$. Cooling experiments, at the slowest rate, showed that the DNA sample undergoes an irreversible evolution, which was not observed for PVAc; and that the enthalpy barriers for both DNA and PVAc before and after the evolution are of the same order, 79/69 kK and 100 kK respectively. This suggests that the thermodynamic evolution of the samples is similar. However, the study of the evolution of the relaxation time τ with aging time showed that relaxation is faster for PVAc than DNA; while after 84 h of annealing the DNA is still evolving towards equilibrium, the PVAc starts to reach saturation. The main differences between the relaxation behaviour of both specimens lie in kinetic effects due to i) the particular structure of DNA, especially the presence of the bases; ii) and the confinement of these molecules in a fibre environment. During relaxation, the slowed reptation of the polymer as a consequence of the bases, increases the chances of partial stacking or formation of hydrogen bonds. These effects are also responsible for the excess of the recovery enthalpy $\triangle H$ at the longest relaxation times of the DNA films over that of PVAc.

Finally, low frequency excitations were studied in Chapter 7 for their role in bubble formation and denaturation, and consequently their importance in understanding the mechanical properties of DNA. Longitudinal phonons on the B-form were measured using INS and IXS techniques. They were compared to previous reports and interpreted using molecular dynamic simulations. Our IXS measurements probed longitudinal phonon dispersion at very low-Q values, $0.09< Q_H <0.42$ Å^{-1}, with a sound velocity of 1.89 km/s using the

humidity cell control. At higher temperatures the sample started to dry yielding in a loss of molecular orientation; which may have impeded the detection of phonon softening. The results are consistent with phonon calculations if described as the combination of optical modes. On the other hand, our results measured on a high symmetry direction on IN14 gave a dispersion of 0.9 km/s. These are puzzling, since they are not consistent with the results obtained on the time of flight IN5 instrument. The optimal experimental conditions used on IN14 suggests that the reason for the discrepancies may be linked to the way the measurements were done, since on IN5 the sample was treated as a powder which we proved not to be the case.

The investigation of transversal phonons were not conclusive and no dispersive signal was detected in the $S(Q, \omega)$ region probed. Furthermore, resolving inelastic scattering from the high incoherent background due to large amounts of hydrogen within the sample became a problem in neutron scattering experiments. We believe that molecular dynamics simulations would shed some light into where to look in order to prepare future experiments.

Future Prospects

First attempts to obtain an expression of the Hamiltonian specifically for DNA [102] were done by M. Peyrard and A.R. Bishop with the Peyrard-Bishop model [5]. To date this model does not yet describe all features of DNA, but our investigations of the structural information of DNA melting transition have shown that it provides a rather good model for DNA thermal denaturation. These studies can be used to improve physics models for DNA. Their importance have been propelled by the consideration of the molecule for possible applications such as in technology. Examples of this field, considered today, are DNA-based computers, in which the computer signal corresponds to the high or low concentrations of the molecule [103], [104]. The advantage of creating tiny-computers promoted the interest of the vast implications in molecular programming, these devices when introduced in cells can control their activity, i.e. practice euthanasia with the cells.

Spatial constraints due to fibre structure should be further investigated, as it could play a role in DNA melting or its glass state. We showed that B-form is highly affected by the fibre structure due to film collapsing at the temperature where 50% of DNA had melted. This was not the case for A-form which proved to be more stable upon heating under this

fibrous environment. However, the experimental width which has not yet been successfully modelled could be affected by these intermolecular barriers. As a first attempt, a qualitative study of the diffraction images as a function of temperature could be carried out using X-ray fibre diffraction. This could provide information about the different Bragg peaks associated to the inter and intra-molecular structure, and thus learn about a possible cooperative phenomenon between DNA melting and film disorientation. This type of measurements can be done on the Macromolecular Crystallography beamline ID23, but a humidity control sample cell is required in order to ensure the structure stability. Within this context, it could be also interesting to study samples where constraints due to fibre structure have been relieved while maintaining the molecular orientation. This has already been investigated by means of osmotic pressure, provided by a polymer solution[105], for example, in PEG, in which the fibre samples are immersed. This results in an expansion of the fibres in the film without the loss of molecular orientation.

Collective modes and their dispersions in DNA is still an open topic. Our longitudinal INS results have shown to be limited by the intrinsic characteristics of the sample. That is, incoherent scattering coming from hydrogen, critical for neutron scattering measurements; and a control of the hydration of the sample, which has not yet been achieved on a X-ray instrument. In order to resolve the acoustic dispersion curve from the optical, in the vicinity of the (0,0,10) Bragg peak, INS is our best tool due to its energy resolution. However, not much can be done about the incoherent signal since total deuteration of a sample of those dimensions will be unreasonable. The quickest tool to map the $S(Q,\omega)$ region of interest at once would be IN5; and by using a rotating table the inelastic signal can be resolved in a particular direction, **Q**. This would be carried out to study longitudinal phonons on A-form DNA in May.

On the other hand our measurements on the transversal excitations of DNA have not been very successful, partly due to the incoherent signal and partly due to kinematic constraints. The finding of the low-Q Bragg peak at (0.5,0.25) Å^{-1} and a careful choice of wavelength would resolve the latter limitation.

The work on the collective excitations is actively in progress because we believe that most of the limitations can be overcome. We believe that samples of oriented DNA fibres are good candidate to continue this research for several reasons: we have an unlimited access of samples of any desirable size (X-ray or neutrons purposes), their fibre orientation

imposes crystal properties, and we have established the optimal conditions to attain stable samples of pure DNA forms.

Another topic which requires attention, and for which diffraction studies could be of great interest is the study of DNA flexibility. Ultimately, this property should be better investigated in solution as it is more representative of the conditions in which biological processes occur. DNA flexibility is responsible for the interaction of the molecule with proteins in genome transactions, but also it quantifies the ability of the DNA to pack in structures such as cell or virus. A proper quantification of the flexibility requires measurements of the persistence length. Many studies made in solution have tried to establish the effects of bubble formation into this characteristic length, as they seem to behave as "flexible joints" where the molecule can sharply bend. This phenomenon motivated recent theoretical studies carried out by M. Peyrard and N. Theodorakopoulos using the PBD model [6]. They were able to successfully model with no free parameters relevant data on the matter measured in the 70's. Their achievements stimulate further interest in a proper systematic study of the effects of bubble formation in the persistence length as a function of temperature. The idea is to use synthetic DNA in solution so that the temperature dependence of the persistence length can be directly modelled. This can be performed using small angle neutron scattering, suitable to measure micrograms of these samples. A proposal on this technique has been submitted in the proposal round of February 2012.

Our studies not only prove the power of scattering techniques to investigate the physics of DNA, but they mean a start point for many other investigations to be carried beyond. The availability of good fibres and film samples has been very important for our achievements, but further developments could even require more efforts in this direction, such as the preparation of deuterated molecules on methods of post-processing of the fibres to modify then and allow investigations of DNA in different conditions.

Appendix A

Optic Microscopy CD

Bibliography

[1] J. Watson, F. Crick, *Nature* **1953**, *171*, 737–738.

[2] A. Rupprecht, *Biochemical and Biophysical Research Communications* **1963**, *12*, 163–168.

[3] J. Duguid, V. Bloomfield, J. Benevides, G. Thomas, *Biophysical Journal* **1996**, *71*, 3350–3360.

[4] R. M. Wartell, A. S. Benight, *Physics Reports (Review Sec of Physics Letters)* **1985**, *126*, 67–107.

[5] M. Peyrard, A. R. Bishop, *Phys. Rev. Lett* **1989**, *62*, 2755.

[6] T. Dauxois, M. Peyrard, A. R. Bishop, *Phys. Rev. E* **1993**, *47*, R44.

[7] A.Wildes, N. Theodorakopoulos, J. Valle-Orero, S. Cuesta-López, J.-L. Garden, M. Peyrard, *Physical Review E* **2011**, *83*, 061923.

[8] A.Wildes, N. Theodorakopoulos, J. Valle-Orero, S. Cuesta-López, J.-L. Garden, M. Peyrard, *Phys. Rev. Lett* **2011**, *106*, 048101.

[9] W. Cochran, *Proc. Royal. Soc. A* **1959**, *253*, 260.

[10] N. Theodorakopoulos, T. Dauxois, M. Peyrard, *Physical Review Letters* **2000**, *85*, 6–9.

[11] L. van Eijck, F. Merzel, S. Rols, J. Olivier, V. T. Forsyth, M. Johnson, *Physical Review Letters* **2011**, *107*, 088102.

[12] J. Valle-Orero, J.-L. Garden, J. Richard, A. Wildes, M. Peyrard, *Journal of Physical Chemistry* **2012. (accepted)**.

[13] G. L. Squires, *Introduction to the theory of thermal neutron scattering*, Cambridge University Press, **1978**.

[14] A. Furrer, J. Mesot, T. Strässle, *Neutron Scattering in Condensed Matter Physics*, J. L. Finney, D. L. Worcester (Eds.), World Scientific, **2009**.

[15] R. Celotta, J. Levine, *Methods of Experimental Physics. Vol 23- part c. Neutron Scattering*, K. Sköld, D. L. Price (Eds.), Academic Press, INC, **1987**.

[16] N. W. Ashcroft, N. D. Mermin, *Solid State Physics*, D. G. Crane (Ed.), Holt-Saunders Internal Editions, **1981**.

[17] L. V. Hove, *Physical Review* **1954**, *95*, 249–262.

[18] P. Giannozzi, S. de Gironcoli, *Phys. Rev. B* **1991**, *43*, 7231–7242.

[19] *http://www.ill.eu/instruments-support/instruments-groups/instruments/in8/.*

[20] *http://www.ill.eu/instruments-support/instruments-groups/.*

[21] *http://www.ansto.gov.au/reseach/bragg_institute/facilities/instruments/taipan.*

[22] M. Cooper, R. Nathans, *Acta Cryst* **1968**, *A 24*, 624.

[23] A.-J. Dianoux, G. Lander (Eds.), *Neutron Data Booklet*, OCP Science, **Second Edition, July 2003**.

[24] J. Als-Nielsen, D. McMorrow, *Elements of Modern X-ray Physics*, Wiley Editorial, **2001**.

[25] J. Baruchel, J. Hodeau, M. Lehmann, J. Regnard, C. Schlenker (Eds.), *Neutron and Synchrotron Radiation for Condensed Matter Studies. Vol 1*, EDP Sciences-Springer-Verlag, **1994**.

[26] *http://www.esrf.eu/UsersAndScience/Experiments/MX/About_our_beamlines/ID14-2.*

[27] *http://www.esrf.eu/UsersAndScience/Experiments/HRRS/ID28/.*

[28] G.Höhne, W. Hemminger, H. J. Flammersheim, *Differential Scanning Calorimetry. An Introduction for Practitioners*, Springer (Ed.).

[29] M. E. Brown, *Handbook of Thermal Analysis and Calorimetry. Vol 1*, Elsevier (Ed.).

[30] H.-J. Hinz, F. P. SCHWARZ, *Pure Appl. Chem* **2001**, *73*, 745–759.

[31] H. K. D. H. Bhadeshia, *Differential Scanning Calorimetry*, Tech. Rep., University of Cambridge, Materials Science & Metallurgy.

[32] R. L. Danley, *Thermochimica Acta* **2003**, *395*, 201–208.

[33] D. R. Nicula, *Introduction to Differential Scanning Calorimetry*, Tech. Rep., Physics Dept., Rostock University, **2002**.

[34] *http://www.dkscience.com/office/p212.htm.*

[35] M. Patt, B. White, B. Stein, E. Cotts, *Thermochimica Acta* **1992**, *197*, 413–424.

[36] I. M. Hodge, R. Heslin, *Journal of Non-Crystalline Solids* **2010**, *356*, 1479–1487.

[37] C. Calladine, H. R. Drew, *UNDERSTANDING DNA. The molecule and how it works.*, Academy Press, **1992**.

[38] M. Peyrard, *Nature Physics* **2006**, *2*, 13–14.

[39] H. B. K J Breslauer, R Frank, L. A. Marky, *PNAS* **1986**, *83*, 3746–3750.

[40] T. Dauxois, N. Theodorakopoulos, M. Peyrard, *Journal of Statistical Physics* **2002**, *107*, 869–891.

[41] E. Ising, *ZEITSCHRIFT FUR PHYSIK* **1925**, *31*, 253–258.

[42] M. Peyrard, S. Cuesta-López, G. James, *J. Biol. Phys* **2009**, *35*, 73–89.

[43] W. Fuller, L. H. Pope, *Biophysical Chemistry* **1998**, *70*, 161–172.

[44] H. Grimm, A. Rupprecht, *Physica B* **1991**, *174*, 291–299.

[45] G. M. T. Cheetham, T. A. Steitz, *Science* **1999**, *286*, 2305–2309.

[46] W. Fuller, T. Forsyth, A. Mahendrasingam, *Phil. Trans. R. Soc. Lond B* **2004**, *359*, 1237.

[47] R. Franklin, R. Gosling, *Nature* **1953**, *171*, 740–741.

[48] R. Langridge, H. R. Wilson, C. W. Hooper, H. F. Wilkins, L. D. Hamilton, *Journal of Molecular Biology* **1960**, *2*, 19–37.

[49] R. Langridge, W. E. Seeds, H. R. Wilson, C. W. Hooper, H. F. Wilkins, L. Hamilton, *Journal of Biophysical and Biochemical Cytology* **1957**, *3*, 767–778.

[50] R. Langridge, D. A. Marvin, W. E. Seeds, H. R. Wilson, C. W. Hooper, H. F. Wilkins, L. D. Hamilton, *Journal of Molecular Biology* **1960**, *2*, 38–64.

[51] W. Fuller, M. H. Wilkins, H. R. Wilson, L. D. Hamilton, *Journal of Molecular Biology* **1965**, *12*, 60–80.

[52] A. A. Lucas, P. Lambin, *Rep. Prog. Phys* **2005**, *68*, 1181–1249.

[53] R. Franklin, R. G. Gosling, *Acta. Cryst* **1953**, *6*, 673–677.

[54] S. Premilat, G. Albiser, *C. R. Acad. Sci. Paris, Sciences de la vie* **1995**, *318*, 553–557.

[55] J. SantaLucia, Jr., H. T. Allawi, P. A. Seneviratne, *Biochemistry* **1996**, *35*, 3555–3562.

[56] K. J. Breslauer, E. Freire, M. Straume, *Methods in Enzymology* **1992**, *211*, 533–567.

[57] G. I. Tsereteli, O. I. Smirnova, *BIOFIZIKA* **1989**, *34*, 905–906.

[58] G. I. Tsereteli, O. I. Smirnova, *BIOFIZIKA* **1990**, *35*, 217–221.

[59] G. I. Tsereteli, O. I. Smirnova, *BIOFIZIKA* **1991**, *36*, 432–436.

[60] G. I. Tsereteli, T. Belopolskaya, N. Grunina, O. Vaveliouk, *Journal of Thermal Analysis and Calorimetry* **2000**, *62*, 89–99.

[61] G. Maret, R. Oldenbourg, G. Winterling, K. Dransfeld, A. Rupprecht, *Colloid & Polymer Sci* **1979**, *257*, 1017.

[62] M. Hakim, S. Lindsay, J. Powell, *Biopolymers* **1984**, *23*, 1185.

[63] H. Grimm, H. Stiller, C. Majkrzak, A. Rupprecht, U. Dahlborg, *Physical Review Letters* **1987**, *59*, 1780–1783.

[64] H. Grimm, P. Gehring, S. Shapiro, R. Kahn, A. Rupprecht, *Physica B-Condensed Matter* **1995**, *213*, 780–782.

[65] M.Krisch, A. Mermet, H. Grimm, V. Forsyth, A. Rupprecht, *Physical Review E* **2006**, *73*.

[66] A. Rupprecht, *Acta Chemica Scandinavica* **1966**, *20*, 494–504.

[67] A. Ziabicki, *Kolloid-Z* **1961**, *175*, 14.

[68] . Piskur, A. Rupprecht, *FEBS Letters* **1995**, *375*, 174–178.

[69] *Sigma Aldrich, Product information sheet D1626: Deoxyribinucleic acid (DNA) sodium salt from salmon testes.*

[70] A. Rupprecht, *Biochimica et Biophysica Acta* **1970**, *204*, 304–316.

[71] A. Rupprecht, *Biochimica et Biophysica Acta* **1970**, *199*, 277–280.

[72] R. Brandes, R. Voldand, D. R. Keans, *Biopolymers* **1988**, *27*, 1159–1170.

[73] S. Zimmerman, B. H. Pheiffer, *J. Mol. Biol* **1980**, *142*, 315–330.

[74] *GenBank [http://www.ncbi.nlm.nih.gov/Genbank/].*

[75] R. Brandes, A. Rupprecht, D. R. Keams, *Biophysics Journal* **1989**, *56*, 683–691.

[76] S. Premilat, G. Albiser, *C. R. Acad. Sci. Paris, Sciences de la vie* **1995**, *318*, 553–557.

[77] S. Zimmerman, B. Pheiffer, *J. Mol. Biol* **1979**, *135*, 1023–1027.

[78] S. Lee, P. Debenedetti, J. Errington, B. Pethica, D. Moore, *J. Phys. Chem. B* **2004**, *108*, 3098–3106.

[79] M. D. Wang, H. Yin, R. Landick, J. Gelles, S. M. Block, *Biophysical Journal* **1997**, *72*, 1335–1346.

[80] I. Rouzina, V. A. Bloomfield, *Biophysical Journal* **1999**, *77*, 3242–3251.

[81] I. Rouzina, V. A. Bloomfield, *Biophysical Journal* **1999**, *77*, 3252–3255.

[82] P. J. Mikulecky, A. L. Feig, *Biochemistry* **2006**, *45*, 604–616.

[83] X.-Q. Mu, *Acta Crystallogr. A* **1998**, *54*, 606.

[84] R. Lavery, M. Moakher, J. H. Maddocks, D. Petkeviciute, K. Zakrzewska, *Nucl. Acids Res.* **2009**, *37*, 5917.

[85] N. Theodorakopoulos, *Phys. Rev. E* **2008**, *77*, 031919.

[86] G. N. Cohen, V. Barbe, D. Flament, M. Galperin, R. Heilig, O. Lecompte, O. Poch, D. Prieur, J. Quérellou, R. Ripp, J. C. Thierry, J. V. der Oost, J. Weissenbach, Y. Zivanovic, P. Forterre, *Mol. Microbiol* **2003**, *47*, 1495.

[87] N. Theodorakopoulos, *Phys. Rev. E* **2010**, *82*, 021905.

[88] C. T. Moynihan, P. B. Macedo, C. J. Montrose, P. K. Gupta, M. Debolt, J. Dill, B. Dom, P. Drake, A. Easteal, P. Elterman, R. Moeller, H. Sasabe, J. Wilder, *Annals of the New York Academy of Sciences* **1976**, *279*, 15–35.

[89] A. Q. Tool, C. G. Eichlin, *J. Am. Ceram. Soc* **1931**, *14 [4]*, 276–308.

[90] J.-L. Garden, H. Guillou, J. Richard, L. Wondraczek, *J. Non-Equilib. Thermodyn.* **2012. (accepted)**.

[91] G. Adam, J. H. Gibbs, *J. Chem. Phys.* **1965**, *43*, 139–146.

[92] R. Svobod, P. Honcova, J. Malek, *Journal of Non-Crystalline Solids* **2011**, *357*, 2163–2169.

[93] R. Svoboda, P. Honcova, J. Malek, *Polymer* **2008**, *49*, 3176–3185.

[94] C. T. Moynihan, A. Easteal, M. A. DeBolt, *Journal of The American Ceramic Societty* **1976**, *59*, 12–15.

[95] J. M. Hutchinson, P. Kumar, *Thermochim. Acta* **2002**, *391*, 197–217.

[96] I. M. Hodge, *J. Non Cryst. Solids* **1994**, *169*, 211–266.

[97] F. Merzel, F. Fontaine-Vive, M. Johnson, G. Kearley, *Physical Review E* **2007**, *76*, 031917.

[98] M. P. T. Dauxois, A. Bishop, *Physical Review E* **1993**, *47*, 684–695.

[99] R. Beger, E.W.Prohofsky, *Biophys. J.* **1992**, *61*, 58–62.

[100] H. Urabe, Y. Tominaga, *Journal of the Physical Society of Japan* **1981**, *50*, 3543–3544.

[101] C. Demarco, S. M. Lindsay, M. Pokorny, J. Powell, A. Rupprecht, *Biopolymers* **1985**, *24*, 2035–2040.

[102] J. Maddox, *Nature* **1989**, *339*, 577.

[103] L. M. Adleman, *Science* **1994**, *266*, 1021–1024.

[104] L. Qian, E. Winfree, *Science* **2011**, *3*, 1196–1201.

[105] R. Podgornik, H. H. Strey, K. Gawrishch, D. C. Rau, A. Rupprecht, V. A. Parsegian, *Proc. Natl. Acad. Sci* **1996**, *93*, 4261–4266.